

Department of Engineering Science

DPhil Thesis

Nanometrology for synchrotron X-ray mirrors

Simone Moriconi

Linacre College



Supervisors:

Prof. Alexander M. Korsunsky

Dr Hongchang Wang (DLS)

Dr Kawal Sawhney (DLS)

January 2024

Acknowledgments

As I culminate this significant milestone of my academic journey with the completion of my DPhil in Engineering Science, I am filled with immense gratitude and a deep sense of appreciation for all those who have guided, supported, and inspired me along this challenging, yet rewarding path.

First and foremost, I extend my heartfelt thanks to my supervisors Professor Alexander M. Korsunsky, Dr Hongchang Wang, and Dr Kawal Sawhney, whose expertise, understanding, and patience have been crucial for the completion of this thesis. Your unwavering support and insightful guidance have been the beacon of light in the intricate journey of my research.

I am deeply grateful to the members of the Optical and Metrology group at Diamond Light Source for their valuable feedback and constructive discussions that significantly shaped my research. Your expertise and thoughtful guidance have been instrumental in refining my work.

My sincere appreciation goes to my colleagues and peers at the University of Oxford, in particular to Dr Alessandro Barberis for the constant encouragement, insightful discussions, shared experiences, and invaluable assistance.

I would like to acknowledge the financial support received from Diamond Light Source and the University of Oxford, which enabled me to fully dedicate myself to my research. I am also grateful to the staff and administrative personnel at Linacre College, whose assistance and support have been fundamental to my research and academic life.

On a personal note, I would like to express my deepest gratitude to my family: my mother Paola Pardini, my father Mauro Moriconi, my sister Catia Moriconi, and my brother-in-law Emanuele Moriconi for their unwavering love, understanding, and support throughout my entire life and my academic pursuits. Your belief in my abilities has been a constant source of strength and motivation. My special thanks go to my partner Luisina Anahí Bello for entering into my life, for her patience, love, and assistance during the last year of my thesis.

Finally, I would like to thank all those who, directly or indirectly, contributed to the success of my research and the completion of this thesis.

Table of Contents

ACKNOWLEDGMENTS ..... **I**

TABLE OF CONTENTS ..... **II**

ABSTRACT ..... **V**

LIST OF FIGURES ..... **VII**

LIST OF TABLES ..... **XII**

LIST OF ABBREVIATIONS ..... **XIV**

1. INTRODUCTION **1**

1.1. BACKGROUND 1

1.2. THE QUEST FOR BETTER METROLOGY 4

2. LITERATURE REVIEW **5**

2.1. NON-CONTACT METROLOGY 5

2.2. PENCIL BEAM INTERFEROMETER 6

2.3. LONG TRACE PROFILER 7

2.4. NANOMETRE OPTICAL METROLOGY 9

2.4.1. Autocollimator *10*

2.5. FIZEAU INTERFEROMETER 13

2.6. STITCHING MICRO-INTERFEROMETER 15

3. SPECKLE ANGLE MEASUREMENT **17**

3.1. EXPERIMENTAL SETUP 21

3.2. DATA ACQUISITION AND STORAGE 22

3.3. ACCURACY AND PRECISION 23

3.4. COORDINATES CONVENTION 25

3.5. CALIBRATION 31

3.5.1. Height Sensitive Angular Scaling Factor *31*

3.6. EFFECTS OF THE SCANNING HEAD ROTATION 32

3.7. EFFECTS OF THE BEAM SPLITTER 33

3.8. EFFECTS OF THE SUT TILTING ANGLE 36

3.8.1. The Associated Systematic Error *38*

3.9. Coordinates Expansion Scaling Factor 41
3.10. SUT Surface Profiles 42
3.10.1. Cylinder 42
3.10.2. Ellipsoid 43
3.11. Simulation 45
3.12. Digital Image Correlation 51
3.12.1. Feature-based Digital Image Correlation 51
3.12.2. Area-based Digital Image Correlation 54
3.13. Object Reconstruction 57
3.14. Digital Filtering 58
3.15. Power Spectral Density 61
4. RESULTS AND DISCUSSION 62
4.1. Calibration 62
4.1.1. Mode 1 63
4.1.2. Mode 2 66
4.1.3. Observations 68
4.1.4. Calibration of Extremely Curved Optics 73
4.2. Simulation of Surface Slope Profiles using NANGO 80
4.3. Stability 83
4.4. Characterisation of Optics 85
4.4.1. Ellipsoid X-ray Mirror 85
4.4.2. Systematic Error Correction 97
4.4.3. Flat Grating Substrate 103
4.4.4. Cylindrical, Low Reflectivity Grating Substrate 109
4.4.5. Comparison between Simulated and Experimental Results 121
4.4.6. Spherical Mirror 123
5. SUMMARY, CONCLUSIONS AND FURTHER WORK 133
5.1. Summary 133
5.2. Conclusions 134
5.3. Further Work 135

5.3.1. SAM for Ion Beam Figuring 135

5.3.2. The Uncertainty Budget 136

5.3.3. Further recommendations 137

6. REFERENCES 138

7. APPENDIX A: COMPARISON OF THE DATA ACQUISITION AND STORAGE METHODS 145

8. APPENDIX B: MODEL OF THE CYLINDRICAL SURFACE PROFILE 147

8.1. SLOPE 147

8.2. INVERSE OF LOCAL RADIUS OF CURVATURE 149

9. APPENDIX C: RESULTS OF THE SLOPE SIMULATION USING NANGO 153

Abstract

Key challenges for developing nanometrology are achieving high precision and accuracy under stringent environmental control to mitigate the impact of temperature, humidity, turbulence, and vibration. Additional complexities arise in accommodating the peculiarities of material behaviour at the nanoscale, in creating complex software to interpret large volumes of data efficiently, and in integrating various technologies within a single user-friendly instrument while managing costs and ensuring accessibility.

This thesis presents advancements in X-ray optics nanometrology using speckle-based analysis on the basis of comprehensive exploration of the full range of innovative techniques for *ex situ* characterisation of X-ray optics.

At the core of this research lies the intellectual challenge of obtaining successful characterisation of strongly curved X-ray mirror profiles (having radii of curvature smaller than 10m) in the form of 2D slope mapping data. The second challenge addressed in the thesis concerns providing the scientific community with an in-depth exploration and analysis of novel techniques and related metrology instrumentation. The thesis elaborates on the advancement of the mathematical models that underpin the new speckle-based metrology techniques. It also details the development of the requisite hardware and software tools.

The research commences with an in-depth background study of synchrotron X-ray mirrors and the necessity for enhanced metrology to underpin further progress at large scale science facilities, such as synchrotron light sources. A thorough literature review is presented to evaluate the existing non-contact metrology methods, including Pencil Beam Interferometer, Long Trace Profiler, Nanometre Optical Metrology, Fizeau Interferometer, and Stitching Micro-Interferometer.

The detailed study of the Speckle Angle Measurement (SAM) technique is presented. The methodology of SAM is expanded upon, including the experimental setup, data acquisition, precision, accuracy, calibration processes, and simulation. Critical analysis is presented of the principal factors influencing SAM, namely, the scanning head rotation and tilting angle of the Sample Under Test (SUT). The findings provide a solid demonstration of the effectiveness of SAM in the complete range of required capabilities, including the calibration, stability, simulation, and characterisation of various optics,

including elliptical X-ray mirrors. The comparison between simulated and experimental results provides validation of the accuracy and applicability of SAM. The thesis concludes by highlighting the potential of SAM for applications such as Ion Beam Figuring at Diamond Light Source (DLS) and by highlighting further areas of research.

List of Figures

Figure 1: Deviations from surface nominal profile 3

Figure 2: Spatial frequency classification of figure errors 3

Figure 3: Schematic of Pencil Beam Interferometer 6

Figure 4: Schematic of the BNL Long Trace Profile 7

Figure 5: Schematic of the LTP-II optical system 8

Figure 6: Schematic of the Diamond-NOM 9

Figure 7: Schematic of an autocollimator 11

Figure 8: SUT tilting effect on the angle of reflection 12

Figure 9: Figure error retrieval of both concave and convex defects 14

Figure 10: Schematic of the HDX, as used at Diamond Light Source Ltd 15

Figure 11: Schematic of the of micro interferometer Buker Contour GT-X 16

Figure 12: F and G represent the speckle images at the reference position and the measured position on the SUT, respectively. Correspondingly, f and g are subsets of F and G. The horizontal and vertical coordinates of the camera are denoted by u and v, while x and y are, respectively, the tangential and sagittal coordinates of the mirror's SUT. Δx is the scanning step size. The real-valued shifts are represented by ξu along the u direction and ξv along the v direction [36]. 19

Figure 13: The SAM instrument is mounted on an air-bearing scan stage, and as the speckle pattern is projected onto different areas of the surface under test (SUT), it shifts due to the reflection from the mirror surface. The angle change can be determined by calculating the speckle displacement between two speckle subset images (f and g) using a sub-pixel tracking algorithm. The pitch error of the carriage slide is measured with an autocollimator, allowing the change in the SUT's slope to be derived from the combined angle data of the SAM and the autocollimator (AC). 20

Figure 14: Schematic of the SAM setup in the Optical and Metrology Lab (OML) at Diamond Light Source Ltd 21

Figure 15: SAM experimental setup in the Optical and Metrology Lab (OML) at Diamond Light Source Ltd 22

Figure 16: Image showing the setup used to test multiple data acquisition techniques 23

Figure 17: Visual representation of accuracy and precision 24

Figure 18: Accuracy and precision in a probability density graph 24
Figure 19: SAM detector image coordinates convention 25
Figure 20: $DIC(x, y)$ sign convention when performing SAM scans along the x-axis of a spherical SUT 26
Figure 21: Schematic of the characterisation of a concave SUT while SAM is translating left to right along the x-axis 27
Figure 22: $DIC(x, y)$ sign convention when performing SAM scan along the y-axis of a spherical SUT. 28
Figure 23: Schematic of the characterisation of a concave SUT while the SUT is translating back to front along the y-axis 29
Figure 24: Schematic representation of SAM scanning head rotation effect on a targeted SUT region of interest 32
Figure 25: Effect of wedged beam splitter on the laser beam path 34
Figure 26: Wedged beam splitter effect simulation when inclined by 45 degrees 36
Figure 27: Schematic of the SUT tilting effect 37
Figure 28: SUT tilting effects on the laser's beam trajectory 39
Figure 29: Simulation results of the SUT tilting effect 40
Figure 30: CESF Vs Radius of Curvature (RoC) 42
Figure 31 SAM simulation software flow diagram 45
Figure 32: Simulated SAM Scan head, SUT tilting and SUT offset effects 49
Figure 33: Simulated effect of beam splitter on laser's beam trajectory 50
Figure 34: Simulated SUT surface profile effects on SAM laser's beam trajectory 50
Figure 35: Simulation of a 1D scan 51
Figure 36: SURF features found in a SAM speckle image 53
Figure 37: SURF method features matches 54
Figure 38: SURF method matches after new constraint is added to the algorithm 54
Figure 39: Two-dimensional digital image (speckles) correlation method (a) and an example of a shifted cameraman image (b) 55
Figure 40: Effect of the strengths of the Gaussian filter on an acquired speckle image 60
Figure 41: Calibration experiment setup using SAM and NANGO 62

Figure 42: (A): Speckle displacement using SAM (mode 1) and NANGO (5000 µrad range). (B): Left picture displaying the calibration's ROI. The right image shows the cross-correlation area used within the ROI. 64
Figure 43: Mode 1 calibration results 66
Figure 44: Mode 2 calibration results using eight different ROI 67
Figure 45: (A): Effect of multiple scans on the mean DIC value and standard deviation reduction, in a 0-5 µrad range. (B): Effect of Averaging scans on ASF, at different calibration ranges 70
Figure 46: (A): Slope of the DIC using mode 1 on the y-axis and the number of steps on the x-axis using only 1 scan, on a 0-5 µrad range. (B): Slope of the DIC using mode 1 on the y-axis and the number of steps on the x-axis using the average of 10 scans, on a 0-5 µrad range 71
Figure 47: XRS-Tech cylindrical crystal physical side scanning setup 73
Figure 48: Calibration scans positions along the x (tangential axis) of the SUT 74
Figure 49: SAM ASF calibration at different SUT's tangential positions 77
Figure 50: Average ASF, calculated at different ROI positions 78
Figure 51: HSASF and SUT distance from SAM detector plane 80
Figure 52: Effect of multiple SAM measurements on accuracy 83
Figure 53: NOM Slope error vs SAM reconstructed slope error 83
Figure 54: Stability results 84
Figure 55: SAM repeatability test results. A second-order polynomial (curve of best fit) was subtracted to reveal the high-frequency error component between multiple scans. 85
Figure 56: Technical drawing of the mirror (a) and of the residuals of the optics elliptical lanes (b) 86
Figure 57: Inverse of local radius of curvature (LRC) from SAM, Diamond-NOM and a Fizeau interferometer (HDX) of the mirror's lane 1 87
Figure 58: CESF to be included when measuring curved optics 87
Figure 59: Image showing the results from all three instruments of the third lane of the ZEISS multilane mirror 88
Figure 60: SAM measurements using different ROI size, compared to the HDX 89
Figure 61: PSD using different SAM ROIs 90
Figure 62: PSD using SAM , HDX and NOM 90
Figure 63: Six scans of the ZEISS ellipse lane slope profile, using the SAM, and their average 92

Figure 64: ZEISS ellipse lane slope error (not filtered) resulting from the subtraction of the ideal ellipse form the various measurements performed with the SAM, the HDX and the NOM.....92
Figure 65: PSD (not filtered) of all metrology instruments (interpolated at SAMs spatial resolution).....93
Figure 66: ZEISS ellipse lane slope error filtered with parameters of Table 27.....93
Figure 67: ZEISS ellipse lane figure error PSD filtered with parameters of Table 27.....94
Figure 68 AC y-axis slope change contribution along the mirror length.....95
Figure 69: Effect on the slope error when adding the AC y slope contribution to SAM slope measurements.....95
Figure 70: ZEISS lane 2 slope error (filtered) using filter parameters of Table 27.....95
Figure 71: Example of a 2D map made using SAM instrument, relative ZEISS multilane mirror lane 2 slope error.....96
Figure 72: ZEISS lane 3 slope error (filtered) using filter parameters of Table 6.....96
Figure 73: Logic used to drive tilting stage motor and reduce its non-linearities.....97
Figure 74: Tilting stage range.....97
Figure 75: Slope estimation using different ROI within SAM acquired images, with tilting stage set to -8000 μrad.....99
Figure 76: Line of best fit using linear regression of each reconstructed slope with different ROI.....101
Figure 77: Flat grating SUT tilt systematic error characterisation.....102
Figure 78: I21PG6 physical side view and experimental setup.....103
Figure 79: Super flat grating slope profiles measured with SAM and SAM scanning head (y-axis) rotation over nine scans.....105
Figure 80: SUT average slope after removing best linear fit.....105
Figure 81: Comparison of SUT slope calculated using SAM, with and without tilt systematic error correction.....106
Figure 82: Comparison between SAM slope without the scanning head rotation correction (red) and with scanning head rotation correction (black).....107
Figure 83: Derivative of the slope. Inverse local radius of curvature of the flat grating.....107
Figure 84: Slope characterisation of the flat grating, using the HDX, NOM, and SAM.....108
Figure 85: Figure characterisation of the flat grating, using the HDX, NOM and SAM.....108
Figure 86: JTEC cylindrical grating experimental setup.....109

Figure 87: Cylindrical grating SUT tilt systematic error characterisation. 113
Figure 88: SUT supported by 3 half spheres at Bessel's points 114
Figure 89: Cylindrical grating slope profiles measured with the SAM and the SAM scanning head (y-axis) rotation, during nine scans 116
Figure 90: SUT average slope after removing best linear fit 117
Figure 91: Comparison of the SUT slope calculated using the SAM, with and without tilt systematic error correction 117
Figure 92: Comparison between the SAM slope without the scanning head rotation correction (red) and with scanning head rotation correction (black) 118
Figure 93: Inverse local radius of curvature of the cylindrical grating 118
Figure 94: CESF effect on the SUT slope measurement and the SUT length retrieved using the SAM .. 119
Figure 95: Slope characterisation of cylindrical grating, using the HDX and the SAM 119
Figure 96: Slope characterisation of the cylindrical grating using the HDX and the SAM 120
Figure 97: Figure characterisation of the flat grating, using the HDX and the SAM 121
Figure 98: Simulation vs Experiment results: a) Flat grating. b) 116m cylinder 122
Figure 99: Difference between simulation and empirical results, for two optics 123
Figure 100: MOONPICS sphere mirror physical side scanning setup (left) / (right) 124
Figure 101: MOONPICS sphere ROI used as template (left) and the ROI used for the DIC (right) 125
Figure 102: Image showing the y-axis rotation angle change of the SAM translation stage along the MOONPICS sphere measured 125
Figure 103: Slope range while measuring the MOONPICS sphere 126
Figure 104: MOONPICS sphere chirped lane slope error (filtered) 126
Figure 105: MOONPICS sphere chirped lane measured inverse LRC during multiple SAM scans 126
Figure 106: Height change of cylindrical profile having RoC of 9.3m 127
Figure 107: Mode 2 detector displacement across the mirror length 129
Figure 108: Mode 2 Slope change at each step across the mirror length 130
Figure 109: Comparison of slope reconstruction techniques 131
Figure 110: Systematic slope error induced by using a fixed ASF and the SAM slope error 131
Figure 111: Systematic slope error induced by using a fixed ASF on multiplied by a factor equal to the fixed percentage change in CESF, compared to with the SAM slope error 132

Figure 112: Slope error after correction 132

Figure 113: SAM for Ion Beam Figuring 136

List of Tables

Table 1: NOM technical specifications 9

Table 2: HDX technical specifications 13

Table 3: Stitching Micro-Interferometer technical specifications 15

Table 4: Metrology instruments at DLS and the SAM benchmark 20

Table 5: SAM results convention and required corrective actions. 30

Table 6: Simulation parameters 40

Table 7: CESF Simulation configuration 41

Table 8: Convolution kernel (low pass filter) 58

Table 9: Calibration hardware settings 63

Table 10: Calibration software setting using mode 1 63

Table 11: Calibration software settings using mode 2 66

Table 12: Difference in ASF using SAM modes 1 and 2. Calibration range: 0-5000 µrad with steps of 100 µrad. 69

Table 13: Difference in ASF calculation of using the SAM mode 2 and derivative of mode 1 cross-correlations techniques 69

Table 14: Difference in ASF calculation of using the SAM mode 1 and integration of mode 2 cross-correlations techniques. 72

Table 15: Difference between the SAM mode 2 (and derivative of mode 1) and mode and mode 1 (and the integration of mode 2) 72

Table 16: Technical details of the XRS-Tech cylindrical crystal 73

Table 17: Calibration configurations 75

Table 18: ASF optimisation at centre of SUT (Sam x-axis coordinate equal to -130 mm) 78

Table 19: XRS-Tech nominal cylindrical profile simulated 79

Table 20: Parameters of the simulation of flat grating slope error profiles using NANGO 81

Table 21: SAM Mode 1-2 accuracy. NOM slope amplified by 100 times 81

Table 22: Mode 1-2 accuracy. NOM slope amplified by 1, used average of 10 scans 82
Table 23: Stability experiment parameters 84
Table 24: Repeatability test parameters 85
Table 25: Technical details of the ZEISS multilane mirror 86
Table 26: Spatial resolution configuration of all instruments 86
Table 27: Low pass filter parameters applied to all instruments figure error data 91
Table 28: ZEISS mirror characterisation experiment hardware and software parameters 91
Table 29: Differences between ZEISS ellipse lane slope errors (not filtered) calculated by different instruments. 93
Table 30: Differences between ZEISS ellipse lane slope errors filtered with parameters of Table 27 94
Table 31: Differences between ZEISS lane 2 slope errors (filtered) using filter parameters of Table 6. 95
Table 32: Differences between ZEISS lane 3 slope errors (filtered) using filter parameters of Table 6. 96
Table 33: ZEISS flat grating characterisation experiment hardware and software parameters 98
Table 34: Line of best fit regressions: results at all tilting angles 100
Table 35: Technical details of the ZEISS flat grating 103
Table 36: Technical specifications of the flat grating SAM scans 104
Table 37: Technical details of the JTEC cylindrical grating 109
Table 38: JTEC Cylindrical silica grating characterisation experiment hardware and software parameters. 110
Table 39: JTEC Cylindrical grating. Line of best fit regressions: results at all tilting angles 111
Table 40: Technical specifications of the cylindrical grating SAM scans: 114
Table 41: SUT radius of curvature characterisation using SAM and HDX 120
Table 42 Technical details of the MOONPICS sphere mirror 124
Table 43: MOONPICS sphere characterisation experiment hardware and software parameters 124
Table 44: Differences between MOONPICS sphere chirped lane slope error (filtered). 126
Table 45: Comparison of the SAM data acquisition and storage methods 145
Table 46: SAM Mode 1-2 accuracy. NOM slope amplified by 50 times 153
Table 47: SAM Mode 1-2 accuracy. NOM slope amplified by 10 times 154
Table 48: Mode 1-2 accuracy. NOM slope amplified by 5, used average of 2 scans 155
Table 49: Mode 1-2 accuracy. NOM slope amplified by 5, used average of 6 scans 156

List of Abbreviations

AC	=	Autocollimator
API	=	Application Programming Interface
CESF	=	Coordinates Expansion Scaling Factor
DIC	=	Digital Image Correlation
EPICS	=	Experimental Physics and Industrial Control System
HDX	=	Zygo Verifire 6” HDX Fizeau interferometer
HSASF	=	Height Sensitive Angular Scaling Factor
NOM	=	Nanometre Optical Metrology
NANGO	=	Diamond Light Source’s nano-angle generator
SAM	=	Speckle Angular Measurement
SUT	=	Sample Under Test
PSD	=	Power Spectral Density
px	=	Pixels
RoC	=	Radius of Curvature
RMS	=	Root Mean Square
RMSE	=	Root Mean Square Error
ROI	=	Region Of Interest

1. Introduction

Dimensional metrology is essential in many high-tech industries, including at synchrotron light sources. One of the most critical aspects of metrology is the ability to measure the topographical features of optical surfaces accurately and precisely. This chapter provides the general background on the metrology of synchrotron X-ray mirrors, and the motivation for developing a novel non-contact metrology instrument.

1.1. Background

Synchrotrons are large scale machines for particle acceleration and storage using electromagnetic devices such as RF cavities, bending magnets, wigglers, and undulators. Synchrotrons can be classified according to their principal field of application into two significant categories: high-energy physics and photon science.

Photon science synchrotrons are optimised to produce electromagnetic waves in the form of 'light' beams with specific characteristics depending on the range of intended applications. Diamond Light Source (DLS) is the UK national synchrotron that provides intense beams of X-rays for more than 30 diverse beamlines using the stored electron beam at 3 GeV, typical of a medium-energy synchrotron. DLS is one of more than 50 such facilities around the world [1].

Diverse X-ray instruments allow studying the characteristics of widely varied objects and processes, such as intrinsic properties of materials, viruses and vaccines, meteorites, antique artefacts, chemical reactions, etc. [2]. Each beamline is optimised for a particular type of experiment, but all beamlines have three main sections: the optics hutch, where the X-ray beam is conditioned; the experimental hutch, where the light interacts with the sample being studied; and the control cabin, where users run the experiment and collect data [2]. Optical components direct, tune, and focus X-ray beams on the samples. Some typical optics components include Laue lenses [3], Fresnel Zone Plates [4], Compound Refractive Lenses [5,6], monochromators [7], and X-ray mirrors.

Total external reflection is encountered under a minimal grazing incidence angle (a few mrad) between an X-ray beam and the material surface. It arises due to the refractive index of solids for X-rays being typically less than unity [8,9,10]. Bragg reflection can be used for multilayer coatings with alternating high and low density sublayers [11]. The advantages of mirrors compared to other optical components (lenses, zone plates) are

achromaticity (independence of the beam wavelength) and high efficiency. Given the shallow angles of incidence, reflecting the entire X-ray beam requires extremely long mirrors that bring with them the challenge of precise characterisation and control of their profile. A beamline may house a few (~5) or many (~20) X-ray mirrors designed to work in particular environments, e.g. under high heat load, cryogenic temperatures, and ultra-high vacuum. Their physical dimensions can vary from around 50 to 1500 mm in length and about 20 to 300 mm in width, depending on the required specifications. X-ray mirror substrates can be made from silicon, glass or silicon carbide, and coating can be made from heavy metals such as gold (Au), rhodium (Rh), platinum (Pt) and palladium (Pd) to enhance the mirror's X-ray reflectivity. An X-ray mirror can also be classed by the nominal profile of its geometrical surface, such as flat, elliptical, parabolic, and toroidal, and are characterised along their meridional plane (i.e. tangentially, along the beam-propagation direction) and in the sagittal (transverse) direction [12,13]. Nominal profiles can have radii of curvature varying from around tens of millimetres to hundreds of kilometres. A single X-ray mirror can take more than one year to manufacture, and its cost can vary from a few thousand GBP to a quarter of a million GBP.

X-ray mirrors can direct and concentrate bright synchrotron X-ray beams into sub-micron focal spots at a sample in the experimental hutch. Given the very short X-ray wavelength from about 0.01 to 10 nm, even small aberrations on the order of nanometres on the mirror surface degrade these mirrors' performance and focusing capabilities. Extremely high resolution, high sensitivity instruments are required to create and maintain X-ray optics components for diffraction-limited and coherence-preserving experiments [14].

The aim of characterising the surface of a mirror or any other sample under test (SUT) is to determine how much the manufactured or current surface deviates from the required profile. This deviation is caused predominantly by roughness, waviness and form errors [15].

High precision deterministic surface polishing methods such as Ion Beam Figuring (IBF) [16], Elastic Emission Machining (EEM) [17], and preferential deposition [18] enable manufacture of mirrors with height error (height deviation from ideal profile) of less than 1 nm peak-to-valley (PV), and slope errors (slope deviations from the ideal form) below 100 nrad root mean square (RMS) [19]. The present state-of-the-art lab-based metrology techniques for X-ray mirrors are limited to the precision of ~25 nrad. To improve further

the polishing quality and the resulting performance of X-ray mirrors, metrology techniques need to be advanced beyond the present state-of-the-art.

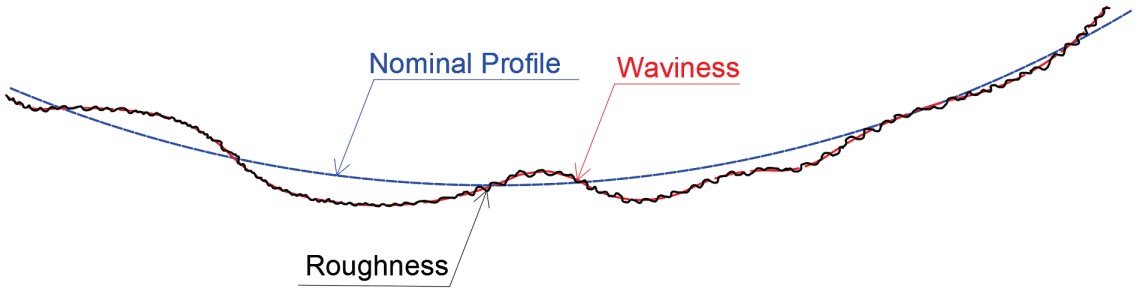

Figure 1: Deviations from surface nominal profile

The deviation from a nominal profile, in the form of waviness and roughness, represented in Figure 1, can be characterised at different spatial frequencies. Low spatial frequency errors have a typical scale (wavelength) above a few millimetres, while middle and high spatial frequency errors correspond to scales from a few millimetres down to ~100 µm and from ~100 µm down to a few nm, respectively [20]. Figure 2 provides an illustration of the power spectral distribution (PSD), also known as power spectral density. If a log-log plot of the PSD is used, the curve follows an inclined, linear trend, due to the prevailing power law relationship [21].

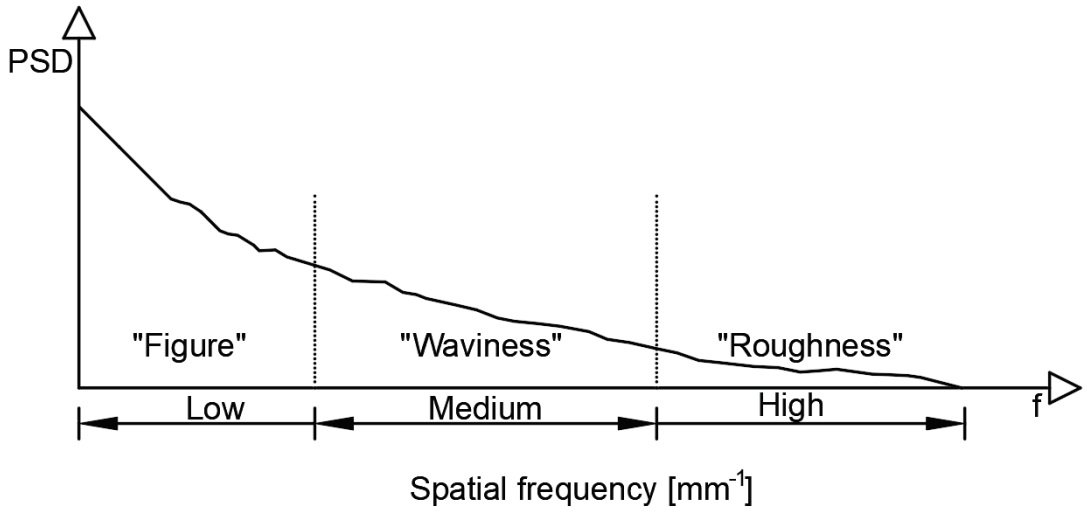

Figure 2: Spatial frequency classification of figure errors

1.2. The Quest for Better Metrology

Wavefront sensing techniques can precisely measure the X-ray beam structure and associated aberrations and thus provide quantitative information about the phase change induced by inserting a sample into the photon beam. Recent years have witnessed the development of various *in situ* metrology and at-wavelength metrology techniques, such as the knife-edge technique [22], Hartmann wavefront sensors [23] (the Shack-Hartmann sensor [24] is one of the most commonly used instruments for wavefront sensing in the visible light regime and plays an important role in adaptive optics and lens testing [25]), Fresnel propagation iterative algorithms [26], ptychography [27], grating interferometry [28] and near-field speckle-based techniques. These methods have been developed and applied to characterise different types of X-ray optics [14]. These techniques also help to minimise the errors due to imperfections and misalignments in the beamline optics used upstream of the sample, including monochromators and transmission windows. These problems become more evident with active optics used in the strive to achieve nano-focusing, such as piezo bimorph mirrors. The principle of X-ray near-field speckle is used in X-ray phase contrast imaging, coherence measurements and mirror metrology [29,30,31,32,33,34]. The X-ray speckle-based technique allows high-sensitivity measurement of deflection angles in a simple experimental arrangement [25]. It has been extensively developed at Diamond Light Source (DLS) in the X-ray regime to reach unprecedented angular sensitivity of <10 nrad [35]. Although measurements with synchrotron X-rays offer powerful metrology tools, synchrotron beamlines are often oversubscribed, and access to beamtime may take weeks or months [14]. Synchrotron beamlines are also not routinely accessible to industrial manufacturers of optics. This leads to the urgent need to develop novel metrology techniques capable of quick, precise, and accurate *ex situ* measurement for optics characterisation to achieve sub-nano-focusing capabilities.

In this thesis, I present the latest development of the speckle angular measurement [36] (SAM) metrology instrument, an off-beamline apparatus operated using a visible light laser, capable of achieving precision and accuracy down to 20 nrad RMS, providing significant benefits to the mirror manufacturers and users of X-ray optics alike.

2. Literature Review

Contact-based measurement methods were traditionally used for form metrology, but they have several limitations, including damaging or altering the object being measured, which leads to measurement inaccuracies. These limitations have motivated the development and advancement of non-contact metrology instruments, which can determine the surface features without touching the measured object. This chapter provides an overview of non-contact metrology instruments used at synchrotron facilities to characterise X-ray mirrors.

2.1. Non-contact Metrology

Current non-contact metrology instruments for X-ray mirror figure determination can be classified into those based on the stitching of sub-aperture maps and those based on deflectometry of a narrow beam (so called "pencil beam"). These methods differ vastly in accuracy, measurement speed, angle range, experimental setup, and signal recorded.

Stitching methods, such as the relative angle determinable stitching interferometry (RADSI) [37,38], the stitching Shack-Hartmann optical Head (SSH-OH)[39], or tilt-measurement-based stitching interferometry (TSI)[40] rely on the measurement in multiple small overlapping sub-aperture regions to overcome the limited spatial or angular range of a single two-dimensional (2D) figure measurement. However, stitching adjacent regions together is often complicated and can be affected by cumulative systematic errors.

Different metrology instruments characterise X-ray mirrors over specific spatial frequency ranges. These instruments are used by many of the synchrotron facilities around the world and by manufacturers of optics. To record low spatial frequency errors of the sample under test (SUT), long trace profilers (LTP) and Nanometre Optical Metrology (NOM) [41] are used at Diamond Light Source (DLS) [2] in the UK, the Advanced Light Source (ALS) and NSLS-II in the United States, Soleil and the European Synchrotron Radiation Facility (ESRF) in France, HZB in Germany, and the Super Photon ring-8 (SPRing-8) in Japan.

2.2. Pencil Beam Interferometer

The pencil beam interferometer (PBI) was initially developed by K. von Bieren at Rockwell International, RoCketdyne Division in 1982 [42], where the *interference* of two pencil beams is used to characterise the surface of the sample under test (SUT).

Figure 3 provides a schematic illustration of the PBI [42,43,44]. A pencil beam generated by a laser source is divided into two pencil beams when passing through a beam splitter. One beam is transmitted towards a mirror, while the other is reflected towards the second beam splitter. The then generated two parallel beams are separated by a fixed spacing distance M and are directed to the SUT using a pentaprism, a five-sided reflecting prism used to deviate a beam of light by the fixed angle of 90°, even if the entry beam is not incident at 90° to the prism. Thanks to the geometry of pentaprisms, the instrument is insensitive to small angle variations and can compensate for imperfections during the translation stage. The reflected beams are then retransmitted through the pentaprism and the second beam splitter. Passing through a Fourier transform lens generates an interference fringe at the focal plane of the lens, caused by the recombination of the two pencil beams. This information is then collected by a detector. The procedure is repeated by moving the pentaprism along the SUT so that the data about the surface profile can be retrieved. A disadvantage of such a system is that it is prone to depth-of-field issues, making it unsuitable to scan long optical surfaces, especially if the nominal profile is not close to a flat surface.

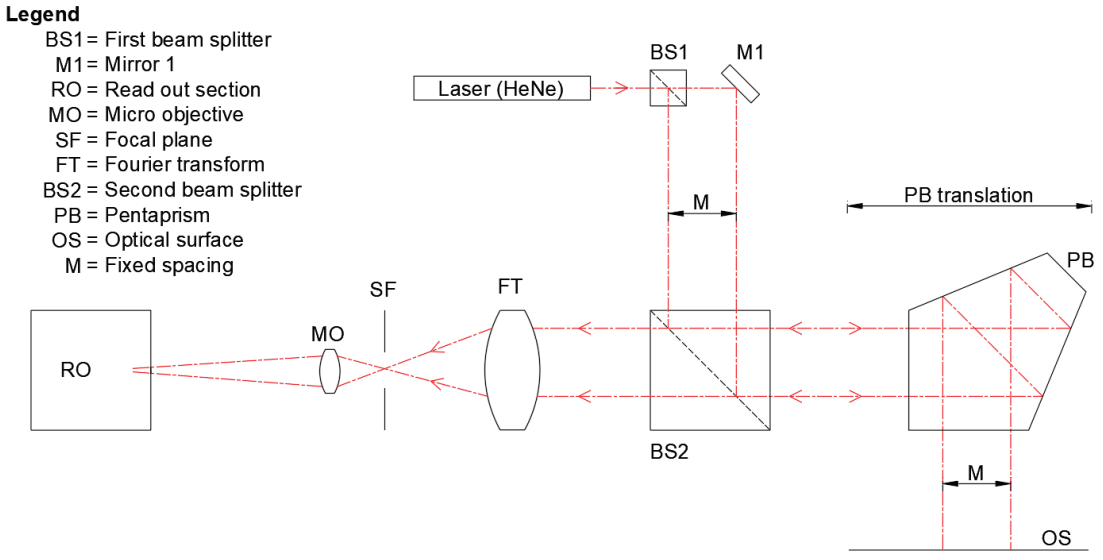

Figure 3: Schematic of Pencil Beam Interferometer

2.3. Long Trace Profiler

Based on the pencil beam interferometer principle, the Long Trace Profiler (LTP) was originally developed in 1987 [45]. Figure 4 is the schematic representation of the LTP. The main difference of this device from the PBI is that it resolved the problem of the limited depth-of-field associated with the use of the pentaprism. To scan the surface under test, the optical head moves along a high-precision linear air bearing translation stage while the SUT is positioned under the beam splitter number two (BS2).

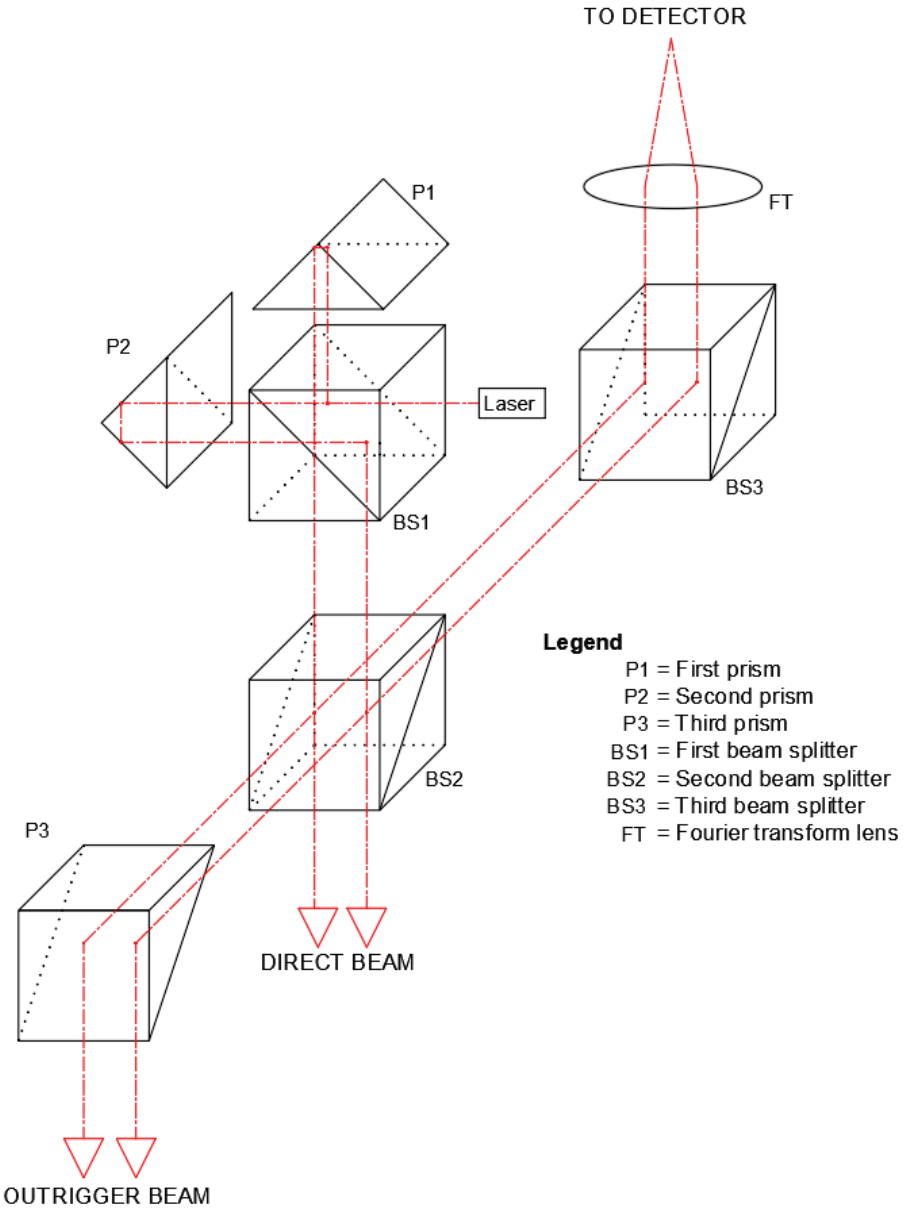

Figure 4: Schematic of the BNL Long Trace Profile

A further development of this approach is the LTP-II shown in Figure 5, where the distance between the two beams can be adjusted by moving a prism, giving the user the flexibility to select the desired lateral spatial resolution of the instrument. Also, a reference mirror is used to track changes in slope due to a pitch angle variation of the Scanning head along the air bearing translation stage. This change in slope is then added to the test surface value to get the correct surface slope. Integration of these slope values along the direction of scanning results in the height information of the surface required to characterise and correct figure errors [46].

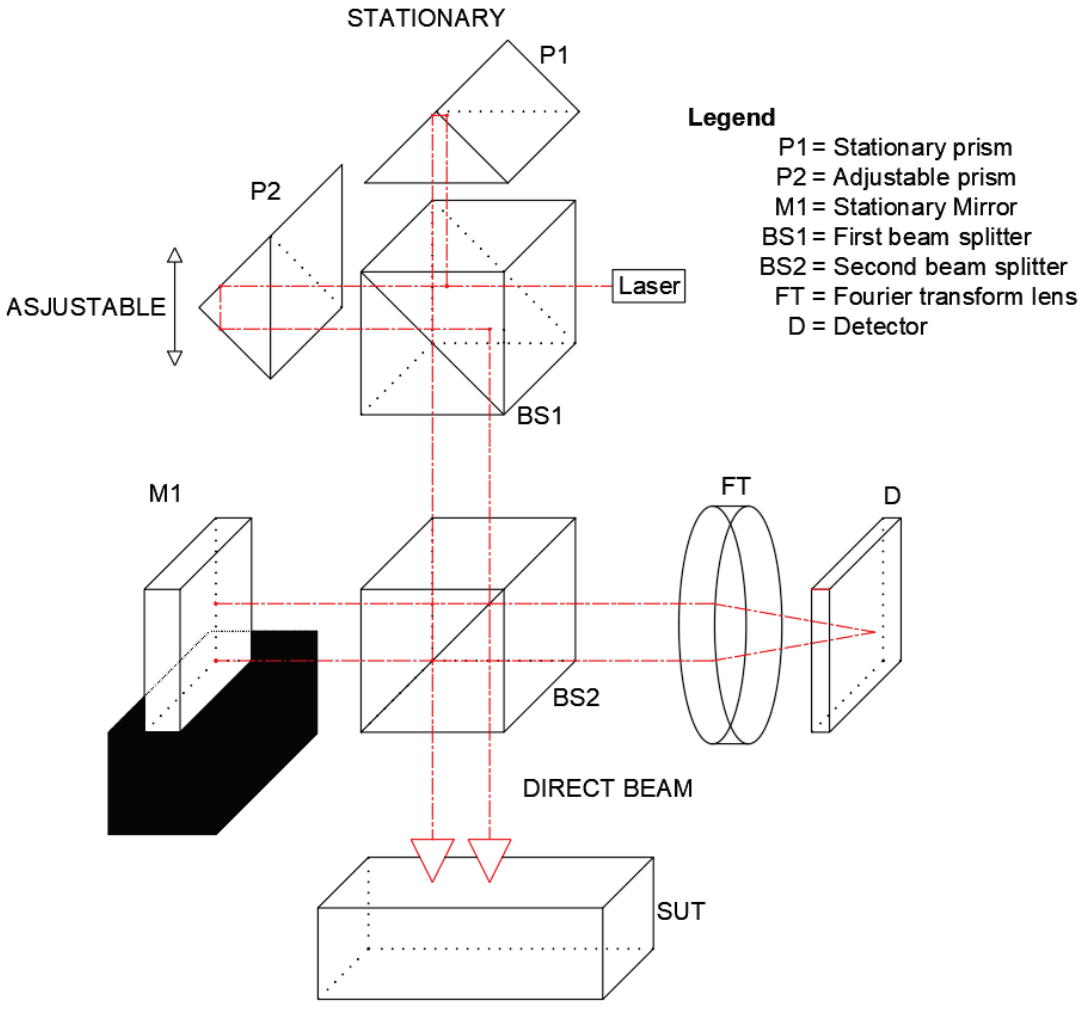

Figure 5: Schematic of the LTP-II optical system

More developments have been made in the last decade, and the LTP evolved with time, resulting in reliable surface slope error measurements down to 0.5 µrad root mean square (RMS).

2.4. Nanometre Optical Metrology

The Nanometre Optical Metrology (NOM) was first developed in Germany at BESSY (now HZB) in early 2000's [47]. As with the LTP, different versions of the NOM have emerged over the years. The Diamond NOM shown in Figure 6 has been in use in the Optics Metrology lab at DLS [48] since 2007. Table 1 presents the main technical specifications of the NOM.

Table 1: NOM technical specifications

Type	Lateral scan size	Lateral resolution	Precision
Slope profilometry	1.5 m	$< 2*10^{-3}$ m	$< 45*10^{-9}$ rad RMS

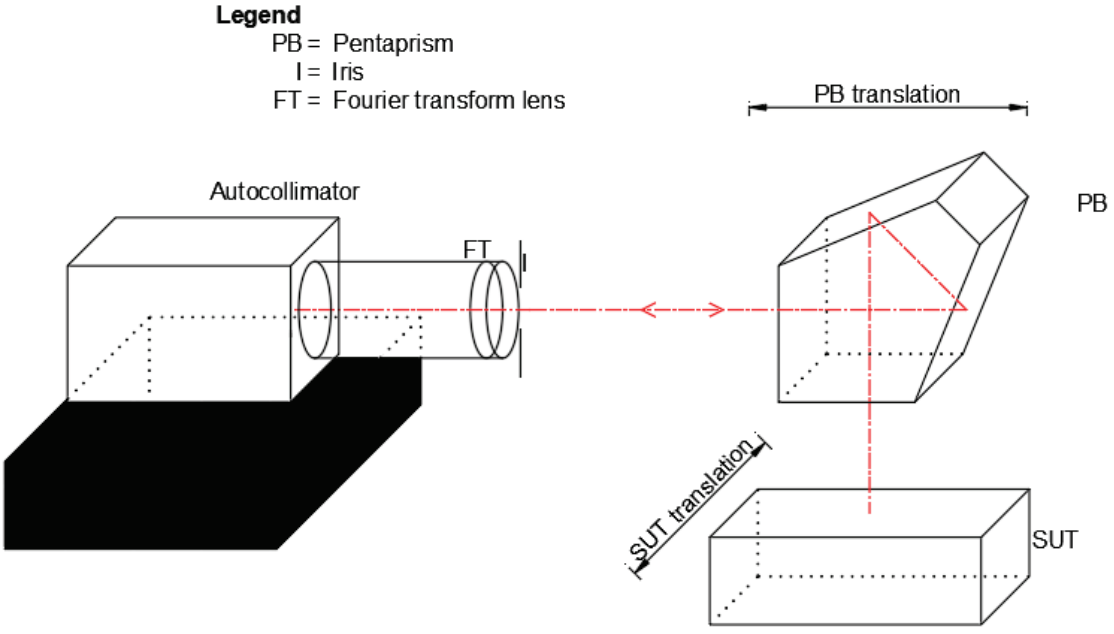

Figure 6: Schematic of the Diamond-NOM

Diamond-NOM can characterise X-ray mirrors with dimensions up to 1.7*1.0*1.0 m^3 in length/width/height respectively and with slope errors of less than 45 nrad RMS. The Diamond-NOM is able to measure the X-ray mirrors facing upwards, downwards, or sideways [49]. The technology is based on a scanning pentaprism and autocollimator concept. The autocollimator used for the Diamond-NOM is a commercial instrument, the ELCOMAT 3000 from Moeller-Wedel [50]. A disadvantage of this method is its reliance on the quality of the optical faces and internal glass structure of the pentaprism, which introduces some (even if minimal) errors in the measurement of the SUT.

The most recent development in the Diamond-NOM, the Diamond Ve-NOM, employs multiple autocollimators, which are synchronised with movements of the motion stage. This enables optical surfaces to be assessed swiftly [51].

2.4.1. Autocollimator

The autocollimator (AC) employs a collimated light source to assess small surface slope deviations in reflecting surfaces. A schematic representation of an autocollimator is shown in Figure 7. It comprises a light source (typically a laser or filament lamp which emits a beam of light), a slit (usually shaped as a cross, pinhole or fixed aperture), and then the emitted, divergent beam is passed through a lens to create a collimated (i.e. parallel) beam. The lateral resolution of the instrument is set by the aperture in front of the objective lens located close to the SUT. When employed to characterise X-ray mirrors, the aperture must be small. A disadvantage of the reduction in the aperture is the increase in aliasing errors of the instrument [52], such as the saw tooth periodic error due to the µm-pixel pitch of the CCD detector [53].

The collimated light beam is directed onto a beam splitter, which reflects it onto a mirror or the target surface under examination. When the collimated light beam strikes the surface, it reflects towards the beam splitter. A fraction of this reflected light passes through the beam splitter and is directed towards a viewing element, such as a reticle, eyepiece, or CCD detector. The position of the reflected light against the reference marks scale within the viewing element or reference image is then observed and measured.

The angular deviation or displacement of the reflected beam, as perceived within the viewing element, is directly proportional to the angular variation of the mirror or target surface. The sensitivity and accuracy of an autocollimator are contingent on several factors, including the quality of optical components, the light source's stability, and the measurement element's resolution and precision.

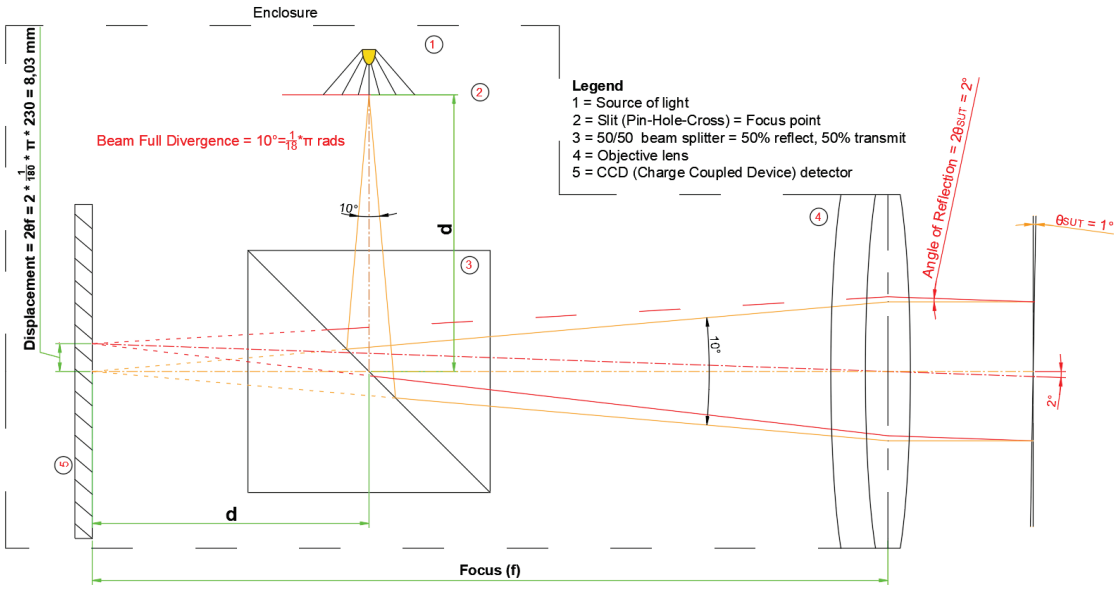

Figure 7: Schematic of an autocollimator

The displacement at the detector Δs (expressed in millimetres) is given by equation (1):

$$\Delta s(mm) = 2\theta_{SUT} * f \tag{1}$$

Here θ_{SUT} is the angle change in radians, and f is the objective lens focal length (in millimetres). Rearranging equation (1), θ_{SUT} can be retrieved, as shown in equation (2):

$$\theta_{SUT} = \frac{\Delta s}{2f} \tag{2}$$

When inducing a change in the angle of the reflecting surface, as represented in Figure 8, the angle of incidence θ_i (the angle between the incident ray and the normal to the surface) remains equal to the angle of reflection θ_r (the angle between the reflected ray and the normal to the surface). A tilt in the SUT angle (θ_{SUT}) generates an absolute angle of reflection change equal to two times the angle θ_{SUT}, leading to the absolute angle of reflection θ, expressed in equation (3).

$$\theta = \theta_r + 2\theta_{SUT} \tag{3}$$

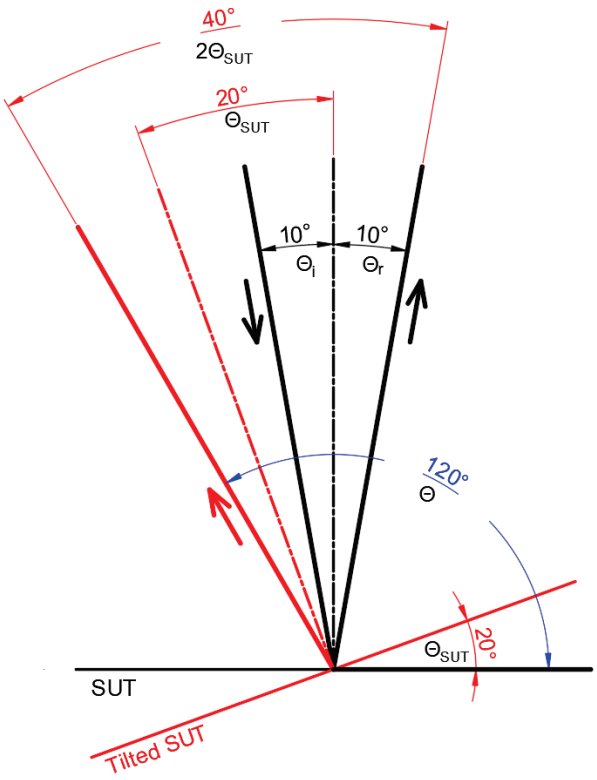

Figure 8: SUT tilting effect on the angle of reflection

2.5. Fizeau Interferometer

The Fizeau Interferometer is a Phase Shifting Interferometer (PSI); It is used to characterise low and medium spatial frequency errors of optical surfaces. Many metrology labs use commercially available Fizeau interferometers, such as the HDX from Zygo, which is capable of producing a stabilised laser beam of 150 mm diameter. An 11-megapixel (3392*3392) CCD sensor acquires interferograms at a frame rate of 96 Hz. This fast rate helps in reducing random noise by performing adequate averaging. The phase shifting is achieved by translating the reference flat optic at set distances from the SUT [54]. The accuracy of this system is limited by the quality and the calibration of the reference flat (λ/20) optic. Recent calibration has enabled the HDX in OML to accurately and precisely measure curved optics with slope errors with an RMS error of less than 50 nrad [21]. Table 2 presents the main technical specifications of the HDX.

Table 2: HDX technical specifications

Type	Lateral max scan size	Beam diameter	Planar accuracy
3D height measurement	1.8 m	$150*10^{-3}$m	λ/100 PV

The SUT is measured in different orientations and at multiple positions to minimise systematic errors associated with the reference flat. These multiple scans are then averaged to "randomise" systematic errors.

The relationship between surface height error for the mirror being tested and fringe deviation is shown in Figure 9 and equation (4).

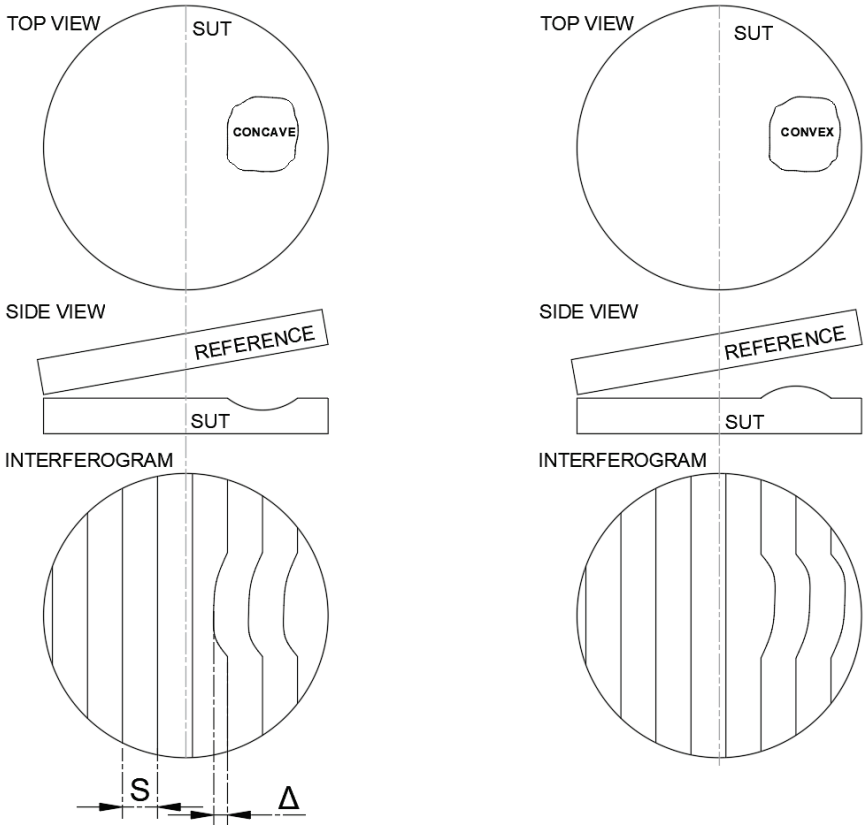

Figure 9: Figure error retrieval of both concave and convex defects

$$Surface\ height\ error\ (nm) = \left(\frac{\lambda}{2}\right) * \left(\frac{\Delta}{S}\right) \quad (4)$$

Here, λ is the wavelength of the light source (nm), while Δ and S are the height deviation and distance between two fringes, respectively, expressed in nm [55].

Most interferometers, to automatically calculate the height profile from the measured phase maps, analyse multiple interference fringes obtained by multiple phase-shifting images.

The system is further augmented by a stitching mechanism, facilitating data integration from a suite of translation stages where the SUT is positioned and moved. Stitching algorithms merge the fringes captured by the interferometer utilising the hardware illustrated in Figure 10 [49], resulting in reliable feedback for the 2D deterministic polishing process [56]. The schematic represents the Zygo Verifire 6" HDX Fizeau interferometer mounted on an in-house-built, modular support platform, as used at Diamond Light Source. Its motorised stages for the HDX stitching system precisely translate and rotate the test optics in front of the Fizeau's beam.

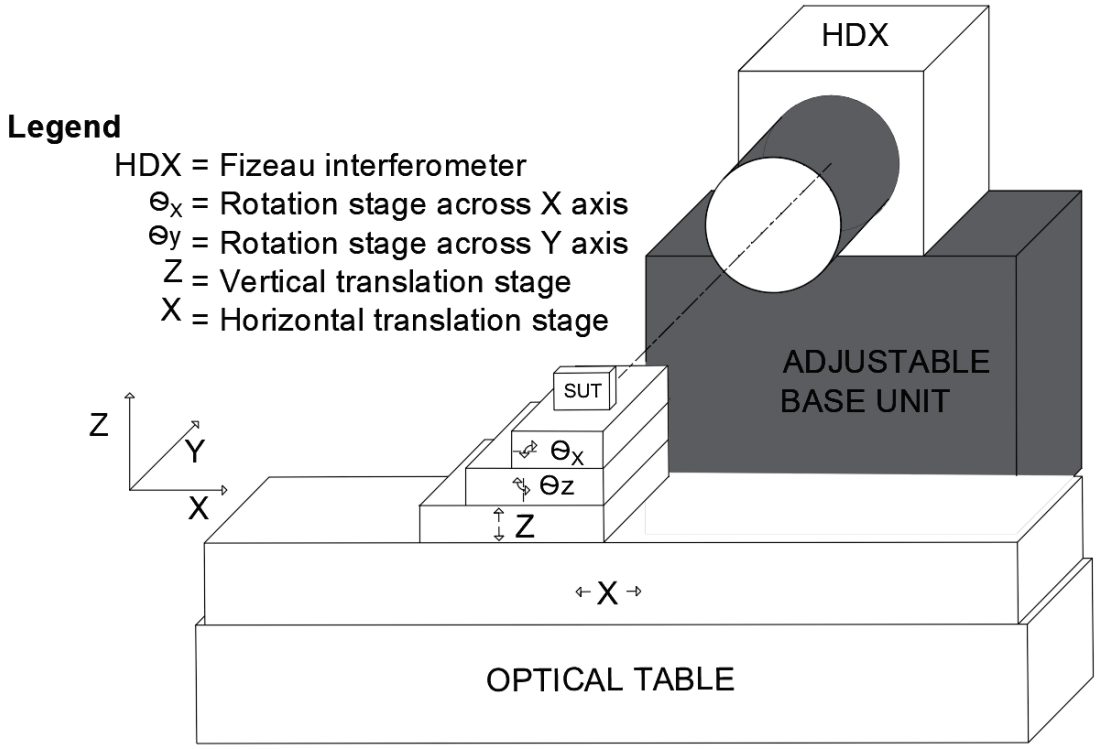

Figure 10: Schematic of the HDX, as used at Diamond Light Source Ltd

2.6. Stitching Micro-interferometer

This phase shifting interference microscope combines an interferometer and a microscope into a single instrument. It is employed to describe errors in surface medium and high spatial frequency. Figure 11 shows a schematic representation of a Bruker Contour GT-X OMM Micro-Interferometer. It supports Vertical Scanning Interferometry (VSI) and Phase-Shifting Interferometry (PSI) measurement modes. Table 3 presents the main technical specifications of the Stitching Micro-Interferometer.

Table 3: Stitching Micro-Interferometer technical specifications

Type	Lateral max scan size	Lateral resolution	Vertical resolution
3D micro-topography	10 mm (stitching)	$0.1*10^{-6}$ m	$<0.05*10^{-9}$ m RMS

The VSI mode is suited for measuring objects with rough surfaces or pixel-height differences of more than 135 nm and typically uses a white light source. When the camera collects images, an internal translation stage moves with respect to the SUT. The modulation peaks every time the surface comes into focus with the instrument during translation.

The PSI mode employs a fixed wavelength light source (about 540nm for green light) when the SUT has a smooth surface with a roughness < 30 nm. This mode reaches its maximum when the height difference between neighbouring pixels approaches a quarter of the wavelength of the light source (135nm).

A piezo-driven translation stage shifts the partially transmitting optic within the interferometric objective, causing a shift in the fringe pattern. The camera captures multiple shifting fringes, resulting in a sequence of interferograms processed by automated algorithms to calculate the SUT's surface height profile. [57].

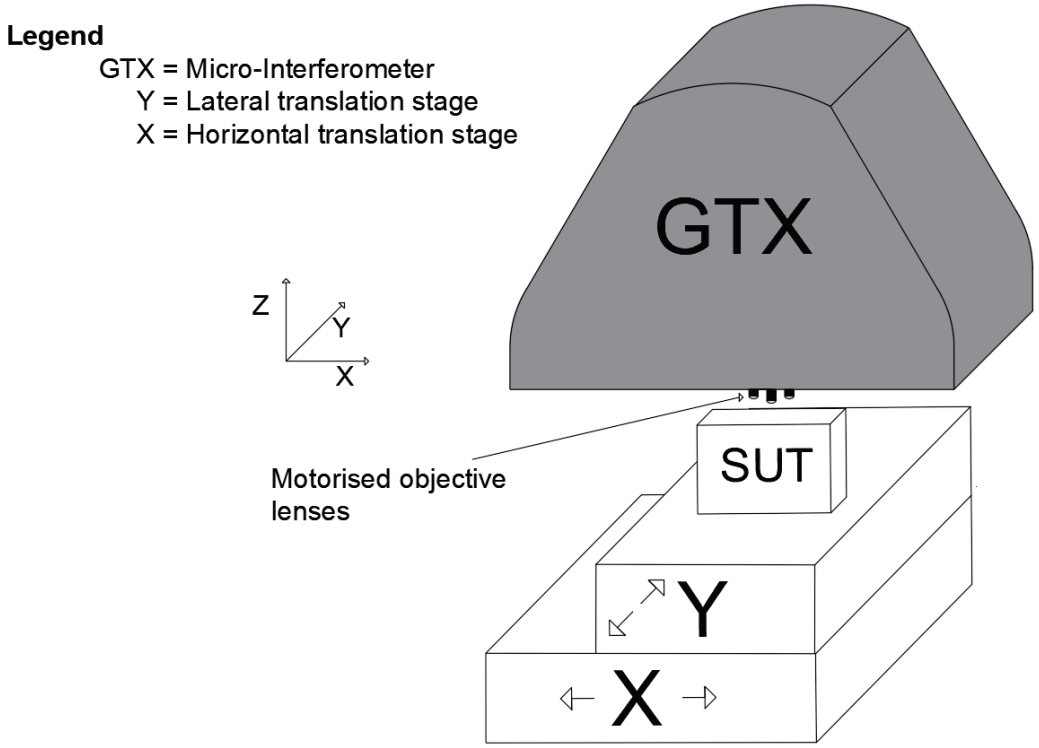

Figure 11: Schematic of the of micro interferometer Buker Contour GT-X

Stitching interferometry is practical for producing dense 2D maps of the SUT, which improves the broad range of data for the entire surface and the capacity to identify surface flaws and shape errors.

3. Speckle Angle Measurement

In this chapter I present the laser Speckle Angular Measurement (SAM). I also explain the methodologies utilised for the development of the novel nanometrology instrument for synchrotron X-ray mirrors, corroborating the capabilities of the SAM.

To overcome the limitations of the present metrology techniques, I propose using the so-called SAM optical scanning head [36]. Shining a laser through a diffuser generates 2D random intensity patterns (speckle). The rays generated in this way can be treated as multiple pencil beams with different features. The variations of the X-ray mirror slope over the area of the mirror under interrogation cause shifts of the speckle pattern. The slope variation of the surface under test (SUT) can then be measured at the nanoradian level in two dimensions by precisely tracking the speckle displacement using an advanced sub-pixel algorithm.

The mean speckle size (ss) at the camera plane can be expressed as follows:

$$ss = \frac{\lambda L}{D} \tag{5}$$

Where λ is the wavelength of the light, D is the aperture of the iris, and L is the distance traversed by the laser beam from the iris to the camera via the SUT and the beam splitter [36].

As the SAM instrument is translated using the scanning carriage, the beam is projected onto various regions of the SUT. In this context, the speckle pattern serves as a carrier of the SUT's surface information. If the surface is of high quality, without any slope discontinuities, the speckle pattern recorded by the camera experiences only a shift that is dependent on the SUT's slope variation. Since each speckle pattern possesses unique characteristics, the speckle can be regarded as a set of multiple wavefront markers. The pitch error of the carriage slide introduces a systematic error by similarly shifting the speckle. To monitor and correct this error, a reference visible-light mirror is attached to the scanning stage to reflect the light beam from the autocollimator (AC) fixed on one side of the carriage's slide. The slide's pitch error remains within tens of micro-radians by using a high-precision air-bearing translation stage. Averaging multiple scans and increasing the samples help in improving the precision.

In this configuration, the tracking of the speckle is characterised by two coordinates system (*x,y*) and (*u,v*), shown in Figure 12.

Considering a single speckle image, a displacement (δ_u,δ_v) between two pixels on the camera corresponds to a displacement between the equivalent observation points (δ_x,δ_y) on the SUT:

$$\begin{cases} \delta_x = \Gamma_x \, \delta_v \\ \delta_y = \Gamma_y \, \delta_u \end{cases} \tag{6}$$

Where Γ_x and Γ_y are scaling factors influenced by the beam's divergence from the diffuser. They can be determined experimentally [36].

Two methods for processing data from linear scans of the SAM head along the SUT are outlined and illustrated in Figure 12. In Mode 1, a speckle image from a selected area of the SUT is designated as the reference image F(u,v). Images G(u,v) from other regions of the SUT are then compared to this reference. This comparison provides a direct measurement of the surface slope, which is the first derivative of the surface height. In Mode 2, the speckle image F(u,v) taken at one scan position is compared with the image G(u,v) from the subsequent position. The difference in speckle patterns between these consecutive images reflects the second derivative of the surface height, or the reciprocal of the local radius of curvature. In both modes, the speckle patterns in F(u,v) and G(u,v) are divided into subsets to provide the required spatial resolution [36].

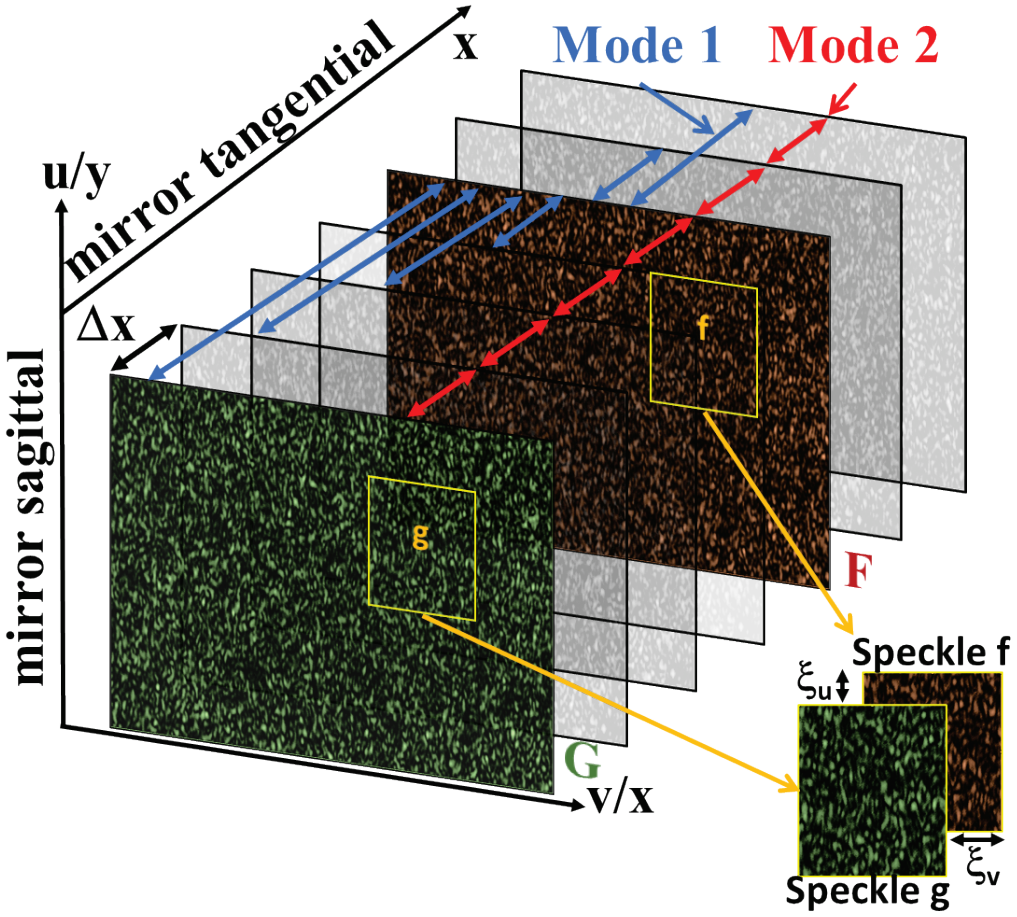

Figure 12: F and G represent the speckle images at the reference position and the measured position on the SUT, respectively. Correspondingly, f and g are subsets of F and G. The horizontal and vertical coordinates of the camera are denoted by u and v, while x and y are, respectively, the tangential and sagittal coordinates of the mirror's SUT. Δx is the scanning step size. The real-valued shifts are represented by ξ_u along the u direction and ξ_v along the v direction [36].

The instrument based on SAM is compact, low-cost, and easy to integrate with most existing pencil beam-based metrology instruments such as the LTP and the NOM. Finally, SAM can measure areas of the mirror as small as 0.1 mm wide, compared with 2-3 mm wide for the LTP or the NOM. All these remarkable features have the potential to make the proposed SAM metrology technique widely available for nanometrology of low and medium spatial frequency errors and consequent advancement of the next generation of X-ray mirror nano-metrology characterisation. The principle components of SAM[36] are illustrated in Figure 13.

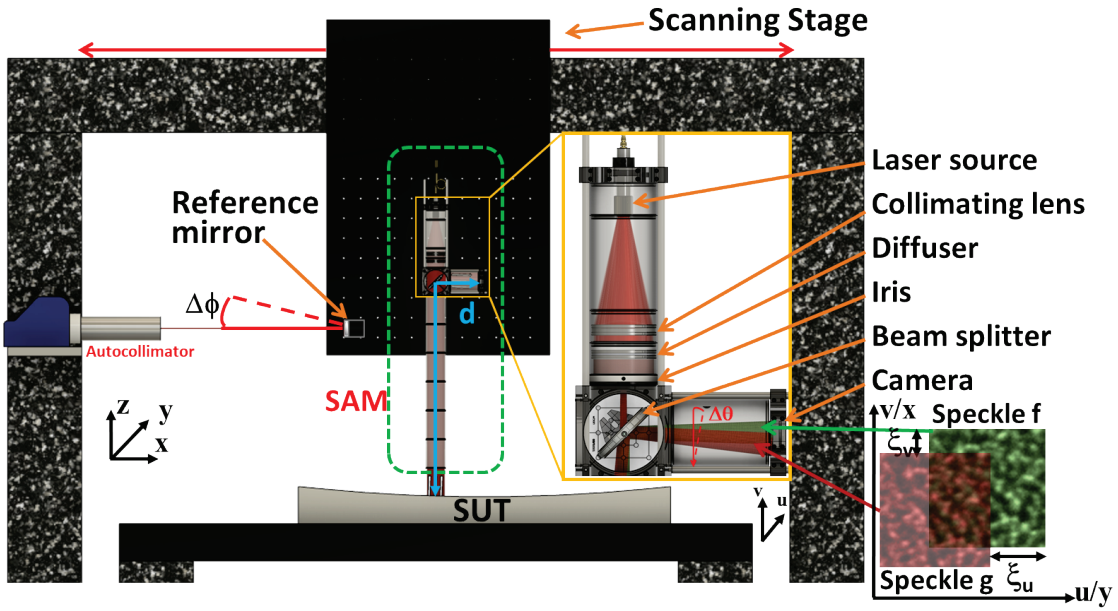

Figure 13: The SAM instrument is mounted on an air-bearing scan stage, and as the speckle pattern is projected onto different areas of the surface under test (SUT), it shifts due to the reflection from the mirror surface. The angle change can be determined by calculating the speckle displacement between two speckle subset images (f and g) using a sub-pixel tracking algorithm. The pitch error of the carriage slide is measured with an autocollimator, allowing the change in the SUT's slope to be derived from the combined angle data of the SAM and the autocollimator (AC).

The benchmarking of the novel instrument compared to the currently available metrology instruments at DLS is shown in Table 4. This highlights its potential in terms of capability and versatility.

Table 4: Metrology instruments at DLS and the SAM benchmark

	Metrology Instrument			
	NOM	**HDX**	**GTX.**	**SAM**
lateral scan size [mm]	≤ 1500	≥ 150 ≤ 1800	≥ 0.050 ≤ 4 (*)	**≤ 1500**
Lateral Resolution [mm]	≤ 2	/	≥ 0.0001 ≤ 0.01	**≥ 0.05 ≤ 6**
Source type	LED	HP HeNe	Dual-LED	**LED**
Source wavelength [nm]	660	633	Multiple	**530**
Direct Measurement type	Slope	Height	Height	**Local RoC**
Spatial Frequency	Low	Medium	High	**Medium**
Minimum RoC [m]	> 5	< 9 (**)	< 0.1	**< 0.5**
2D Map	No	Yes	Yes	**Yes**
Open-source hardware	No	No	No	**Yes**
Open-source software	No	No	No	**Yes**
(*) Plus stitching				
(**) If using flat reference optics and without zoom factor				

3.1. Experimental Setup

All experiments were carried out at Diamond Light Source Ltd, in the Optical and Metrology Laboratory, using the Nanometre Optical Metrology enclosure, gantry, and translation stages, as shown in Figure 14.

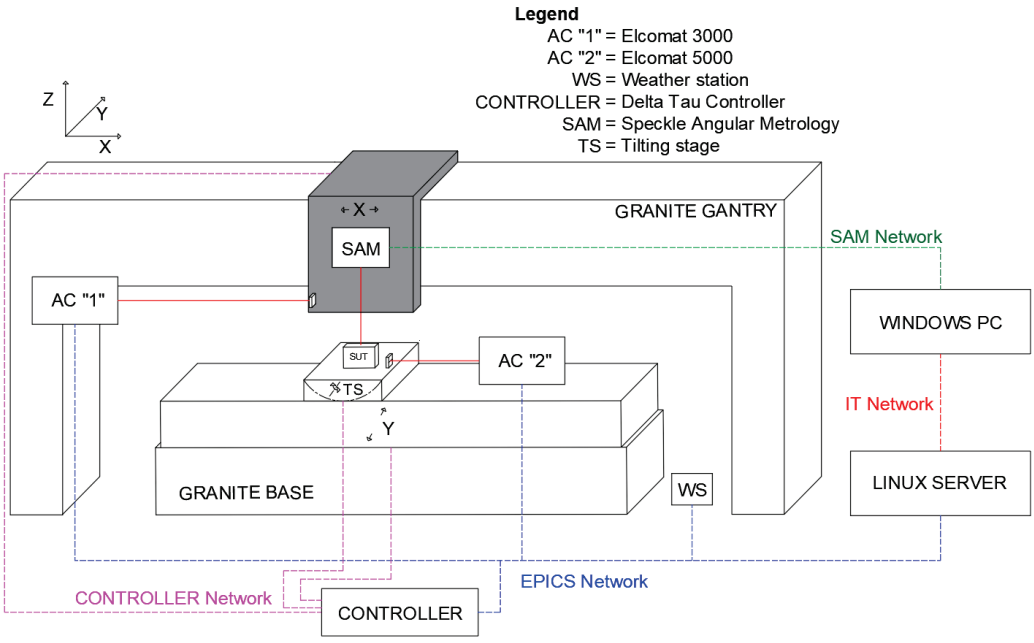

Figure 14: Schematic of the SAM setup in the Optical and Metrology Lab (OML) at Diamond Light Source Ltd

The Elcomat 3000 (25Hz sample rate) was used to detect parasitic angle changes around the y-axis. This resulted in a systematic error in the X-ray mirror characterisation in the form of change in the SUT slope. At the same time, the SAM scanning head moved along the translation stage (x-axis), also referred to as the tangential scans in either the right or left direction[13], over the SUT. 2D speckle images were collected at set spatial intervals along the translation axes to characterise the optics. The Elcomat 5000 (250Hz sample rate) was used to accurately detect the angle variations of the tilting stage (TS). This stage was also used to calibrate the SAM. It can also be used to increase the measuring range of the SAM when characterising strongly curved optics. To provide a 2D surface map of a sample under test, the SUT was shifted, at set spatial intervals, along the y-axis.

A Vaisala weather station was also used to monitor and record temperature, humidity, and atmospheric pressure. DLS control systems primarily employ embedded computer systems that interface with the controlled equipment. These systems are interconnected via a network to workstations and offer additional functionalities. They rely on the

Experimental Physics and Industrial Control System (EPICS) toolkit, an open-source software platform widely adopted by numerous large-scale facilities [58]. The detector used to develop the SAM is from XIMEA, and the software used to control is installed in a Windows operating system. To combine DLS control systems with the SAM control system, a Python package designed to work on Python 3.7 was developed as part of this thesis. A Python Interface to the Epics Channel Access protocol of the Epics control system, called PyEpics, was used to control the DLS hardware (Diamond-NOM translation stages, autocollimators and weather station) via a Linux server. To control the Ximea detector, a Python Application Programming Interface (API) called xiAPI was used. This approach enabled the synchronisation of the hardware and the ability to perform multiple tasks simultaneously, from data acquisition to data analysis. The outcome is a finite state automation system capable of self-calibration, alignment, data acquisition and analysis. As both SAM hardware and software are open-source, they allow the user to customise the instrument, for example, choosing the most suitable filter or the region of interest (ROI) to optimise the characterisation of the SUT.

An accurate representation of the experimental setup is shown in Figure 15.

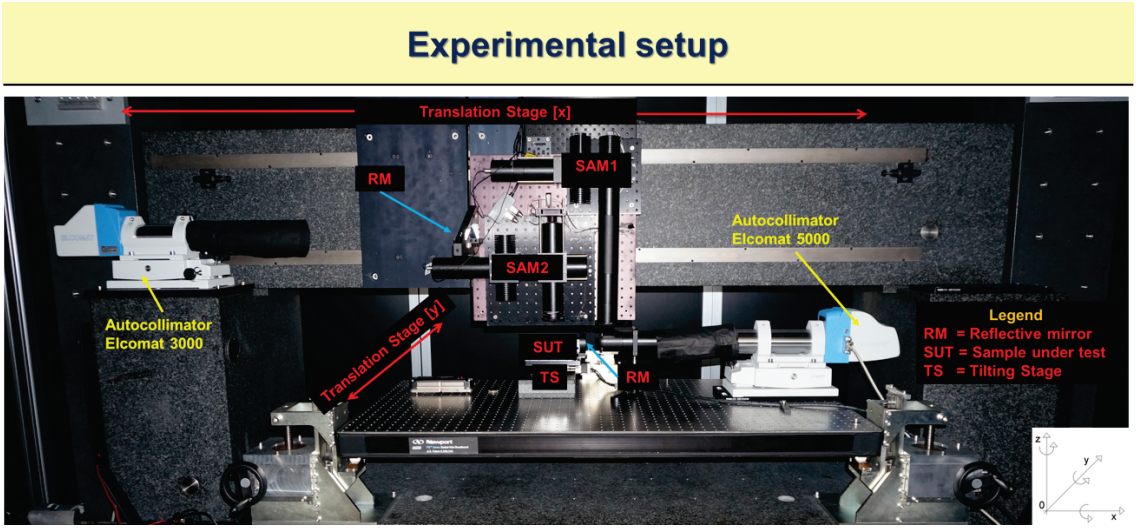

Figure 15: SAM experimental setup in the Optical and Metrology Lab (OML) at Diamond Light Source Ltd

3.2. Data Acquisition and Storage

To evaluate and compare several strategies to determine the best method for rapid and reliable data acquisition and storage, an experiment was carried out in the Precision Metrology Lab (PML) at Diamond Light Source Ltd. The experiment gathered stability

data from the SAM and employed the detector XIMEA MU181CR-ON. A reflecting mirror was added to the SAM tube to achieve optimal stability. A schematic of the SAM hardware used is shown in Figure 16. The cross-correlation method used was mode 1.

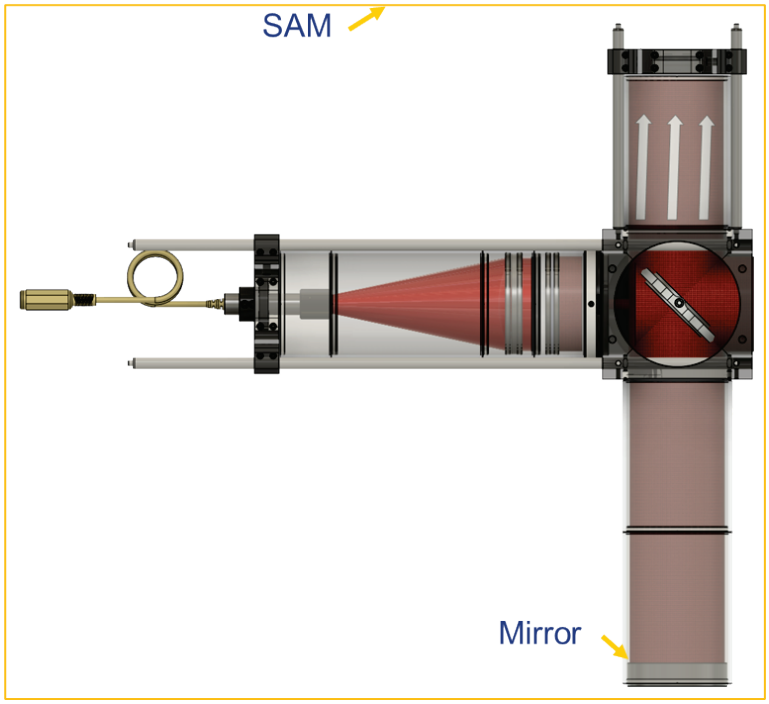

Figure 16: Image showing the setup used to test multiple data acquisition techniques

The quickest and most stable solution has been identified as acquiring single images and saving them on a solid-state drive, as shown in Appendix A. Unless otherwise specified, this configuration was used as the default mode of operation for SAM data acquisition and storage.

3.3. Accuracy and Precision

When performing measurements, the paramount factors to consider are both the accuracy (how close the measured values are to the true value) and precision (how close the measured values are to each other) of the metrology instrument used. They can be visualised using the target analogy, as shown in Figure 17.

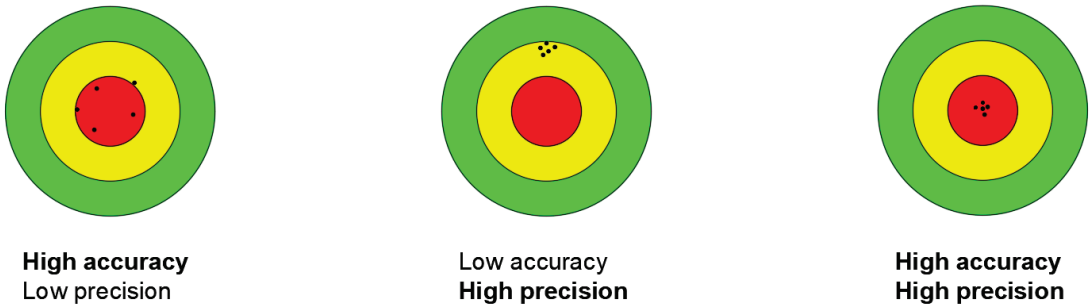

Figure 17: Visual representation of accuracy and precision

Another way to characterise accuracy and precision is by observing the measurements probability density graph, where accuracy can be expressed as the distance between the true (or reference) value and the average of the measured values, and precision as the range between the minimum and maximum measured values, as shown in Figure 18.

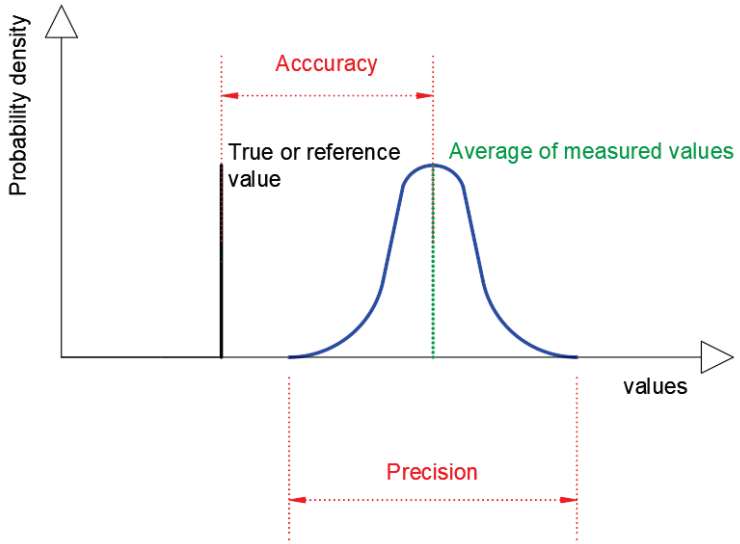

Figure 18: Accuracy and precision in a probability density graph

The SAM precision is capable in ideal conditions to measure slope profiles having an RMS error of 20 nrad [36].

It is impossible to know with 100% accuracy a true measurement of an object; there always will be uncertainty in the measurement obtained. When testing a metrology instrument, the most used and widely accepted way to test its accuracy is to compare the surface characterisation obtained with the instrument under test (in this case, the SAM) with other metrology instruments. This procedure helps to test various working principles and expose each instrument to various systematic and random errors. The Nano Optical Metrology (NOM) and the Fizeau Interferometer (HDX) were used to compare and

certify the quality of the measurements obtained with the SAM. In particular, the measured slope and figure error between each instrument were compared.

3.4. Coordinates Convention

The drawback of installing SAM on a translation stage, as shown in Figure 14, is that it is prone to accumulating errors derived by all axes used during measurement, resulting in a potential false characterisation of the SUT's slope. To understand and correct such systematic errors while performing a 1D scan along the x-axis, two autocollimators are employed, as shown in Figure 15. To standardise the SAM measurement outputs, I established a coordinates convention system.

First, I established the SAM detector image coordinates convention. The speckle image acquired by SAM can be represented by a matrix (M_{ixj}), being i the row and j the column of the image's pixel intensities. The origin point is the top left corner of the speckle image, also called M_{0x0}, with increasing numbering going towards the image's bottom (matrix rows) and right (matrix columns), as shown in Figure 19. Any anticlockwise rotation around the x or y axis is considered positive.

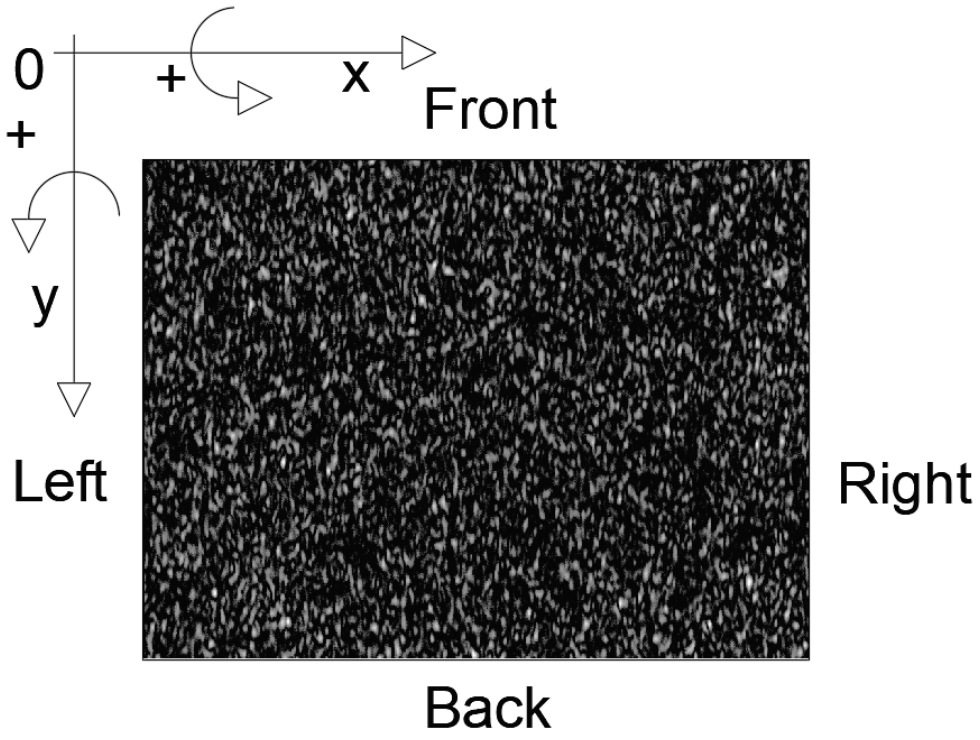

Figure 19: SAM detector image coordinates convention

When measuring a concave, cylindrical surface profile with SAM, as illustrated in Figure 21, the translation of SAM scanning head from left to right shall result in a positive 1D slope measurement, assuming that the SUT is perfectly aligned with respect to SAM. When calculating the DIC using SAM Mode 2 [36], the cross-correlation output shall be a positive DIC_x (equivalent to a shift of the speckles from right to left), as shown in Figure 20. If, instead, the SAM cross-correlation method Mode 1 [36] is used, the DIC is performed by comparing all images obtained during a 1D scan with a single reference image. In this case, all the images acquired before the reference image shall result in a negative DIC_x, while all images taken after the reference image shall result in a positive DIC_x. DIC_y will be equivalent to zero across the entire scan.

If instead, for example, a 2D concave surface, such as a sphere is measured using SAM, the DIC_y sign will depend on the SUT y-position used when the scan along the x-axis is performed), as illustrated in Figure 20.

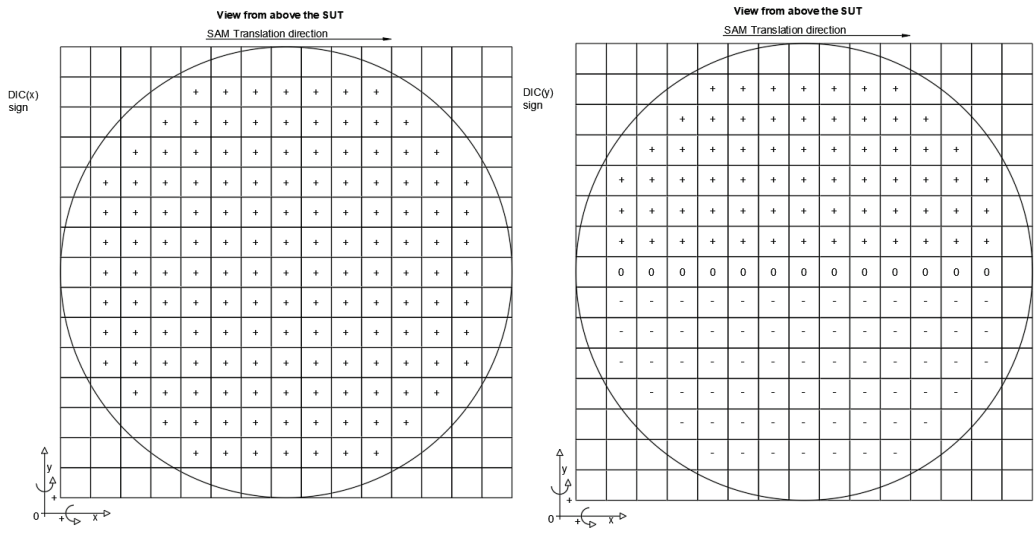

Figure 20: $DIC_{(x,y)}$ *sign convention when performing SAM scans along the x-axis of a spherical SUT*

Suppose I assume that the DIC results $(DIC_x,\ DIC_y)$ after all the possible corrections from Table 5 are met, any anticlockwise SAM scanning head rotation around the y-axis results in an added speckle shift that shall be quantified and removed, as shown in Figure 21. Anticlockwise rotations of the SAM scanning heads result in positive measurements along the autocollimator's y-axis that must be subtracted from the SAM slope measurements.

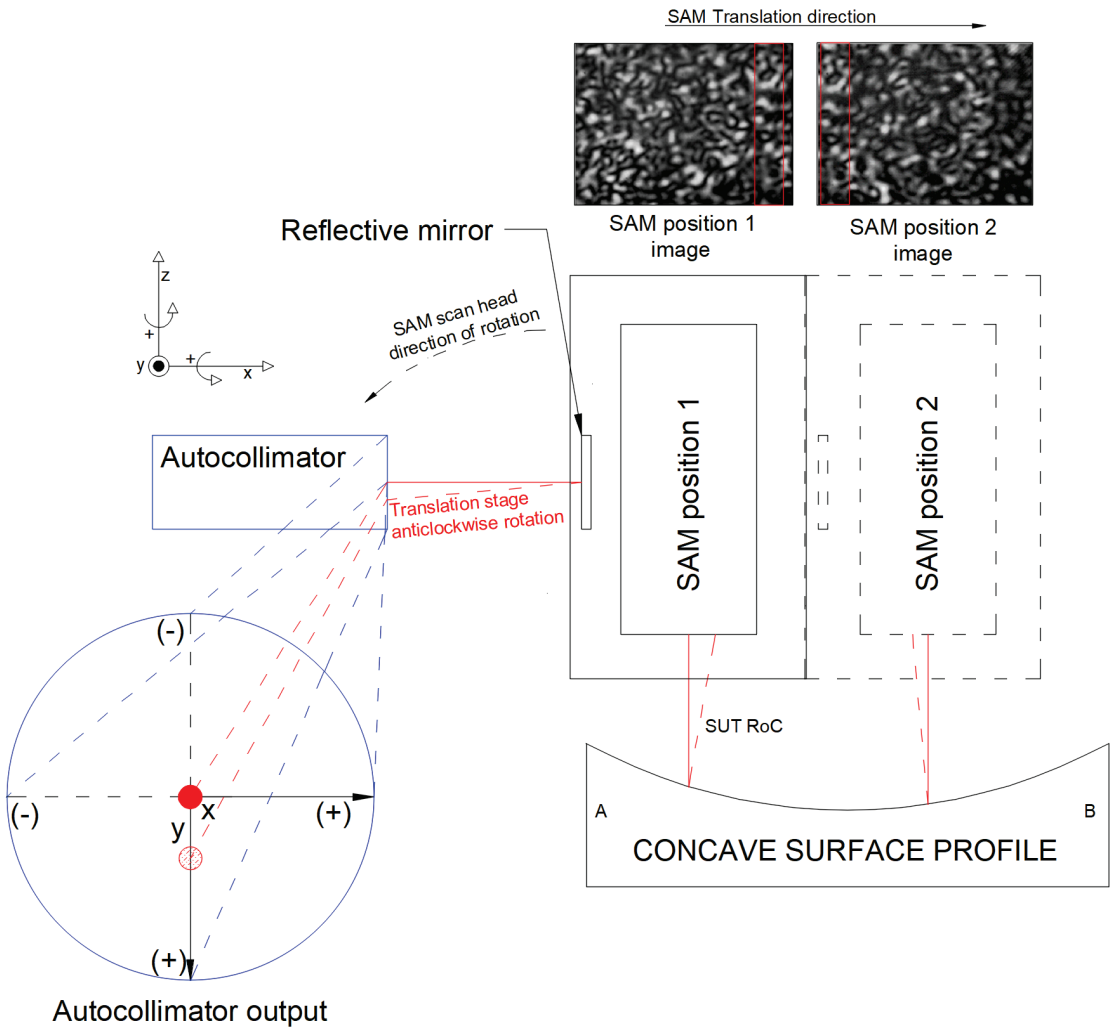

Figure 21: Schematic of the characterisation of a concave SUT while SAM is translating left to right along the x-axis

If a scan along the y-axis is performed instead, and assuming that the DIC results (DIC_x, DIC_y) after all the possible corrections from Table 5 are met, and an autocollimator is positioned perpendicular to the y-axis, any anticlockwise rotation around the x-axis of the translating stage, in this case, the y-axis, results in a reduced shift to the speckle pattern, equivalent to a positive autocollimator measurement along its y-axis, thus the latter must be added to SAM slope measurements. A schematic representation of this example is shown in Figure 22 and Figure 23.

Any detected change in the autocollimator measurements along its x-axis represents a rotation of the SAM scanning head around the z-axis.

To conclude, if the DIC_x results after possible corrections from Table 5 are met, the slope profile of the SUT can be retrieved using the SAM and autocollimator (AC) setup, as shown in equations (7) and (8) :

$$For\ left\ to\ right\ scan\ along\ x-axis$$

$$SAM_{corrected\ slope\ (x)} = SAM_{X\ slope} + AC_{Y\ slope} \tag{7}$$

- Here the AC is installed perpendicular to the x-axis

$$For\ \ back\ to\ front\ scan\ along\ y-axis$$

$$SAM_{corrected\ slope\ (x)} = SAM_{y\ slope} - AC_{Y\ slope} \tag{8}$$

- Here the AC is installed perpendicular to the y-axis

When characterising a close to flat optical surface profiles using SAM, the scanning head parasitic angle change is a major systematic error, because the figure slope range is very narrow. For a strongly curved optical profile, this error becomes almost negligible. For example, if a tangentially cylindrical profile with a radius of curvature of about 9.3m, and thus a slope range of more than 8000 μrad across a mirror length of 100 mm, a SAM scanning head rotation along the x-axis of about 3 μrad overall, would generate a slope error of less than 0.04%.

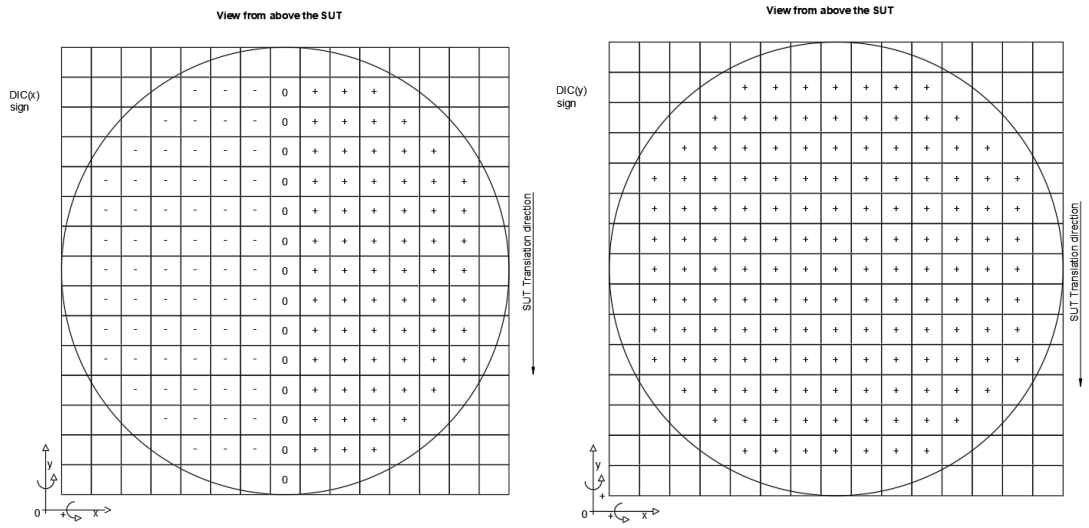

Figure 22: $DIC_{(x,y)}$ sign convention when performing SAM scan along the y-axis of a spherical SUT

When it is required to measure a concave surface profile via translating the y-axis, the SAM scanning head remains stationary at a determined position (x-axis). In contrast, the SUT is translated along the y-axis, thanks to the dynamic optical table where the SUT is installed, as shown in Figure 23. In this condition, the y-stage is the active part of the system. Therefore, the y-stage shall be monitored for possible parasitic angle changes using the autocollimator. The translation of the SUT from positive to negative y-axis

coordinates (back to front direction) shall result in a positive slope measurement, as the result of a positive DIC_y (equivalent to a shift within the images of the speckles from bottom to top) and a variable sign of the DIC_x, depending on the x-axis coordinate position used when the scan along the y-axis is performed, as shown in Figure 22. To produce a 2D characterisation of a SUT, scans along the x and y axes are required.

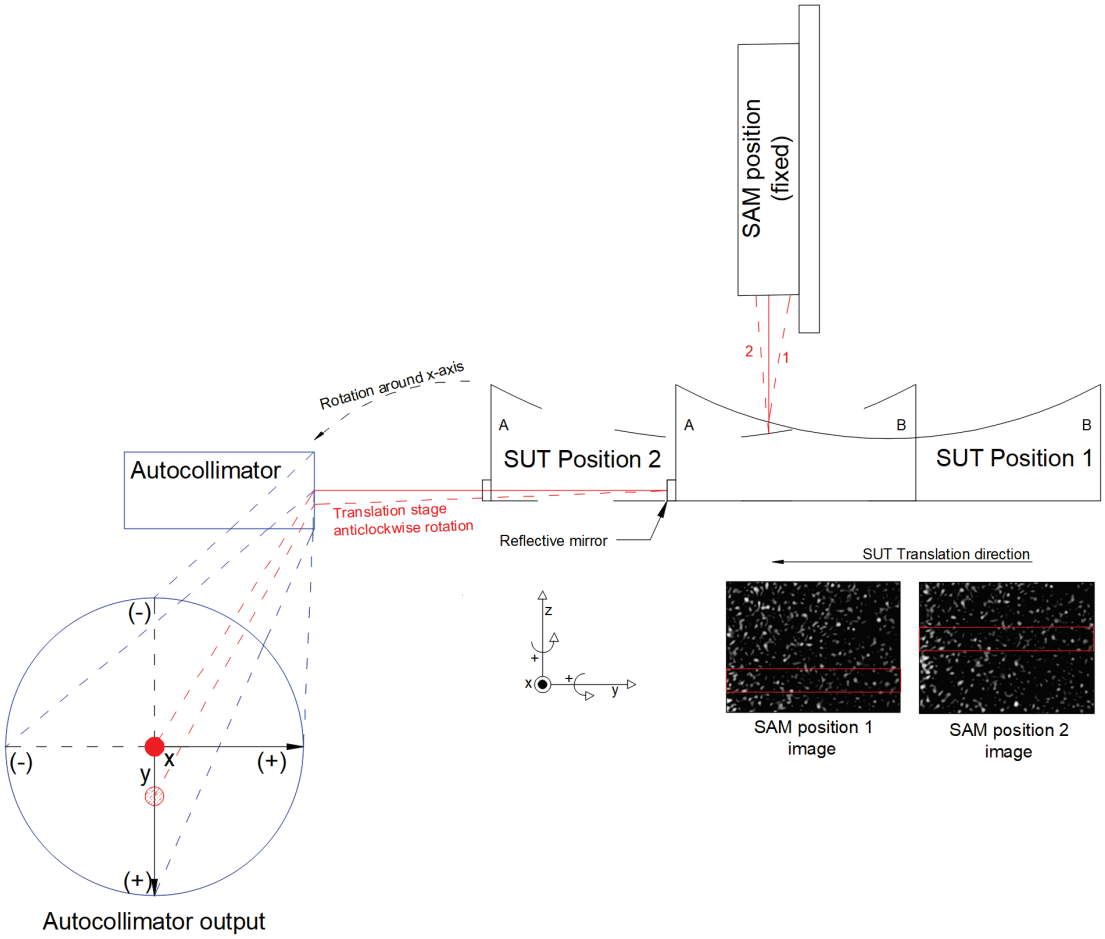

Figure 23: Schematic of the characterisation of a concave SUT while the SUT is translating back to front along the y-axis

Table 5: SAM results convention and required corrective actions.

DIC Mode		2	
SUT Profile Measured		Concave	
SUT direction of translation (x-axis scan)		Left to right (negative to positive)	
SUT direction of translation (y-axis scan)		Back to front (positive to negative)	
Speckle shift from Reference (Image 1) to Translated (Image 2)	**DIC result (Sign)**	**First Correction action required**	**DIC result after correction (Sign)**
Right to Left	DIC_x Positive	DIC_x: None	DIC_x Positive
Right to Left	DIC_x Negative	Exchange position of reference and translated image during DIC	DIC_x Positive
*** Left to right**	DIC_x Negative	Rotate the SAM detector camera by 180°	DIC_x Positive
*** Left to right**	DIC_x Negative	Rotate Images digitally by 180° before performing any data analysis	DIC_x Positive
*** Left to right**	DIC_x Negative	Multiply the DIC results by-1	DIC_x Positive
*Only one of the three actions is required to solve the same problem			
Speckle shift from Reference (Image 1) to Translated (Image 2)	**DIC result (Sign)**	**First Correction action required**	**DIC result after correction (Sign)**
Bottom to Top	DIC_y Positive	DIC_y: None	DIC_y Positive
Bottom to top	DIC_y Negative	Exchange position of reference and translated image during DIC	DIC_y Positive
****Top to bottom**	DIC_y Negative	Rotate the SAM detector camera by 180°	DIC_y Positive
**** Top to bottom**	DIC_y Negative	Rotate Images digitally by 180° before performing any data analysis	DIC_y Positive
**** Top to bottom**	DIC_y Negative	Multiply the DIC results by-1	DIC_y Positive
**Only one of the three actions is required to solve the same problem			

3.5. Calibration

To convert the speckle displacement to an angle displacement, the calibration coefficient, referred to as Angular Scaling Factor (ASF) throughout this thesis, can be calculated if two parameters are known [36]:

$$ASF = \frac{P}{2d} \tag{9}$$

Where d is the distance traversed by the laser beam from SUT to the camera, and P is the camera pixel size. The problem with this method is that to exactly calibrate SAM, while P can be retrieved from the technical specification of the CCD detector, d is harder to evaluate, due to the change in beam path trajectory, as shown in section 3.7.

An empirical method to calibrate SAM is achieved by positioning the SUT on a tilting stage. By changing the angle of the latter and detecting the relative speckle displacement, it is possible to calibrate SAM accurately. This method will be discussed in greater details in section 4.1.

3.5.1. Height Sensitive Angular Scaling Factor

SAM is precisely calibrated based on the distance from the SUT to the SAM detector's plane. A change in the SUT surface height profile changes the ASF, generating a systematic error. Therefore, such change shall be considered during data analysis to improve the accuracy of measurements, as follow:

1) Define an initial ASF Calibrating SAM to the central point in the SUT surface height profile. This location is considered as the mirror coordinates origin $SUT_{x,y}(0,0)$.
2) Determine the change in height at different locations along the ideal mirror profile length.
3) Correct the ASF taking in consideration the change of mirror surface height profile. This new calibration is now called Height Sensitive Angular Scaling Factor (HSASF)
4) Use the HSASF for data Analysis.

3.6. Effects of the Scanning Head Rotation

When translating the SAM along the x-axis, as shown in Figure 21, the effect of any SAM scanning head rotation angle around the y-axis corresponds to a different SUT measured position, resulting in a different measured region of interest on the SUT, instead of the originally intended. Also, a different ASF should be used rather than the initially calibrated, as the path length of the reflected beam, from the SUT to the detector, will change. To detect such effect on SAM measurements, a schematic of a possible scenario is shown in Figure 24, where d is the distance from the targeted SUT surface profile to the SAM detector, Θ is the rotation angle of SAM scanning head and its consequent effect is named x_{offset}.

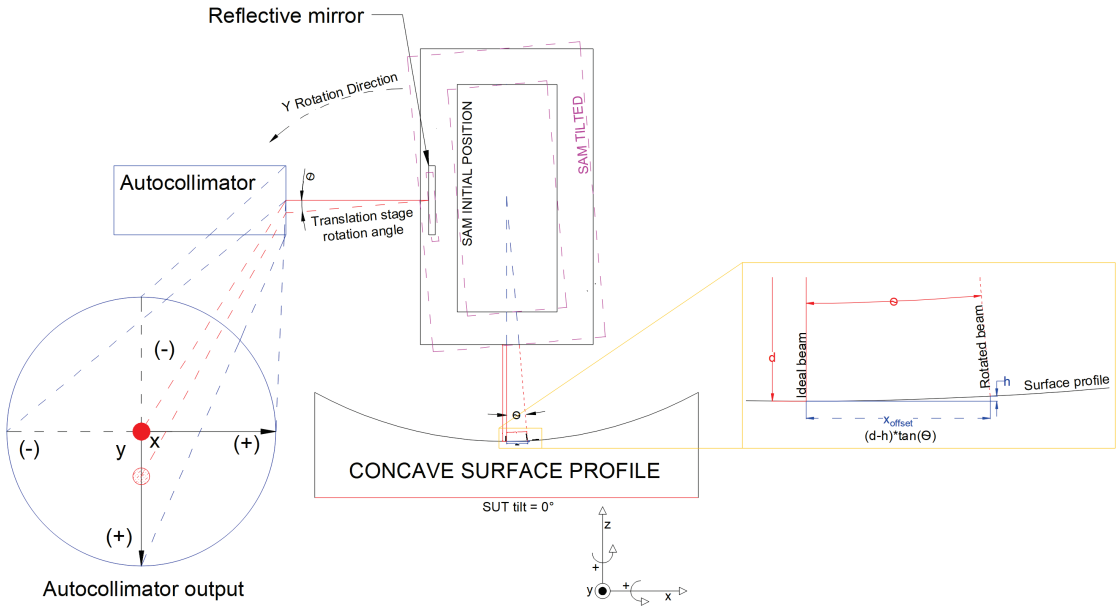

Figure 24: Schematic representation of SAM scanning head rotation effect on a targeted SUT region of interest

As an example, assuming that the SUT is a perfectly flat surface, it is possible to determine the systematic error introduced when a rotation of SAM scanning head ($\Delta\theta$) is added to the scan step measurement.

Assuming:

- $\Delta x = 0.2$
- $\Theta = 1\mu rad = 0.0000573°$
- $h = 0$
- $d = 450mm$

- $x_{offset} = (d - h) * tan(\Theta) \ = \ 0.00045\, mm$
- $Step\ scan \ = \ 0.2\, mm$

The error, expressed in percentage deviation from Δx, is equal to 0.22%, as shown in equation (10).

$$Error\ (\%) = \frac{x_{offset} * 100}{\Delta x} \cong 0.22\% \tag{10}$$

It is noteworthy that this error is the result of a single measurement and is assumed to be systematic. When considered as a random error, multiple scans will help reduce its effect by averaging the obtained measurements at the same scanned position.

During the experiments presented in the following chapter, it has been observed that the error contribution of the SAM scanning head rotation angle is even smaller than what was assumed above. Therefore, for the scope of this thesis, such error will be considered negligible.

The effects of the change in the SUT surface height profile will be extensively discussed in sections 3.10 and 4.1.4.1.

3.7. Effects of the Beam Splitter

Figure 25 and Figure 26 show the schematics of the beam splitter and highlight that its wedge (commonly used to remove the problematic ghost reflection) creates a divergence between the primary reflected beam and the secondary ghost beam at the transmitting side of the beam splitter, changing the path length and direction of the beam. The deviation of the beam from the original trajectory after being transmitted by the beam splitter results in a compression or expansion of the beam, depending on the angle of the wedged beam splitter.

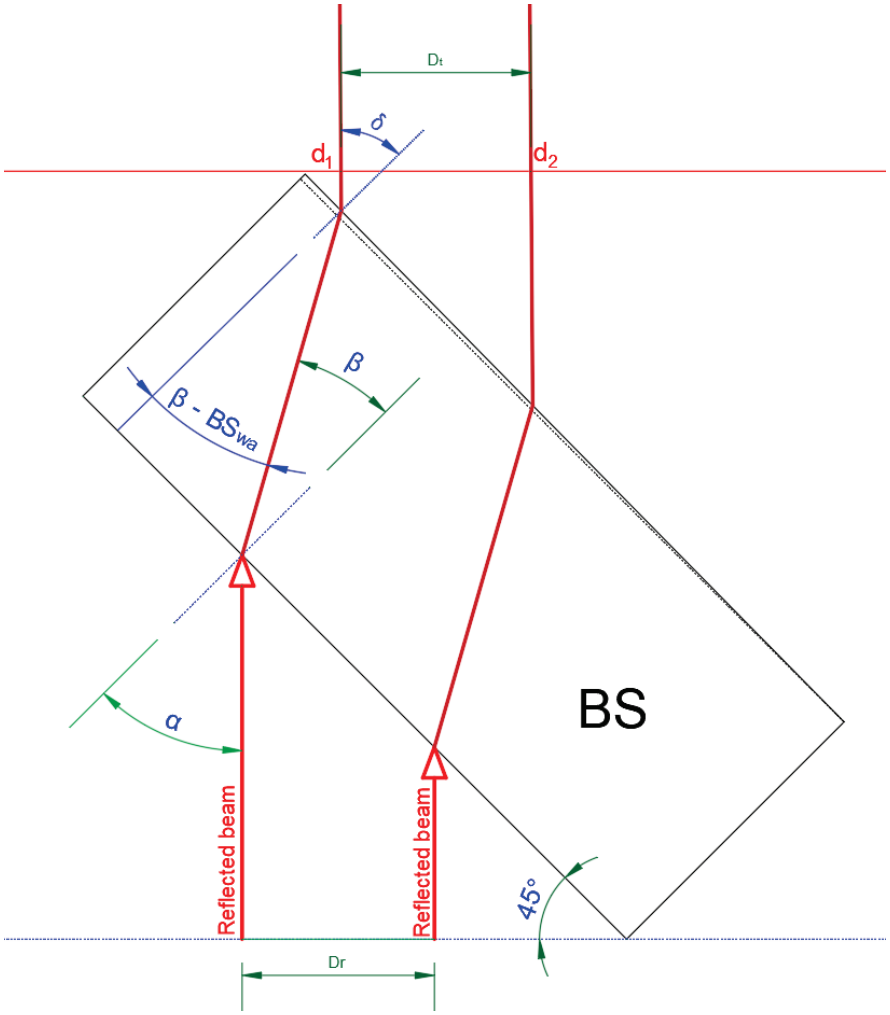

Figure 25: Effect of wedged beam splitter on the laser beam path

Here "BS" is the beam splitter, "BS_{wa}" is the beam splitter wedge angle, "α" is the angle between the reflected beam and the normal to the beam splitter reflective surface, "β" is the first angle of refraction, "δ" is the second angle of refraction, d_1 and d_2 are the path lengths of the point laser beams, "D_r" is the distance between the two beams after being reflected by a flat SUT and "D_t" is the distance between the two beams after being transmitted out of the beam splitter.

From Snell law of refraction, the effect of the wedged beam splitter on the path travelled by single rays of an ideally collimated point laser beam, is shown in equation (11).

$$n_1 * sin(\alpha) = n_2 * \ sin\ (\beta) \tag{11}$$

Where n_1 is the refractive index of air, approximated to 1.000277, and n_2 is the refractive index of UV fused silica. From the Sellmeier equation, a wavelength of 532nm, n_2 is equal to 1.4607063, as shown in equation (31).

Assuming the beam splitter inclination angle "α" is equal to 45°, a simulation of the effect on single beams path length and direction is shown in equations (12) and (13).

$$\beta = sin^{-1}\left(\frac{n_1 * \sin(\alpha)}{n_2}\right) = sin^{-1}\left(\frac{1.000277 * \sin(45)}{1.460706}\right) \simeq 28.96° \quad (12)$$

$$\delta = sin^{-1}\left(\frac{n_2 * \sin(\beta - BS_{wa})}{n_1}\right) = sin^{-1}\left(\frac{1.460706 * \sin(28.96 + 0.5)}{1.000277}\right) \simeq 45.91° \quad (13)$$

An example of the transmitted path difference between two single beams, reflected from the SUT back to the beam splitter is shown in Figure 26. Here it is possible to notice a small difference in the beams path length, with d_2 0.015% shorter than d_2, a difference almost negligible. To note instead is the effect of the wedge of the beam splitter on the distance between the two parallel beams, that after transmission is reduced by 1.14%. This simulation simplifies a speckle image to a single beam, but the extent of such systematic error on speckle images DIC will need to be investigated.

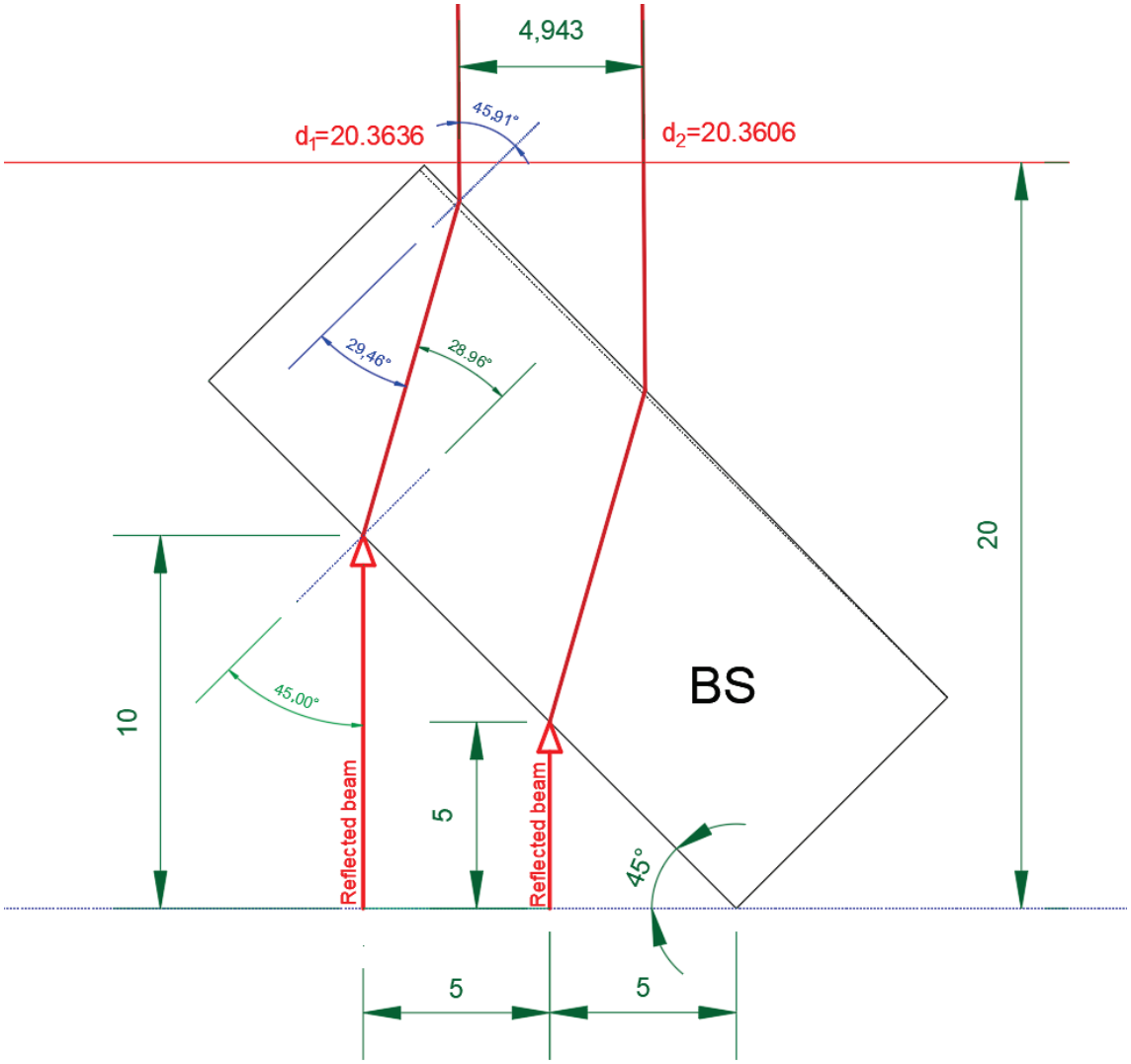

Figure 26: Wedged beam splitter effect simulation when inclined by 45 degrees

3.8. Effects of the SUT Tilting Angle

SAM exhibits a high degree of sensitivity towards variations in distance between its detector plane and the surface analysed. Among the contributing factors, the angle between the sample under test (SUT) surface profile and the SAM detector plane, plays a pivotal role in shaping the results. This influence is not solely dependent upon the SUT's tilting angle; rather, it is also dependent upon the specific surface profile of the SUT. Figure 27 shows the SUT effect on height and angle change between the SUT and SAM detector plane in ideal (black profile) and tilted (blue profile) conditions.

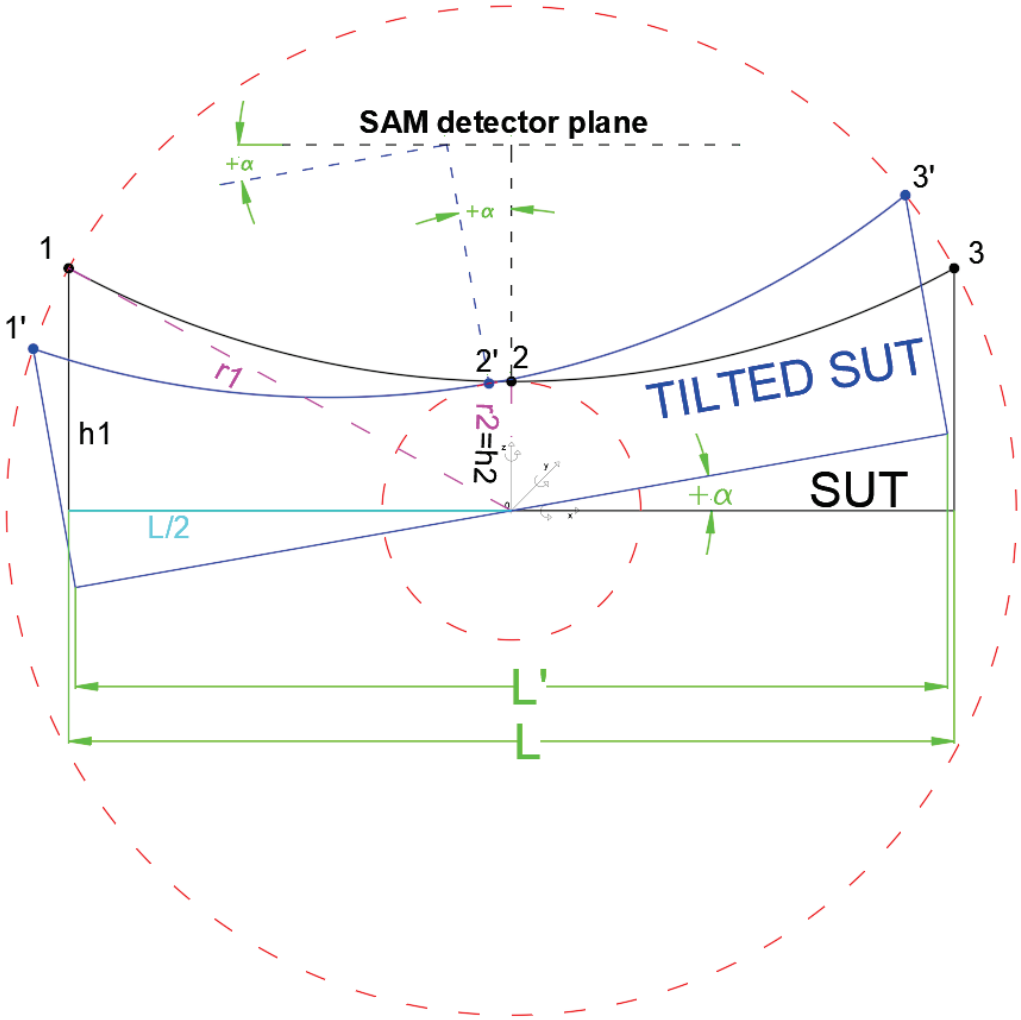

Figure 27: Schematic of the SUT tilting effect

Unless the SUT used has a perfectly flat surface profile and is perfectly located at the centre of rotation, any offset (due to either height changes due to SUT height profile or material added to the SUT to improve the mechanical stability or any added SUT support, like half cylinders at its Bessel points), generates both x and y coordinates translation of each point of the SUT profile.

The first consequence is the compression of the SUT length coordinates, now called Tilt Compression Factor (TCF) proportional to the SUT tilting angle α, and expressed in equation (14):

$$TCF = cos(\alpha) \tag{14}$$

Where α is the SUT tilt angle, positive if the angle is generated counterclockwise and negative if generated clockwise.

Translating SAM across the tilted SUT, along the x-axis, SUT profile coordinates need to be adjusted, using equation (13):

$$L' = L * TCF \tag{15}$$

Where L is the SUT original surface profile coordinates and L' is the SUT new surface profile coordinates.

The tilting angle will also introduce a translation along x and z coordinates, proportional to the distance from the centre of tilt rotation.

Knowing the position of a point of the sample under test called P of coordinates P(x,z), where the coordinate P(0,0) is the middle of the SUT along the x-axis and the bottom of the SUT along the z-axis, the translated coordinates after tilting by an angle (α) are expressed in equation (16).

$$\begin{cases} x' = \left(\left(x + x_{offset}\right) * \cos(\alpha)\right) - \left(\left(z + z_{offset}\right) * \sin(\alpha)\right) \\ z' = \left(\left(x + x_{offset}\right) * \sin(\alpha)\right) + \left(\left(z + z_{offset}\right) * cos(\alpha)\right) \end{cases} \tag{16}$$

Where (x', z') are the coordinates of the translated point P after rotation, x_{offset} and z_{offset} are the distances of the point P of coordinates $P\left(\frac{L}{2} + 0\ , h1 + 0\right)$, from the centre of rotation along x and z axis, respectively.

Using the data from Figure 27, considering that the point $1(-\frac{L}{2}, h1)$ and that the centre of rotation has coordinates (0,0), after rotation by a positive (anticlockwise direction) angle (α), the coordinates of point 1' are expressed in equation (17).

$$\begin{cases} x' = \left(\left(-\frac{L}{2} + 0\right) * \cos(\alpha)\right) - \left((h1 + 0) * \sin(\alpha)\right) \\ z' = \left(\left(-\frac{L}{2} + 0\right) * \sin(\alpha)\right) + \left((h1 + 0) * cos(\alpha)\right) \end{cases} \tag{17}$$

The difference between the original and translated coordinates can then be calculated and used to determine the change in distance between the tilted SUT and SAM detector and therefore use the appropriate ASF.

3.8.1. The Associated Systematic Error

When performing a lateral scan with SAM over the SUT, a systematic error will be introduced in SAM measurements if the SUT surface profile is not perfectly aligned with the translation stage.

While SAM output measurements represent the inverse of the local radius of curvature of the targeted surface, its accuracy is linked to the ASF used.

The SAM speckles are generated by the interaction of a laser with a diffuser. When the SAM operates in mode 1 [36], the speckles are used as markers of the slope of the SUT surface profile, and the spatial shift of the speckle can be linked to the change in slope in the surface profile analysed. Considering the speckles subjected to the laws of reflection and refraction in the visible electromagnetic spectrum, different SUT tilting angles will also add or remove (depending on the tilting orientation) a slope to the SAM measurements, inevitably introducing the aforementioned systematic error.

This error is more pronounced when measuring close to perfectly flat surfaces (small DIC), while it is less significant for stronger optics with a smaller radius of curvature (large DIC). For visualisation purposes, the SUT tilting effect systematic error is shown in Figure 28, where the blue arrows represent SAM incident laser beam, and the reflected beam by the orange arrows, and the black lines represent a convex SUT surface profile.

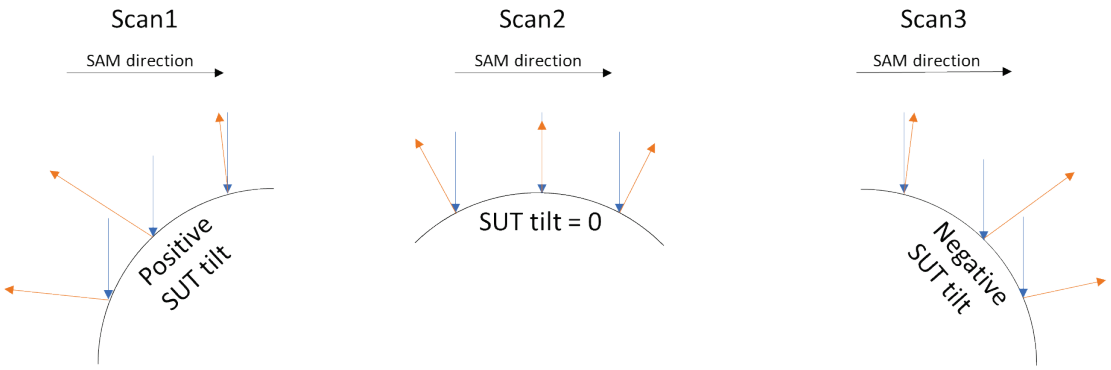

Figure 28: SUT tilting effects on the laser's beam trajectory

3.8.1.1. Example

Considering a concave, cylindrical SUT surface profile, having radius of curvature of 116m, the SUT tilting effect can be simulated using the Python script, described in section 3.11.

To quantify the systematic error induced by SUT tilting angle, I choose the mean gradient of the simulated slope. The parameters used for this simulation are shown in Table 6.

Table 6: Simulation parameters

SIMULATION PARAMETERS	
Detector pixel size [µm]	2.2
Detector size (y*x) [px]	1944*2592
LASER type [collimated or divergent]	Collimated
Active mirror range [mm]	-50 to 50
SAM scan step used [mm]	0.2
Calibrated ASF (Fixed or HSASF) [µrad/px]	(Fixed) 3.9125
SAM cross-correlation mode [1 or 2]	1
Coordinates Expansion Scaling Factor (CESF)	1
Detector distance from SUT [mm]	287.155
Tilting stage angles used [µrad]	-8000, -6000, -4000, -2000, 0, +2000, +4000, +6000, +8000

The results of the simulation are shown in Figure 29. A linear change in the SUT tilting angle corresponds to a second-order systematic error. These results will be compared with empirical results in section 4.4.5.

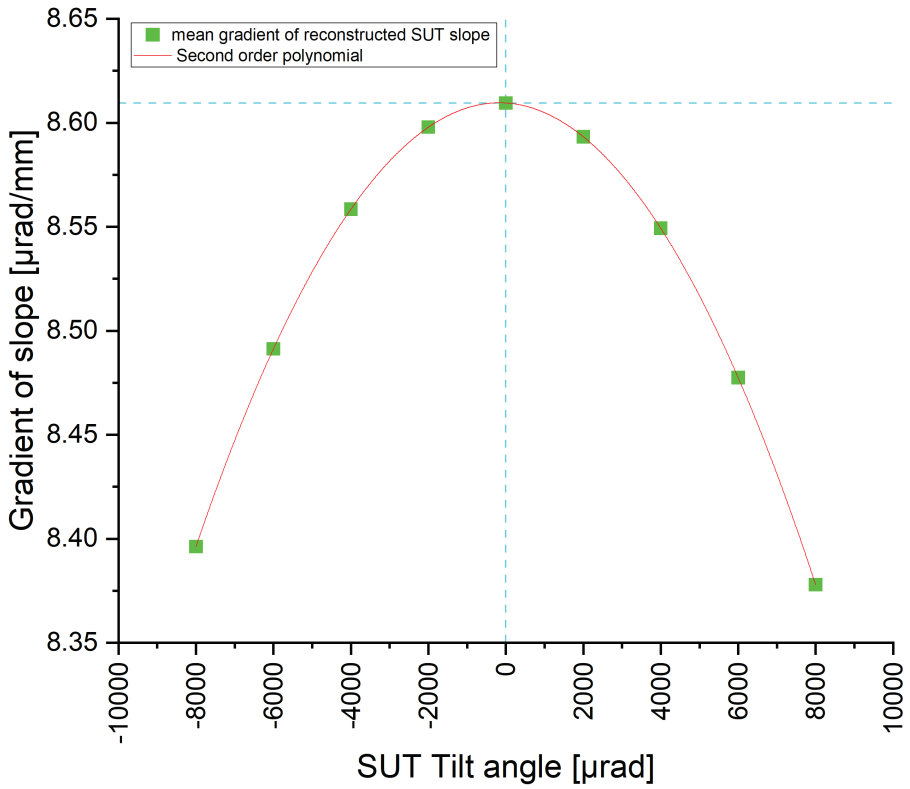

Figure 29: Simulation results of the SUT tilting effect

3.9. Coordinates Expansion Scaling Factor

When the SUT surface profile differs from a flat surface, it will affect the size and shape of the speckles, resulting in a shrinking effect in case of a concave surface, or an expanding effect, in case of a convex surface. I called such effect Coordinates Expansion Scaling Factor (CESF).

The method used to calculate the correct CESF is presented in equations (18), (19), (20).

$$SAM\ distance\ from\ SUT\ focal\ plane = SAM\ distance\ from\ SUT - SUT\ RoC \quad (18)$$

Where "SAM distance from SUT focal plane" and "SUT RoC" are expressed in m.

$$Ratio\ = \frac{SAM\ distance\ from\ SUT\ focal\ plane}{SUT\ RoC} \quad (19)$$

$$CESF = \frac{1}{Ratio} \quad (20)$$

It is worth to note that the expansion scaling factor not only needs to be applied to the SUT length coordinates, but also to the slope measured, as the CESF effects generate systematic errors in multiple dimensions, as shown in equation (21).

$$SAM\ Slope = SAM\ Slope_{compressed} * CESF \quad (21)$$

The simulation parameters related to a simulation of the effects of CESF are listed in Table 7, while the results are illustrated in Figure 30.

Table 7: CESF Simulation configuration

SAM Distance from the SUT [m]	1
RoC range [m]	From -10 to +10
RoC steps [m]	0.1

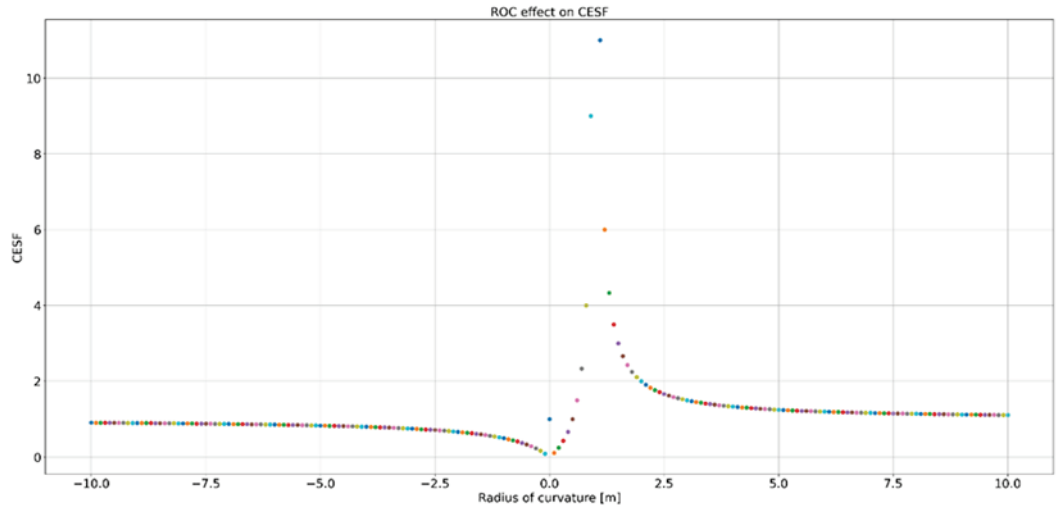

Figure 30: CESF Vs Radius of Curvature (RoC)

As shown in Figure 30, when the RoC gets closer to the distance between the SUT and the SAM detector, the value the CESF approaches infinite. This is valid in case of a concave SUT. In case of a convex SUT (RoC $<$ 0), the CESF will be $<$ 1 and $>$ 0.

3.10. SUT Surface Profiles

3.10.1. Cylinder

The mathematical model used to simulate cylindrical surface height profiles is shown in equation (22).

$$Tangential\ Figure\ height = z = \tau * \sqrt{RoC^2 - \left(x - x_{offset}\right)^2} + z_{offset} \qquad (22)$$

Where:

τ = +1 if generating a convex surface or -1 if generating a concave surface

RoC = Radius of curvature

x = x coordinate

x_{offset}= offset along x coordinates

z_{offset}= offset along z coordinates

The nominal slope profile can be generated using three different methods:

1) From mathematical model
2) From integration of inverse local radius of curvature data
3) From derivative of figure profile data

The problem with the second and third method is that they will introduce approximation errors, especially at the edge of the selected data set. For this reason, where possible, any surface profile during this thesis will be determined from its mathematical models.

The mathematical model for a cylindrical surface slope profile is shown in equation (23).

$$Figure\ slope\ [rad] = -\left(\tau * \frac{\left(x - x_{offset}\right)}{\sqrt{RoC^2 - \left(x_{offset} - x\right)^2}} \right) \tag{23}$$

To find the inverse of the local radius of curvature, as derivative of the slope model can also be calculated, and the model is presented in equation (24).

$$Figure\ Inv.LRC = -\tau * \frac{RoC^2}{\left(-x_{offset}{}^2 + RoC^2 + 2 * x_{offset} * x - x^2\right)^{3/2}} \tag{24}$$

The step-by-step procedure to derive equations (23) and (24) are shown in appendix B.

3.10.2. Ellipsoid

Extensive studies have been performed to determine the mathematical models associated to the figure, slope and Inv. LRC of Ellipsoidal shaped objects, widely used in X-Ray mirrors for synchronization [59,13,60].

Figure profile mathematical models [13] are shown in equations (25), (26), (27), where tangential and sagittal profiles are considered.

Considering:

- p = source distance [m]
- q = image focus plane distance from mirror [m]
- θ = mirror incidence angle (incidence ray angle)
- $h = (p - q) * \cos(\theta)$
- Profile figure = z
- τ = +1 if generating a convex surface or -1 if generating a concave surface

$$z(y,x) = \frac{p+q}{4pq+h^2} * \left(sin(\theta) * (2pq - h * x) + \tau * \sqrt{4pq * sin^2(\theta) * (pq - hx - x^2) - (4pq + h^2) * y^2}\right) \quad (25)$$

$$z(0,x) = -\tau * \left(\frac{(p+q)*sin(\theta)}{4pq+h^2} * \left(2pq - (hx * -\tau) - \left(2\sqrt{pq} * \sqrt{pq - \left(hx * (-\tau)\right) - x^2}\right)\right)\right) \quad (26)$$

$$z(y,0) = \frac{p+q}{4pq+h^2} * \left((2pq * sin(\theta)) - \tau * \sqrt{(2pq * sin(\theta))^2 - (4pq + h^2) * y^2}\right) \quad (27)$$

The surface slope profile can then be derived, as expressed in equation *(28)*.

$$Figure\ slope = \left.\frac{dz}{dx}\right|_{y=0} = -\tau * \frac{(p+q)*sin(\theta)}{(4*p*q)+h^2} * \left(\frac{(h+(2*x*(-\tau)))}{\sqrt{1-\frac{\left((h*x*(-\tau))-x^2\right)}{(p*q)}}}\right) \quad (28)$$

The mathematical model of the surface slope profile can also be derived from a different surface height profile equation [60], expressed in equation (29).

$$Figure\ slope = \tau * \frac{(p+q)*sin(\theta)}{(p+q)^2-((p-q)^2*sin(\theta)^2)} * \left((p-q) * cos(\theta)\right) - \sqrt{(p*q)} * \frac{\left((p-q)*cos(\theta)\right)-(2*\tau*x)}{\sqrt{(p*q)+\left((p-q)*cos(\theta)\right)*(\tau*x)-x^2}} \quad (29)$$

By performing the derivative of the slope from equation *(28)*, the Inverse of the local radius of curvature can be obtained, as shown in equation (30) [13].

$$Inverse\ LRC = \left.\frac{d^2y}{dx^2}\right|_{z=0} = \frac{sin(\theta)}{2} * \left(\frac{p+q}{pq}\right) * \frac{1}{\left(1-\frac{\left((hx*(-\tau))+x^2\right)}{pq}\right)^{3/2}} \quad (30)$$

3.11. Simulation

To better understand the SAM physics, I developed a simulation package, written in Python, structured to facilitate a simulation environment and capable of predicting and preventing possible systematic errors introduced in the measurements when SAM is used to characterise optics. It can be considered as a ray-trace simulator designed explicitly for SAM. The flow diagram is shown in Figure 31.

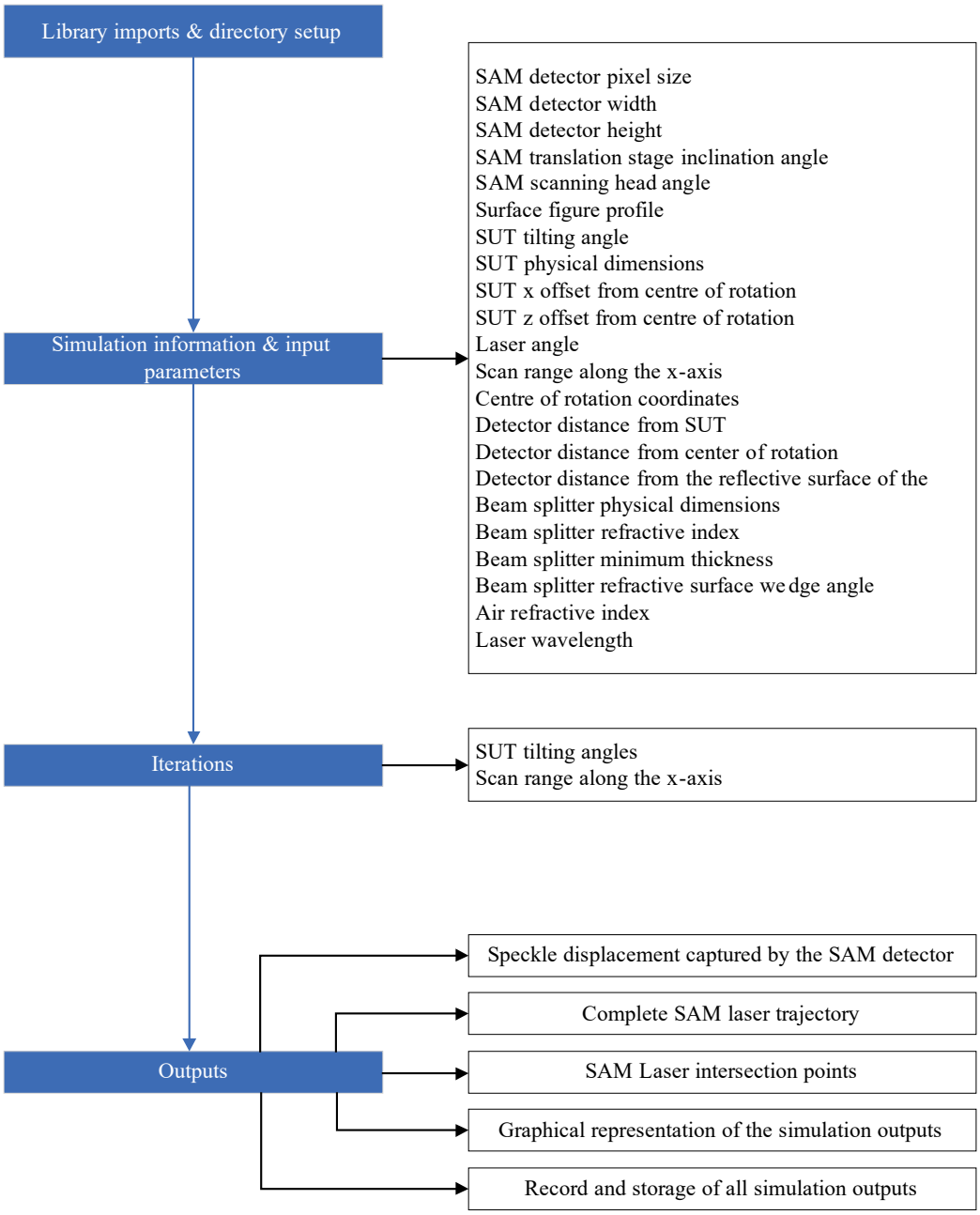

Figure 31 SAM simulation software flow diagram

The script begins by importing several libraries, including Matplotlib for plotting, NumPy for numerical operations, SymPy for symbolic mathematics, and system-specific and file-related functionalities. A directory path is established for storing simulation results. The script proceeds to define a range of parameters crucial for the simulation. This includes details about the SAM detector, its physical dimensions, the angle of inclination for the SUT, the laser specification, translation stage inclination angle, as well as the specifications of the shape of the SUT and the scan range across the simulated translation stage (x-axis). Various conditional statements handle different units (degrees or radians) for angles. Additional information about the simulation, such as the SAM laser misalignment, the SAM scanning head rotation angle, offset coordinates from centre of rotation, the SAM detector distance from SUT surface, the SAM detector distance from its beam splitter, the SAM beam splitter physical dimensions and its refractive index are recorded, and used as input parameters for the simulation.

A loop iterates over various SUT tilt angles, calculating and generating simulation outputs. Within this loop, the script defines the shape of the SUT, considering options like a cylinder, ellipse, or flat surface. The SUT profile is modified by applying specified offsets.

The script also creates directories for storing simulation results, copying the script file into each newly created folder, and logging the simulation configuration in a CSV file. The latter provides a comprehensive record of the simulation setup, aiding in result interpretation and reproducibility.

A figure is initialised using the Matplotlib library to visualise simulation results. The aspect ratio of the plot is explicitly set to 'equal' to ensure uniformity in graph coordinates along the x and y axes.

A loop iterates through a range of x-values, equivalent to the scan range, where the corresponding z-values (the height of the SUT in the (x,z) plane are computed based on the chosen SUT shape ('cylinder, 'ellipse', or 'flat').

Transformation equations are formulated to effectuate the rotation of the SUT profile by the specified tilt angle. Derivatives of the SUT profile $\frac{\Delta z}{\Delta x}$ are computed to determine the slope at the point of intersection with the laser beam.

Subsequent calculations involve determining angles associated with reflection and refraction. The Sellmeier equation is invoked to determine the refractive index of the beam splitter (BS) material.

The beam splitter used is made of Fused Silica, and knowing that the SAM laser wavelength (λ) is equal to 0.532 μm, the refractive index (n) can be calculated [61], as shown in equation (31):

$$n = \sqrt{\frac{0.6961663*\lambda^2}{\lambda^2-0.0684043^2} + \frac{0.4079426*\lambda^2}{\lambda^2-0.1162414^2} + \frac{0.8974794*\lambda^2}{\lambda^2-9.896161^2} + 1} = 1.4607063 \qquad (31)$$

Various equations representing lines, such as the refractive line, are defined and solved to accurately detect the intersection points. The thickness of the BS and other pertinent lines are depicted visually.

Parameters for the refractive surface of the splitter are established and the equation representing the second beam splitter plane is formulated based on the specified wedge angle and associated coordinates. Like the methodology applied for the other beam splitter surface, the script computes the profile of the second beam splitter plane.

The intersection point between the second beam splitter plane and the first refractive beam is computed and labelled. The second angle of refraction is then computed. This angle provides insights into the deviation of the first refracted beam as it traverses through the second surface of the beam splitter.

The script generates profiles for the line representing the normal to the intercept point and the line representing the second refracted ray. Equations describing the detector plane are derived, allowing for a comprehensive understanding of the detector's location.

Precise distance calculations are performed between various critical points, considering both the inclusion and exclusion of the beam splitter within the SAM hardware. The computed distances are documented in specific lists, quantitatively analysing the simulated optical paths.

The script incorporates a visualisation component, generating plots that highlight different aspects of the simulation. The incident, refracted, and reflected laser beams, as well as the detector plane are visualised to comprehensively represent the simulated optical scenario.

In summary, this Python script showcases a sophisticated simulation framework, incorporating principles of optics and geometry to model intricate light-ray interactions within the SAM system. The thoroughness of the simulation is reflected in the detailed computations, profile generation, and systematic analysis of optical paths and detector displacements. The script is designed for robustness, facilitating a comprehensive exploration of the simulated optical scenario.

As an example of a simulation output, Figure 32 illustrates the combination of the SAM scanning head rotations, which in an ideal scenario would be set to 90° counterclockwise, and the SUT tilting angle. This procedure simulates the rotations induced to the SUT by changing the angles of the tilting stage (TS). The SUT surface used for this simulation was an ideal flat surface. The legend is the same for all the illustrations shown in Figure 32, Figure 33, and Figure 34.

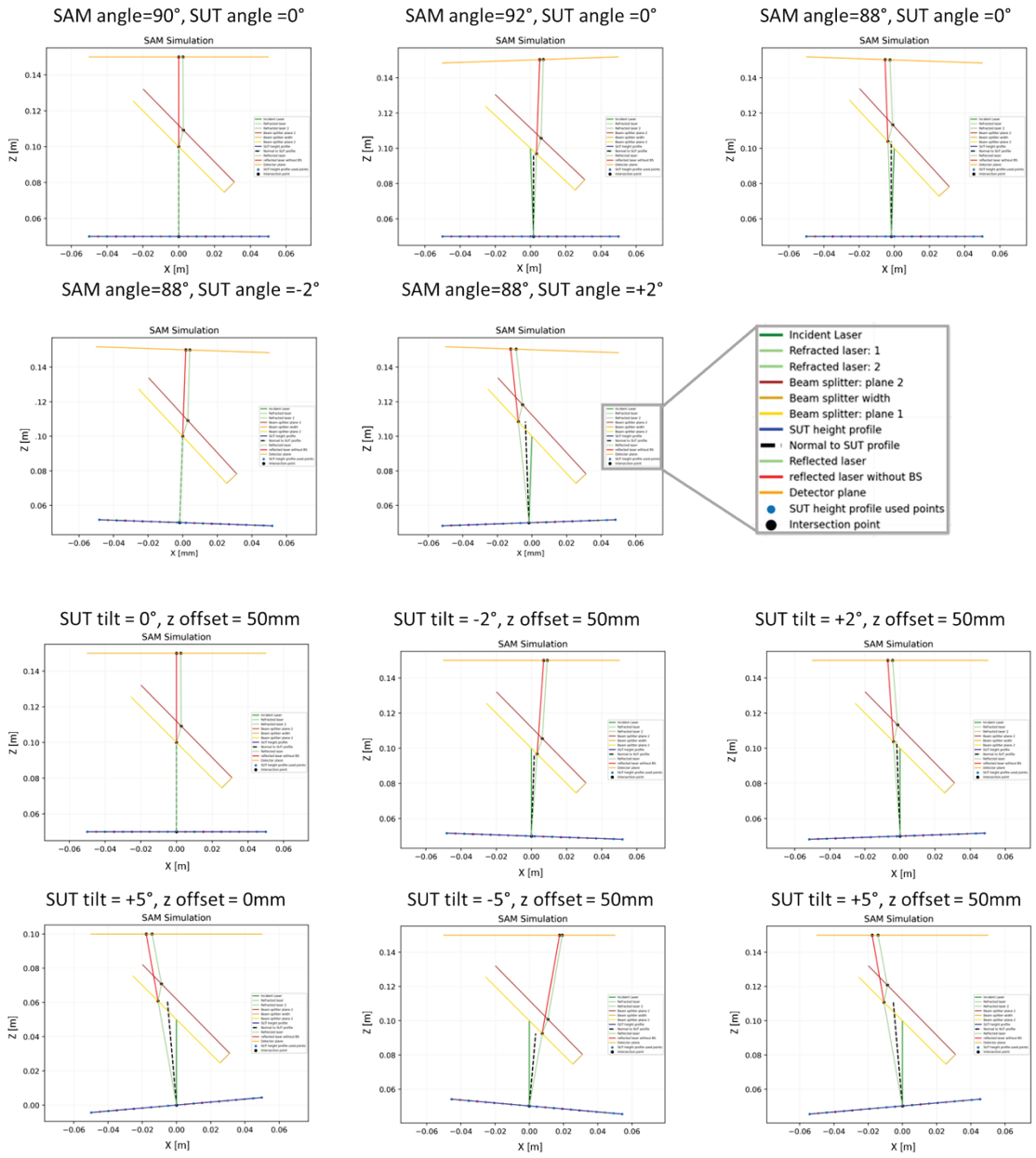

Figure 32: Simulated SAM Scan head, SUT tilting and SUT offset effects

The main optical component of the SAM is the beam splitter. It is used to reflect the laser beam and to transmit the speckle image of the SUT back to the detector. The effects of the beam splitter physical dimensions on the laser trajectory are shown in Figure 33. The beam splitter transmissive plane used in the SAM has a wedge angle of -0.5°, compared to the angle of the reflective beam splitter plane.

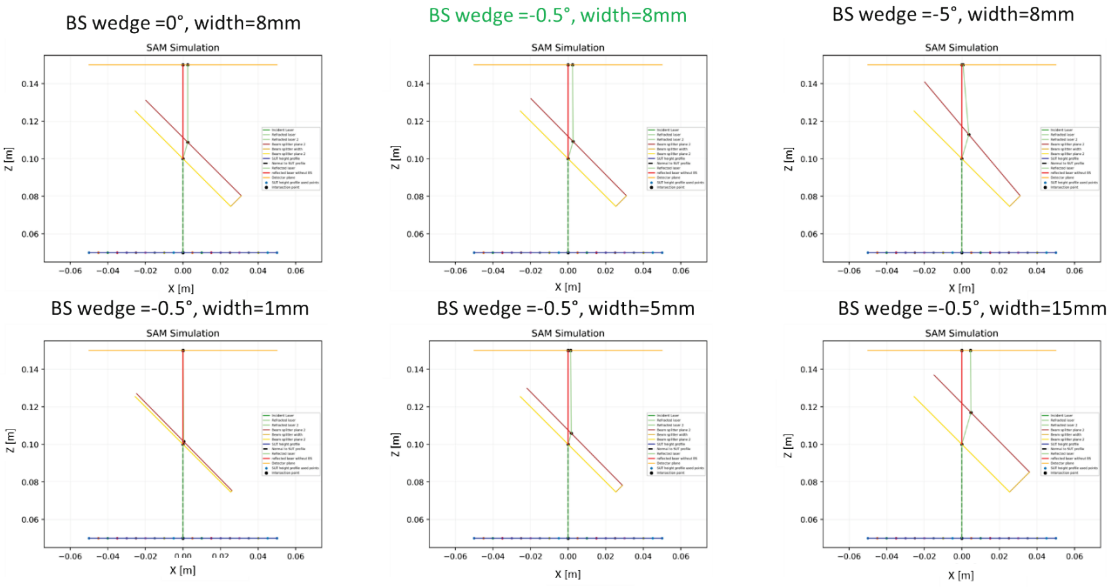

Figure 33: Simulated effect of beam splitter on laser's beam trajectory

It is also very important for the SAM simulation tool to be capable of simulating different surface profiles. Example of the simulated 1D surface profiles (flat, cylinder and ellipse) are illustrated in Figure 34.

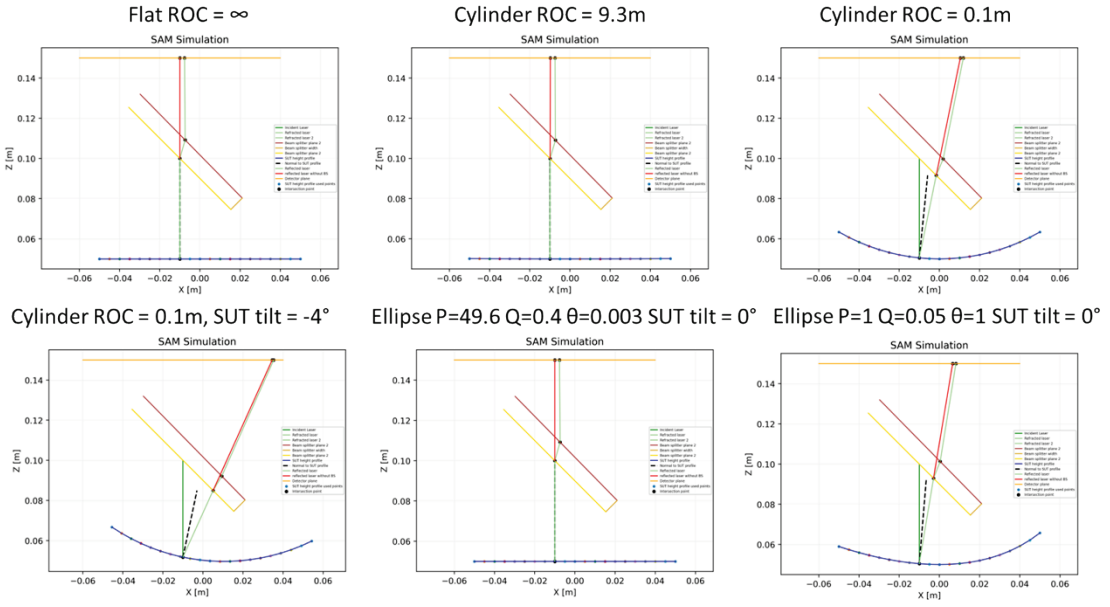

Figure 34: Simulated SUT surface profile effects on SAM laser's beam trajectory

The tool can simulate a 1D scan. To do so, the SAM scanning head is virtually translated, using specified steps, across the SUT. Each time the SAM scanning head translates, the resulting shift of the reflected laser beam at the detector plane is measured and recorded, simulating a real scenario. A simulation of the SAM laser ray-tracing when characterising

a SUT having concave, elliptical surface (P = 10 m, Q = 0.5 m, θ = 1 rad), 0.05m long, at a SUT Initial distance from the detector of 0.1m, and centre of the reflective beam splitter plane at 0.045 m from the detector, is represented in Figure 35. The accuracy of the simulation results will be discussed in section 4.4.5.

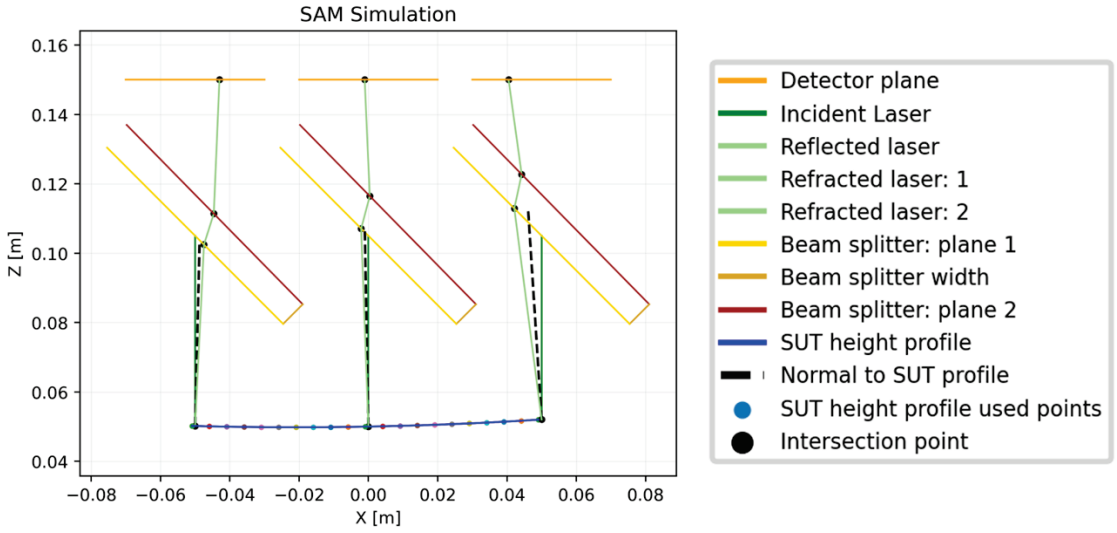

Figure 35: Simulation of a 1D scan

3.12. Digital Image Correlation

Digital Image Correlation (DIC) is a powerful technique used in image analysis and computer vision to measure and quantify the displacement and deformation of objects or materials.

The fundamental principle of DIC involves comparing corresponding regions of interest (ROIs) between two images to determine the displacement and deformation fields. These ROIs can be small subsets of an image, and the correlation process involves finding the best match between these subsets in the reference and deformed images. This matching is achieved by evaluating the similarity between pixel intensities or patterns within the ROIs [62].

3.12.1. Feature-based Digital Image Correlation

The SURF (Speeded-up robust feature algorithm) [63,64] comprises scale and rotation-invariant interest point detector and descriptor. The SURF method is widely used as a tracking technique in computer vision and can be divided into different steps. SURF starts by detecting key points in an image. These are points in the image that are distinctive and

can be reliably detected under various conditions like scale, rotation, and lighting changes. SURF uses a Hessian matrix-based detector, which is faster compared to other methods like SIFT. SURF determines the scale and orientation of the detected key points to ensure they are invariant to these transformations. This allows the algorithm to recognize the same object even if it appears at a different size or rotated in the image. After detecting the key points, SURF generates descriptors that describe the region around each key point. These descriptors are usually vectors that capture the intensity patterns in the neighbourhood of the key points. SURF uses a distribution of the Haar wavelet responses in the neighbourhood of the key points to create these descriptors.

When this technique is used to track the displacement of features within speckle images, first the key points (interest points) are detected and selected at specific coordinates of the image (for example, a particular speckle), as shown in Figure 36. Second, the region surrounding the interest points is represented as a feature vector. A feature vector can be considered a vector with an n-dimension of numerical features that characterise an object in the image (the descriptor vector). A high dimension of the descriptor results in a higher processing time, but as an advantage, the precision is increased. A balance between precision and processing time must be found, depending on the application. Third, the descriptor vectors of the reference image are matched with the displaced images. These matches are generally based on the distance between the vectors, such as the Euclidean or Mahanalobis distance.

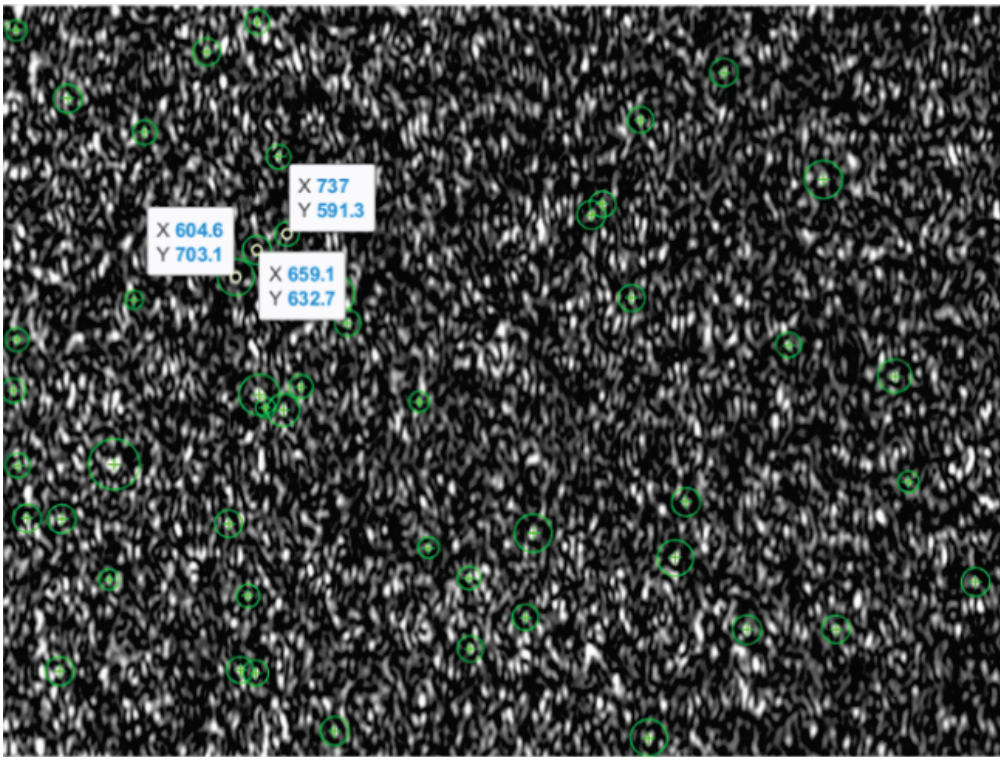

Figure 36: SURF features found in a SAM speckle image

Once the features have been detected in the ROI of the reference image, they are matched with the matching features found in the displaced image, as shown in Figure 37.

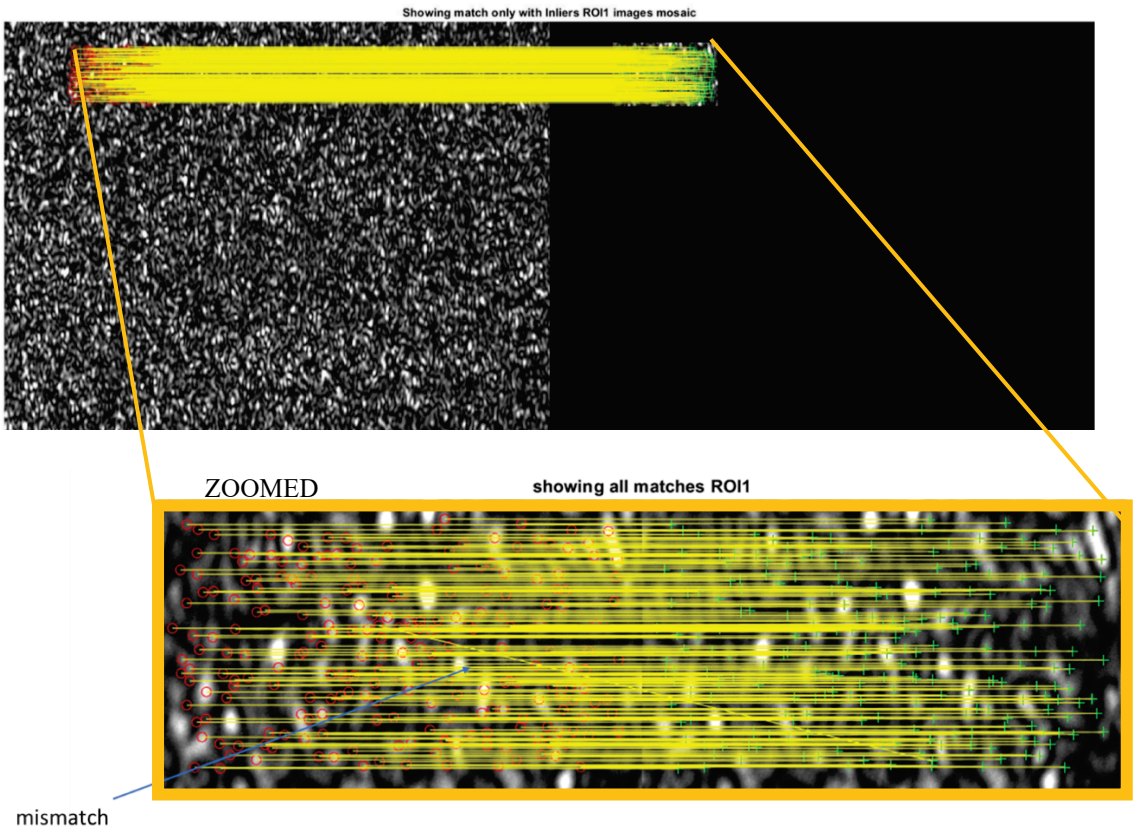

Figure 37: SURF method features matches

To remove potential mismatches, as shown in the zoomed part of Figure 37, another constraint is introduced in the algorithm to enable just affine matches, generating the most precise results, as shown in Figure 38.

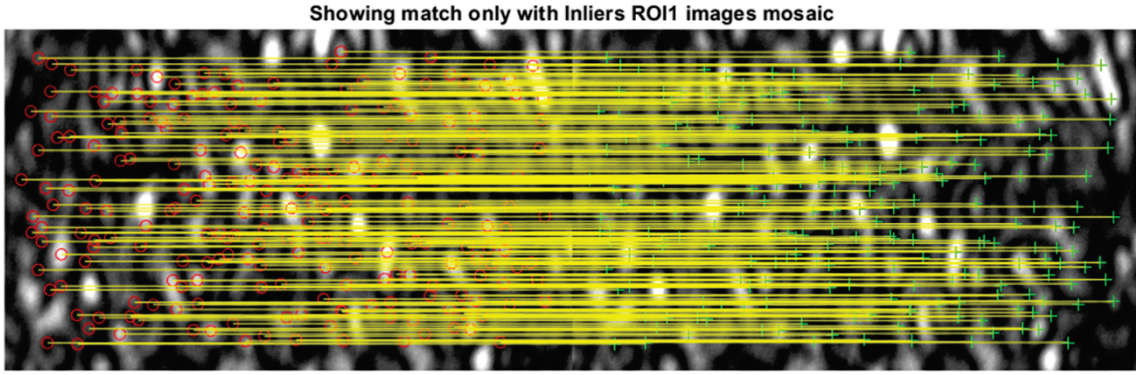

Figure 38: SURF method matches after new constraint is added to the algorithm

A limitation of the SURF method is that it relies on highly reliable features and sharp feature's edges, which are not contained in the random speckles.

3.12.2. Area-based Digital Image Correlation

Area-based based DIC provides detailed insights into localized deformation patterns. Its versatility and capability to capture nuanced surface deformations make it a desired tool in metrology. Its principles are illustrated in Figure 39.

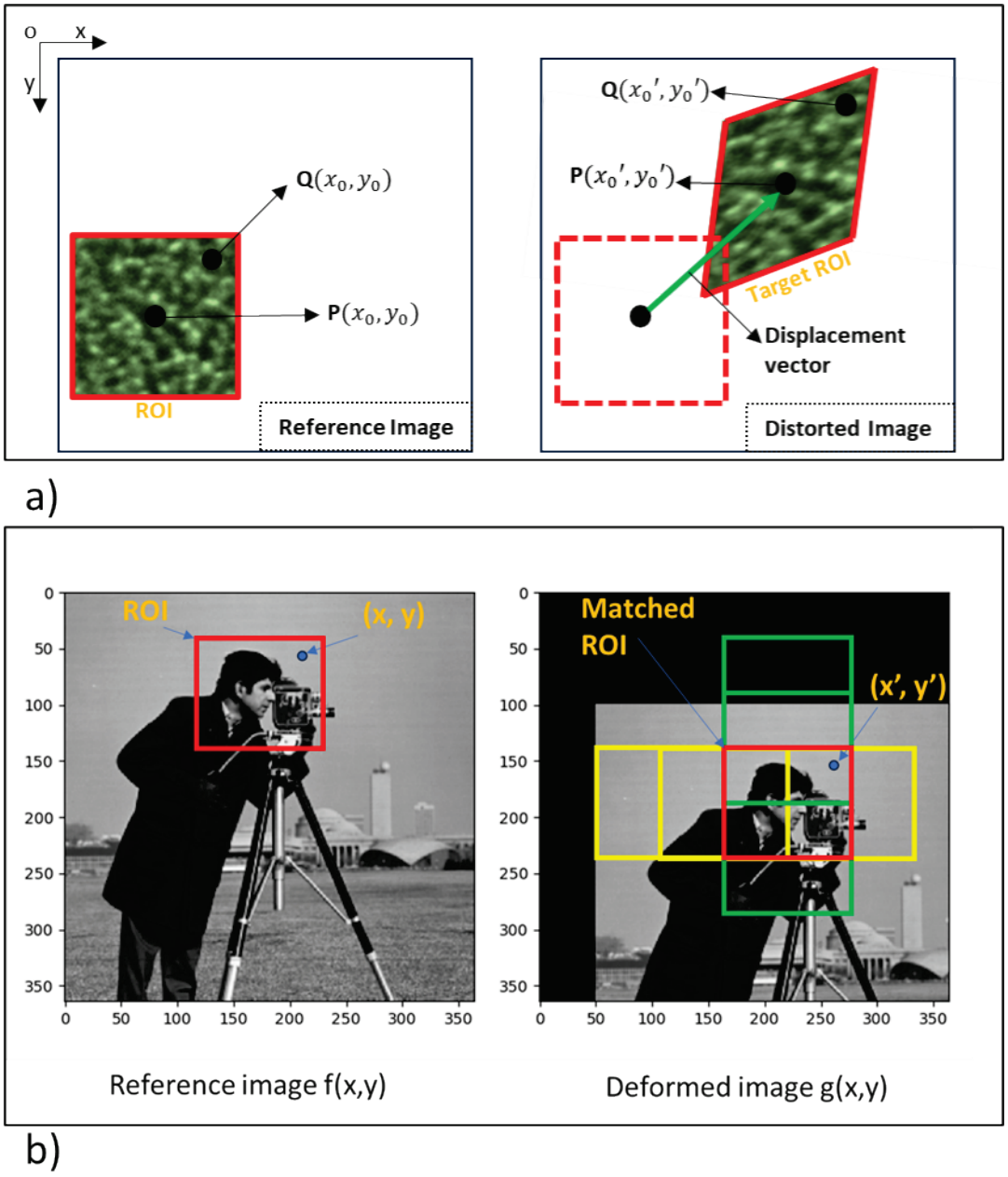

Figure 39: Two-dimensional digital image (speckles) correlation method (a) and an example of a shifted cameraman image (b)

To correlate two digital images, various algorithms are used and are based on the Sum of Absolute Difference (SAD), Sum of squared difference (SSD) and Normalized Cross Correlation (NCC), represented in equations (32), (33), (34):

$$C_{SSD}(x,y,d) = min\left\{\sum_{i,j}[I_1(x+i,y+j) - I_2(x-d+i,y+j)]^2\right\} \qquad (32)$$

$$C_{SAD}(x,y,d) = min\left\{\sum_{i,j} |I_1(x+i,y+j) - I_2(x-d+i,y+j)|\right\} \quad (33)$$

$$C_{NCC}(x,y,d) = max\left\{\frac{\sum_{i,j}[I_1(x+i,y+j) - \bar{I}_1(x,y)] * [I_2(x-d+i,y+j) - \bar{I}_2(x+d,y)]}{\{\sum_{i,j}[I_1(x+i,y+j) - \bar{I}_1(x,y)]^2 * [I_2(x-d+i,y+j) - \bar{I}_2(x+d,y)]^2\}^{1/2}}\right\} \quad (34)$$

Where:

- C is the cross-correlation coefficient.
- i is the row of the digital image matrix.
- j is the column of the digital image matrix.
- The intensity of the pixels (x, y) in the reference picture and the displaced image are represented by $I_1\ (x, y)$ and $I_2\ (x, y)$, respectively.
- d is the disparity (distance between two corresponding points of the same object obtained from a detector placed at different locations). It was assumed that disparity only existed in one way (x-axis).

The probability of a wrong match decreases with the increase of the ROI dimension. The use of bigger ROI increases the reliability of the results because bigger ROIs have more information to be matched, reducing the possibility of erroneous results from the noise present within the images.

On the other side, using a bigger ROI is a disadvantage because it reduces the spatial frequency of the measurement.

When DIC is applied, the difference between two identical images results in a cross-correlation output equal to zero. This can only be obtained in theory. A more realistic scenario is when images are acquired in a stable environment and hardware setup; the resultant DIC can be used to determine the stability of the instrument. The ROI match between the reference and target images is algebraically correlated, yielding a single DIC output, equivalent of two displacement values (DIC_x, DIC_y) for a monochrome image or six values, two for each channel, for RGB images.

3.13. Object Reconstruction

When reconstructing an object (an inverse problem that consists of estimating a scene, the shape of an X-ray optic mirror from diffraction intensities), images(x,y) of an object can be analysed and the magnitude of the Fourier transform [65,66] of the diffraction patterns present in the images(x,y) can be measured. The error metric used to check the result of the reconstruction is the NRMSE (normalised root mean square error) between any two cross-correlated images f(x,y) and g(x,y). The cross-correlation method is performed using OpenCV (Open-Source Computer Vision Library, an open-source library of computer vision algorithms) to compare templates against overlapped image regions. The flag used in OpenCV's template matching functions is "TM_CCOEFF_NORMED", and it stands for Template Matching with Normalized Cross-Correlation, based on the Normalized cross-correlation described in equation (32) , where you have an input image and a smaller template image in template matching. The goal is to find the region in the input image that best matches the template.

To increase the accuracy, an up-sampled cross-correlation between the image under examination (translated image) and a reference image can be computed using the Fast Fourier Transform (FFT). The main disadvantage of this method is that increased memory is also required to improve accuracy. For example, to perform a cross-correlation within 1/10 of a pixel of a 2592*1944 image (size of the Image from the XIMEA MU9PC-MH camera) requires storage and computation of 25920*19440 inverse FFT.

To overcome these disadvantages, efficient algorithms based on nonlinear optimisation and discrete Fourier transforms (DFTs) have been developed [67] where the correlation between two ROIs is calculated as the complex multiplication of the reference ROI's Fourier spectrum by the complex conjugate of the displaced ROI's Fourier spectrum. As a result, these algorithms require less time to compute and reduce the amount of memory needed.

For subpixel cross-correlation, to evaluate the NRMSE, the location of the cross-correlation maximum is found using a method first developed by Fisher based on Fourier local correlation tracking (FLCT) [68].

3.14. Digital Filtering

Digital filtering can be explained using a convolution kernel. A kernel is a small matrix highlighting how a pixel's filtered intensity value depends on the intensity of its adjacent pixels.

Table 8: Convolution kernel (low pass filter)

o x / y			
	$P_{0,0}$ 1/5	$P_{0,1}$ 1/5	$P_{0,2}$ 1/5
	$P_{1,0}$ 1/5	$P_{1,1}$ 1/5	$P_{1,2}$ 1/5
	$P_{2,0}$ 1/5	$P_{2,1}$ 1/5	$P_{2,2}$ 1/5

For example, in Table 8, each number in the kernel represents a weight or coefficient. When performing convolution with this kernel and an image, each pixel in the resulting image will be the average of the surrounding pixels in a 3x3 neighbourhood. This has the effect of blurring the image. Choosing the correct low-pass filters is very important; it must be able to reduce enough noise without blurring the image too much to keep the relevant SUT surface features detectable. The kernel could also get more prominent. The example above considered a 3x3 matrix, but could increase in size (for example, 5x5). The disadvantage of using larger kernels is the associated increase in computation power required.

Another technique is a Gaussian Blur, which is a variation of the above method, where a blur kernel can be defined using only the Standard deviation (sigma) of the Gaussian distribution, where a more significant standard deviation results in a more substantial effect. The one-dimensional impulse response function $G(x)$, having σ as a parameter, is shown in equation (35) [69]:

$$G(x) = \frac{1}{\sqrt{2\pi} * \sigma} * e^{\frac{-x^2}{2\sigma^2}} \tag{35}$$

Where σ is the standard deviation, expressed in its physical units, for example, time and frequency in seconds and Hertz. The distribution is assumed to have a mean equal to 0.

When performing the filtering of a 2D image, the Gaussian filter response function $G(x,y)$ is the product of two Gaussian functions, one in each dimension, as shown in equation (36) [70]:

$$G(x,y) = \frac{1}{2\pi\sigma^2} * e^{-\frac{x^2+y^2}{2\sigma^2}} \quad (36)$$

For the scope of this thesis, The Gaussian filter has been chosen as the method used to reduce random noise, enhance the signal to noise ratio of the images, and to overall improve the DIC technique.

The camera detector used for the SAM is the XIMEA MU9PC-MH, offering a 2.2µm pixel size and a digitalisation of 12-bit, where the intensity of each pixel can be represented, in theory, on a scale between 0 and 4095 (2^{12}). The manufacturer set the usable intensity scale to be between 0 and 4058, lowering the functional saturation level of the pixel. The 12-bit image is then interpolated and saved as a monochromatic, greyscale, 16-bit image, ready for further data processing.

The impact of the filter's intensity on the speckle images used during the experiments is shown in Figure 40. The application of a Gaussian filter to an acquired speckle image from SAM increases the maximum pixel intensity (a) of the histogram maximum frequency (b), improving the Signal-to-Noise Ratio (SNR) (a). The SNR in decibels (dB) is calculated using equation (37):

$$SNR_{db} = 10 * log_{10} * \left(\frac{P_{signal}}{P_{noise}}\right) \quad (37)$$

where:

- SNR_{db} is the Signal-to-Noise Ratio in decibels.
- P_{signal} is the power of the signal.
- P_{noise} is the power of the noise.

For a digital image, the pixel intensity values are interpreted as the representation of the signal and noise, and substituting them to equation (37) , becomes equation (38):

$$SNR_{db} = 10 * log_{10} * \left(\frac{\bar{x}}{\sigma_{noise}}\right) \quad (38)$$

Where:

- $\bar{x}$ is the mean pixel intensity of the entire image.

- σ_{noise} is the standard deviation, representing the spread of pixel intensities around the mean, expressed in equation (39):

$$\sigma_{noise} = \sqrt{\frac{\sum_{i=1}^{N}(x_i - \bar{x})^2}{N-1}} \tag{39}$$

Here, N is the total number of pixels in the image and x_i represents the intensity value of each pixel.

On the other hand, the right compromise shall be achieved, as a stronger Gaussian filter will also generate a greater convolution effect in the speckle image (c), resulting in a loss of the high-frequency surface details of the SUT.

During the entire course of this thesis, σ has been experimentally tested and set to 10.

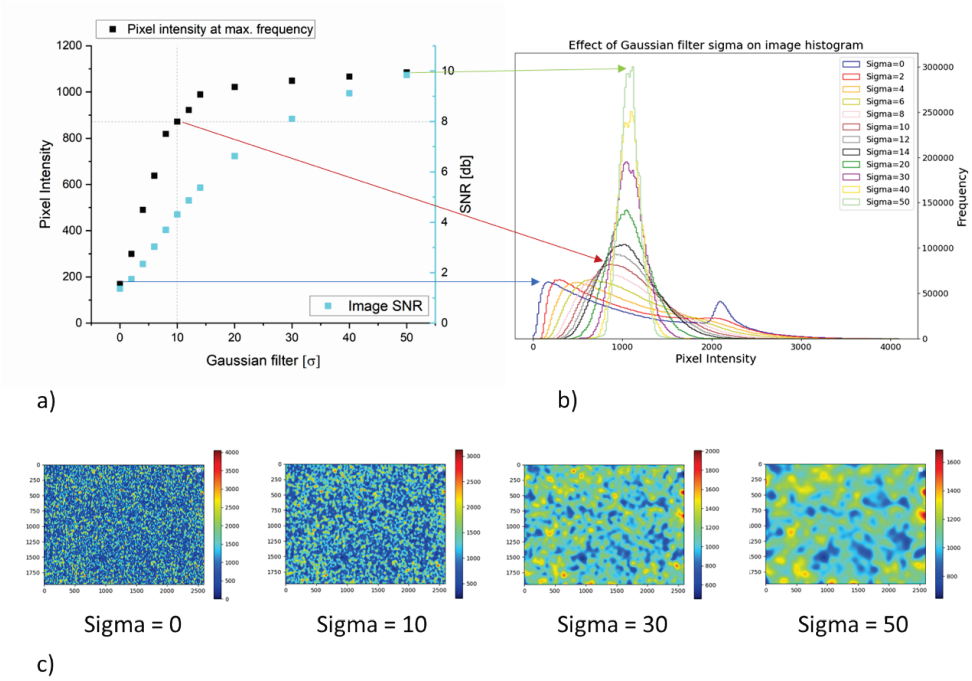

Figure 40: Effect of the strengths of the Gaussian filter on an acquired speckle image

3.15. Power Spectral Density

Metrology instruments can generate one (1D), two (2D) or higher dimensional maps of the SUT. Generally, coordinate space representation of the surface topography is used to analyse the results of such maps and characterise the surface of the SUT. Such data, representing the SUT height profile, forms the basis for 3.1.14. Power Spectral Density (PSD) analysis. Therefore, also the PSD function of the surface height distribution can be used to describe the surface of SUT [71,72].

Before applying PSD analysis, Nyquist sampling criterion [73] is considered to ensure accurate frequency representation. Windowing techniques, such as the Blackman window [74], help minimise spectral leakage and enhance the accuracy of the PSD results.

The heart of PSD analysis lies in the Fourier transform of the surface profile data. By transforming the data into the frequency domain, insights into power distribution across different spatial frequencies are obtained. The PSD is then calculated, highlighting the contribution of each frequency component.

The PSD values are normalised to make meaningful comparisons based on the ensemble average of the surface profile data. This normalisation factor ensures that the PSD reflects the surface characteristics relative to the overall amplitude of the mirror's profile.

In this thesis, I restrict to calculating one-dimensional PSD from surface profile data [75], particularly the surface height error, integrated from a measured surface profile slope error. The PSD will be used to compare the measurements obtained by SAM, HDX, NOM, and GTX of the various SUT characterised during the experiments.

4. Results and Discussion

The characterisation of real optics plays a pivotal role in the design and development of metrology instruments. In this chapter I will provide a comprehensive overview of the methodologies employed and the results obtained during the characterising X-ray optics using the SAM, along with explorations of the challenges inherent in these measurements.

4.1. Calibration

Figure 41 shows the version of the hardware utilised for testing the calibration methodology of the SAM, using the Diamond Light Source's nano-angle generator (NANGO) [76].

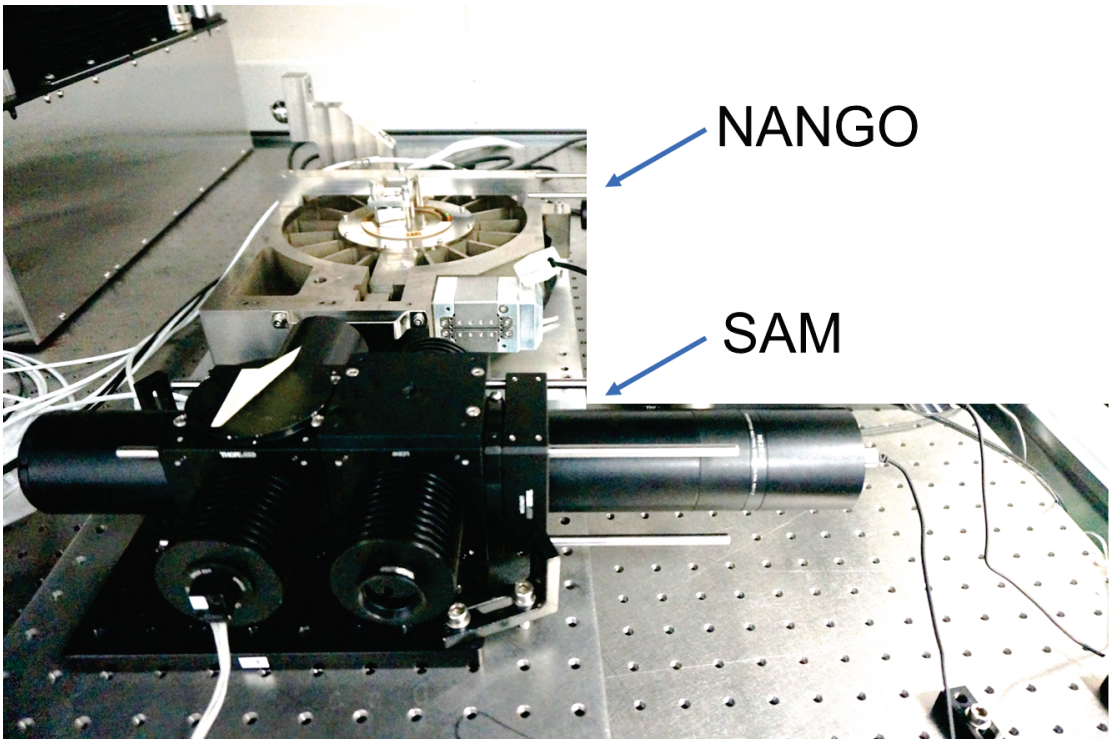

Figure 41: Calibration experiment setup using SAM and NANGO

The main components of the SAM hardware are listed in Table 9.

Table 9: Calibration hardware settings

HARDWARE	
Detector Used [Brand / Model]	XIMEA MU9PC-MH
Detector pixel size [µm]	2.2
Detector size [y*x] [px]	1944*2592
Speckle creation method	glass diffuser
LASER used [Brand / Model]	THORLABS CPS532
LASER wavelength [nm]	532
LASER type [collimated or divergent]	Collimated

No correction methodology is implemented to correct the parasitic angular alterations during calibration. This is attributed the SAM scanning head being fixed to a single position. Consequently, variations in angles are due to the angular adjustments of the reflecting cube situated at the rotation centre of the NANGO.

This section focuses on the calibration process, specifically examining the use of various Regions of Interest (ROI) and their influence on calibration outcomes. The investigation involved assessing if the results varied when different ROIs were selected. For calibration, a range of 0 to 5000 µrad was employed, with incremental steps of 100 µrads, and each scanning iteration was conducted 10 times. Additionally, calibration was performed utilising SAM cross-correlation modes 1 and 2 [36]. The respective software configurations for these modes are detailed in Table 10 and Table 11.

4.1.1. Mode 1

In mode 1 only one ROI could be utilised, over the entire width of the detector, with crop edges left/right and top/bottom for cross-correlation of 1100/1100 and 50/50 pixels, respectively, as shown in Table 10 and Figure 42.

Table 10: Calibration software setting using mode 1

SOFTWARE	
ASF [µrad/px] (fixed or adapted)	1.804 (Fixed)
SAM cross-correlations mode [1 or 2]	1
CESF	1
Fine tuning to align SAM slope error to NOM and HDX [mm]	0
ROI used [y*x] [px]	1400*2592
ROI used y [px]	310 - 1710

ROI used x [px]	0 - 2592
DIC Edge y top/bottom [px]	50
DIC Edge x left/right [px]	1100
Gaussian filter sigma [σ]	10

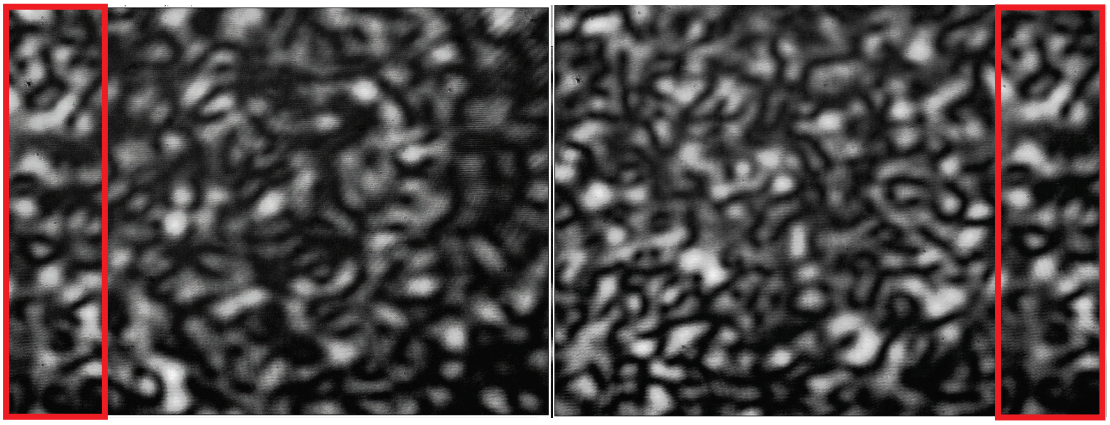

(A)

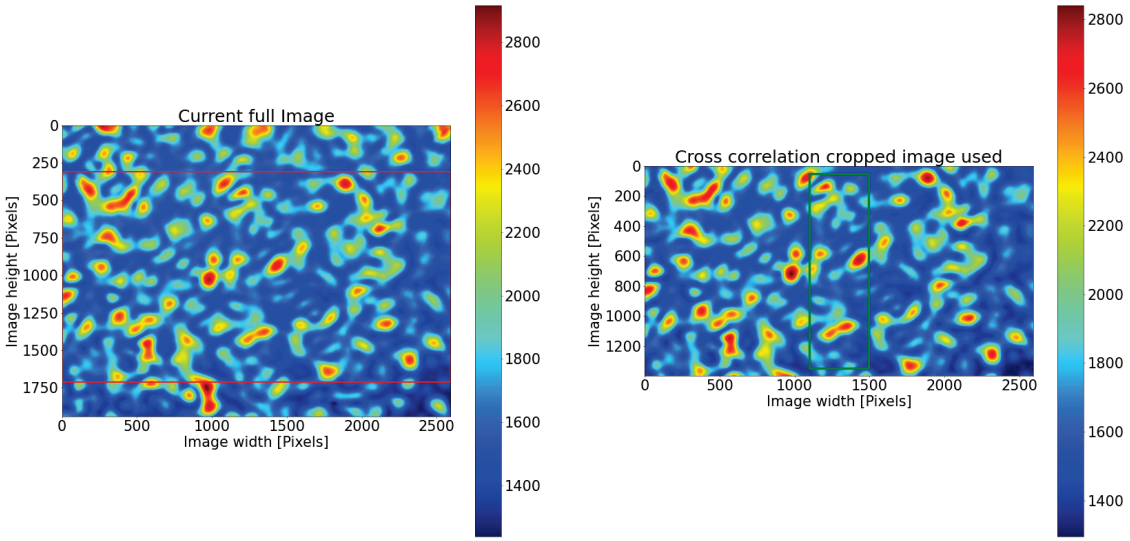

(B)

Figure 42: (A): Speckle displacement using SAM (mode 1) and NANGO (5000 µrad range). (B): Left picture displaying the calibration's ROI. The right image shows the cross-correlation area used within the ROI.

Considering that there were ten calibration scans in total, with each scan comprising 50 images, the central image from each scan's dataset was selected as the reference image. The average of all values in each NANGO calibration position was used to calculate the ASF, as follows:

1) Run a linear regression on the averaged cross-correlations from all ten scans, as illustrated in Figure 43.

2) Compute the gradient of the modelled linear regression using the calibration number (from 0 to 49 in this case) as x coordinates.
3) Assess the linear regression model using the root mean square error (RSME), shown in equation (40).

$$RMSE = \sqrt{\frac{1}{N} * \sum (E_{model})^2} \tag{40}$$

Here, E_{model} is equal to the difference between the linear regression model output and the expected output and N is the total number of model errors.

4) Calculate the ASF as the absolute value of the ratio between the calibration step size and the gradient of the modelled linear regression.

To detect the spread of the values from the mean value of the data set, the root mean square formula (RMS) can be used, as shown in equation (41).

$$RMS = \sqrt{\frac{1}{N} * \sum (E_{model} - \overline{E_{model}})^2} \tag{41}$$

Following the steps above, and utilising the data from Figure 43:

- $Linear\ fit = y = mx + C = -42.94x + 1073.72$
- $gradient = m = -42.94$
- $ASF = \frac{100}{42.94} = 2.3288\ \mu rad/px$

The RMSE is 0.32 px. The total slope range during the calibration is equal to 2103 px. Therefore, the RSME is equal to 0.015% of the total range.

A graphical representation of the calibration using mode 1 is illustrated in Figure 43. The differences between the two lines are indistinguishable by the naked eye.

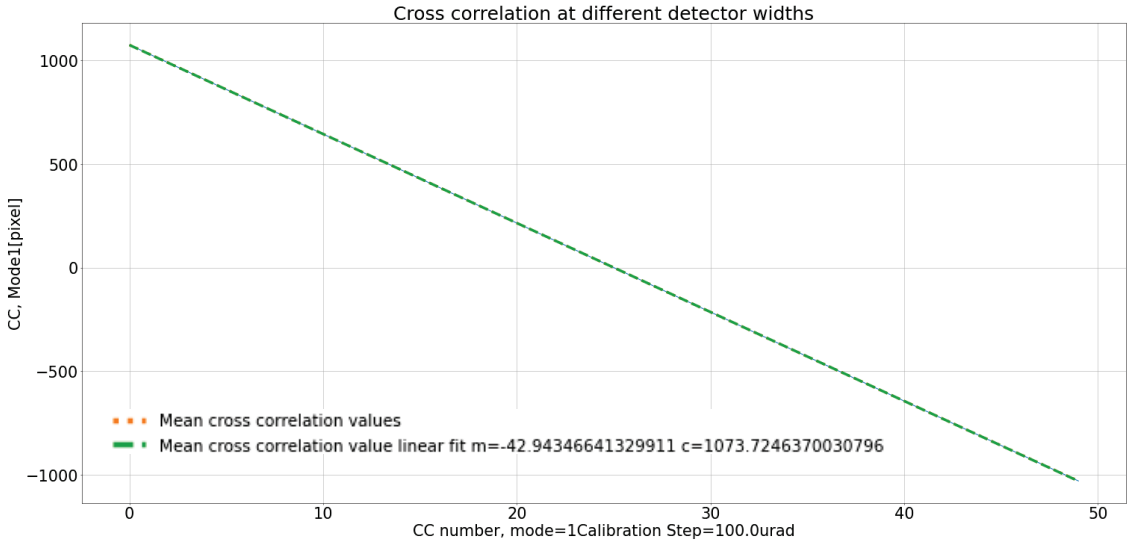

Figure 43: Mode 1 calibration results

4.1.2. Mode 2

In mode 2, an average NANGO displacement of 100 µrad corresponded to 42.9 pixels displacement at the SAM detector plane, for a total displacement of 2145 pixels when multiplied by fifty (the number of NANGO calibration steps in each scan). Each ROI size used during mode 2 calibration was 1400*1400 pixels (y*x), with cropped edges left/right and top/bottom during cross-correlation of 300/300 and 50/50 pixels, respectively.

Each triangle in Figure 44 symbolises the average derived from 10 calibration scans, along with its standard deviation.

Table 11: Calibration software settings using mode 2

SOFTWARE	
ASF [µrad/px] (fixed or adapted)	1.804 (Fixed)
SAM cross-correlations mode [1 or 2]	2
Compression Expansion Scaling Factor	1
Fine tuning to align SAM slope error to NOM and HDX [mm]	0
ROI used [y*x] [px]	1400*1400
ROI used y [px]	310 - 1710
ROI used x [px]	0 – 1400; 170 – 1570; 340 – 1740; 510 – 1910; 681 – 2081; 851 – 2251; 1021 – 2421; 1192 – 2592
DIC Edge y top/bottom [px]	50/50
DIC Edge x left/right [px]	300/300

ROIs used [image]	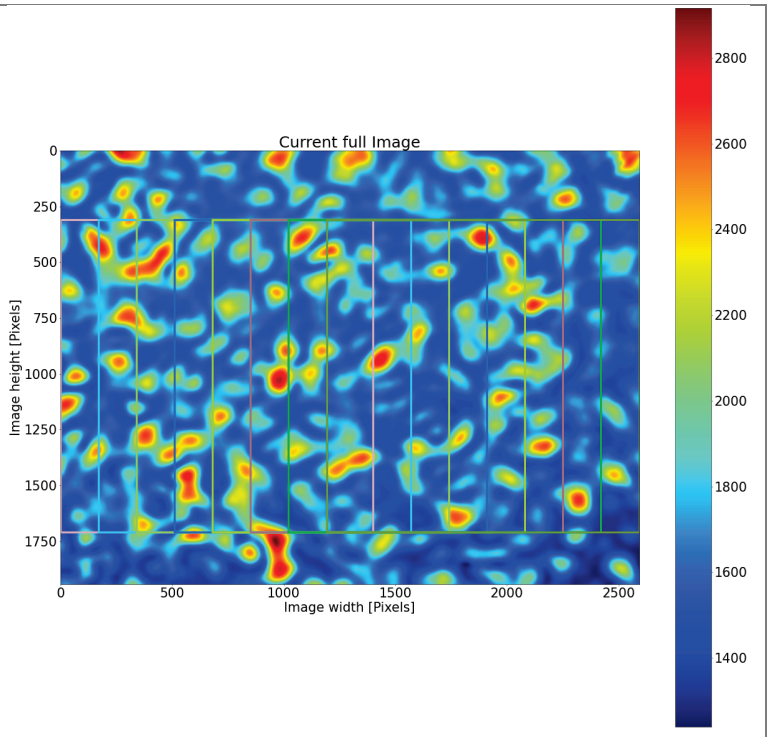
Gaussian filter sigma [σ]	10

These scans consist of 50 cross-correlation values for each Region of Interest (ROI), correlated utilising the SAM mode 2 and expressed in pixel units. The employment of multiple scans in this context aims to diminish random noise.

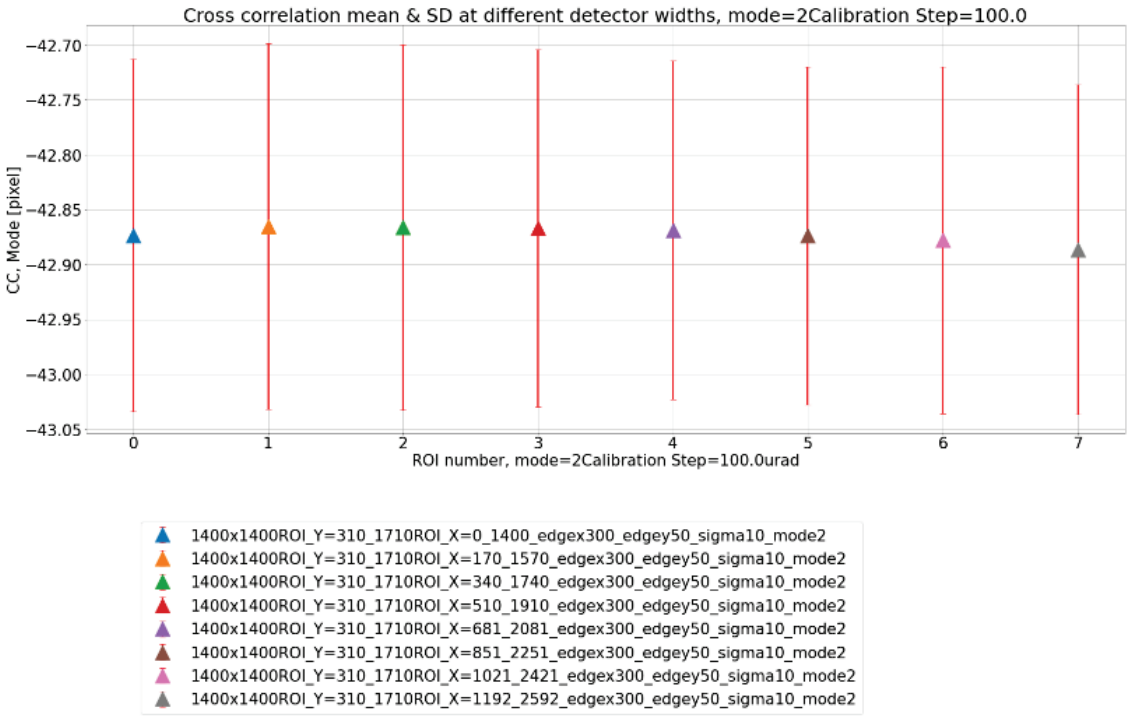

Figure 44: Mode 2 calibration results using eight different ROI

Mode 2 is based on the cross-correlation between adjacent images, therefore the ASF can be defined as the ratio between NANGO displacement (for each step) and the mean displacement obtained across all ROIs, as shown in Figure 44. The results are expressed in equations (42) and (43):

$$ASF_{min} = \frac{100}{42.89} = 2.331546 \ \frac{\mu rad}{px} \tag{42}$$

$$ASF_{max} = \frac{100}{42.86} = 2.333178 \ \frac{\mu rad}{px} \tag{43}$$

Considering the ASF of 2.333178 µrad/px as reference the change in the average ASF across all the ROIs, is equal to -0.07%.

If the standard deviation is considered, the results are reported in equations (44) and (45):

$$ASF_{min} = \frac{100}{43.04} = 2.323420 \ \frac{\mu rad}{px} \tag{44}$$

$$ASF_{max} = \frac{100}{42.70} = 2.341920 \ \frac{\mu rad}{px} \tag{45}$$

Considering the ASF of 2.341920 µrad/px as reference, the ASF error within the calibrated range, including standard deviation (in percentage), is equal to -0.79%.

4.1.3. Observations

In the present analysis, a modest disparity is observed between the calibration procedures using Mode 1 and Mode 2. This is because mode 1 requires a wider ROI compared to mode 2. An effective way of comparing the two modes is achieved by comparing the mode 2 results with the derivative of mode 1. For an accurate comparison, it is imperative that both methods utilise identical Regions of Interest (ROIs) for the reference and the displaced images. The outcomes of this comparative study are detailed in Table 12, highlighting that the results exhibit minimal variation contingent upon the configuration employed.

Table 12: Difference in ASF using SAM modes 1 and 2. Calibration range: 0-5000 µrad with steps of 100 µrad.

Mode	DIC edge x [px]	DIC edge y [px]	ROI [y*x]	N. of scans	Calibrated ASF [µrad/px]	Percentage difference [%]
2	300	50	1400*1400	10	2.33250	0%(REFERENCE)
1	300	50	1400*1400	10	n/a	n/a
2	1100	50	1400*2592	10	2.33255	+0.022%
1	1100	50	1400*2592	10	2.32867	-0.164%
2	1100	50	1400*2592	1	2.33305	-0.086%
1	1100	50	1400*2592	1	2.3288	-0.159%

The greater the signal to noise ratio (S/N), the better. With SAM, the signal's amplitude is represented by the magnitude of the DIC. The noise is represented by the speckle vibrations due to mechanical and environmental conditions. The higher the S/N ratio, the fewer scans are necessary to accurately perform measurements using SAM.

Table 13 lists the multiple experiments carried out to validate such effect while calibrating the SAM, using three separate calibration ranges, 0-5000 µrad, 0-50 µrad, and 0-5 µrad, using mode 2 and the derivative of mode 1.

Table 13: Difference in ASF calculation of using the SAM mode 2 and derivative of mode 1 cross-correlations techniques

Mode	DIC edge x [px]	DIC edge y [px]	ROI [y*x]	Calibration range /step size [µrad]	Mean DIC using one scan [px]	Mean DIC using ten scans [px]	Difference between one and ten scans [%]
2	1100	50	1400*2592	0-5000 / 100	-42.86223	-42.86636	-0.01
Derivative of mode 1	1100	50	1400*2592	0-5000 / 100	-42.93426	-42.93825	-0.01
2	1100	50	1400*2592	0-50 / 1	-0.42827	-0.42776	+0.11
Derivative of mode 1	1100	50	1400*2592	0-50 / 1	-0.42784	-0.42758	+0.06
2	1100	50	1400*2592	0-5 / 0.1	-0.03206	-0.03579	-11.63
Derivative of mode 1	1100	50	1400*2592	0-5 / 0.1	-0.0397	-0.04253	-7.12
2	10	5	1944*2592	0-5 / 0.1	-0.03923	-0.04244	-7.76
Derivative of mode 1	10	5	1944*2592	0-5 / 0.1	-0.03929	-0.04234	-7.76

During the calibration, for step sizes of 50 µrad and greater, adequate accuracy (less than 1% error) can be obtained with only one scan. Visual representation of the findings is shown in Figure 45.

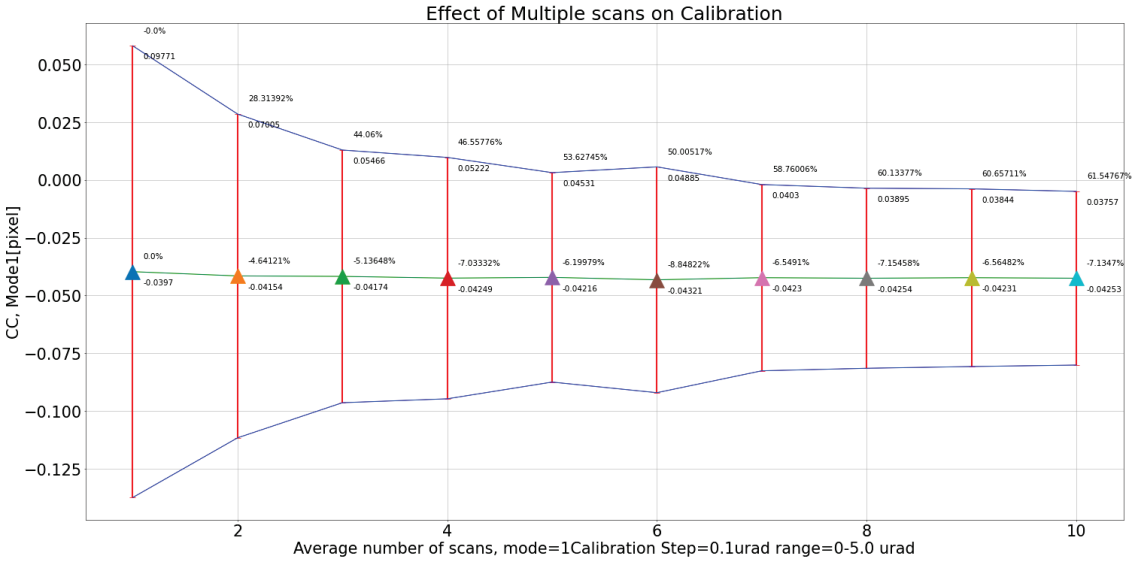

(A)

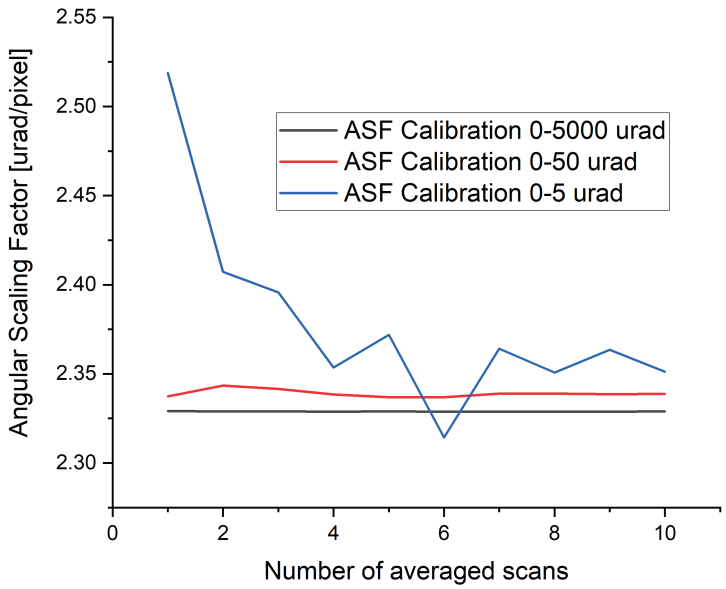

(B)

Figure 45: (A): Effect of multiple scans on the mean DIC value and standard deviation reduction, in a 0-5 µrad range. (B): Effect of Averaging scans on ASF, at different calibration ranges

Results can also be expressed using mode 1 or the ideally equivalent integration of mode 2, and are visually represented in Figure 46, where the 0-5 µrad range results are represented after 1 and 10 scans, respectively.

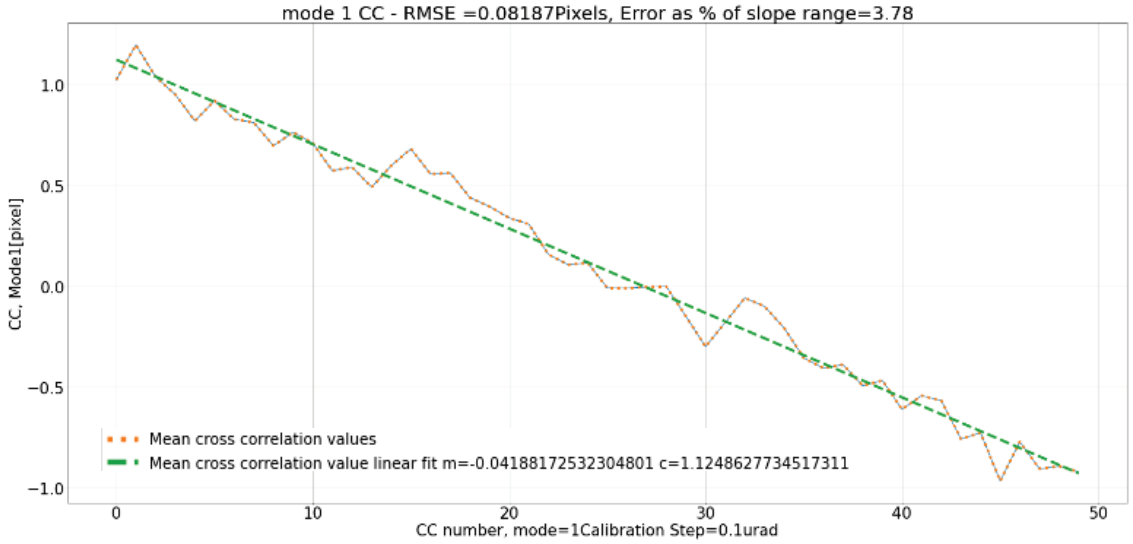

(A)

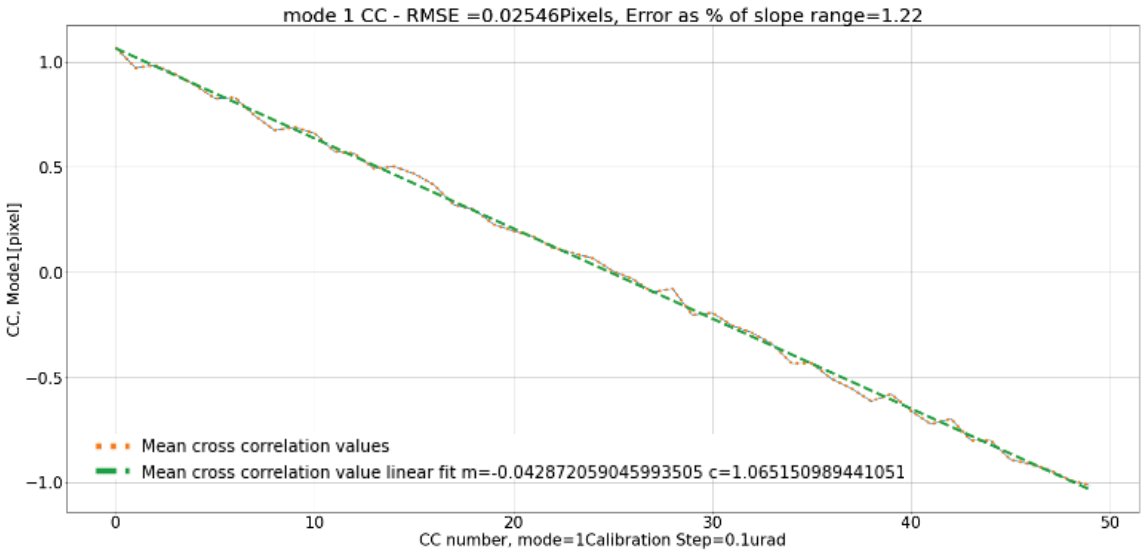

(B)

Figure 46: (A): Slope of the DIC using mode 1 on the y-axis and the number of steps on the x-axis using only 1 scan, on a 0-5 µrad range. (B): Slope of the DIC using mode 1 on the y-axis and the number of steps on the x-axis using the average of 10 scans, on a 0-5 µrad range

Table 14 lists the multiple experiments carried out to validate the SAM calibration procedure, using three separate calibration ranges, 0-5000 µrad, 0-50 µrad, and 0-5 µrad, using mode 1 and the integration of mode 2.

Table 14: Difference in ASF calculation of using the SAM mode 1 and integration of mode 2 cross-correlations techniques.

Mode	DIC edge x [px]	DIC edge y [px]	ROI [y*x]	Calibration range / step size [µrad]	Mean DIC using one scan [px]	Mean DIC using ten scans [px]	Difference between one and ten scans [%]
Integration of mode 2	1100	50	1400*2592	0-5000 / 100	-42.88067	-42.87917	-0.003
1	1100	50	1400*2592	0-5000 / 100	-42.94429	-42.94347	-0.002
Integration of mode 2	1100	50	1400*2592	0-50 / 1	-0.42805	-0.42764	0.01
1	1100	50	1400*2592	0-50 / 1	-0.42648	-0.42643	0.01
Integration of mode 2	1100	50	1400*2592	0-5 / 0.1	-0.03495	-0.03599	-2.97
1	1100	50	1400*2592	0-5 / 0.1	-0.04188	-0.04287	-2.36
Integration of mode 2	10	5	1944*2592	0-5 / 0.1	-0.04156	-0.04294	-3.32
1	10	5	1944*2592	0-5 / 0.1	-0.04156	-0.04299	-3.44

Finally, Table 15 compares the ASF estimated using various methodologies and procedures. It is relevant to note that just one arrangement produces an outlier in the ASF. This occurs when the ROI for mode 2 cross-correlation and the calibration steps are too small (0.1 µrad) and the calibration range is too narrow (0-5 µrad).

Table 15: Difference between the SAM mode 2 (and derivative of mode 1) and mode and mode 1 (and the integration of mode 2)

Mode	DIC edge x [px]	DIC edge y [px]	ROI [y*x]	Calibration range / step size [µrad]	ASF using 10 scans	
					Mode 2 or derivative of mode 1	Mode 1 or integration of mode 2
2	1100	50	1400*2592	0-5000 / 100	2.3328	2.3321
1	1100	50	1400*2592	0-5000 / 100	2.3289	2.3286
2	1100	50	1400*2592	0-50 / 1	2.3378	2.3384
1	1100	50	1400*2592	0-50 / 1	2.3387	2.3456
2	1100	50	1400*2592	0-5 / 0.1	2.7941	2.78
1	1100	50	1400*2592	0-5 / 0.1	2.3513	2.3326
2	10	5	1944*2592	0-5 / 0.1	2.3563	2.3288
1	10	5	1944*2592	0-5 / 0.1	2.3618	2.3261

4.1.4. Calibration of Extremely Curved Optics

This optic was characterised by a very strong radius of curvature, approximately 0.4 m. The surface profile was cylindrical on the tangential axes (x-axis). The experimental setup and SUT characteristics are shown in Figure 47 and Table 16.

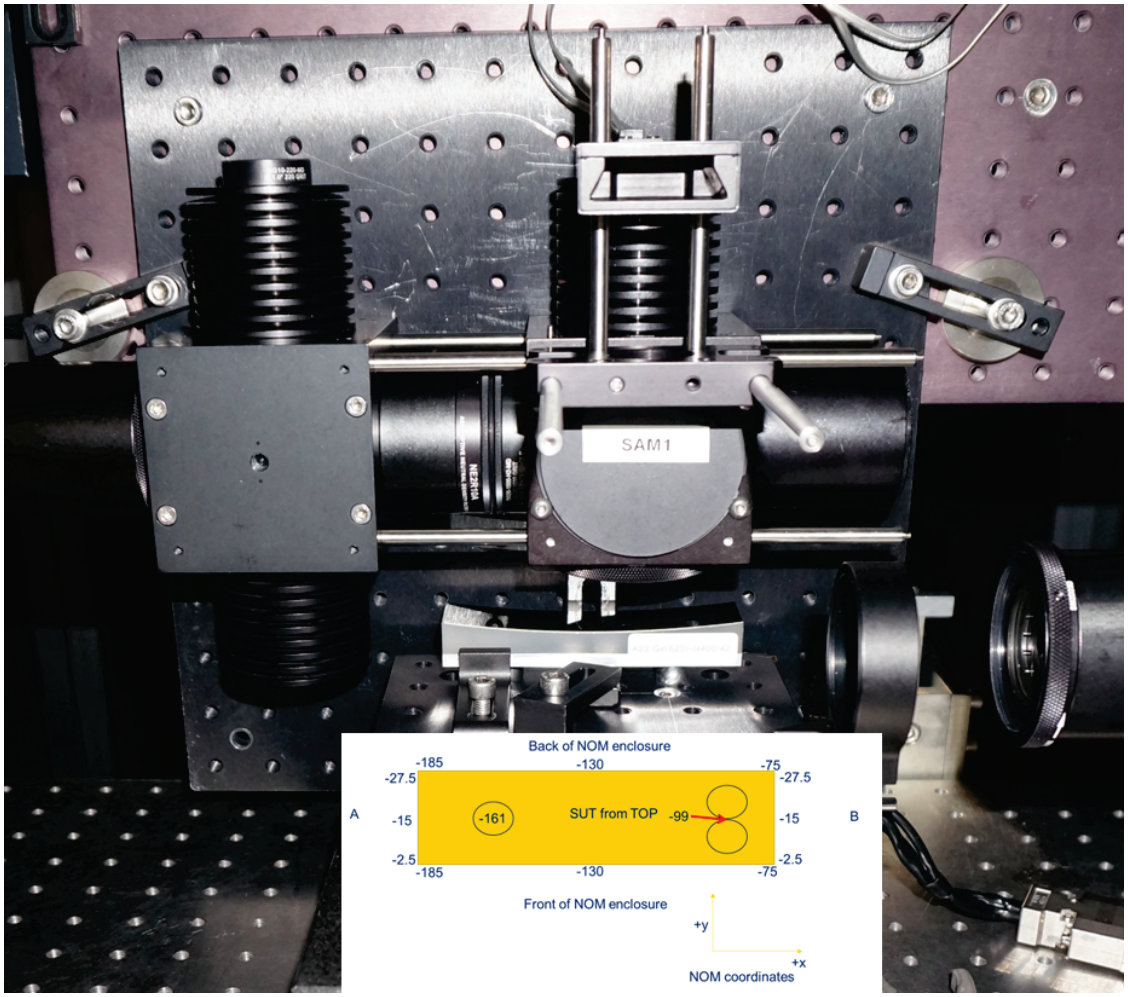

Figure 47: XRS-Tech cylindrical crystal physical side scanning setup

Table 16: Technical details of the XRS-Tech cylindrical crystal

Supplier	XRS-Tech
Substrate	Germanium
Dimensions	110(L) x 25 (W) mm^2
Shape	Cylindrical
Tangential Cylinder	RoC = 0.4 m (nominal).

For strongly curved optics, a fixed ASF cannot be used, as it will generate a systematic error, as explained in section 4.4.6.

To show the extent of the change in ASF at different location within the tangential axis of the SUT, calibrations were run at different locations within the SUT, as shown in Figure 48.

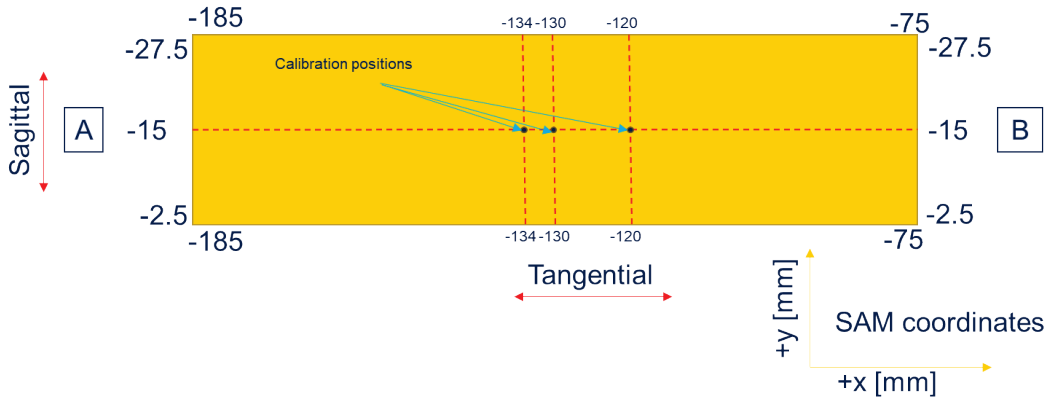

Figure 48: Calibration scans positions along the x (tangential axis) of the SUT

For each calibration's scanning positions, 5 ROIs positions were considered, as shown in Table 17.

Table 17: Calibration configurations

SOFTWARE	
SAM gantry: Sagittal axis coordinate [mm]	-15
SAM gantry: Tangential axis coordinates [mm]	-134; -130; -120
SAM cross-correlations mode [1 or 2]	1 and 2
Number of Calibration scans	10
Scan tilt stage start position [µrad]	4800
Scan tilt stage finish position [µrad]	6800
Scan tilt stage scan step size [µrad]	100
Number of images in each scan	21
Total number of data points used to determine ASF for each ROI chosen position	210
CESF	N/A
Fine tuning to align SAM slope error to NOM and HDX [mm]	N/A

Tilt angle [µrad]	**ROI 1 [pixel]**	**ROI 2 [pixel]**	**ROI 3 [pixel]**	**ROI 4 [pixel]**	**ROI 5 [pixel]**
+5800	Size 1400*1400				
	ROI y position 272 – 1672				
	ROI x position 0 - 1400	ROI x position 298 - 1698	ROI x position 596 - 1996	ROI x position 894 - 2294	ROI x position 1192 - 2592
	Edge x 400				
	Edge y 100				
	Gaussian blur sigma 10				
	SAM DIC mode 1 and 2				
	ROI sample 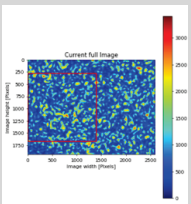	ROI sample 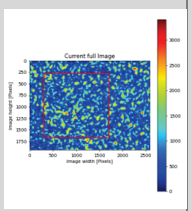	ROI sample 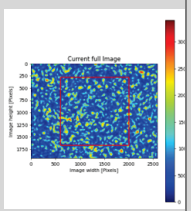	ROI sample 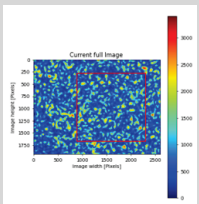	ROI sample 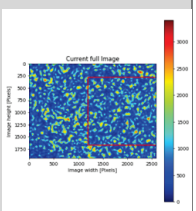

Mode 1 and mode 2 calibrations have been conducted, together with multiple calibration scans. The results are shown in Figure 49. Such results highlight the difficulty of accurately determine the angular scaling factor and its variance when characterising a strongly curved optic.

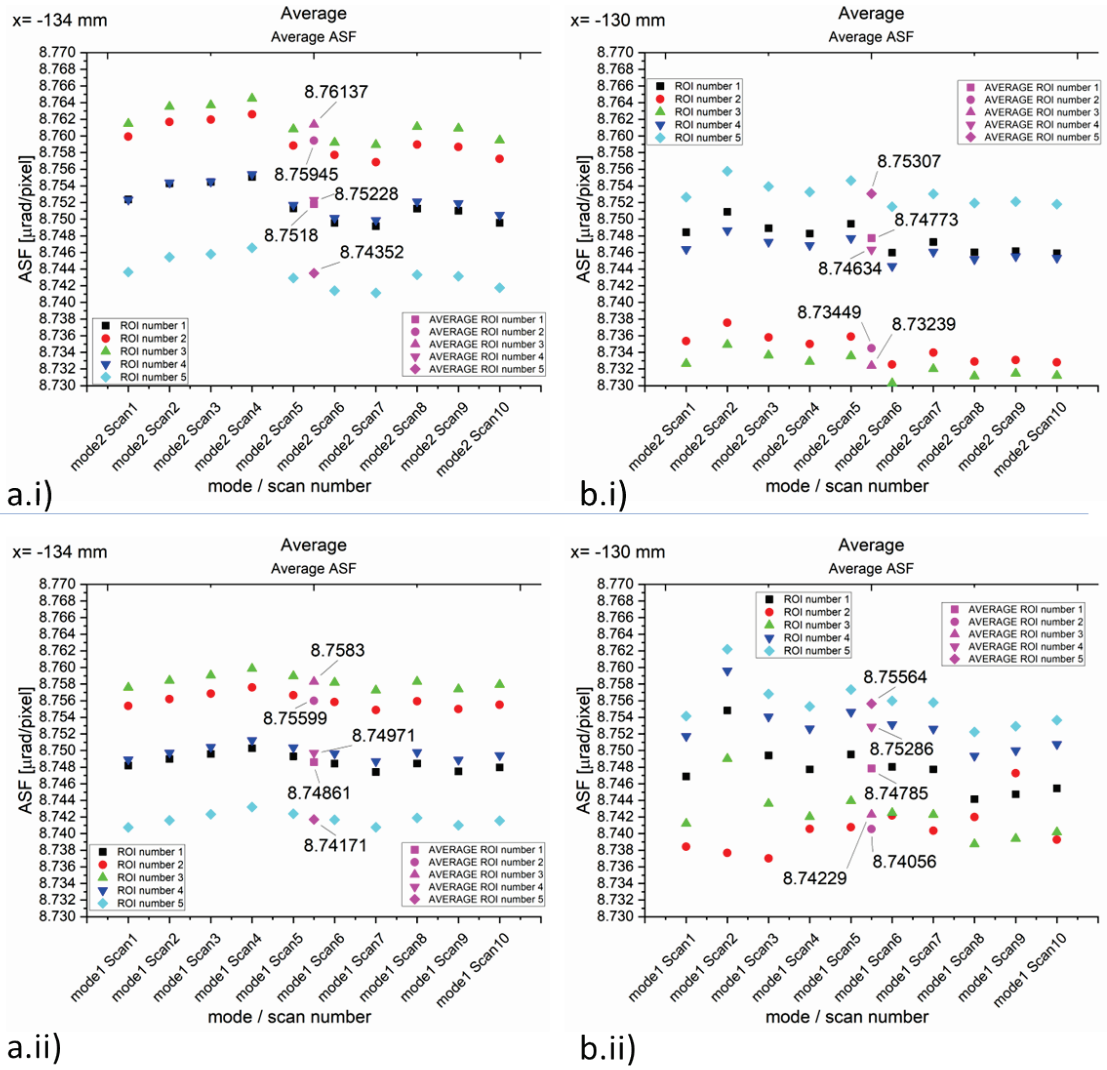

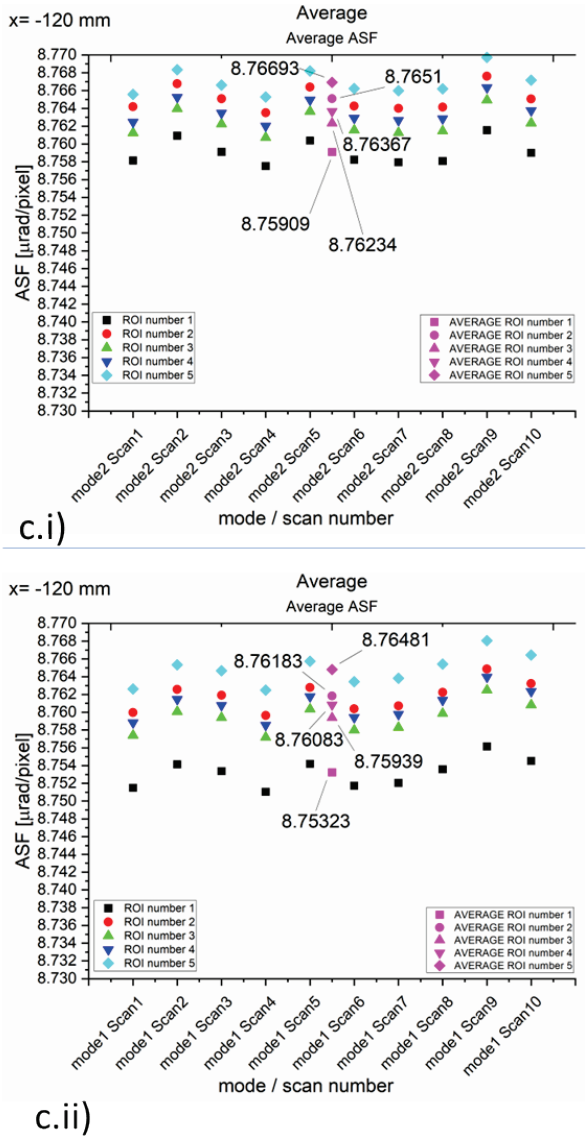

Figure 49: SAM ASF calibration at different SUT's tangential positions

The average ASF at each ROI position, and for each calibration's tangential position, is illustrated in Figure 50. It is worth noting that there is a small discrepancy from using mode 1 and mode 2, as the two modes of calculating the ASF are comparable, but different. Mode 2 ASF is calculated as the simple average of the DIC values, while mode 1 uses the gradient of the best linear line of fit, corresponding to the minimum root mean square error (RMSE) between the modelled and input values. What can be validated from these results is the significant change in ASF at different SUT's tangential positions, which shall be taken in consideration while retrieving its surface profile of the optics using the SAM. Such systematic error can be compensated using the HSASF as explained in section 3.5.1 and 4.4.6.

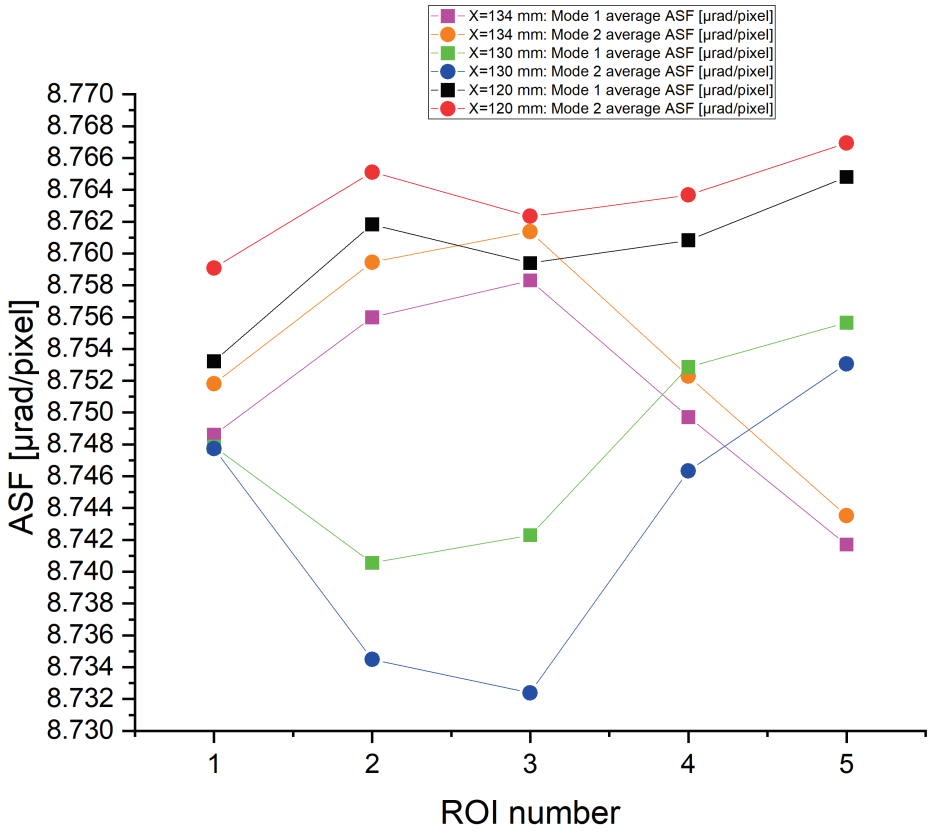

Figure 50: Average ASF, calculated at different ROI positions

Being the ASF calculated at the SAM x-axis coordinate position of -130 mm, the average between all the ASF, calculated using mode 1 and mode 2, is equal to 8.74532 µrad/pixel, as shown in Table 18.

Table 18: ASF optimisation at centre of SUT (Sam x-axis coordinate equal to -130 mm)

ROI number	**DIC mode**	$\boldsymbol{ASF}$ [$\boldsymbol{\mu rad/pixel}$]	$\overline{\boldsymbol{ASF}}$ [$\boldsymbol{\mu rad/pixel}$]	$\frac{\sum \overline{ASF}}{2}$ [$\boldsymbol{\mu rad/pixel}$]
1	1	8.74785	8.74784	8.74532
2		8.74056		
3		8.74229		
4		8.75286		
5		8.75564		
1	2	8.74773	8.7428	
2		8.73449		
3		8.73239		
4		8.74634		
5		8.75307		

4.1.4.1. Ideal Cylindrical Profile and HSASF Calculation

By knowing the ASF at the centre of the SUT, the distance from the optic's surface to the SAM detector plane can be retrieved, as follow:

$$\tan(ASF) = \tan\left(\frac{ASF}{1{,}000{,}000}\right) \tag{46}$$

Where:

- $\tan(ASF)$ is the tangent to the angular scaling factor.
- $1{,}000{,}000$ is the conversion factor used to convert µrad to rad.

Importing equation (46) into equation (63), the distance from SAM detector can be established, as shown in equation (47).

$$d = P_{s(x)} * \left(\frac{1}{\tan(ASF)}\right) * \frac{1}{2} \tag{47}$$

Where:

- d is SAM's detector distance from the SUT's surface, expressed in meter
- $P_{s(x)}$ is the SAM detector pixel size, expressed in meter.
- $\frac{1}{2}$ is the factor used, taking in consideration that the incident laser beam path is the same length as the reflected beam path to the detector.

Applying equation (63), the distance of SAM's detector from the SUT's surface, considering an ASF of 8.74532 µrad/pixel, is shown in equation (48).

$$d = 0.0000022 * \left(\frac{1}{8.74532 * 10^{-6}}\right) * \frac{1}{2} = 0.125782\ m = 125.782\ mm \tag{48}$$

Considering the entire length of the cylindrical SUT, equal to 110 mm, it is possible to calculate its nominal height profile along the tangential plane, having a radius of curvature equal to 0.4m, using equation (22). The parameters selected are shown in Table 19.

Table 19: XRS-Tech nominal cylindrical profile simulated

Direction	-1
$\boldsymbol{RoC}$ **[m]**	+0.4
$\boldsymbol{x}$ **range [m]**	From -0.055 to +0.055 in steps of 0.0001
$\boldsymbol{x_{offset}}$ **[m]**	0
$\boldsymbol{y_{offset}}$ **[m]**	- RoC = -0.4

The modelled SAM's detector plane distance from the SUT (d) and the respective HSASF are shown in Figure 51.

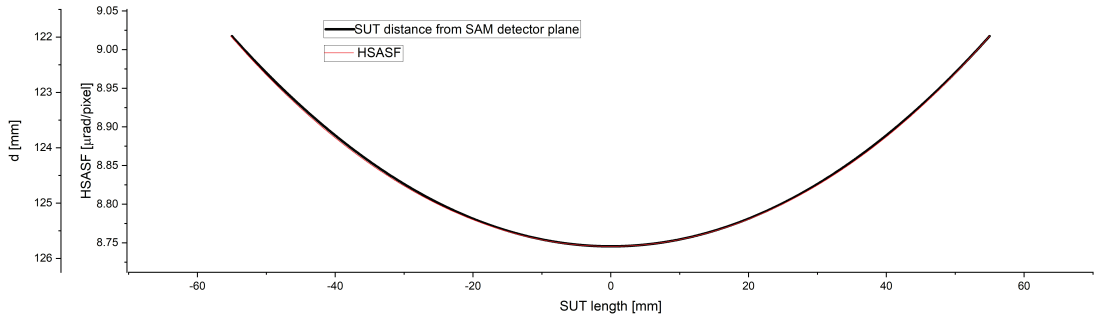

Figure 51: HSASF and SUT distance from SAM detector plane

4.2. Simulation of Surface Slope Profiles using NANGO

To test SAM capabilities in a different environment, the NANGO [76] was used as a tool for simulating surface slope profiles. The hardware configuration used is shown in Figure 41. The environment was not the most stable available in OML.

The methodology used was the following:

1) Define the optical slope profile to be simulated.
2) Calibrate SAM instrument.
3) Simulate the slope profile using the NANGO.
4) Use SAM DIC techniques to assess the precision and accuracy of SAM measurements.

Characterisation of SUT surface profiles with an average radius of curvature exceeding 30km presents specific difficulties. Challenges arise when the SAM instrument is positioned too close to the SUT. This proximity can lead to a Digital Image Correlation (DIC) between adjacent images that is less than 1/100 of a pixel during SAM scanning head translations across the SUT with scan step sizes under 0.5mm. This situation approaches the operational limits of the SAM instrument. Consequently, several simulations have been executed to ascertain the accuracy of the SAM instrument when used to characterise various surface slope profiles. The configurations used are listed in Table 20. The simulated slope data was provided the metrology instrument NOM.

Table 20: Parameters of the simulation of flat grating slope error profiles using NANGO

Reference Instrument	NOM
Generated slope amplification	x100; x50; x10; x5; x1
SAM ASF	2.3578
Optics used and simulation range [mm]	ZEISS flat grating I21PG6 (-74 to +74)
Simulated step size [mm]	0.25

First, I simulated the SUT surface slope profile amplified by 100 times, this ensured SAM mode 2 cross-correlation to be greater than 1/10 of a pixel. Results are listed in Table 21. Such amplification simulates a strong signal and a strong curvature from the mirror, making it easier from SAM to reconstruct the simulated slope profile. The surface slope profile has been simulated only twice, and the results are the average of the two scans. To compare the low frequency accuracy between the simulated NANGO input slope and the SAM reconstructed slope profiles, the slope of linear regression of NANGO input and SAM measurements of the SUT slope profile was used, expressed in µrad/mm.

Results are shown in Table 21. After only two simulated scans, an error of only 1% was achieved, in any configuration.

Table 21: SAM Mode 1-2 accuracy. NOM slope amplified by 100 times

Mode	**DIC Edge x [px]**	**DIC Edge y [px]**	**ROI [y*x]**	**DIC ROI [y*x] diff. [%]**	**N. of scans**	**ASF [urad/px]**	**Slope [µrad/mm]**	**Diff. [%]**
Profile simulated: NOM slope multiplied 100 times [µrad] **Method of comparison:** Comparing slope of linear regression of NOM and SAM measurements of the SUT slope profile (µrad/mm)							Slope=-1.45 SD=0.00898	0
2	300	50	1400*1400	0	2	2.3578	Slope=- 1.45739 SD=0.00896	+0.5
1	300	50	1400*1400	0	2	2.3578	Slope=- 1.46287 SD=0.00902	+0.88
2	300	50	2592*1944	+253	2	2.3578	Slope=- 1.45944 SD=0.00896	+0.65
1	300	50	2592*1944	+253	2	2.3578	Slope=- 1.46478 SD=0.00901	+1.01
Average displacement (mode 2) DIC [px]					0.154440134			
Total range (mode 1) DIC [px]					From -49.26126611 to 53.32141022			

Next, I simulated the NOM slope, amplified by 50 and 10 times, resulting in similar outcomes, and highlighted in Appendix C, Table 46 and Table 47.

In the previous configuration, mode 2 DIC_x resulted, on average, in a value greater than 1/100 of a pixel, therefore challenging, but still possible to accurately retrieve using few SAM scans. Next was to simulate NOM slope error by 5 times. In this configuration, the average mode 2 DIC_x was less than 1/1000 of a pixel displacement. Therefore, few SAM scans were not sufficient to acurately characterise the simulated slope, as the signal to noise ration was getting weaker. More scans were required, and improvement from using two to six scans are shown in Appendix C, Table 48 and Table 49, respectively.

This effect was even stronger when the data from NOM was simulated (without amplification). The effect of increasing the number of NANGO simulations required to reconstruct the simulated slope profile is shown in Figure 52, and the corresponding comparison with NOM slope, after ten scans, are shown in Figure 53 and Table 22.

Table 22: Mode 1-2 accuracy. NOM slope amplified by 1, used average of 10 scans

Mode	DIC Edge x [px]	DIC Edge y [px]	ROI [y*x]	DIC ROI [y*x] diff. [%]	N. of scans	ASF [urad/px]	Slope [µrad/mm]	Diff. [%]
Profile simulated: NOM slope error [µrad] **Method of comparison:** Comparing slope of linear regression of NOM and SAM slope error (µrad/mm)							Slope=-0.0145 SD=8.98272E-5	0
2	300	50	1400*1400	0	10	2.3578	Slope=-0.01736 SD=9.61661E-5	-19.72
1	300	50	1400*1400	0	10	2.3359	Slope= -0.01566 SD=9.53276E-5	-8
2	10	5	1400*1400	+84.44	10	2.3578	Slope= -0.01537 SD=9.69361E-5	-6
1	10	5	1400*1400	+84.44	10	2.3359	Slope= -0.0155 SD=9.62649E-5	-6.8
2	10	5	2592*1944	+378.29	10	2.3578	Slope= -0.01514 SD=9.69178E-5	-4.41
1	10	5	2592*1944	+378.29	10	2.3359	Slope= -0.01555 SD=9.71345E-5	-7.24

Average displacement (mode 2) DIC [px]	0.001757867
Total range (mode 1) DIC [px]	From -0.771255435 to 0.660851323

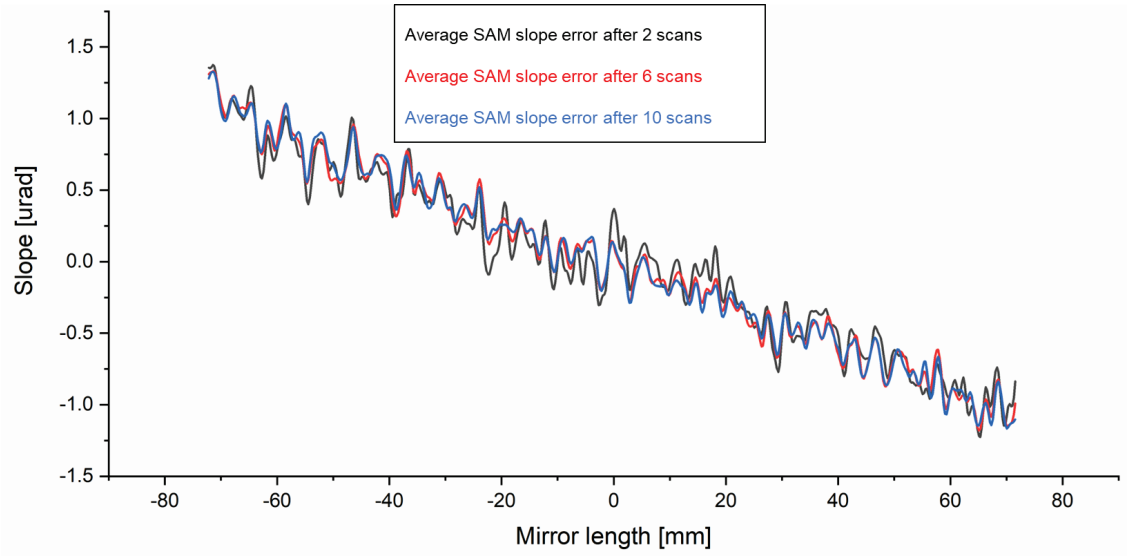

Figure 52: Effect of multiple SAM measurements on accuracy



Figure 53: NOM Slope error vs SAM reconstructed slope error

Table 22 shows that in this configuration, the size of the ROI selected for DIC becomes more significant because a larger size corresponds to a greater number of data points (speckles). The greater are the number of simulated scans, the maximum size of ROI, and stability of the environment, the greater is the accuracy of the SAM.

4.3. Stability

Metrology stability tests are crucial in guaranteeing the accuracy and precision of measurement apparatus and systems. The objective of these trials is to evaluate the long-term stability of a measurement system, encompassing its capacity to preserve calibration and measurement efficacy amidst fluctuating environmental conditions.

In a metrology stability experiment, the measurement system undergoes exposure to diverse environmental factors, such as temperature and humidity, to appraise its

functionality under different conditions. Moreover, the outcomes of these trials can be employed to pinpoint potential issues prior to their impact on measurement outcomes.

To measure dynamic stability of the system, six scans were performed of the elliptical X-ray mirror, shown in Figure 56. The cross-correlation technique used was mode 1 and the environmental parameters are shown in Table 23.

Table 23: Stability experiment parameters

Mean temperature	20.804 °C	**Standard deviation**	0.006 °C
Mean Humidity	32.113 RH	**Standard deviation**	0.061 RH
Mean Atmospheric pressure	1006.809 mbar	**Standard deviation**	0.095 mbar
Time	21 minutes		
Total number of images	250		
SD along x	28 nrad		
SD along y	26 nrad		

Figure 54 displays the absolute stability results. After SAM calibration was performed, the stability SD of 28 and 26 nrad along the x and y axes was achieved.

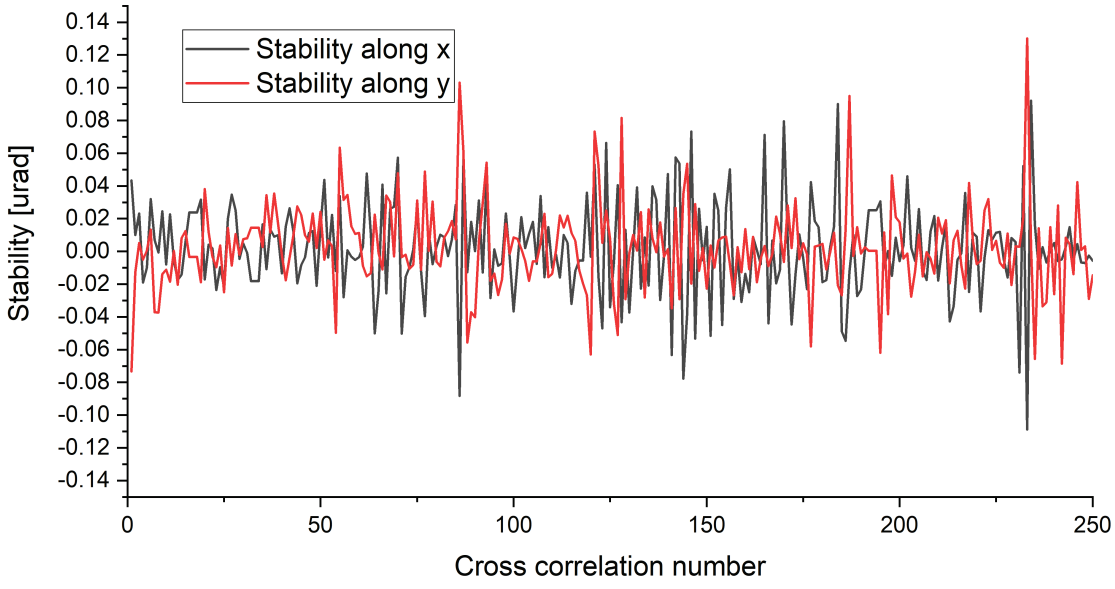

Figure 54: Stability results

The environment was very stable, helping to achieve stability below 30 nrad. Also, regarding the dynamic stability, and thus SAM precision, results are represented in Table 24 and Figure 55,where over 6 different scans, taken over a 2 hours period, an RMSE of only 32 nrad was achieved.

Table 24: Repeatability test parameters

RMSE	32 nrad
Number of scans	6 scans
Time	2 hours

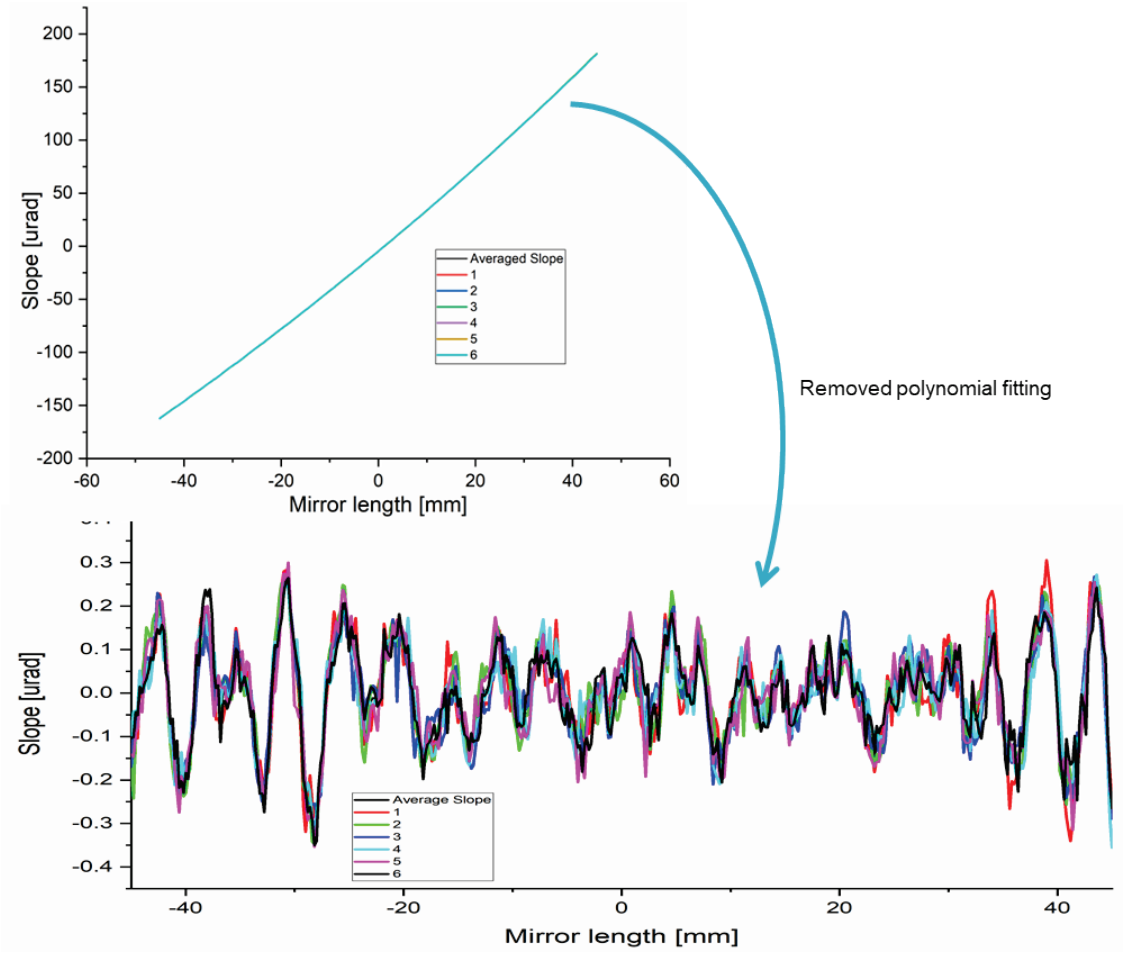

Figure 55: SAM repeatability test results. A second-order polynomial (curve of best fit) was subtracted to reveal the high-frequency error component between multiple scans.

4.4. Characterisation of Optics

4.4.1. Ellipsoid X-ray Mirror

The mirror, detailed in Table 25, was measured by different metrology labs around the world, as part of a project called MOONPICS. It has three different elliptical lanes and fiducials on the sides of each lane, which is very useful to perform the correct alignment of the SUT.

Lane one is a pure ellipse, while lanes two and three have parabolic arcs figures on the top of the ellipse, and the 1D theoretical slope of these arcs is represented in Figure 56.

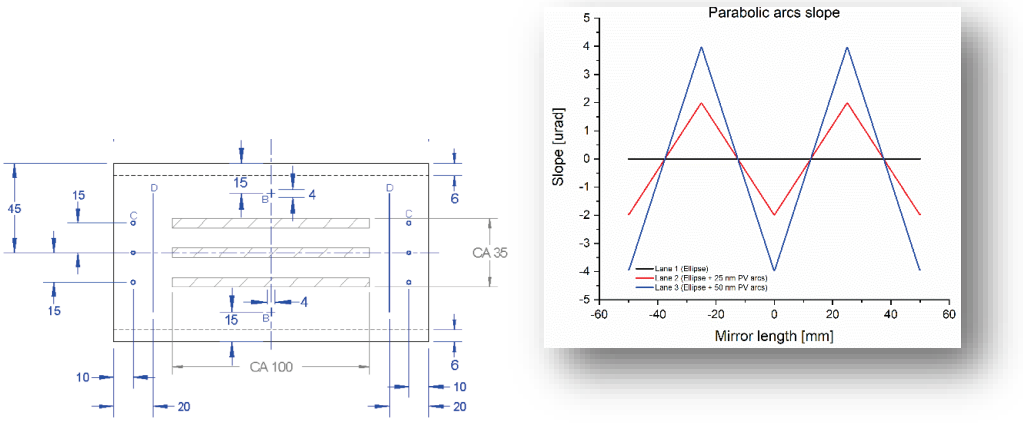

(a) (b)

Figure 56: Technical drawing of the mirror (a) and of the residuals of the optics elliptical lanes (b)

Table 25: Technical details of the ZEISS multilane mirror

Supplier	**Zeiss (Germany)**
Substrate	Silicon
Dimensions	160 (L) x 90 (W) x 50 mm (H)
Analysis length	Clear aperture = 100 mm (centred on fiducials)
Shape	Tangential ellipse + 2 lanes with additional parabolic arcs superimposed on top of the ellipse. This is to purposefully create a broadened X-ray beam [77]
Tangential ellipse	P = 46 m, Q = 0.4 m, θ= 3 mrad

At first, the spatial resolution of different instruments was set using different methods, represented in Table 26:

Table 26: Spatial resolution configuration of all instruments

SAM	**HDX**	**NOM**
Region Of Interest of 3.85 by 5.28mm	Butterworth low pass filter with cut-off period of 1mm was chosen	Aperture size of 3.5 mm was used

The next step was to align the data from the metrology instruments. The second derivative of the surface figure is ideal for alignment of a mirror with fiducials. Once the SAM data on the left fiducial was aligned (at -70mm from the centre of the mirror), as shown in Figure 57, the right fiducial position was observed, and from Figure 58 I show how SAM mirror length coordinates are compressed. Such is due to the Coefficient Expansion Scaling Factor (CESF), explained in section 3.9.

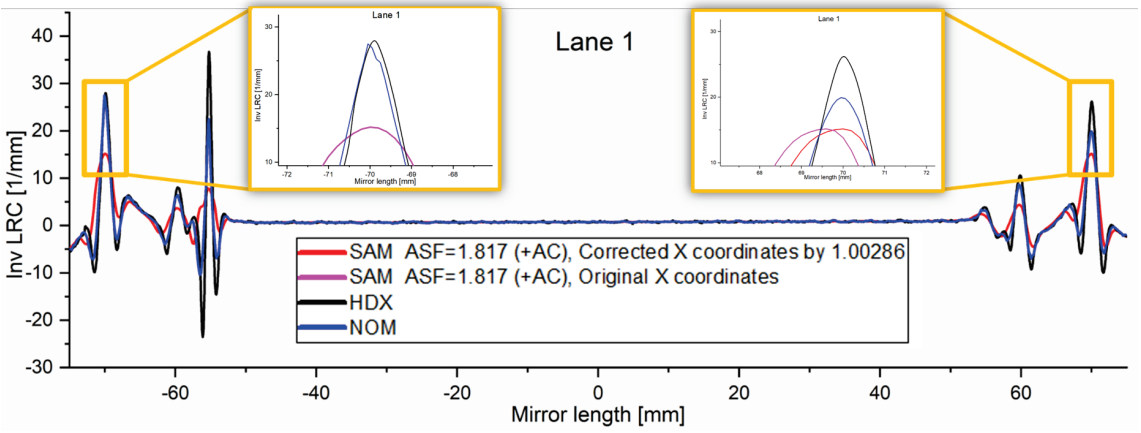

Figure 57: Inverse of local radius of curvature (LRC) from SAM, Diamond-NOM and a Fizeau interferometer (HDX) of the mirror's lane 1

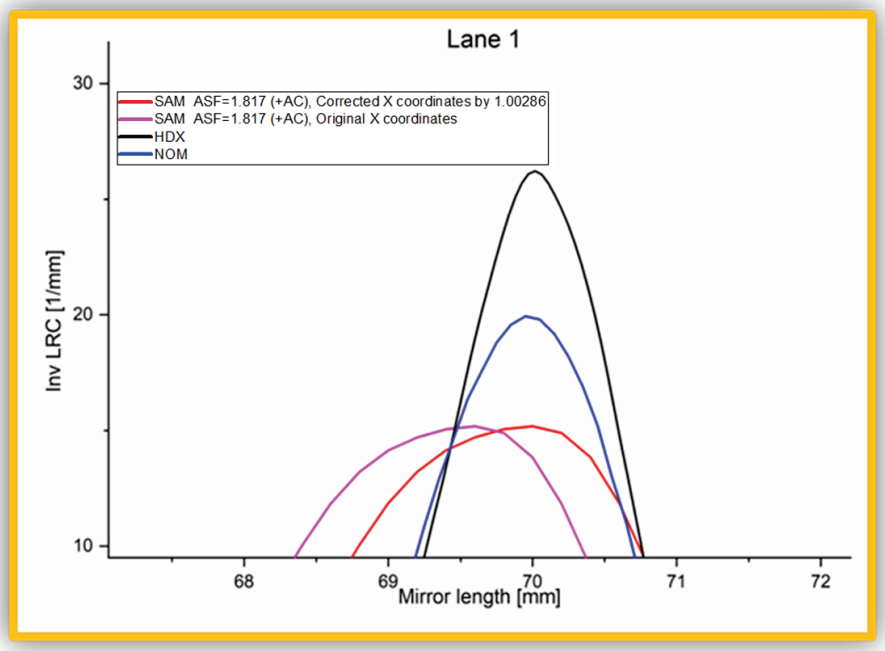

Figure 58: CESF to be included when measuring curved optics

The NOM, HDX and SAM metrology instruments characterised this mirror independently and at different times (months apart from each other). The calculated slope errors were calculated by removing the nominal ellipse figure slope, as specified by the mirror's manufacturer, from the measured slope profiles. As a result, I was able to analyse the residual high frequency errors, as shown in Figure 59.

While the amplitude SAM data is lower compared to the other two instruments, this is only because of the size of the ROI purposely chosen for SAM data analysis during this experiment.

On lane 2 and lane 3 the high frequency residuals are combined with a low frequency profile, related to the parabolic arcs presented in Table 25.

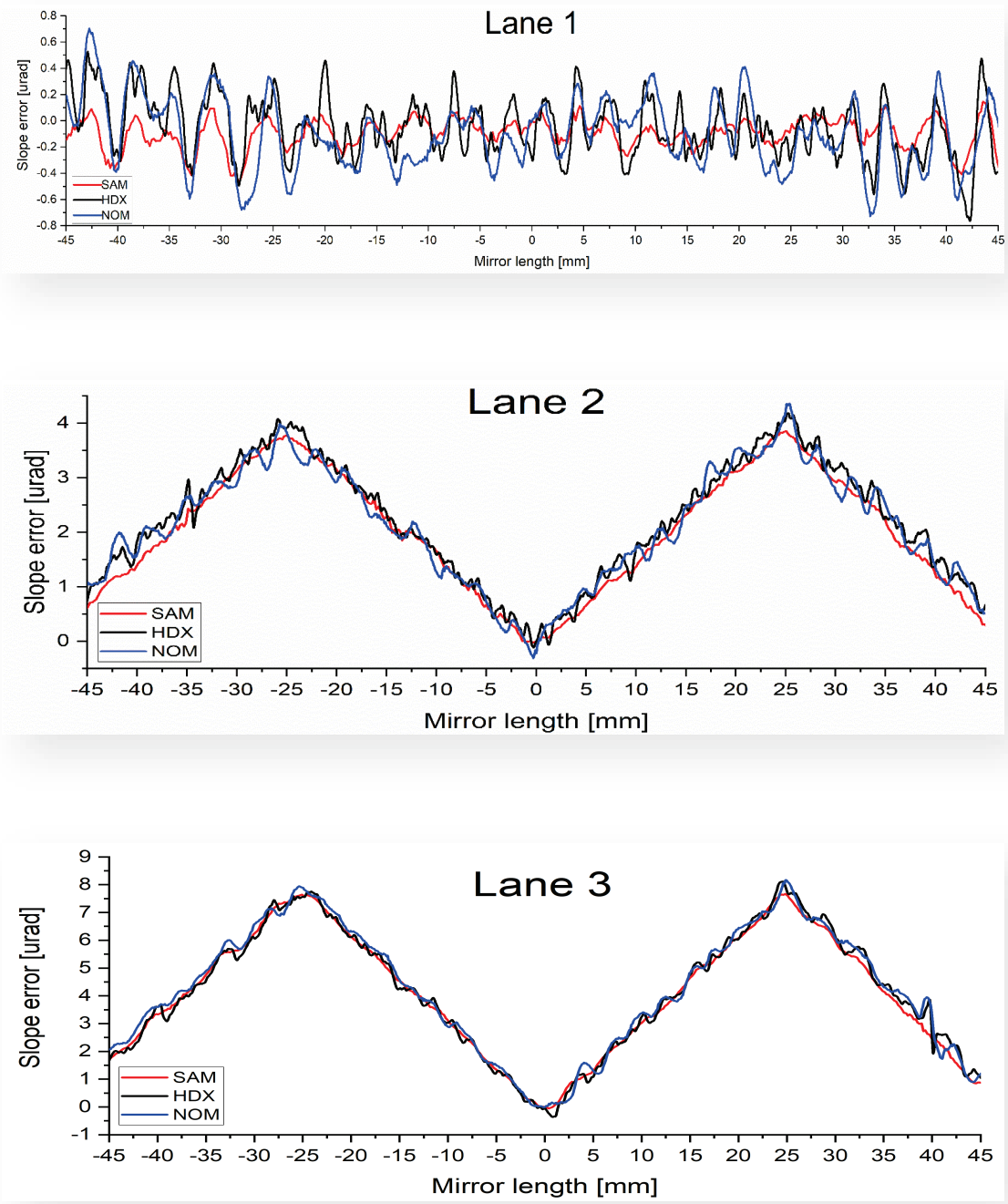

Figure 59: Image showing the results from all three instruments of the third lane of the ZEISS multilane mirror

SAM spatial resolution depends on the size of the illuminated speckle membrane (hardware) and region of interest selected for data analysis (software). Figure 60 shows the effect of different ROIs on SAM's spatial resolution. In red and black are shown the slope error calculated by SAM and HDX, as shown in the previous picture, and in green is the result with a much smaller ROI, highlighting how changing the size of the region of interest changes the spatial resolution of SAM. With a ROI of 600 by 600 pixels the results obtained match the HDX measurement, in both low and high frequency domains.

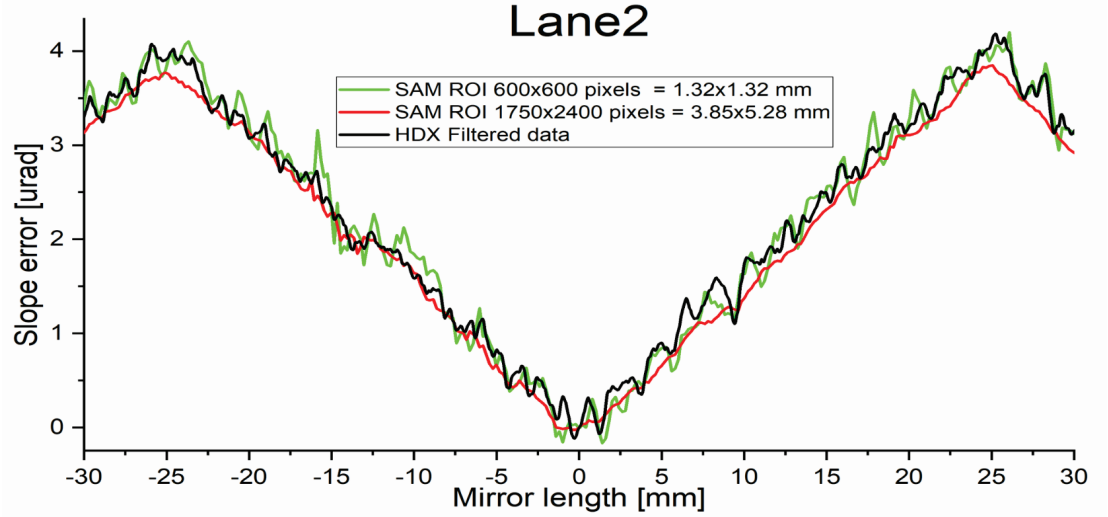

Figure 60: SAM measurements using different ROI size, compared to the HDX

The change in spatial resolution can also be observed by analysing the Power Spectral Density (PSD) distribution of the figure error (integration of the slope error). The ROIs act similarly to digital low-pass filters, and different sizes effect their relative cut-off frequency/period, thus helping retrieve different features from the surface of the sample under test, as shown in Figure 61.

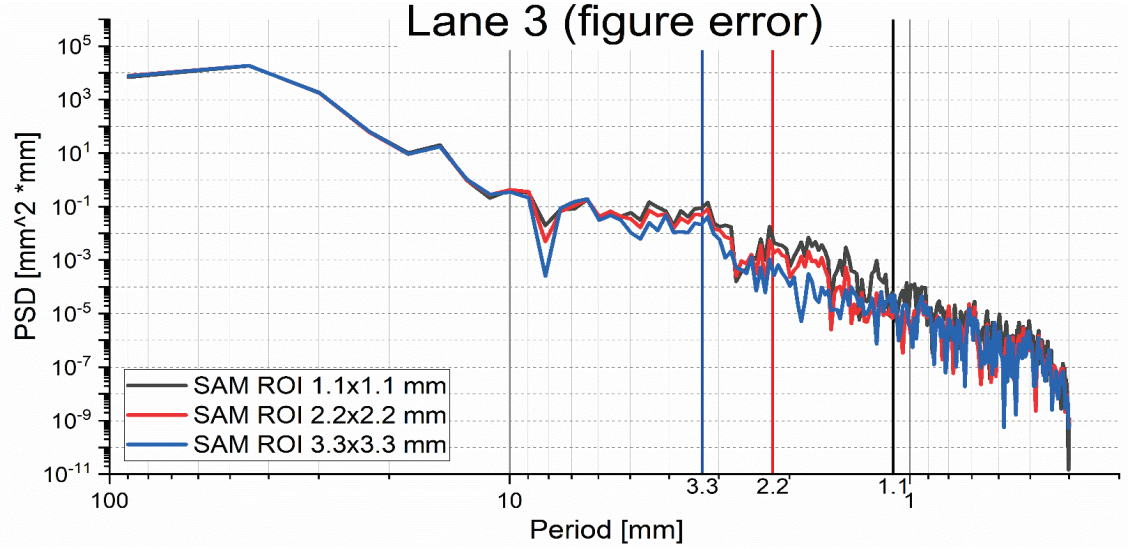

Figure 61: PSD using different SAM ROIs

Power spectral density function is also a useful tool to compare different instruments. From Figure 62 it is possible to notice the influence of the lateral scan size of both SAM and NOM on the right part of this graph. The SAM collected samples every 0.2mm along the tangential axis of the SUT, while NOM every 0.1mm.

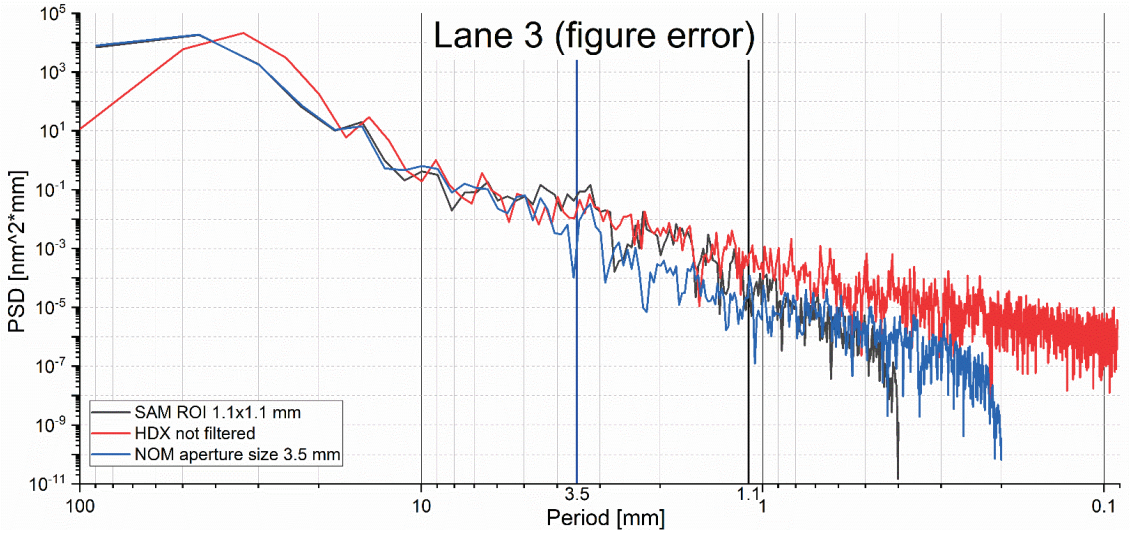

Figure 62: PSD using SAM , HDX and NOM

It is important to notice that to perform a fair comparison between different metrology instruments, they should also provide the same measurements in the same spatial frequency domain. This can be achieved by filtering all the data from all the instruments to provide a common, achievable to all, spatial resolution.

For this purpose, a method to compare all three instruments using the same spatial resolution was developed as follow:

1. Apply the same low pass filter to all instruments measurements to have comparable PSD between different instruments.
2. Define the digital low pass filter parameters.
3. Define the interpolation step size for all the instruments, which should not be smaller than the instrument with lower spatial resolution.

For the current experiments and unless specified otherwise in this report, the low pass filter specification used is defined in Table 27. The spatial resolution was determined by the step size used to translate the SAM scan head across the SUT, set to 0.2mm for this experiment.

Table 27: Low pass filter parameters applied to all instruments figure error data

LOW PASS FILTER PARAMETERS		Notes
Filter design	Butterworth	
Filter type	Low pass filter	
Cut off frequency	1/1.8	1.8 is the period of the filter in mm
Order of the filter	2	Second order

4.4.1.1. Characterisation using Comparable Spatial Resolution

The SAM configuration used is expressed in Table 28.

Table 28: ZEISS mirror characterisation experiment hardware and software parameters

HARDWARE	
Detector Used [Brand / Model]	XIMEA MU9PC-MH
Detector pixel size [µm]	2.2
Detector size [y*x] [px]	1944*2592
Speckle creation method	Double side tape on glass window
LASER used [Brand / Model]	THORLABS CPS532
LASER wavelength [nm]	532
LASER type [collimated or divergent]	Collimated
SOFTWARE	
Active mirror range [mm]	-50 to 50
Interpolation step used [mm] (instrument)	0.2mm (SAM)
ASF [µrad/px] (fixed or adapted)	1.811 (Fixed)
SAM cross-correlations mode [1 or 2]	1
CESF	1.00230284

Fine tuning to align SAM slope error to NOM and HDX	-0.3mm
ROI used [y*x] [px]	1400*1400
ROI used y [px]	272 - 1672
ROI used x [px]	596 - 1996
DIC Edge y top/bottom [px]	50
DIC Edge x left/right [px]	300
Gaussian filter sigma [Standard deviation for Gaussian kernel]	10

Lane one was scanned a total of 6 times and the resultant averaged tangential slope profile is shown in Figure 63.

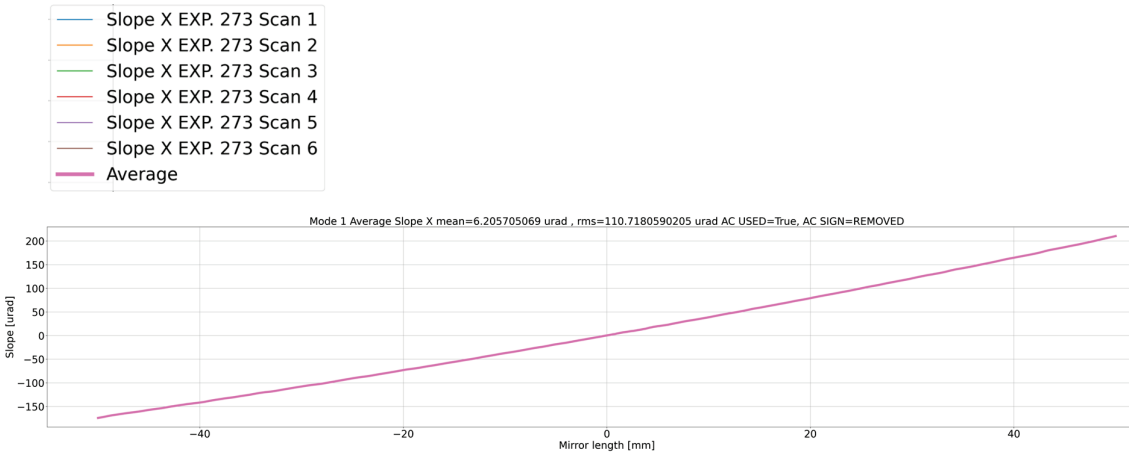

Figure 63: Six scans of the ZEISS ellipse lane slope profile, using the SAM, and their average

Once the nominal ellipse slope was removed from the slope calculated using SAM and the CESF was applied, the slope error results, obtained with NOM, SAM and HDX instruments, are presented in Figure 64 and their relative differences are listed in Table 29.

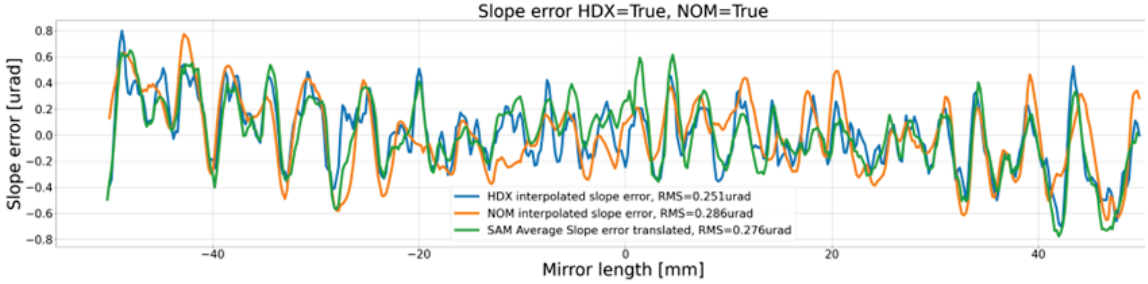

Figure 64: ZEISS ellipse lane slope error (not filtered) resulting from the subtraction of the ideal ellipse form the various measurements performed with the SAM, the HDX and the NOM.

Table 29: Differences between ZEISS ellipse lane slope errors (not filtered) calculated by different instruments.

Instrument	Slope error RMS [µrad]	% Difference (SAM as reference)	% Difference (NOM as reference)	% Difference (HDX as reference)
SAM	0.276	Reference = 0%	-3.49%	+9.9%
NOM	0.286	+3.6%	Reference = 0%	+13.8%
HDX	0.251	-9.05%	-12.83%	Reference = 0%

The three instruments work on three separate spatial resolutions, as shown in the PSD of Figure 65.

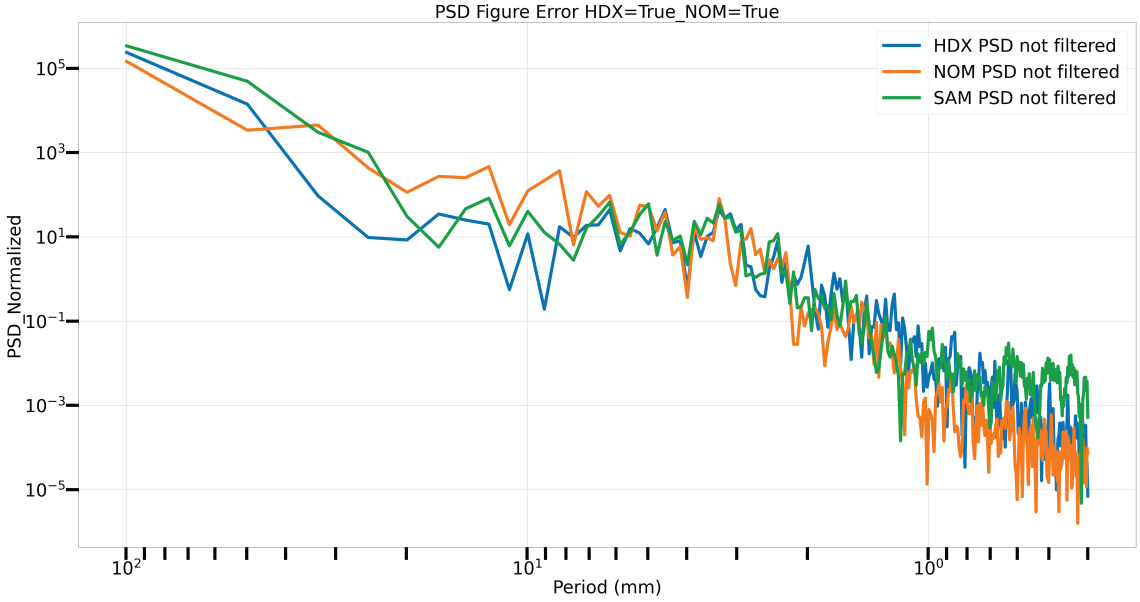

Figure 65: PSD (not filtered) of all metrology instruments (interpolated at SAMs spatial resolution)

For this reason, the filter introduced in Table 26 was used, and all the following results are presented after the filter is applied to all instruments measurements. The results are presented in Figure 66 and Table 30, while Figure 67 shows the relative PSD.

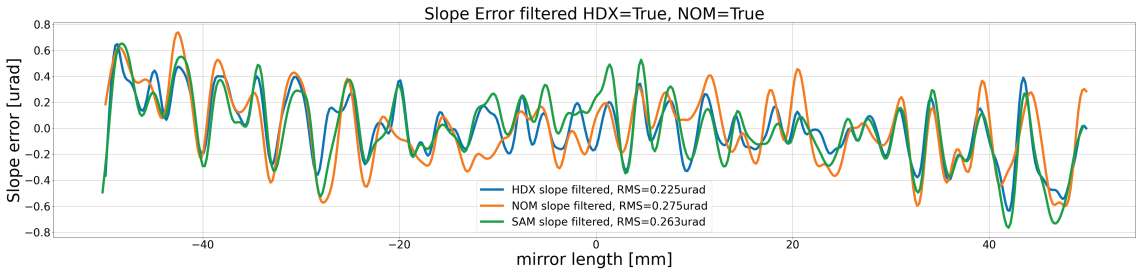

Figure 66: ZEISS ellipse lane slope error filtered with parameters of Table 27

Table 30: Differences between ZEISS ellipse lane slope errors filtered with parameters of Table 27.

Instrument	Slope error RMS [µrad]	% Difference (SAM as reference)	% Difference (NOM as reference)	% Difference (HDX as reference)
SAM	0.263	Reference = 0%	-4.36%	+16.37%
NOM	0.275	+4.56%	Reference = 0%	+21.68%
HDX	0.226	-14.06%	-17.81%	Reference = 0%

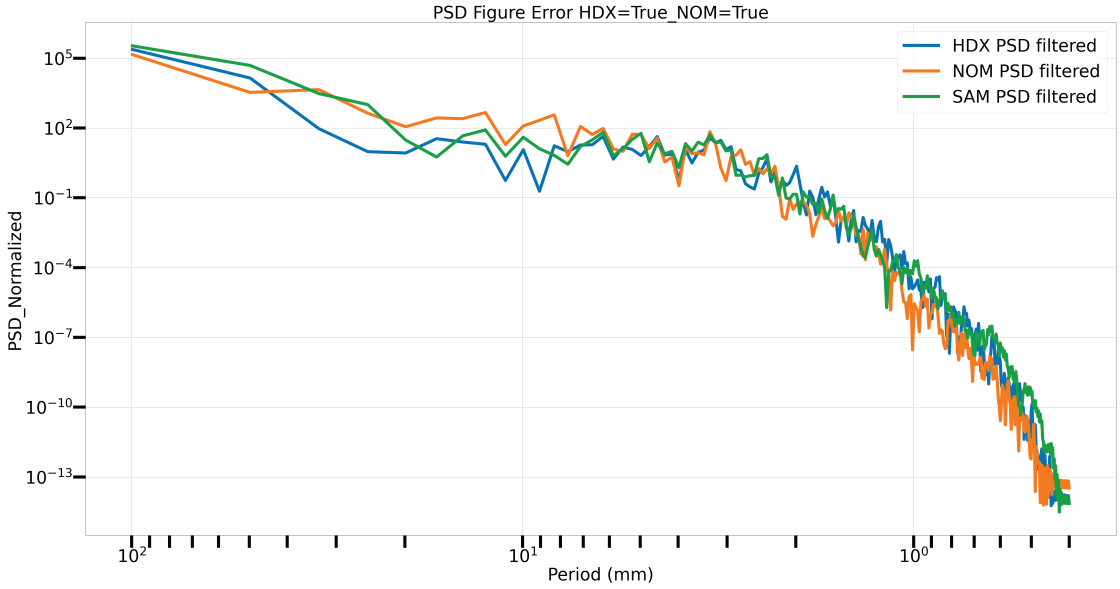

Figure 67: ZEISS ellipse lane figure error PSD filtered with parameters of Table 27

For each experiment, data from the Elcomat 3000, once calibrated along the experiment global axes shown in Figure 14, have been collected at each SAM scan position, resulting in a 1D profile of both y and z axes contributions that can be either subtracted or added to the calculated SAM slope measurements, as explained in section 3.4. Each Elcomat 3000 slope value was obtained collecting a single sample rate measurements (25 values) and performing the average of this values. Once all scans were completed, the average of all scans was performed to minimise the influence of the random errors. Thus, for each scan position an average of 150 Elcomat 3000 measurement values were used, as shown in Figure 68.

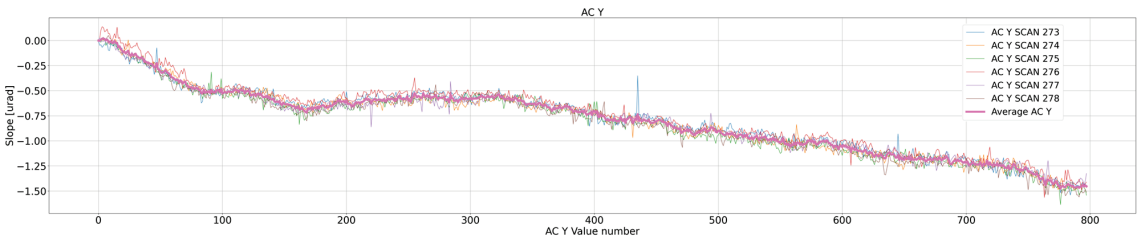

Figure 68 AC y-axis slope change contribution along the mirror length

Data from the autocollimator was added to the SAM measured slope to correct parasitic angle changes. The results on the figure error, as integration of the slope error, is shown in Figure 69.

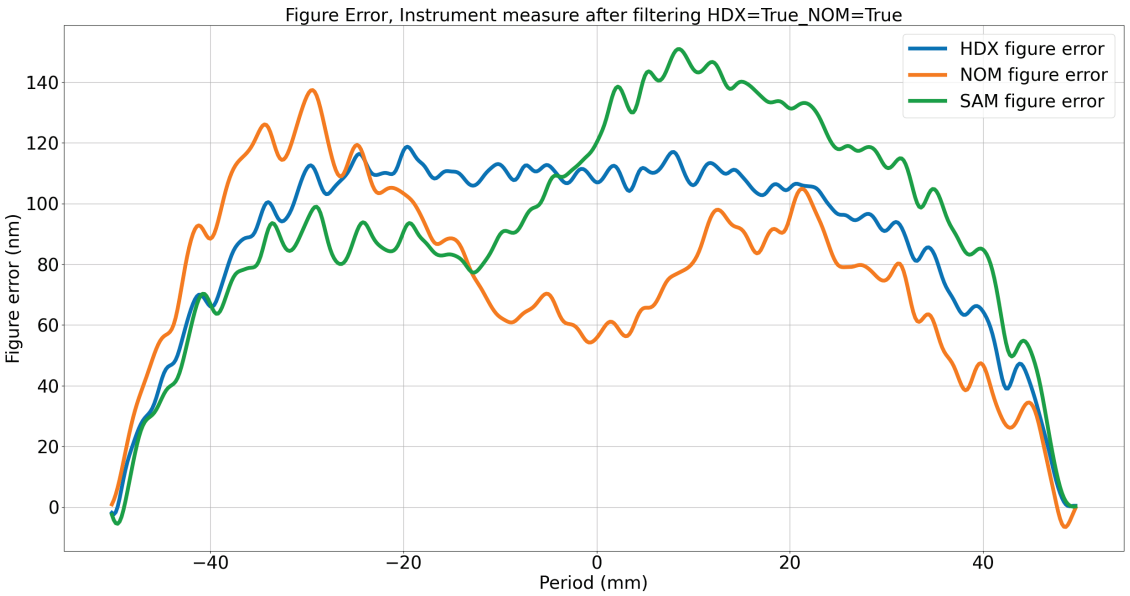

Figure 69: Effect on the slope error when adding the AC y slope contribution to SAM slope measurements

Lane two slope error results are shown in Figure 70 and Table 31.

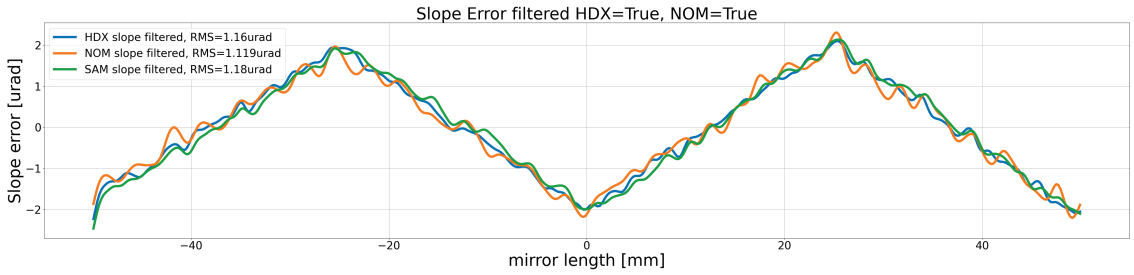

Figure 70: ZEISS lane 2 slope error (filtered) using filter parameters of Table 27

Table 31: Differences between ZEISS lane 2 slope errors (filtered) using filter parameters of Table 6.

Instrument	**Slope error RMS [µrad]**	**% Difference (SAM as reference)**	**% Difference (NOM as reference)**	**% Difference (HDX as reference)**
SAM	1.18	Reference = 0%	+5.45%	+1.72%
NOM	1.119	-5.16%	Reference = 0%	-3.53%
HDX	1.16	-1.69%	+3.66%	Reference = 0%

A sample of a 2D map of the lane 2 of the ZEISS multilane elliptical mirror has been generated to test SAM capabilities.

A ROI of 500 px across the height of the detector and 800 px across the width of the detector was chosen. The ROI was translated across the height of the detector, shifted by 10 px each time. Because each px is 2.2 µm wide, each shift corresponded to a displacement of 22 µm. 83 scans were performed, which is equivalent of taking 1.826 mm of the detector height. The results are shown below. What has not been considered in this example is the spatial scaling f[illegible]lent on how much a displacement on the detector correspond [illegible] the sample under test.

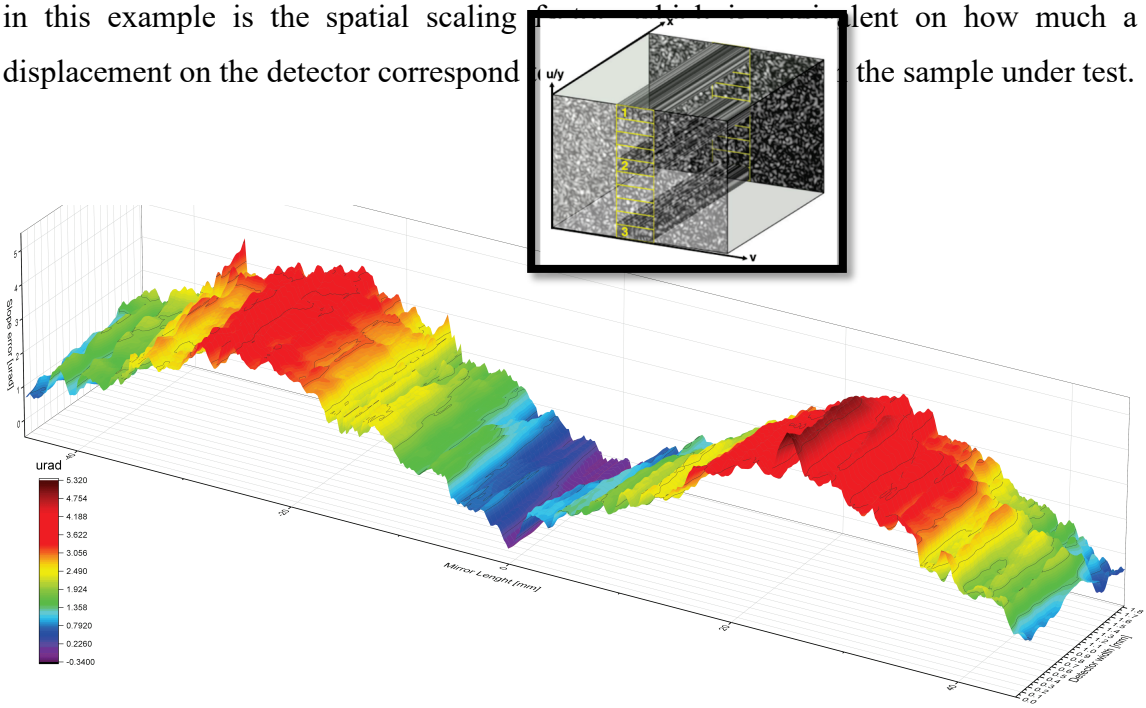

Figure 71: Example of a 2D map made using SAM instrument, relative ZEISS multilane mirror lane 2 slope error

Lane three results are shown in Figure 72 and Table 32. The agreement between all the metrology instruments should be noted. The relative difference is less than 0.3% RMS.

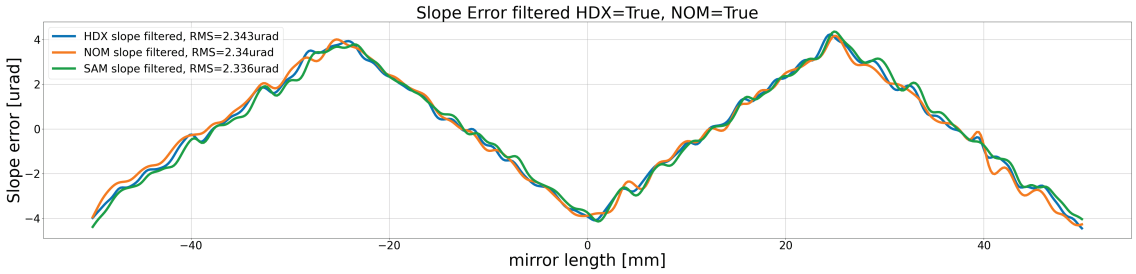

Figure 72: ZEISS lane 3 slope error (filtered) using filter parameters of Table 6

Table 32: Differences between ZEISS lane 3 slope errors (filtered) using filter parameters of Table 6.

Instrument	**Slope error RMS [µrad]**	**% Difference (SAM as reference)**	**% Difference (NOM as reference)**	**% Difference (HDX as reference)**
SAM	2.336	Reference = 0%	-0.17%	-0.29%
NOM	2.34	+0.17%	Reference = 0%	-0.12%
HDX	2.343	+0.29%	+0.12%	Reference = 0%

4.4.2. Systematic Error Correction

In instances where the SAM detector plane and the surface of the SUT exhibit non-parallel alignment, resulting from an imperfect perpendicular configuration between the SAM laser and the surface on which the SUT is placed, a systematic error arises leading to an artificial alteration of the retrieved SUT radius of curvature when the tilted SUT surface profile is characterised using the SAM. This effect varies depending on the magnitude of not parallelism and on the specific location within the SAM detector images where Digital Image Cross-Correlation (DIC) is performed.

To validate this hypothesis, a flat grating shown in Figure 78, was used. The SUT was placed on an electromechanical tilting stage, which was meticulously regulated using the EPICS and a dedicated python script. This setup allowed for precise adjustments with increments as small as 100 µrad, ensuring accuracy and repeatability. To counteract the adverse and non-linear effects, such as backlash, that might undermine the precision of the tilting stage, a precautionary protocol was implemented whenever the SUT underwent tilting, as illustrated in Figure 73.



Figure 73: Logic used to drive tilting stage motor and reduce its non-linearities

The experimental setup, shown in Figure 74, displays the possible tilting range.

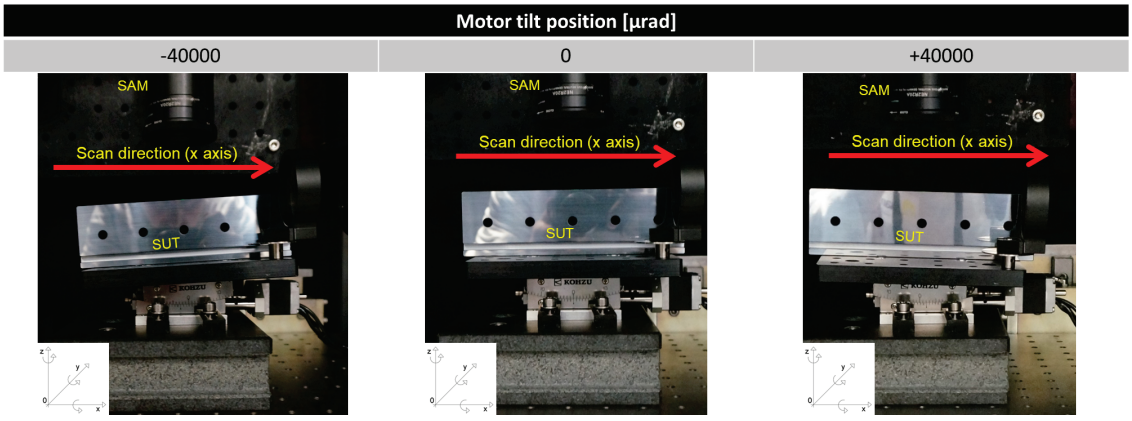

Figure 74: Tilting stage range

Several scans were performed, setting the tilting stage at various angles. To assess the systematic error associated with each tilting angle, the images obtained from each scan were subjected to digital analysis using five distinct regions of interest (ROI), while using SAM $DIC_{(x,y)}$ in mode 1. This procedure generated one-dimensional DIC profiles for each scan. The parameters used to perform data analysis are shown in Table 33.

Table 33: ZEISS flat grating characterisation experiment hardware and software parameters

HARDWARE				
Detector Used [Brand / Model]	XIMEA MU9PC-MH			
Detector pixel size [µm]	2.2			
Detector size (y*x) [px]	1944*2592			
Speckle creation method	Glass diffuser			
LASER used [Brand / Model]	THORLABS CPS532			
LASER wavelength [nm]	532			
LASER type [collimated or divergent]	Collimated			
SOFTWARE				
Active mirror range [mm]	-50 to 50			
SAM scan step used [mm]	0.2			
Calibrated ASF (Fixed or HSASF) [µrad/px]	(Fixed) 3.9125			
SAM cross-correlations mode [1 or 2]	1			
CESF	1			
Tilting stage angles used [µrad]	-8000, -4000, 0, +4000, +5813, +6500, +6750, +7000, +8000, +12000			
ROI 1	**ROI 2**	**ROI 3**	**ROI 4**	**ROI 5**
Size (y*x) [px * px] 1400 * 1400	**Size (y*x) [px * px]** 1400 * 1400	**Size (y*x) [px * px]** 1400 * 1400	**Size (y*x) [px * px]** 1400 * 1400	**Size (y*x) [px * px]** 1400 * 1400
y start [px] 272	**y start [px]** 272	**y start [px]** 272	**y start [px]** 272	**y start [px]** 272
y finish [px] 1672	**y finish [px]** 1672	**y finish [px]** 1672	**y finish [px]** 1672	**y finish [px]** 1672
x start [px] 0	**x start [px]** 298	**x start [px]** 596	**x start [px]** 894	**x start [px]** 1192
x finish [px] 1400	**x finish [px]** 1698	**x finish [px]** 1996	**x finish [px]** 2294	**x finish [px]** 2592
DIC Edge x [px] 50	**DIC Edge x [px]** 50	**DIC Edge x [px]** 50	**DIC Edge x [px]** 50	**DIC Edge x [px]** 50
DIC Edge y [px] 50	**DIC Edge y [px]** 50	**DIC Edge y [px]** 50	**DIC Edge y [px]** 50	**DIC Edge y [px]** 50
Low pass filter [σ] 10	**Low pass filter [σ]** 10	**Low pass filter [σ]** 10	**Low pass filter [σ]** 10	**Low pass filter [σ]** 10

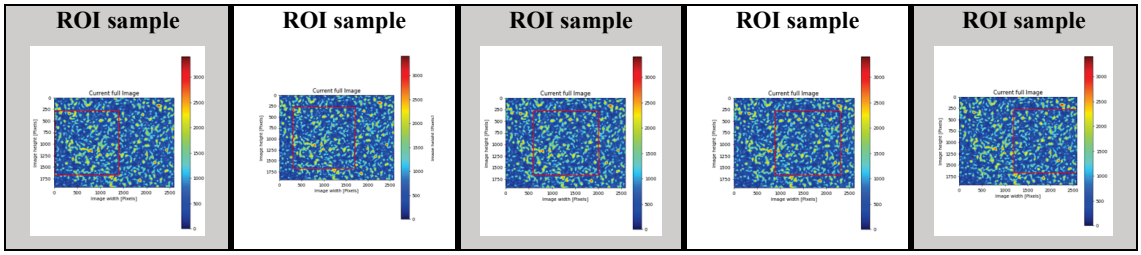

Once all the $DIC_{(x,y)}$ were calculated, the associated slope profiles were calculated by multiplying the one-dimensional $DIC_{(x)}$ by the calibrated ASF. The results are shown in Figure 75.

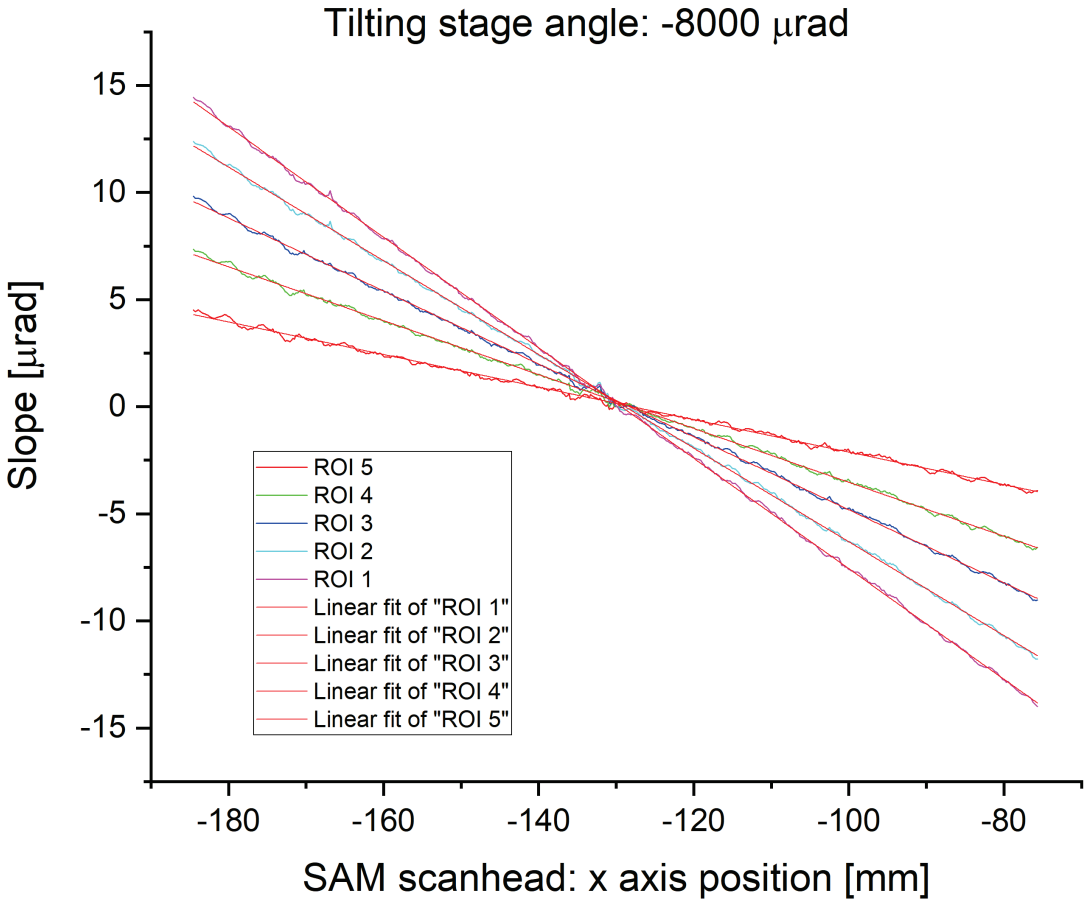

Figure 75: Slope estimation using different ROI within SAM acquired images, with tilting stage set to -8000 µrad

For each tilting stage angle selected, and for all the slopes measured using the aforementioned ROIs, a line of best fit using linear regression was applied. The resulting gradient for each measured slope of Figure 75 (for a tilting angle equal to -8000 µrad), and subsequent tilt angles are reported in Table 34, column m_1.

Table 34: Line of best fit regressions: results at all tilting angles

		Average gradient of slopes	Line of best fit using linear regression of each reconstructed slope with different ROI.		Gradient of line of best fit using linear regression of all m_1 values
ROI number	**Tilting stage angle [µrad]**	$\overline{m_1}$	m_1	c_1	m_2
1	-8000	-0.16977	-0.25798	-33.36	0.0457
2			0.21877	-28.19	
3			-0.17034	-21.85	
4			-0.12580	-16.11	
5			-0.07597	-9.72	
1	-4000	-0.09105	-0.16486	-21.45	0.03541
2			-0.12752	-16.56	
3			-0.08476	-10.83	
4			-0.05308	-6.63	
5			-0.02504	-2.97	
1	0	-0.04662	-0.09069	-11.86	0.02294
2			-0.0697	-9.14	
3			-0.04977	-6.46	
4			-0.02421	-3.04	
5			0.00127	+0.30	
1	+4000	-0.02106	-0.03907	-5.07	0.00907
2			-0.03013	-3.94	
3			-0.02121	-2.87	
4			-0.0121	-1.76	
5			-0.00273	-0.51	
1	+5813	-0.01811	-0.02454	-3.01	0.00315
2			-0.02128	-2.66	
3			-0.0179	-2.33	
4			-0.0148	-2.01	
5			-0.01205	-1.72	
1	+6500	-0.0206	-0.0224	-2.99	0.000960216
2			-0.02173	-2.97	
3			-0.02066	-2.84	
4			-0.0195	-2.62	
5			-0.01871	-2.34	
1	+6750	-0.02073	-0.02047	-2.76	-0.0000962973
2			-0.0207	-2.84	
3			-0.02079	-2.85	
4			-0.02075	-2.79	
5			-0.02092	-2.69	

1	+7000	-0.0206	-0.0187	-2.45	-0.00093764
2			-0.01965	-2.58	
3			-0.02066	-2.70	
4			-0.02156	-2.82	
5			-0.02244	-2.91	
1	+8000	-0.0214	-0.01287	-1.42	-0.00436
2			-0.01699	-1.94	
3			-0.02111	-2.57	
4			-0.02573	-3.25	
5			-0.03032	-3.94	
1	+12000	-0.04638	-0.01343	-1.84	-0.0166
2			-0.02887	-3.81	
3			-0.04744	-6.12	
4			-0.06259	-7.99	
5			-0.07956	-10.16	

The change in Table 34, column m_1 values, for each tilt angle, is also linear, as shown in Figure 76.

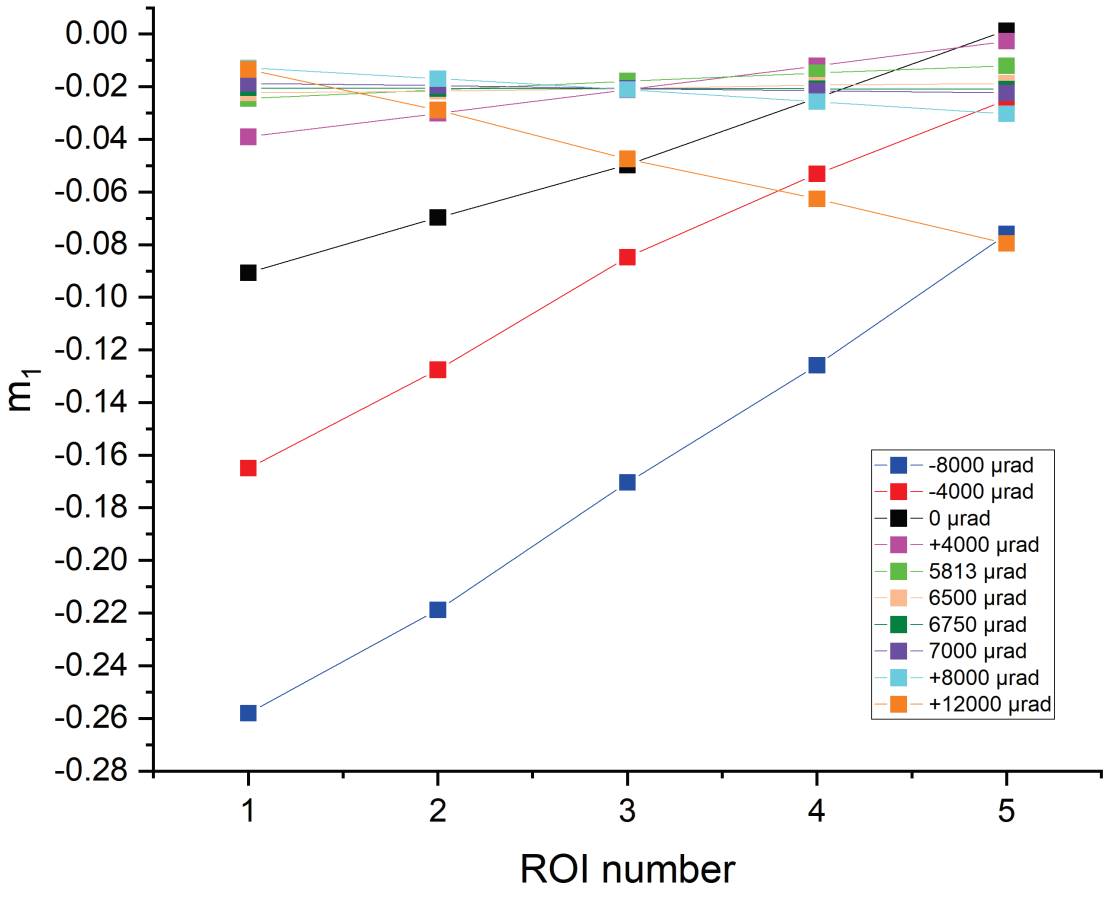

Figure 76: Line of best fit using linear regression of each reconstructed slope with different ROI

For each tilting angle, if a line of best fit using a linear regression on m_1 values is applied, its gradient, called m_2, is presented in Table 34.

The results are shown in Figure 77, where both m_1 and m_2 values are represented. By running a line of best fit linear regression of Table 34, column m_2 values, m_2 at any tilting stage angle can be retrieved, as shown in equation (49).

$$m_2 = -3.18509 * 10^{-6} * T_a + 0.02165 \quad (49)$$

Where:

- m_2 is the gradient of line of best fit using linear regression of all $\overline{m_1}$ values.
- T_a is the tilting stage angle, expressed in µrad.

By solving equation (49) for m_2 equal to zero, it is possible to estimate that the optimal tilting stage angle is 6,797.3 µrad, as shown in equation (50).

$$T_a = \frac{-m_2 + 0.02165}{3.18509 * 10^{-6}} = \frac{0 + 0.02165}{3.18509 * 10^{-6}} = 6{,}797.3\ \mu rad \quad (50)$$

If on the same graph is plotted the average of m_1 values at each tilting angle (Table 34, column $\overline{m_1}$ values) it is possible, by solving its line of best fit (second order polynomial) to estimate the most accurate slope gradient to be used, while characterising the SUT surface profile using the SAM.

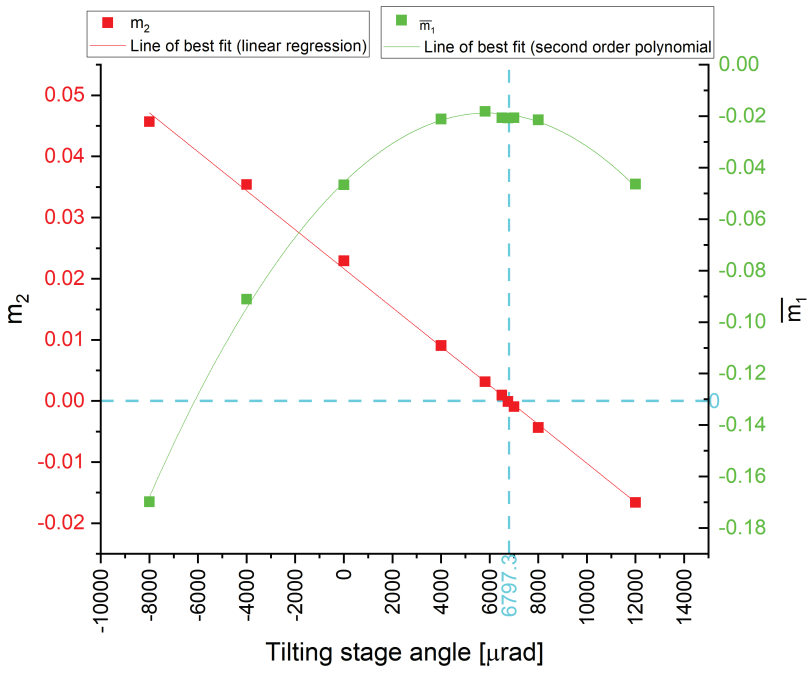

Figure 77: Flat grating SUT tilt systematic error characterisation

4.4.3. Flat Grating Substrate

The following experiment aimed to test the limits of the SAM capabilities, when characterising a flat optics, as described in previous chapters. The Experimental setup and the SUT characteristics for this optic are shown in Figure 78, Table 35 and Table 33.

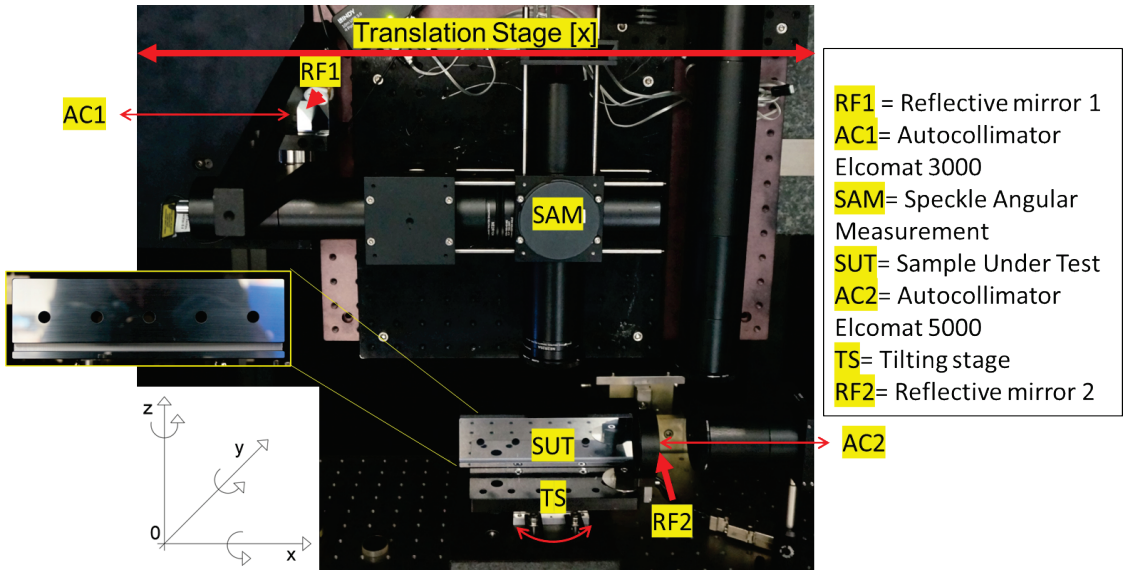

Figure 78: I21PG6 physical side view and experimental setup

Table 35: Technical details of the ZEISS flat grating

Supplier	Zeiss (Germany)
Dimensions	170 (L) x 40 (W)
Analysis length	clear aperture = 100 mm (centred on mirror length)
Shape	Flat
Tangential radius of curvature	> 30km
Tangential slope error	< 0.1 µrad rms

When performing measurements using the SAM, understanding the difference in slope measurements when performing multiple DICs, using mode 1, and different ROIs, as explained in chapter 4.4.2, lead to a correct procedure to use to counteract the systematic error introduced while scanning a SUT placed at an incorrect tilting position.

In this experiment, first, an average of 9 scans using the SAM was obtained. To do so, the SAM captured speckle images every 0.2 mm, while translating along the tangential axis of the SUT profile (x-axis of the translation stage), having the tilt stage angle fixed at 5813.0 µrad. During the scan, the rotation of the SAM scanning head, across the y-

axis, was monitored using the autocollimator "AC1", represented in Figure 78. After, the SAM mode 1 DIC was performed on the set of images acquired in each scan. The technical specifications are shown in Table 36.

Table 36: Technical specifications of the flat grating SAM scans

HARDWARE	
Detector Used [Brand / Model]	XIMEA MU9PC-MH
Detector pixel size [µm]	2.2
Detector size (y*x) [px]	1944*2592
Speckle creation method	Glass diffuser
LASER used [Brand / Model]	THORLABS CPS532
LASER wavelength [nm]	532
LASER type [collimated or divergent]	Collimated
SOFTWARE	
Active mirror range [mm]	-50 to 50
SAM scan step used [mm]	0.2
Calibrated ASF (Fixed or HSASF) [µrad/px]	(Fixed) 3.9125
SAM cross-correlations mode [1 or 2]	1
CESF	1
Tilting stage angles used [µrad]	+5813

ROI 1	
Size (y*x) [px * px]	1400 * 1400
y start [px]	0
y finish [px]	1944
x start [px]	0
x finish [px]	2592
DIC Edge x [px]	800
DIC Edge y [px]	400
Low pass filter [σ]	10

ROI sample **DIC Sample**

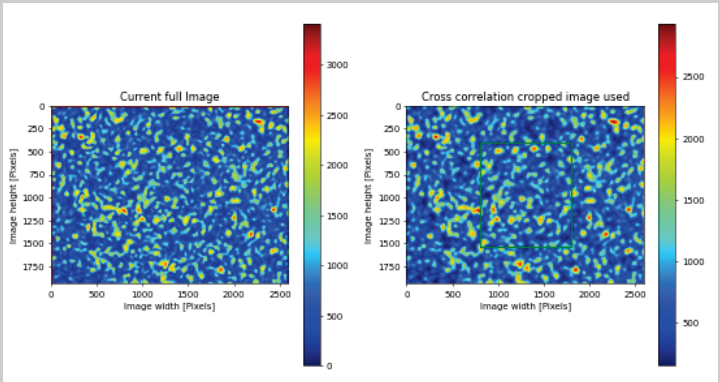

The results of the SAM DIC were then multiplied by the ASF. This converted the DIC_x into slope profiles. These results, together with the monitored SAM scanning head angle changes during single scans, are represented in Figure 79.

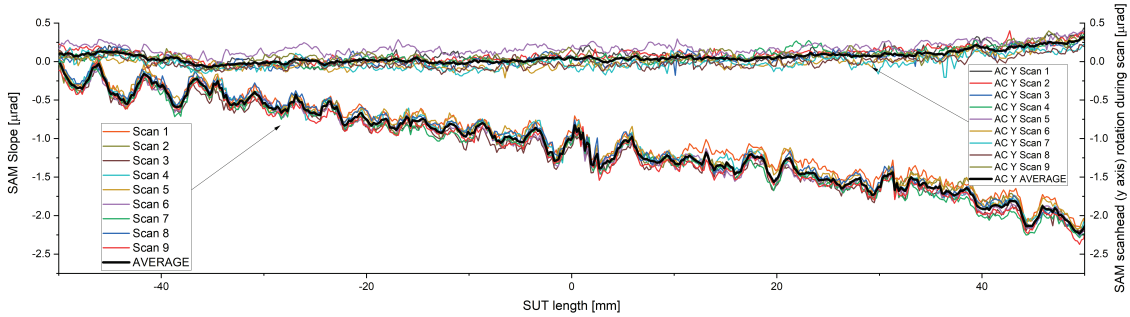

Figure 79: Super flat grating slope profiles measured with SAM and SAM scanning head (y-axis) rotation over nine scans

From Figure 77, by solving the line of best fit of m_2 values, for $m_2 = 0$, it is possible to detect at which tilting angle the SUT is most parallel with SAM detector plane during a measurement scan, which is equal to 6,797.3 µrad. From the same figure, taking in consideration the line of best fit of the second order polynomial of $\bar{m}_1$ values, the most accurate slope gradient to be applied to SAM measurements, for a tilting angle of 6797.3 µrad, can also be retrieved, using equation (51).

$$\begin{aligned} \bar{m}_1 &= (9.11224 * 10^{-6} * T_a) - \left(7.71162 * 10^{-10} * {T_a}^2\right) - 0.04572 \\ &= (9.11224 * 10^{-6} * 6{,}797.3) \\ &- (7.71162 * 10^{-10} * 6{,}797.3^2) - 0.04572 \\ &= 0.06194 - 0.03563 - 0.04572 = -0.01941 \ \mu rad/mm \end{aligned} \tag{51}$$

The slope gradient coefficient from equation (51) can now be used to correct the measured slope from SAM. First the linear best fit line was removed from the average of the SAM slopes, resulting in a residual profile, shown in Figure 80.

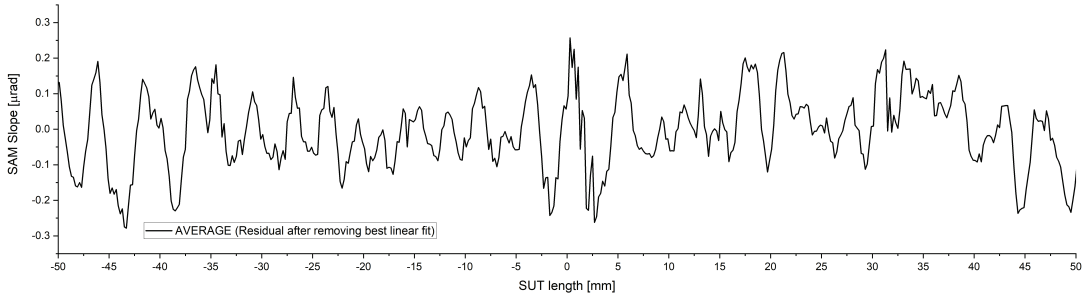

Figure 80: SUT average slope after removing best linear fit

Second, the slope coefficient from equation (51) was added to the residual slope of Figure 80, using the formula in equation (52).

$$y = -0.01941 * x + c \tag{52}$$

Where:

- "y" is the SAM slope, including the most accurate slope gradient, expressed in µrad.
- "x" is the mirror length, expressed in mm.
- "c" is the slope residual profile, shown in Figure 80.

The results, shown in Figure 81, highlight the average slope retrieved using the SAM instrument, both with and without the slope gradient correction.

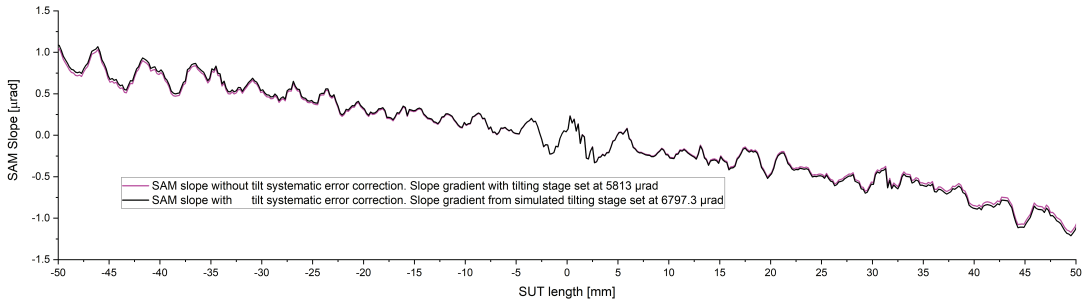

Figure 81: Comparison of SUT slope calculated using SAM, with and without tilt systematic error correction

Next was to correct the effect of the SAM scanning head rotation around the y-axis on the optimal, averaged slope from SAM, corrected using the accurate slope gradient, shown in Figure 81, using the average measurements form the autocollimator, shown in Figure 79, as shown in equation (53).

$$S(x) = SAM\ S(x) + AC1(y) \tag{53}$$

Where:

- "S(x)" is the slope along the tangential axis of the SUT.
- "SAM S(x)" is the optimal slope from SAM, with tilt correction.
- "AC1(y)" is the averaged, y output measurement, of the Elcomat 3000, as shown in Figure 79.

A comparison between the slope with and without the scanning head rotation correction is shown in Figure 82. The most accurate slope profile (black) is then compared with the slope profiles obtained using other metrology instruments.

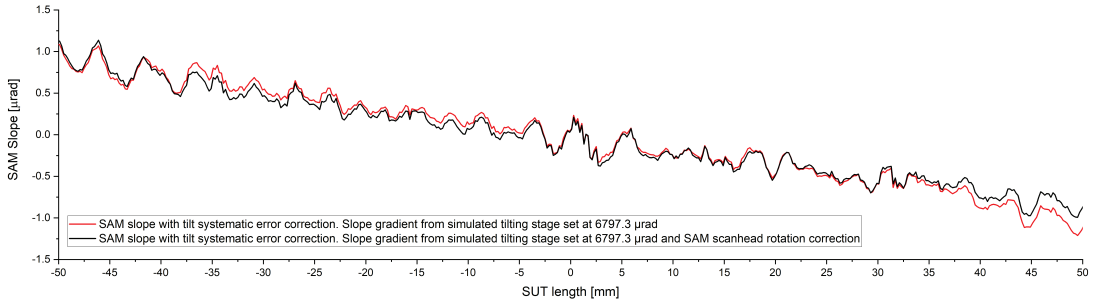

Figure 82: Comparison between SAM slope without the scanning head rotation correction (red) and with scanning head rotation correction (black)

By performing the derivative of the slope in Figure 82, it is possible to retrieve the inverse of the local radius of curvature profile along the length of the SUT.

From that, the average radius of curvature can be retrieved, as shown in equation (54).

$$\overline{RoC} = \frac{\sum \frac{1}{RoC}}{n} \tag{54}$$

Where:

- $\overline{RoC}$ is the average radius of curvature, expressed in m. The RoC is positive or negative if the SUT surface profile is concave or convex, respectively.
- $\sum \frac{1}{RoC}$ is the cumulative sum of the derivative of the slope values, expressed in 1/m.
- n is the total number of inverse local radius of curvature values used.

The Inverse local of curvature profile is shown in Figure 83.

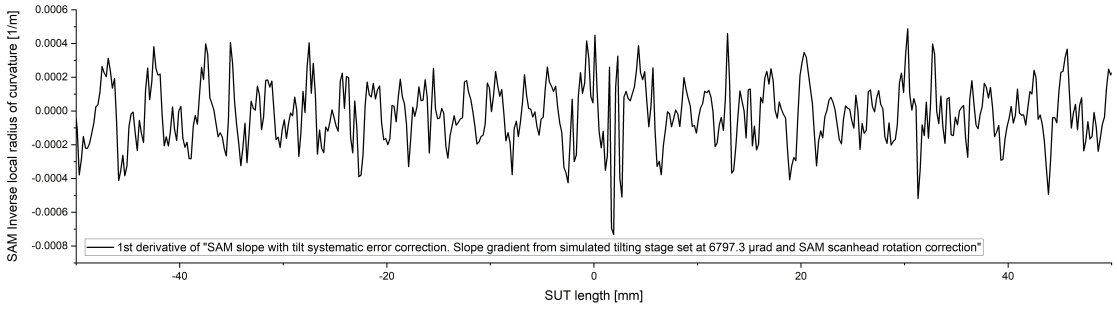

Figure 83: Derivative of the slope. Inverse local radius of curvature of the flat grating

Importing equation (54) into equation (55), The mean radius of curvature of this SUT is equal to -55,823.005 m.

$$\overline{ROC} = \frac{\sum \frac{1}{RoC}}{n} = \frac{545}{-0.009763} = -55{,}823.005\ m \tag{55}$$

A comparison between the SUT slope profiles, measured by SAM, HDX and NOM, is shown in Figure 84, while the Figure profiles is shown in Figure 85.

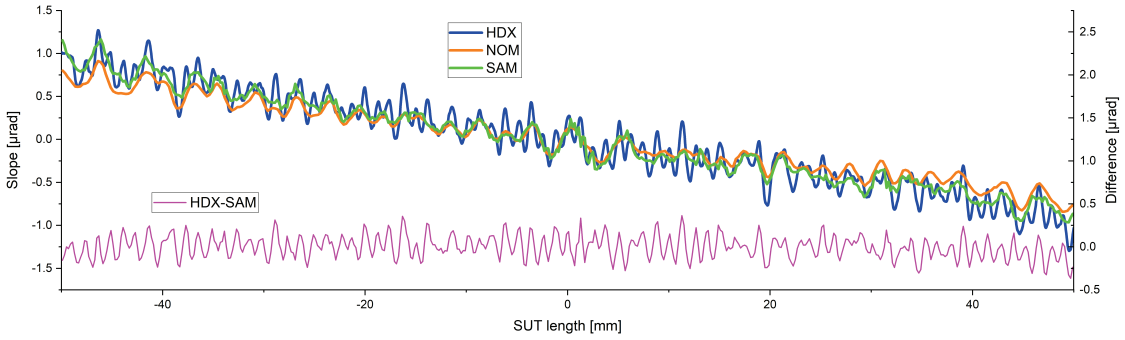

Figure 84: Slope characterisation of the flat grating, using the HDX, NOM, and SAM

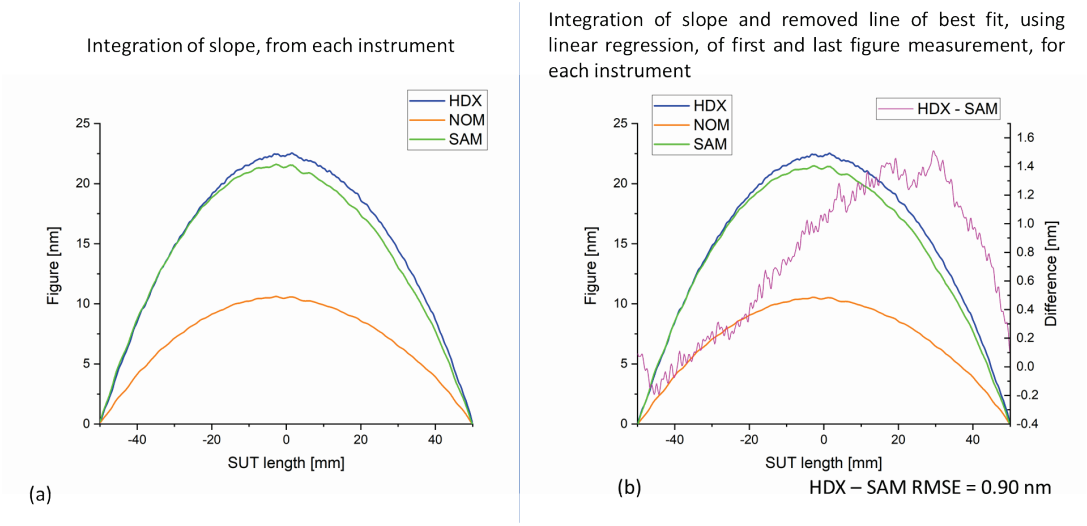

Figure 85: Figure characterisation of the flat grating, using the HDX, NOM and SAM

The root mean square error between the Fizeau Interferometer (HDX) and SAM figure profile, as integration of the respective slope measurements, is 0.9 nm.

Therefore, it is possible to conclude that the difference on slopes in the low spatial frequency domain are strictly related to the degree of not parallelism between the SUT's base surface and SAM detector plane, during scan measurements.

4.4.4. Cylindrical, Low Reflectivity Grating Substrate

In this section the characterisation of a low reflectivity (below 4%) optics, having a cylindrical profile on the tangential axis (x-axis), and nominal RoC of 116m will be discussed. The experimental setup and the SUT characteristics are shown in Figure 86 and Table 37.

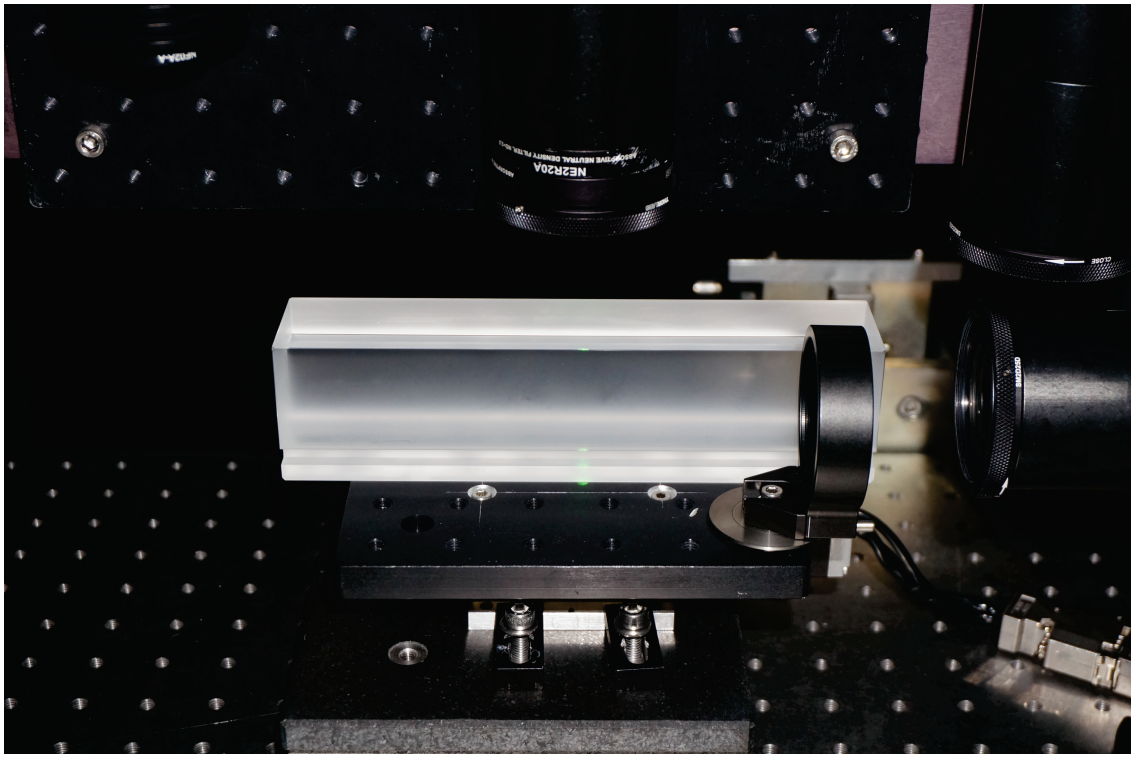

Figure 86: JTEC cylindrical grating experimental setup

Table 37: Technical details of the JTEC cylindrical grating

Supplier	JTEC (Japan)
Substrate	Silica (uncoated)
Dimensions	200(L) x 40 (W) x 50 (H) mm^3
Analysis length	clear aperture = >190 mm (centred on mirror length)
Shape	Cylindrical
Tangential Cylinder	RoC = 115.729 m (nominal). Slope error < 0.05 µrad RMS
Mid-spatial frequency errors	< 1.0 nm PV

To characterise this optic, a similar approach as of Chapter 4.4.2 was applied. Multiple scans were conducted at different tilting stage angles. For each scan, SAM DIC was performed, using mode 1, at different positions along the width of the detector's image, as shown in Table 38.

Table 38: JTEC Cylindrical silica grating characterisation experiment hardware and software parameters.

HARDWARE	
Detector Used [Brand / Model]	XIMEA MU9PC-MH
Detector pixel size [µm]	2.2
Detector size (y*x) [px]	1944*2592
Speckle creation method	Glass diffuser
LASER used [Brand / Model]	THORLABS CPS532
LASER wavelength [nm]	532
LASER type [collimated or divergent]	Collimated
SOFTWARE	
Active mirror range [mm]	-90 to 90
SAM scan step used [mm]	1
Calibrated ASF (Fixed or HSASF) [µrad/px]	(Fixed) 3.915
SAM cross-correlations mode [1 or 2]	1
CESF	1
Tilting stage angles used [µrad]	-10000, -6000, -2000, +2000, +6000, +10000, +14000

ROI 1	**ROI 2**	**ROI 3**	**ROI 4**	**ROI 5**
Size (y*x) [px * px] 1400 * 1400	**Size (y*x) [px * px]** 1400 * 1400	**Size (y*x) [px * px]** 1400 * 1400	**Size (y*x) [px * px]** 1400 * 1400	**Size (y*x) [px * px]** 1400 * 1400
y start [px] 272	**y start [px]** 272	**y start [px]** 272	**y start [px]** 272	**y start [px]** 272
y finish [px] 1672	**y finish [px]** 1672	**y finish [px]** 1672	**y finish [px]** 1672	**y finish [px]** 1672
x start [px] 0	**x start [px]** 298	**x start [px]** 596	**x start [px]** 894	**x start [px]** 1192
x finish [px] 1400	**x finish [px]** 1698	**x finish [px]** 1996	**x finish [px]** 2294	**x finish [px]** 2592
DIC Edge x [px] 600	**DIC Edge x [px]** 600	**DIC Edge x [px]** 600	**DIC Edge x [px]** 600	**DIC Edge x [px]** 600
DIC Edge y [px] 100	**DIC Edge y [px]** 100	**DIC Edge y [px]** 100	**DIC Edge y [px]** 100	**DIC Edge y [px]** 100
Low pass filter [σ] 10	**Low pass filter [σ]** 10	**Low pass filter [σ]** 10	**Low pass filter [σ]** 10	**Low pass filter [σ]** 10
ROI sample 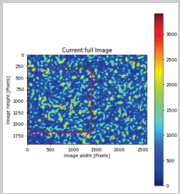	**ROI sample** 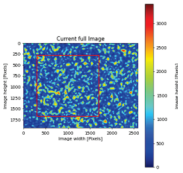	**ROI sample** 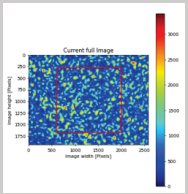	**ROI sample** 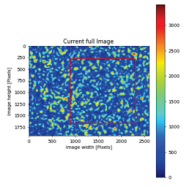	**ROI sample** 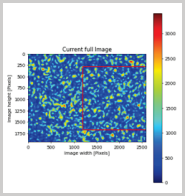

For each tilting stage angle selected, and for all the slopes measured using the aforementioned ROIs, a line of best fit using linear regression was applied, and the gradient of each slope are reported in Table 39, column m_1.

Table 39: JTEC Cylindrical grating. Line of best fit regressions: results at all tilting angles

		Average gradient of slopes	**Line of best fit using linear regression of each reconstructed slope with different ROI.**		**Gradient of line of best fit using linear regression of all m_1 values**
ROI number	**Tilting stage angle [µrad]**	$\overline{m_1}$	m_1	c_1	m_2
1	-10000	8.44974	8.33154	-46.6633	0.06028
2			8.38455	-47.5244	
3			8.45828	-48.2954	
4			8.49821	-47.7678	
5			8.57612	-49.3910	
1	-6000	8.51583	8.42419	-35.0943	0.04202
2			8.48262	-35.3896	
3			8.51799	-34.7790	
4			8.55749	-34.7966	
5			8.59687	-35.5886	
1	-2000	8.57268	8.51092	-35.2028	0.02942
2			8.54568	-35.2025	
3			8.57418	-34.7504	
4			8.60349	-35.4524	
5			8.62913	-35.3250	
1	+2000	8.60275	8.56958	-17.8257	0.01597
2			8.58852	-17.8425	
3			8.60255	-17.7099	
4			8.61882	-17.4219	
5			8.63428	-17.3926	
1	+6000	8.61088	8.60522	-9.2000	0.0031
2			8.60466	-8.6302	
3			8.61088	-9.2034	
4			8.6159	-8.7243	
5			8.61511	-8.1015	
1	+10000	8.60034	8.62089	9.2003	-0.01208
2			8.61428	8.2234	
3			8.60177	10.2670	
4			8.59425	8.4275	
5			8.5705	8.4924	

1	+14000	8.56422	8.62131	8.9945	-0.0265
2			8.58567	8.83046	
3			8.56538	9.16474	
4			8.53418	8.24269	
5			8.51454	9.6031	
1	+18000	8.50119	8.58766	18.37979	-0.04078
2			8.54882	17.92719	
3			8.48161	17.84302	
4			8.4594	17.90196	
5			8.42846	17.53823	

The Results from Table 39 are shown in Figure 87, where it is possible to visually determine the systematic error generated by tilting the SUT. By deriving a linear line of best fit of Table 39, column m_2 values, m_2 at any tilting stage angle can be retrieved, as shown in equation (56).

$$m_2 = -3.53414 * 10^{-6} * T_a + 0.02307 \quad (56)$$

Where:

- m_2 is the gradient of line of best fit using linear regression of all $\overline{m_1}$ values.
- T_a is the tilting stage angle, expressed in µrad.

By solving equation (56) for m_2 equal to zero, it is possible to estimate that the optimal tilting stage angle is 6,527.8 µrad, as shown in equation (57).

$$Ta = \frac{-m_2 + 0.02307}{3.53414 * 10^{-6}} = \frac{0 + 0.02307}{3.53414 * 10^{-6}} = 6527.8\mu rad \quad (57)$$

If on the same graph is plotted the average of m_1 values at each tilting angle (Table 41, column $\overline{m_1}$ values) it is possible, by solving its line of best fit (second order polynomial) to estimate the most accurate slope gradient to be used, while characterising the SUT surface profile using the SAM.

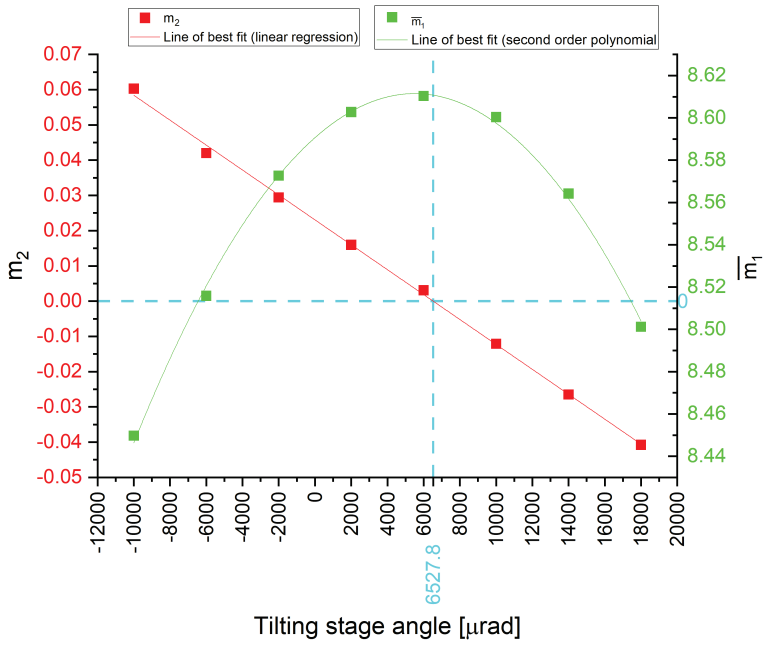

Figure 87: Cylindrical grating SUT tilt systematic error characterisation.

From Figure 87, taking in consideration the line of best fit of the second order polynomial of $\bar{m}_1$ values, the most accurate slope gradient to be applied to SAM measurements, for a tilting angle of 6,527.8 µrad, can also be retrieved using equation (58).

$$\begin{aligned}\bar{m}_1 &= (7.56143 * 10^{-6} * T_a) - \left(6.875 * 10^{-10} * {T_a}^2\right) + 8.59064 \\ &= (9.11224 * 10^{-6} * 6{,}527.8) \\ &\quad - (7.71162 * 10^{-10} * 6{,}527.8^2) + 8.59064 \\ &= 0.05948 - 0.03286 + 8.59064 = \ 8.61726\ \mu rad/mm\end{aligned} \tag{58}$$

After, the support of the SUT was changed, from being placed directly onto the tilting stage, to being placed on top of 3 half spheres, placed at the SUT Bessel's points. This helped to reduce noise and unwanted systematic error caused by the interaction of the SUT profile and the tilting stage sample holder (the top of the tilting stage). This changed SAM ASF, updated in Table 40. The new experimental setup is shown in Figure 88.

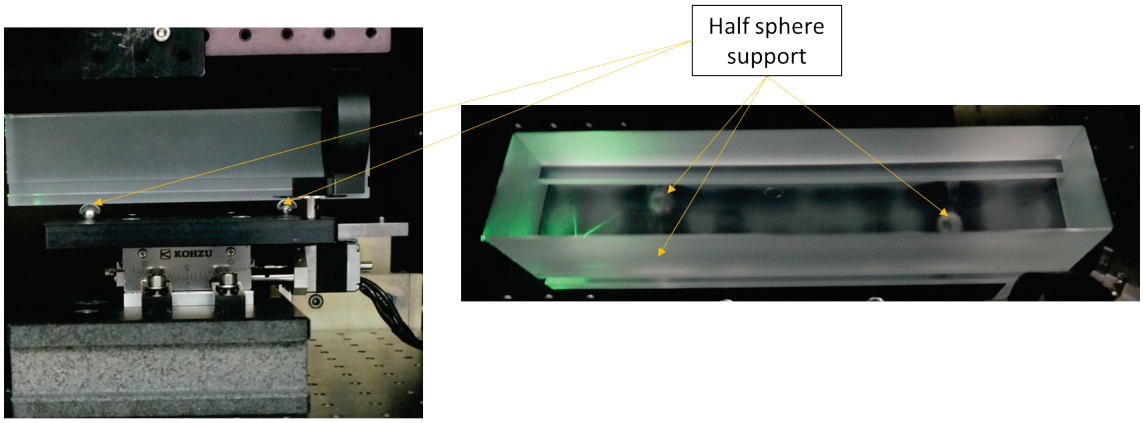

Figure 88: SUT supported by 3 half spheres at Bessel's points

In this experiment, an average of 9 scans using SAM were obtained. To do so, SAM captured speckle images every 1 mm, while translating along the tangential plane of the SUT profile (x-axis of the translation stage). During the scan, the rotation of the SAM scanning head, across the y-axis, was monitored using the autocollimator "AC1", represented in Figure 78. After, SAM mode 1 DIC was performed on the set of images acquired in each scan.

Table 40: Technical specifications of the cylindrical grating SAM scans:

HARDWARE	
Detector Used [Brand / Model]	XIMEA MU9PC-MH
Detector pixel size [µm]	2.2
Detector size (y*x) [px]	1944*2592
Speckle creation method	Glass diffuser
LASER used [Brand / Model]	THORLABS CPS532
LASER wavelength [nm]	532
LASER type [collimated or divergent]	Collimated
SOFTWARE	
Active mirror range [mm]	-90 to 90
SAM scan step used [mm]	1
Calibrated ASF (Fixed or HSASF) [µrad/px]	(Fixed) 4.0359
SAM cross-correlations mode [1 or 2]	1
CESF	1.002354
Tilting stage angles used [µrad]	+5800
ROI 1	
Size (y*x) [px * px]	1400 * 1400

y start [px]	0
y finish [px]	1944
x start [px]	0
x finish [px]	2592
DIC Edge x [px]	800
DIC Edge y [px]	400
Low pass filter [σ]	10

ROI sample **DIC Sample**

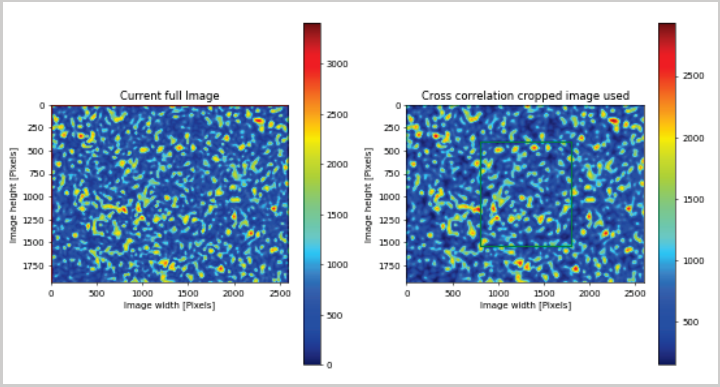

The results of the SAM $DIC_{(x)}$ were then multiplied by the ASF of Table 40. This converted the digital image cross-correlations into slope profiles. These results, together with the monitored SAM scanning head angle changes across single scans, are represented in Figure 89.

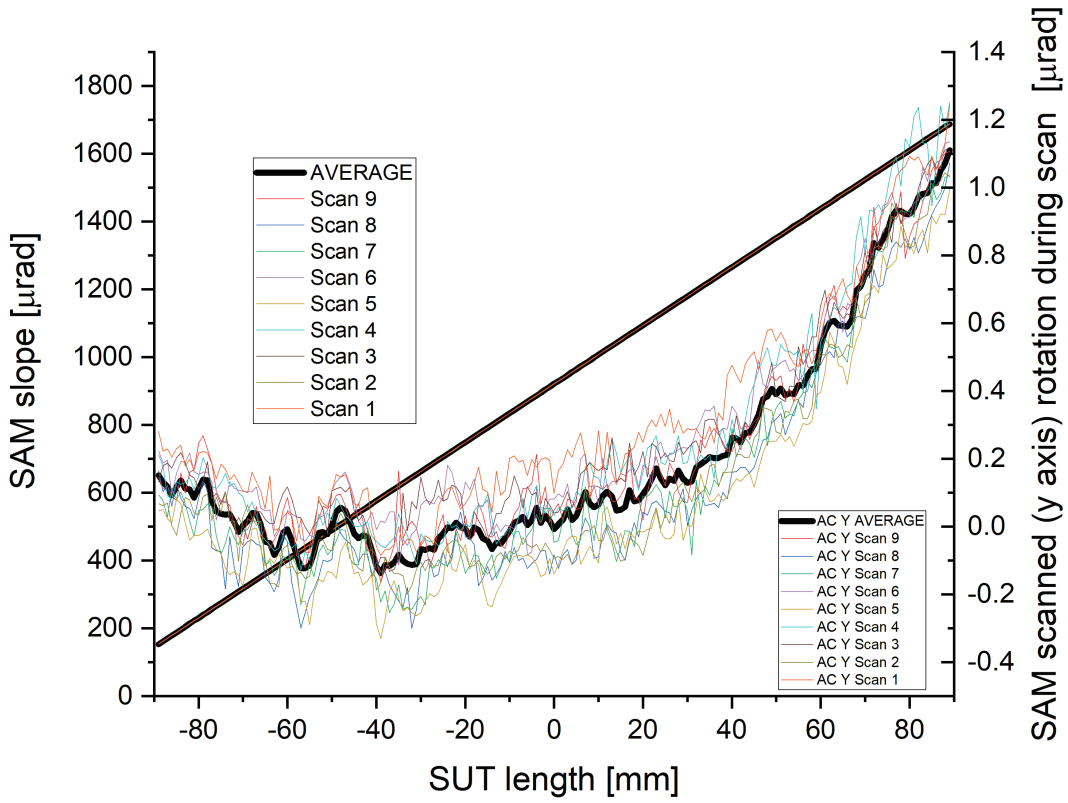

Figure 89: Cylindrical grating slope profiles measured with the SAM and the SAM scanning head (y-axis) rotation, during nine scans

The slope gradient coefficient from equation (58) can now be used to correct the measured slope from SAM, as follow:

First the linear best fit line was removed from the average of SAM slopes, resulting in a residual profile, shown in Figure 90.

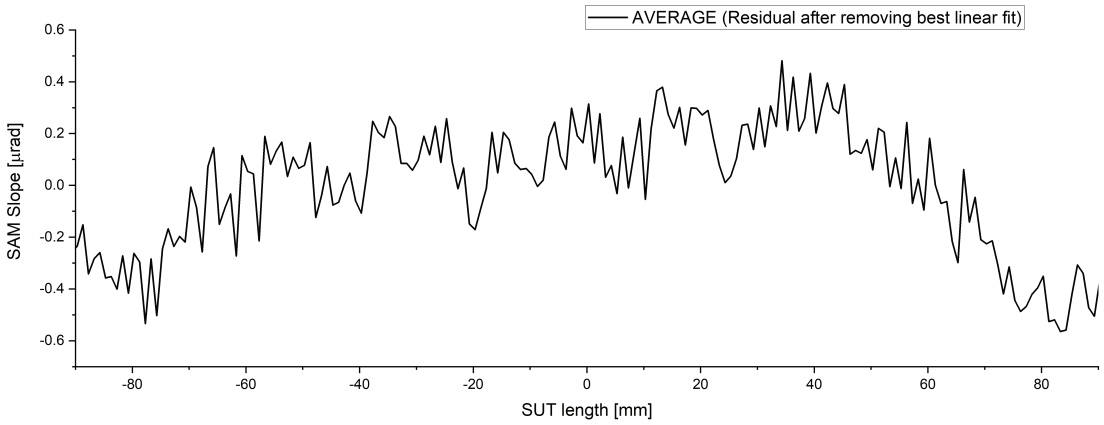

Figure 90: SUT average slope after removing best linear fit

Second, the slope gradient coefficient from equation (58) was added to the residual slope of Figure 90, using the formula in equation (59).

$$y = 8.61726 * x + c \tag{59}$$

Where:

- "y" is the SAM slope, including the most accurate slope gradient, expressed in µrad.
- "x" is the mirror length, expressed in mm.
- "c" is the slope residual profile, shown in Figure 90.

The results, shown in Figure 91, highlight the average slope retrieved using the SAM instrument, both with and without the slope gradient correction.

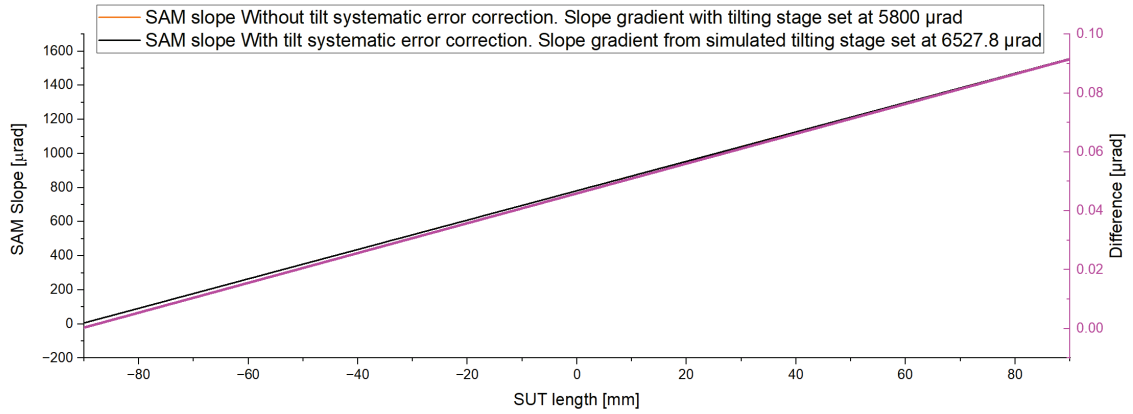

Figure 91: Comparison of the SUT slope calculated using the SAM, with and without tilt systematic error correction

Next was to correct the effect of SAM scanning head rotation around the y-axis on the optimal, averaged slope from SAM, corrected using the accurate slope gradient, shown in Figure 81, using the average measurements form the autocollimator, shown in Figure 79, using equation (53).

A comparison between the slope with and without the scanning head rotation correction is shown in Figure 92. The most accurate slope profile (black) is then compared with the slope profiles obtained using other metrology instruments.

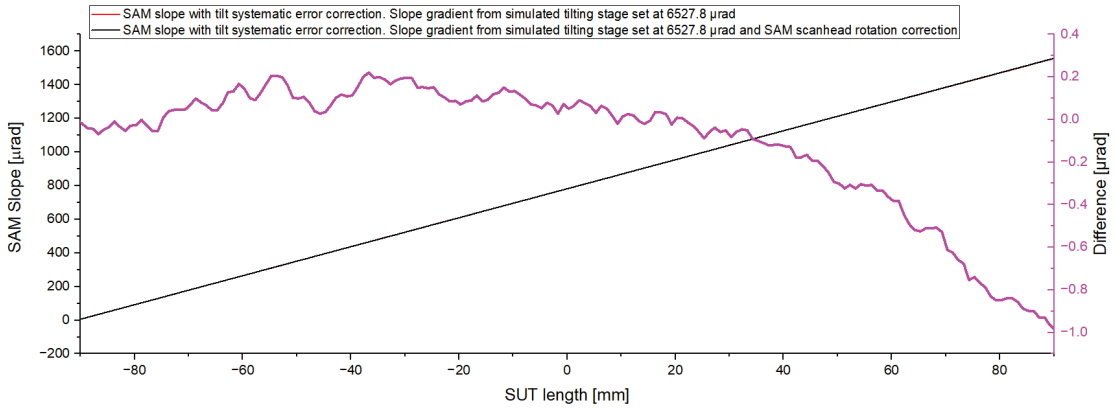

Figure 92: Comparison between the SAM slope without the scanning head rotation correction (red) and with scanning head rotation correction (black)

By performing the derivative of the slope in Figure 92, it is possible to retrieve the inverse of the local radius of curvature profile along the length of the SUT.

The inverse local of curvature profile is shown in Figure 93.

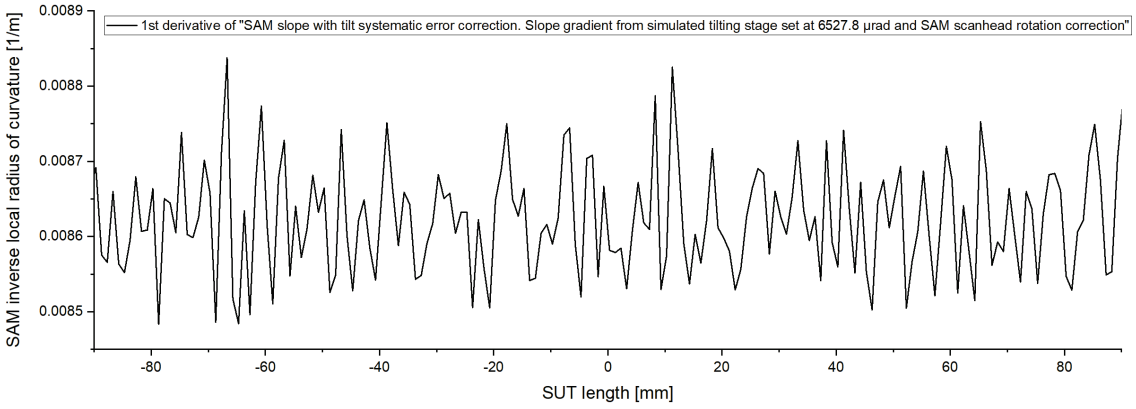

Figure 93: Inverse local radius of curvature of the cylindrical grating

Importing equation (54) into equation (60), the mean radius of curvature of this SUT is equal to 115.972 m.

$$\overline{ROC} = \frac{\Sigma \frac{1}{RoC}}{n} = \frac{182}{1.56934} = +115.972\ m \tag{60}$$

Having the SUT a curved surface height profile, the CESF, explained in chapter 3.9, shall also be considered. The scaling factor is linked to the SUT RoC and the distance between the SUT surface profile SAM detector plane. For this optic, the estimated CESF is 1.002354. The effect on both Expansion of the SUT length coordinates and the slope is shown in Figure 94.

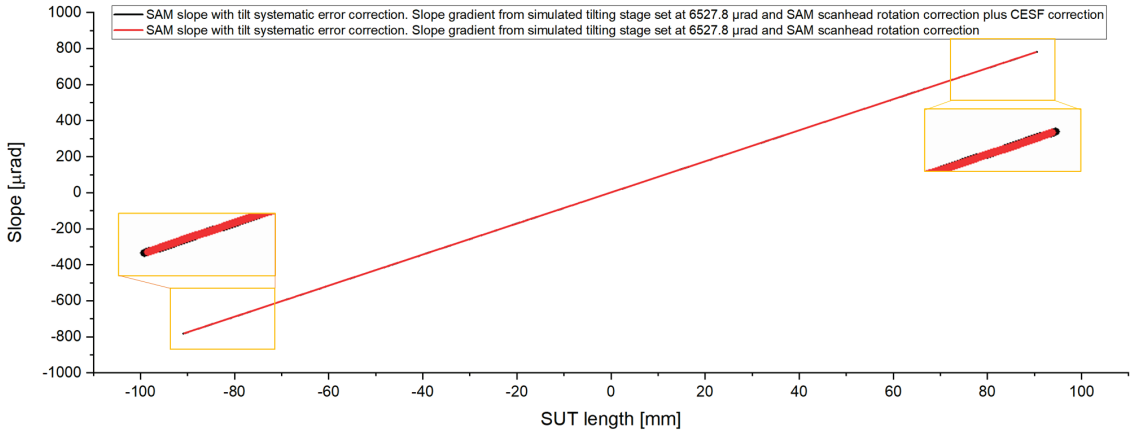

Figure 94: CESF effect on the SUT slope measurement and the SUT length retrieved using the SAM

4.4.4.1. Low Spatial Frequency Characterisation

A comparison between the same SUT slope profile, measured by SAM and a Fizeau Interferometer, is shown in Figure 95. It is worth noting that the HDX measurement has been down-sampled to match SAM spatial resolution, defined by the scanning step size of 1 mm, during this experiment.

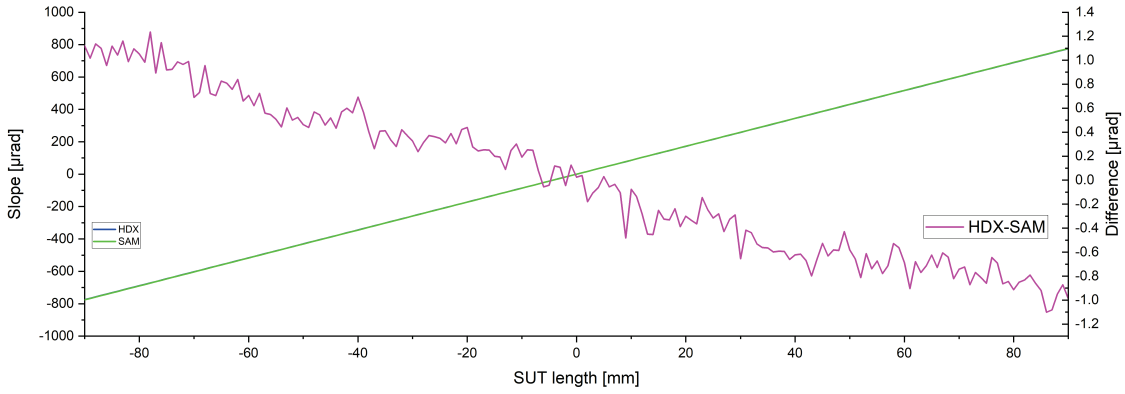

Figure 95: Slope characterisation of cylindrical grating, using the HDX and the SAM

The small disparity in the gradient of the slope between the SAM and the HDX measurements can be ascribed to various contributing factors. These encompass, but are not confined to, the imperfect calibration of the SAM instrument and the distinct configurations in which these two instruments assessed the same Sample Under Test (SUT). Specifically, SAM examined the surface profile of the optic with the SUT surface facing upwards, whereas HDX characterised the SUT surface in a sideways orientation. These differing conditions during measurement likely account for the observed variation in the slope gradient.

The effect of such discrepancy is a different SUT's radius of curvature, calculated as the inverse of the linear regression's slope gradient of each instrument's measured slope profiles. Such difference is shown in Table 41. It is worth noting that the measurements with the HDX are the average of scans performed in both AB and BA directions, while SAM scans were only performed in AB direction. Also, the most accurate SUT slope coefficient, from equation (58), was calculated when the SUT was placed at a slightly different distance from SAM's Detector.

Table 41: SUT radius of curvature characterisation using SAM and HDX.

SUT measured radius of curvature			
SAM		**HDX**	
Gradient of slope [rad/m]	0.00862179	**Gradient of slope [rad/m]**	0.00860988
RoC [m]	1/0.0086227= 115.972	**RoC [m]**	1/0.00860988 = 116.146
Absolute and % difference with SUT nominal RoC from Manufacturer (115.729 m)			
SAM		**HDX**	
+0.243 m	+0.21%	0.417 m	+0.36%

4.4.4.2. High Spatial Frequency Characterisation

To test the high spatial frequency characterisation of this SUT, by using both the SAM and the HDX, the best linear fit line is removed from both slopes, which corresponds to removing a cylindrical profile, having a radius of curvature of 115.972 m and 116.146 m, respectively. A comparison between the SUT slope error profiles measured by the SAM and the down-sampled HDX data to match SAM spatial resolution used for this experiment is shown in Figure 96, while the Figure error profiles are shown in Figure 97.

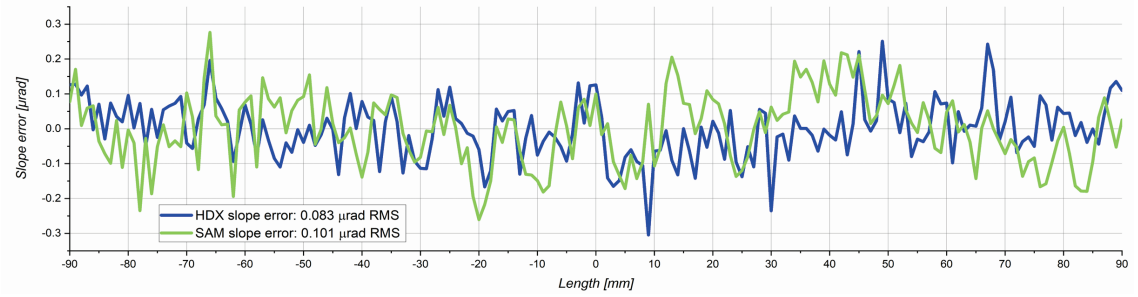

Figure 96: Slope characterisation of the cylindrical grating using the HDX and the SAM

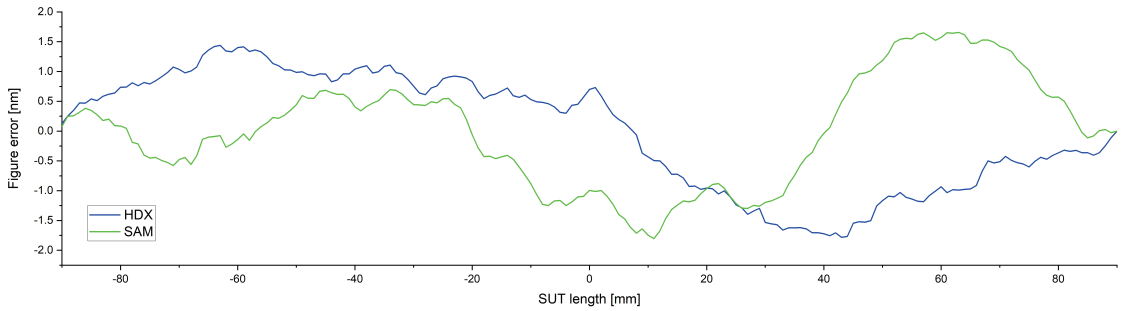

Figure 97: Figure characterisation of the flat grating, using the HDX and the SAM

The root mean square error between the Fizeau Interferometer (HDX) and SAM figure profile, as integration of the respective slope error measurements, is 1.37 nm.

These results prove the ability of the SAM to characterise accurately and precisely surface profiles of challenging optics.

4.4.5. Comparison between Simulated and Experimental Results

Simulations offer predictions based on theoretical frameworks and mathematical algorithms. In contrast, experimental results are grounded in empirical observations and direct measurements in controlled environments. The comparison between these two methodologies is crucial for several reasons. Firstly, it allows for the validation or refinement of simulation models, ensuring they accurately reflect real-world phenomena. Secondly, it aids in identifying the limitations of both approaches, as discrepancies between simulated and experimental results can highlight areas where our understanding of underlying principles is incomplete or where the simulation might be oversimplified.

This comparison is not without its challenges. Discrepancies between simulated and experimental results can arise due to a multitude of factors including, but not limited to, model simplifications, assumptions in the simulation process, measurement errors, or unaccounted variables in the experimental setup.

In section 3.8.1.1 I presented an example of the simulation of a 116 m, concave, cylindrical optics. The empirical measurements of such optics were also presented in section 4.4.4. The comparison results between the two is presented in Figure 98 (b).

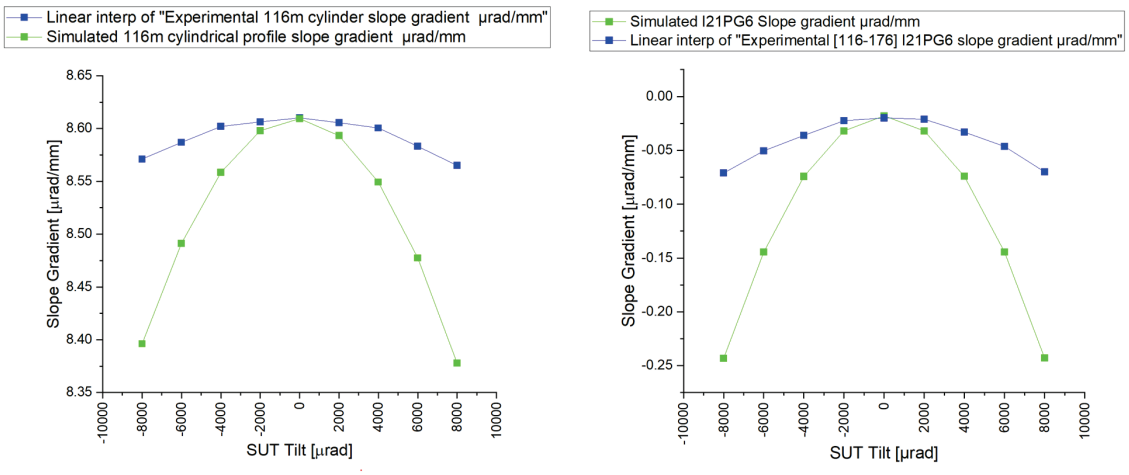

Figure 98: Simulation vs Experiment results: a) Flat grating. b) 116m cylinder

A discrepancy between the two curves is noted, and to investigate the origin of the difference, a comparison between the simulation and empirical results of the optics presented in section 4.4.2 was conducted. The results are shown in Figure 98 (a).

It is possible to conclude that the difference between the simulated and the empirical measurements differ by a constant, second order polynomial trend, which is independent from the SUT radius of curvature, as shown in Figure 99. Such systematic error, being independent of the radius of curvature of the SUT can then be removed from the simulation model, improving the accuracy of the simulation. Further investigation is required to determine the root cause.

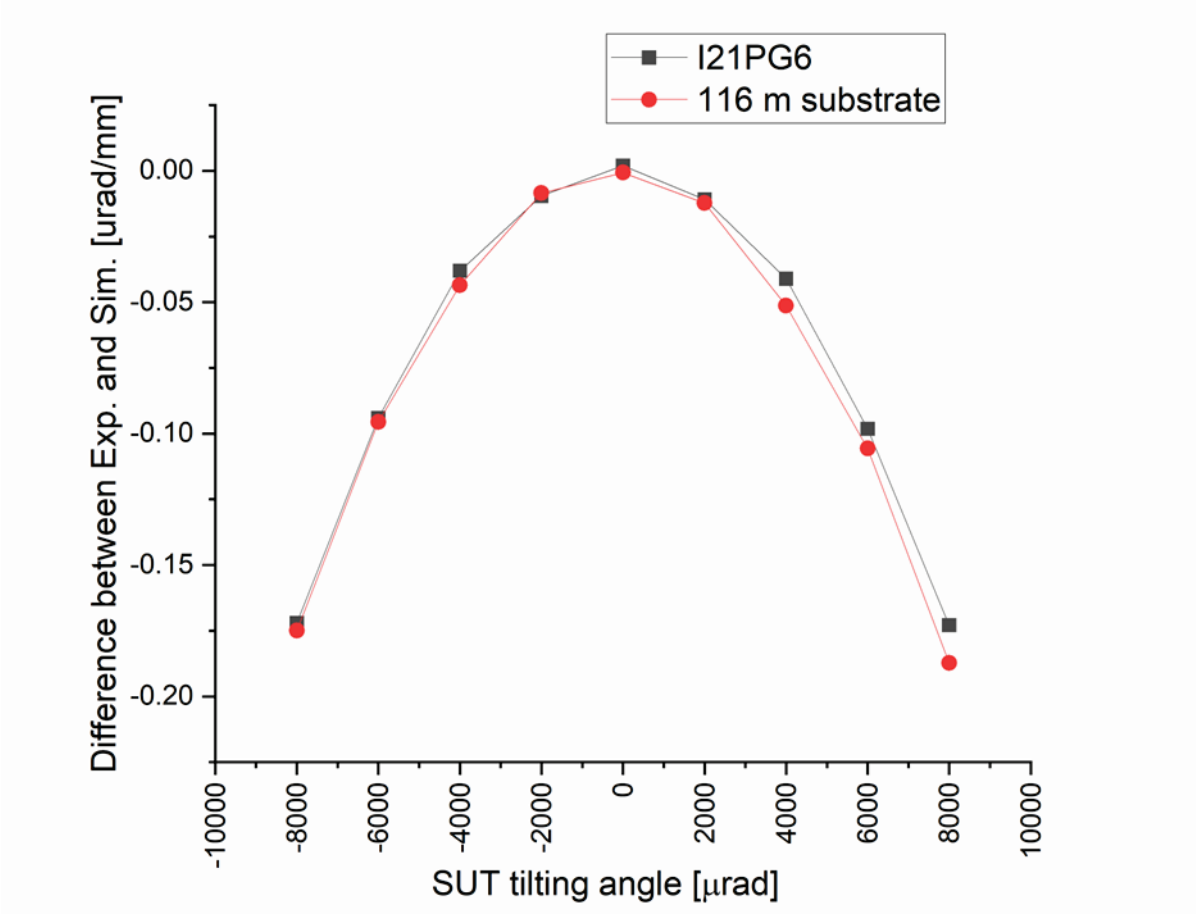

Figure 99: Difference between simulation and empirical results, for two optics

4.4.6. Spherical Mirror

This optic was characterised by two lanes, each having a nominal radius of curvature equal to 9.3m. The experimental setup and SUT characteristics are shown in Figure 100, Figure 101,

Table 42 and Table 43.

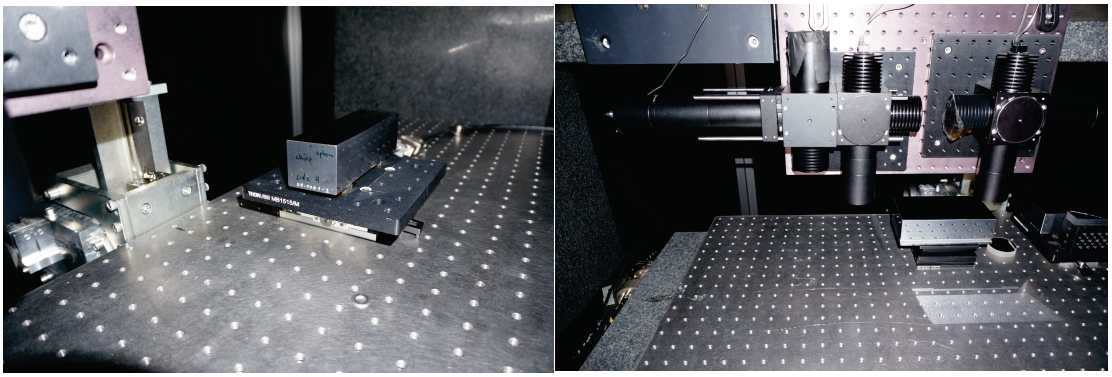

Figure 100: MOONPICS sphere mirror physical side scanning setup (left) / (right)

Table 42 Technical details of the MOONPICS sphere mirror

Supplier	Zeiss (Germany)
Substrate	Silicon (uncoated)
Dimensions	145 (L) x 45 (W) x 45 (H) mm^3
Analysis length	clear aperture = 100 mm (centred on mirror length)
Shape	Centred line with a chirped profile (width of about 10mm) and a second lane spherical. Both lanes are marked at the edges of the substrate
Tangential Sphere	RoC = 9.3m (nominal). Slope error < 2 µrad RMS

Table 43: MOONPICS sphere characterisation experiment hardware and software parameters

HARDWARE	
Detector Used [Brand / Model]	XIMEA MU181CR-ON
Detector pixel size [µm]	1.25
Detector size [y*x] [px]	3686*4896
Speckle creation method	Double side tape on glass window
LASER used [Brand / Model]	THORLABS CPS532
LASER wavelength [nm]	532
LASER type [collimated or divergent]	Collimated
SOFTWARE	
Active mirror range [mm]	-50 to 50
Interpolation step used [mm] (instrument)	0.22 (SAM)
ASF [µrad/px] (fixed or adapted)	4.23 (Fixed)
SAM cross-correlations mode [1 or 2]	2
CESF	1.02883103
Fine tuning to align SAM slope error to NOM and HDX [mm]	-1.05
ROI used [y*x] [px]	3000*3000
ROI used y [px]	340 – 3340
ROI used x [px]	948 - 3948
DIC Edge y top/bottom [px]	5
DIC Edge x left/right [px]	1000
Gaussian filter sigma [Standard deviation for Gaussian kernel]	10

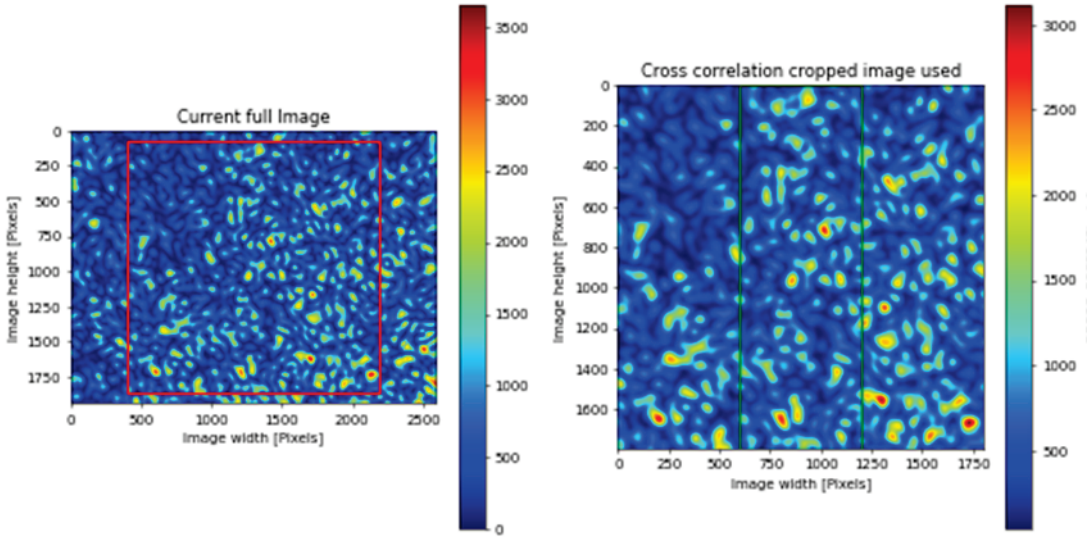

Figure 101: MOONPICS sphere ROI used as template (left) and the ROI used for the DIC (right)

The y-axis rotation angle change during SAM scanning head translation across the SUT is not significant for this experiment. It could almost be omitted because the slope across the SUT, as shown in Figure 103, is of over 8000 µrad. Therefore, the error generated by the translation stage rotation across y-axis of 3 µrad, shown in Figure 102, is equal to 0.033% of the total SUT slope range, as shown in equation (61):

$$Y\ axis\ rotation\ error\ \ (\%) = \frac{AC\ (y)\ slope\ range}{SUT\ Slope\ Range} * 100 = \frac{3}{9000} * 100 = \ 0.033\% \quad (61)$$

Where $AC\ (y)\ slope\ range$ and $SUT\ Slope\ Range$ are expressed in µrad.

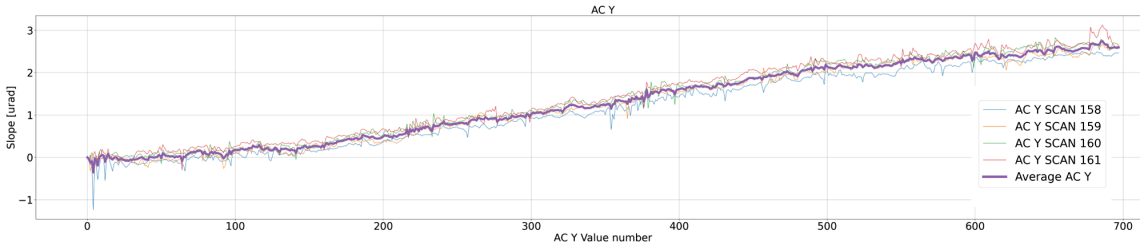

Figure 102: Image showing the y-axis rotation angle change of the SAM translation stage along the MOONPICS sphere measured

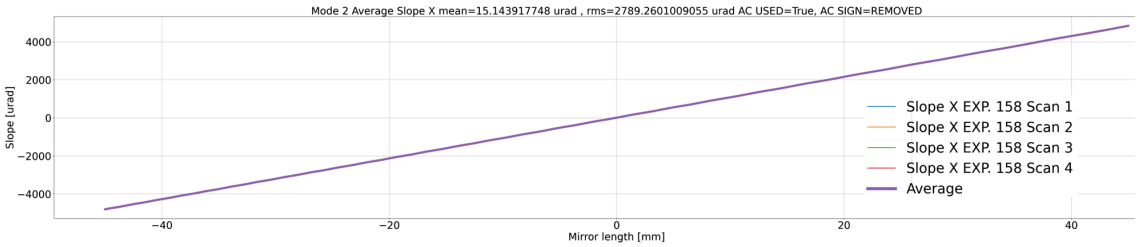

Figure 103: Slope range while measuring the MOONPICS sphere

The slope error is calculated by subtracting the best linear regression of best fit line from SAM, HDX, and NOM slope measurements and subtract it from the respective metrology instruments slope data.

The chirped lane slope error results are shown in Figure 104 and Table 44.

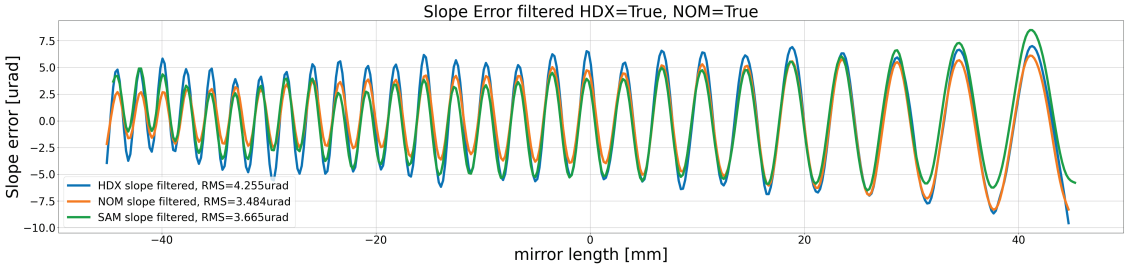

Figure 104: MOONPICS sphere chirped lane slope error (filtered)

Table 44: Differences between MOONPICS sphere chirped lane slope error (filtered).

Instrument	**Slope error RMS [µrad]**	**% Difference (SAM as reference)**	**% Difference (NOM as reference)**	**% Difference (HDX as reference)**
SAM	3.665	Reference = 0%	+5.19%	-13.25%
NOM	3.484	-4.93%	Reference = 0%	-17.53%
HDX	4.225	+15.27%	+21.26%	Reference = 0%

Using a calibrated ASF of 4.23 µrad/px and after applying a CESF of ~1.02865 to the mirror length coordinates, the RoC experimentally calculated using the Inverse local of radius of curvature was ~9.33m, as shown in Figure 105.

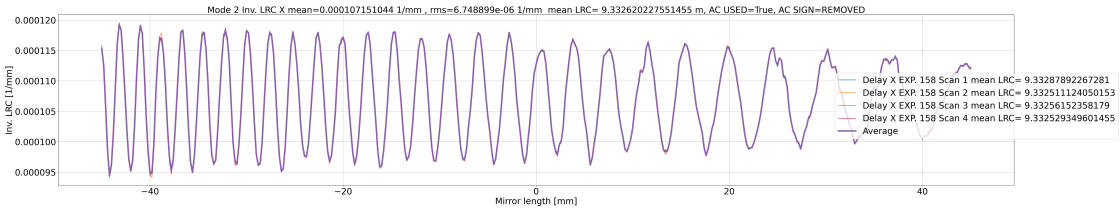

Figure 105: MOONPICS sphere chirped lane measured inverse LRC during multiple SAM scans

It was possible to characterise the chirped lane on the MOONPICS sphere SUT, having a slope range of more than 8000 µrad and showed the potential of measuring such optic with only few scans, with the potential of characterising strongly curved mirror quickly and precisely in any 1D profile required.

Using the sphere lane and assuming that a 1D figure profile is measured in the centre of a sphere, resulting in a simplified cylinder figure, it is possible to determine the ideal height change based on such profile, as shown in Figure 106.

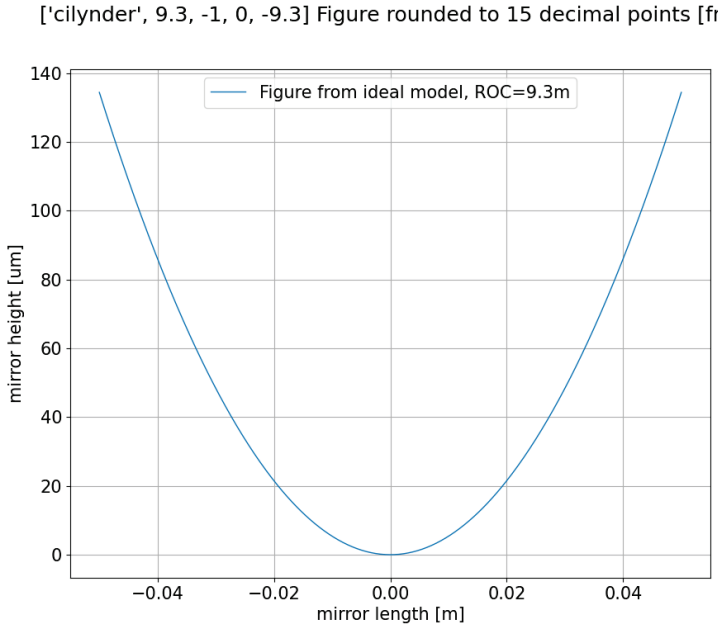

Figure 106: *Height change of cylindrical profile having RoC of 9.3m*

Using a fixed ASF of 2.469600 means that the distance from the SUT remains constant throughout the scan at 251.052802 mm. A 9.3m cylindrical figure profile will generate a linear slope change across the mirror length, and assuming that the scan is overing across the figure in steps of 0.2mm, at each step, from equation (23), there will be a slope change equal to 21.506 µrad.

It is possible to detect the ideal speckles displacement, in pixels, as the results of the DIC_x of adjacent images [36], as shown in equation (62):

$$\frac{ASF * \xi_2^v(x,y)}{\Delta x} = \frac{1}{R(x,y)} = \frac{2.469600 * \xi_2^v(x,y)}{1000000 * 0.0002} = \frac{1}{9.3} \rightarrow \xi_2^v(x,y) = \frac{0.0002 * 1000000}{2.469600 * 9.3} = 8.7080\ px \quad (62)$$

Given that SAM distance from the SUT varies with the mirror length, the ideal expected pixel displacement between the SUT's centre and the highest point to the detector, 134.4 µm closer to the detector, is shown in equation (63):

$$\begin{aligned} ASF[\mu rad] &= \frac{P}{2d} = \frac{mm}{mm} * 1000000 \\ &= \frac{1.24}{1000 * 2 * (251.052802 - 0.134410)} * 1000000 \\ &= 2.4709 \end{aligned} \tag{63}$$

Therefore, the expected displacement, in terms of pixel would be:

$$\xi_2^v(x,y) = \frac{0.0002 * 1000000}{2.470923 * 9.3} = 8.7034\ px \tag{64}$$

The difference that the SAM should detect during cross-correlation between the images at the centre of the SUT and at the edge of the SUT is:

$$8.7080 - 8.7034 = 0.00466\ px \tag{65}$$

Being a strong focused mirror, mode 2 is used instead of mode 1 to fully characterise the mirror surface slope profile. The difference between adjacent images would be even smaller than aforementioned. Such narrow difference is shown in the equations (66) to (68) if the adjacent images are at the edge of the SUT, or in equations (69) to (71) if they are at the centre of the SUT.

$$\begin{aligned} ASF[\mu rad] &= \frac{1.24}{1000 * 2 * (251.052802 - 0.1333364)} * 1000000 \\ &= 2.470912 \end{aligned} \tag{66}$$

$$\xi_2^v(x,y) = \frac{0.0002 * 1000000}{2.470912 * 9.3} = 8.703417\ px \tag{67}$$

$$8.703417 - 8.703377 = 0.000040\ px \tag{68}$$

$$\begin{aligned} ASF[\mu rad] &= \frac{1.24}{1000 * 2 * (251.052802 - 0.002150)} * 1000000 \\ &= 2.469621 \end{aligned} \tag{69}$$

$$\xi_2^v(x,y) = \frac{0.0002 * 1000000}{2.469621 * 9.3} = 8.707966\ px \qquad (70)$$

$$8.708040 - 8.707966 = 0.000074\ px \qquad (71)$$

Because SAM cannot reliably detect changes below 1/100 of a pixel unless multiple scans are performed and an average cross-correlation value is used, system accuracy at these levels is severely affected. When the slope is generated in mode 2, all of these errors add up to increase the systematic slope error.

The SAM angular scaling factor and the distance from the SUT have an inverse relationship. By calculating the HSASF at each detector distance (pixels displacement found using equation (62) and multiplying it by the corresponding HSASF), the resultant slope change, for each step of 0.2 mm is equal to 21.50538 µrad. The distance from the centre of the SUT to the SAM detector is fixed at 251.052802 mm. The associated ASF, at this specific location, is 2.4696 µrad/px. Therefore, the speckles displacement (expressed in pixels) found using equation (30) at this location is equal to 8.708040 pixels. When such displacement is multiplied by the ASF, the resulting slope change for each 0.2mmm step is also 21.50538 µrad.

During the SAM scan, there is a height change in the sample due to the spherical profile of the SUT, which results in a slightly different pixel displacement at the SAM detector, as shown in Figure 107.

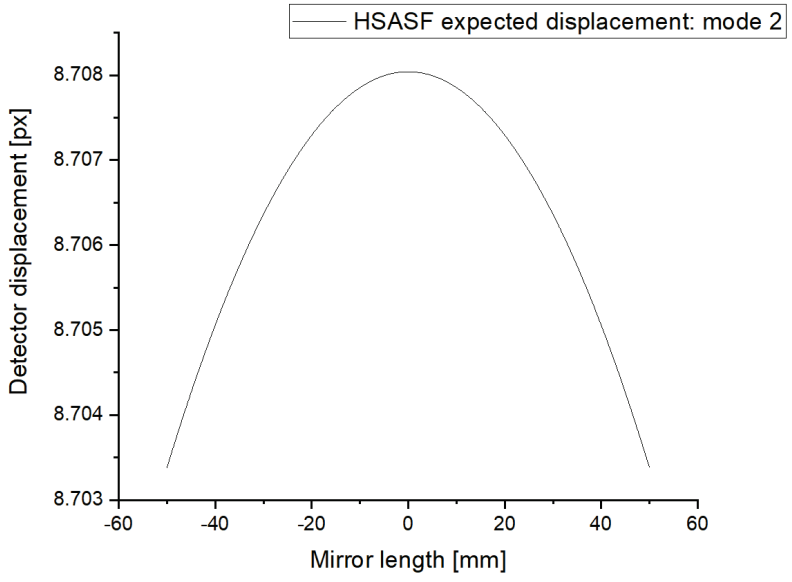

Figure 107: Mode 2 detector displacement across the mirror length

If the fixed ASF is used, each of these displacements will be multiplied by the same ASF of 2.4696 µrad/px.

This will generate different slope changes at any adjacent steps, as shown in Figure 108, generating a systematic error.

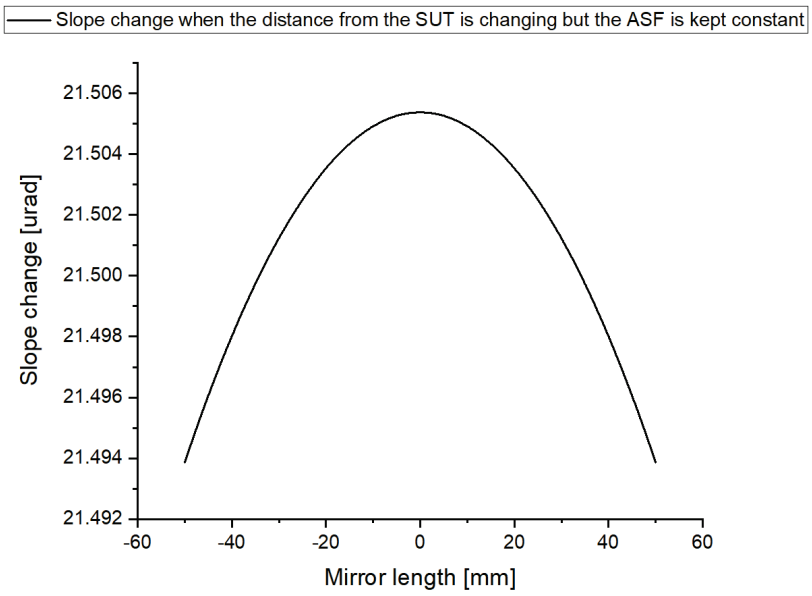

Figure 108: Mode 2 Slope change at each step across the mirror length

To create the total slope change across the entire mirror a cumulative sum of the data in Figure 108 was performed, and the result is shown in Figure 109, where the slope range from the ideal case, where the HSASF is correctly used and the slope range where the fixed ASF is used, but the different pixel displacement across the SUT length are considered, is shown.

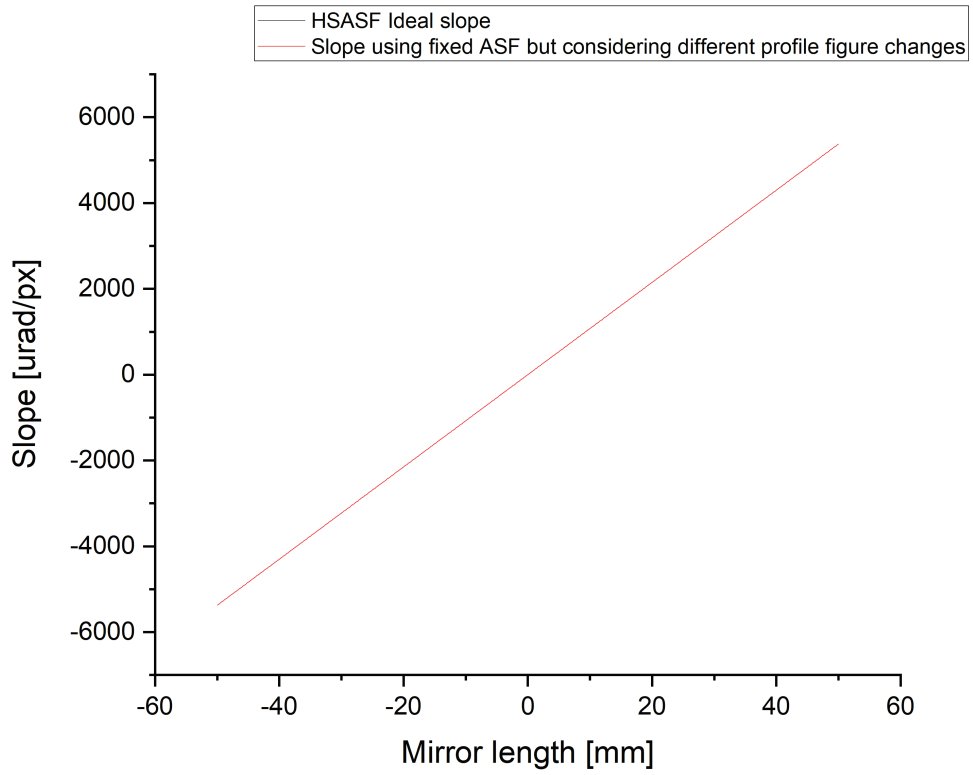

Figure 109: Comparison of slope reconstruction techniques

The difference between the two graphs is illustrated in Figure 110.

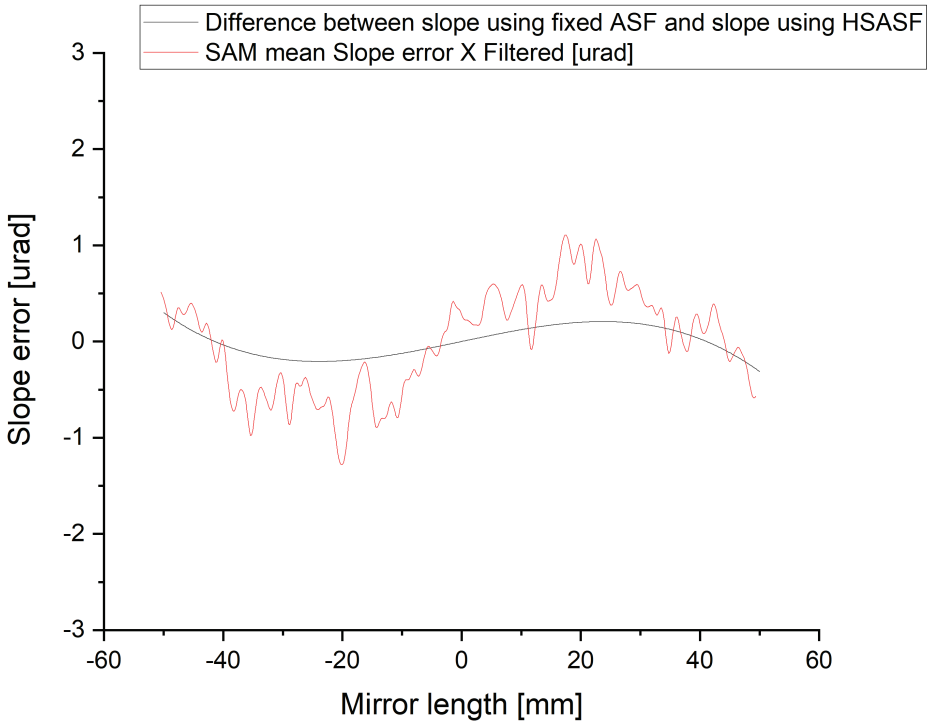

Figure 110: Systematic slope error induced by using a fixed ASF and the SAM slope error

If this error is multiplied by a factor equal to the fixed percentage increase in CESF, equal to 2.88, the result is shown in Figure 111.

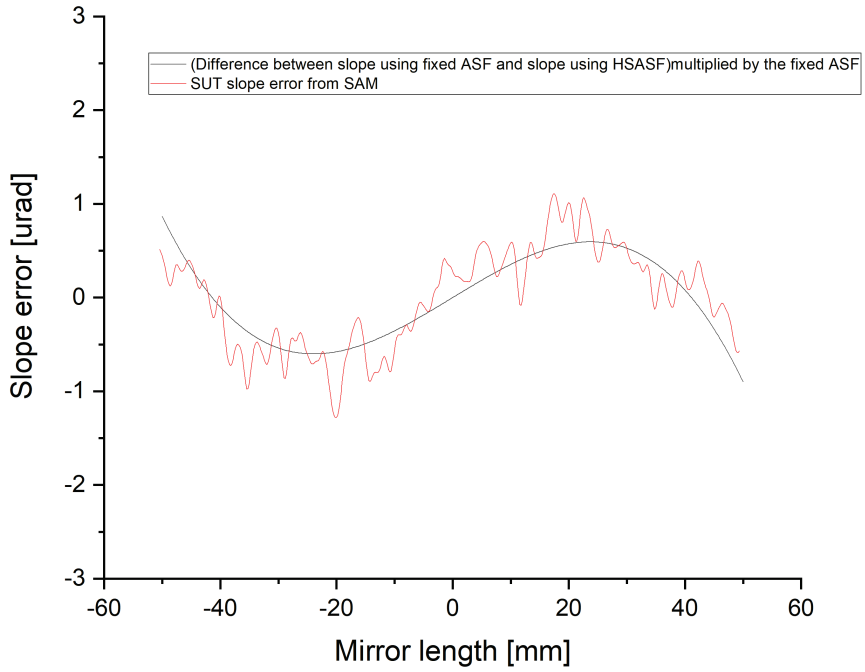

Figure 111: Systematic slope error induced by using a fixed ASF on multiplied by a factor equal to the fixed percentage change in CESF, compared to with the SAM slope error

The difference between the latest model and the SAM slope error originally calculated is now shown and compared with the NOM and the HDX measurements in Figure 112.

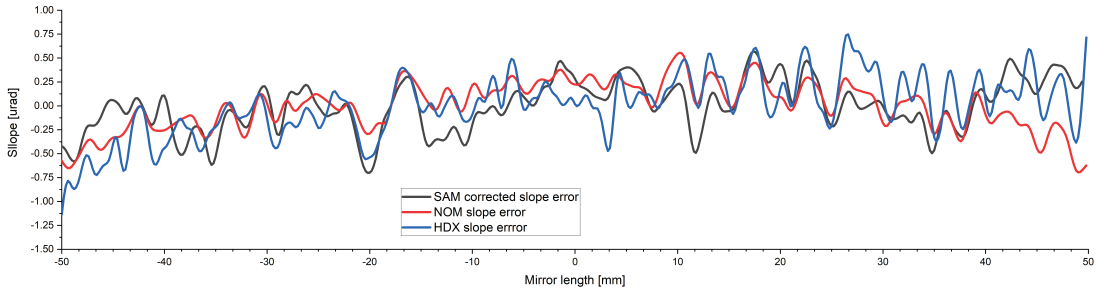

Figure 112: Slope error after correction

The RMSE between HDX and NOM is equal to 0.246 µrad, The RMSE between SAM and HDX is equal to 0.305 µrad and the RMSE between SAM and NOM is equal to 0.297 µrad.

5. Summary, Conclusions and Further Work

The chapter begins with a summary of the advancements made using the laser speckle angular measurement technique, particularly in the characterisation of X-ray mirror profiles. It then discusses the development and implementation of the Speckle Angle Measurement (SAM), addressing the limitations of existing metrology methods. The conclusions drawn from the research are outlined, highlighting the precision and accuracy of the SAM instrument. Finally, the chapter explores recommendations for further work, including the integration of SAM with ion beam figuring systems, the establishment of an uncertainty budget, and other enhancements to improve the instrument's accuracy and performance in various environmental conditions.

5.1. Summary

This research advanced X-ray optics nanometrology through the use of speckle-based analysis, specifically for the *ex situ* characterisation of X-ray optics. A central focus was the successful characterisation of strongly curved X-ray mirror profiles, with radii of curvature less than 10 metres. The thesis further provided an in-depth examination of novel techniques and the related metrology instrumentation, detailing the development of new mathematical models and the necessary hardware and software tools.

The SAM technique employed in this thesis addressed the limitations of existing metrology methods by employing an optical scanning head that generated 2D random intensity patterns, or speckle, through a laser diffuser. Variations in the X-ray mirror's slope caused shifts in the speckle pattern, which were measured with nanoradian precision in two dimensions using an advanced sub-pixel algorithm, demonstrating the instrument's high accuracy and precision.

This thesis addressed key challenges in the field of nanometrology, particularly focusing on achieving high precision and accuracy under strict environmental conditions to minimise the effects of temperature, humidity, pressure, turbulence, and vibration. It also tackled the complexities of understanding material behaviour at the nanoscale, developing sophisticated software to handle large data sets, and integrating multiple technologies into a single, cost-effective, metrology instrument.

5.2. Conclusions

In this thesis, I have embarked on an extensive exploration of the advancements in non-contact metrology, underpinning the quest for improved precision and accuracy in the measurement of surfaces at the nanoscale. The literature review provided a foundational understanding of the current state of non-contact metrology, and its applications. A significant portion of the thesis was dedicated to the novel Speckle Angle Measurement (SAM) [36] metrology instrument. The methodology was thoroughly discussed. The results and discussion section presented an in-depth analysis of the calibration processes, and the characterisation of different optics, including an ellipsoid X-ray mirror and various grating substrates. This thesis confirmed the capabilities of SAM as a nanometrology instrument, highlighting its versatility, with a demonstrated precision and accuracy < 50 nrad. Additional recommendation for research and potential enhancements to the proposed SAM technique were also provided, thereby contributing to the advancement of nanometrology in scientific research and industry.

Trying to push the boundaries of metrology is a quest. There are a lot of variables and physical phenomena to consider when you try to characterise angles of 20 nrad and smaller. These are angles ≤ 0.000001146 degrees. To put in perspective, if you were to draw a circle with a radius of 1 meter, 20 nrad would correspond to an arc length of just 20 nanometre (20-billionth of a meter). This is smaller than the wavelength of visible light and around 5000 smaller than the width of an average human hair. Such challenge is even increased by the environment where the SAM instrument was placed. The monochromatic, visible light laser used for the SAM is susceptible to changes in the refractive index of air due to temperature, humidity and other external factors. The speckle stability is impacted by the laser stability, the air turbulence surrounding the instrument and by the mechanical, intrinsic characteristics of the components used in the SAM instrument.

An accurate and precise method to calibrate the instrument has been developed, together with a software package capable of modelling and simulating the SAM physics, but research is still underway to find the root cause of the slight discrepancy between simulation and empirical data.

During this thesis I also demonstrated the potential of SAM in measuring the slope profile of optics with surface reflectivity below 4% and optics having a radius of curvature below 10 m. This means that the optical and metrology community now have an additional tool capable of characterising the surface of reflective optics.

The SAM instrument has also been demonstrated to precisely reconstruct optical surface profiles having radius of curvature below 1 m [36]. In addition, the SAM metrology instrument is made by open-source hardware and software, offering several advantages such as making SAM appealing in various fields, from technology and education to business and research.

This thesis is a contribution to the quest for better metrology.

5.3. Further Work

5.3.1. SAM for Ion Beam Figuring

Diamond Light Source (DLS) has developed its own ion beam figuring system for producing ultra-high-quality X-ray optics, essential for advanced scientific applications [78]. This move was driven by the need to overcome the limitations and risks associated with external procurement and transportation of X-ray optics. The in-house system, designed with cutting-edge features and aligned with DLS's technical standards, not only reduces the risk of damage to optics but also streamlines the process, enhancing efficiency and control over the production of high-precision optics. The SAM can be used to provide closed loop feedback to the Ion Beam Figuring (IBF) process, and its current implementation is shown in Figure 113. Further investigation and characterisation of the DLS IBF translation stages shall be undertaken. Also, a vacuum-compatible SAM shall be developed to increase the precision and accuracy of this metrology instrument in such challenging environmental conditions. This recommendation is aimed to remove the systematic error from the deformation under vacuum of the clear window, currently placed as separator between the SAM and the IBF vacuum chamber.

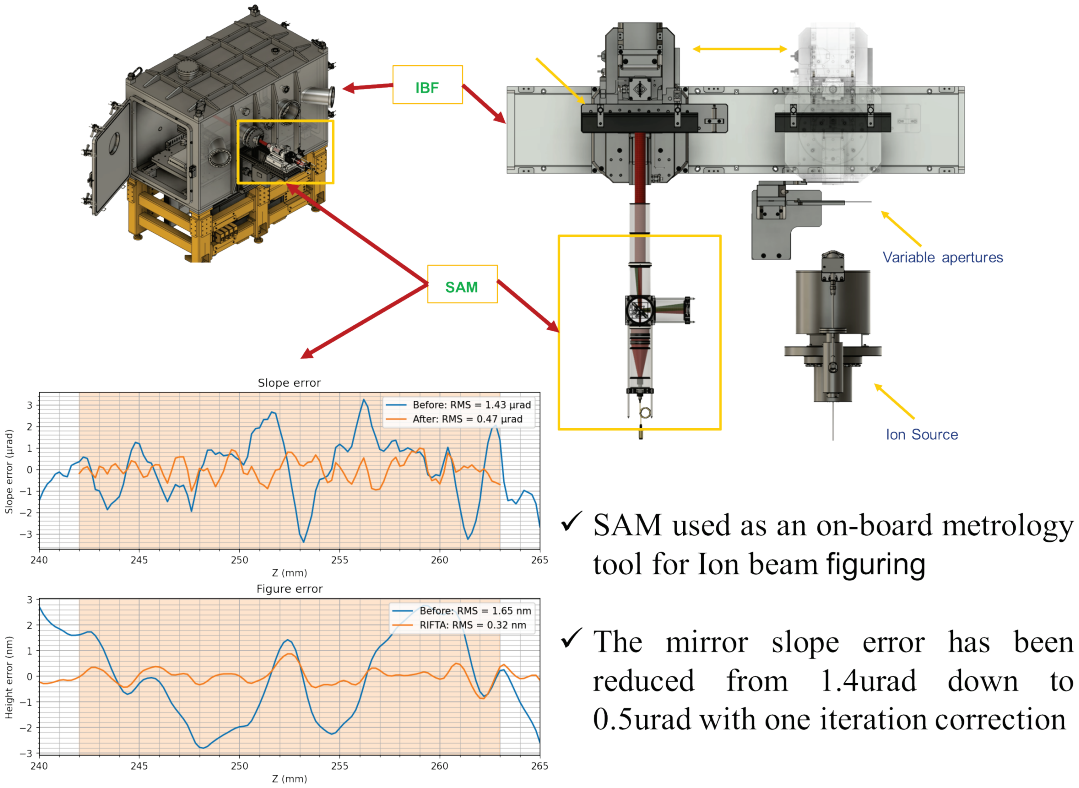

Figure 113: SAM for Ion Beam Figuring

5.3.2. The Uncertainty Budget

To address the limitations of this study, the uncertainty budget (UB) should prove to be effective since it is a widely used tool in the field of metrology and quality control. It is used to quantify the uncertainties associated with measurement systems and to provide a systematic framework for evaluating their performance [79]. The UB approach involves characterising the errors in a measurement system by assigning them to different error sources and then propagating these errors through the measurement system to estimate the overall uncertainty of the metrology instrument.

Different types of error sources should be included in an UB, such as the SAM systematic errors, the calculation of the uncertainty associated with the SAM angular scaling factor, the uncertainties associated with a slope measured by the SAM for each mode of operation, the uncertainties related to the autocollimator, and how these errors can be quantified and propagated through the SAM system.

5.3.3. Further recommendations

Further work should identify the root cause of the discrepancy between the simulated and the empirical data obtained with the developed simulation tool and the SAM measurements, respectively.

Another challenge posed by the development of the SAM as a metrology instrument was its sensitivity to the variation in distance between the SUT and the SAM camera detector. I recommend further investigations on the impact of systematic errors associated with the beam splitter. To further increase the precision and accuracy of SAM I also recommend the installation of the metrology instrument in an enclosed, stable, and vacuum environment. Moreover, to compensate with the degrees of freedom of SAM, an engineered tilt/rotation/translation stage should be used to successfully calibrate and improve the precision and accuracy of SAM measurements.

6. References

1. Lightsources of the world. https://lightsources.org/lightsources-of-the-world.

2. Diamond Light Source ltd. https://www.diamond.ac.uk/Home/About.html.

3. Kocharyan, V. R., Movsisyan, A. E. & Gogolev, A. S. On the Possibility of Two-Dimensional Focusing of Reflected X-Rays from Quartz Single Crystal in the Presence of External Temperature Gradient. *J. Contemp. Phys.* **53**, 263–269 (2018).

4. Wang, H. *et al.* X-ray wavefront characterization of a Fresnel zone plate using a two-dimensional grating interferometer. *Opt. Lett.* **38**, 827 (2013).

5. Snigirev, A., Kohn, V., Snigireva, I., Souvorov, A. & Lengeler, B. Focusing high-energy x rays by compound refractive lenses. *Appl. Opt.* **37**, 653 (1998).

6. Lengeler, B., Benner, B., Kuhlmann, M. & Schroer, C. G. Parabolic refractive X-ray lenses. *Acta Crystallogr. Sect. A Found. Crystallogr.* **61**, c20–c21 (2005).

7. Bilderback, D. H., Freund, A. K., Knapp, G. S. & Mills, D. M. The historical development of cryogenically cooled monochromators for third-generation synchrotron radiation sources. *J. Synchrotron Radiat.* **7**, 53–60 (2000).

8. Cocks, F. H. & Gettliffe, R. Total external X-ray reflection: A novel method of surface chemical analysis. *Mater. Lett.* **3**, 133–136 (1985).

9. A. H. Compton. Die Totalreflexion der Röntgenstrahlen. *Naturwissenschaften* **11**, 890–891 (1923).

10. Edwards, H. W. Total reflection of X-Rays and the index of refraction of certain metals. *Phys. Rev.* **30**, 91--94 (1927).

11. Salditt, T. & Egner, A. Nanoscale Photonic Imaging. in *Topics in Applied Physics* (ed. D. Russell, L.) vol. 134 84–87 (2020).

12. Thiess, H., Lasser, H. & Siewert, F. Fabrication of X-ray mirrors for synchrotron applications. *Nucl. Instruments Methods Phys. Res. Sect. A Accel. Spectrometers, Detect. Assoc. Equip.* **616**, 157–161 (2010).

13. Goldberg, K. A. Derivation of closed-form ellipsoidal X-ray mirror shapes from

Fermat ’ s principle. *J. Synchrotron Radiat.* **29**, 991–996 (2022).

14. Sawhney, K., Wang, H., Sutter, J., Alcock, S. & Berujon, S. At-wavelength Metrology of X-ray Optics at Diamond Light Source. *Synchrotron Radiat. News* **26**, 17–22 (2013).

15. David, W. J. Characterization. in *Handbook of Surface and Nanometrology* 5–167 (CRC Press, 2011).

16. Zhou, L. *et al.* One-dimensional ion-beam figuring for grazing-incidence reflective optics. *J. Synchrotron Radiat.* **23**, 182–186 (2016).

17. Mori, Y., Yamauchi, K. & Endo, K. Elastic emission machining. *Precis. Eng.* **9**, 123–128 (1987).

18. Alcock, S. G. & Cockerton, S. A preferential coating technique for fabricating large, high quality optics. *Nucl. Instruments Methods Phys. Res. Sect. A Accel. Spectrometers, Detect. Assoc. Equip.* **616**, 110–114 (2010).

19. Alcock, S. G., Nistea, I. & Sawhney, K. Nano-metrology: The art of measuring X-ray mirrors with slope errors <100 nrad. *Rev. Sci. Instrum.* **87**, (2016).

20. Harvey, J. E. & Thompson, A. K. Scattering effects from residual optical fabrication errors. *Int. Conf. Opt. Fabr. Test.* **2576**, 155–174 (1995).

21. da Silva, M. B., Alcock, S. G., Nistea, I. T. & Sawhney, K. A Fizeau interferometry stitching system to characterize X-ray mirrors with sub-nanometre errors. *Opt. Lasers Eng.* **161**, 107192 (2023).

22. Dhamgaye, V., Laundy, D., Baldock, S., Moxham, T. & Sawhney, K. Correction of the X-ray wavefront from compound refractive lenses using 3D printed refractive structures. *J. Synchrotron Radiat.* **27**, 1518–1527 (2020).

23. de La Rochefoucauld, O. *et al.* Euv and hard x-ray hartmann wavefront sensing for optical metrology, alignment and phase imaging. *Sensors (Switzerland)* **21**, 1–19 (2021).

24. Zhou, W., Raasch, T. W. & Yi, A. Y. Design, fabrication, and testing of a Shack–Hartmann sensor with an automatic registration feature. *Appl. Opt.* **55**, 7892 (2016).

25. Wang, H., Kashyap, Y. & Sawhney, K. Speckle based X-ray wavefront sensing with nanoradian angular sensitivity. *Opt. Express* **23**, 23310 (2015).

26. Yumoto, H. *et al.* At-wavelength figure metrology of hard x-ray focusing mirrors. *Review of Scientific Instruments* vol. 77 (2006).

27. Moxham, T. E. J. *et al.* Hard X-ray ptychography for optics characterization using a partially coherent synchrotron source. *J. Synchrotron Radiat.* **27**, 1688–1695 (2020).

28. Weitkamp, T., Nöhammer, B., Diaz, A., David, C. & Ziegler, E. X-ray wavefront analysis and optics characterization with a grating interferometer. *Appl. Phys. Lett.* **86**, 1–3 (2005).

29. Berujon, S., Wang, H. & Sawhney, K. J. S. At-wavelength metrology using the X-ray speckle tracking technique: Case study of a X-ray compound refractive lens. *Journal of Physics: Conference Series* vol. 425 (2013).

30. Wang, H., Sutter, J. & Sawhney, K. Advanced in situ metrology for x-ray beam shaping with super precision. *Opt. Express* **23**, 1605 (2015).

31. Kashyap, Y., Wang, H. & Sawhney, K. Development of a speckle-based portable device for in situ metrology of synchrotron X-ray mirrors. *J. Synchrotron Radiat.* **23**, 1131–1136 (2016).

32. Wang, H., Zhou, T., Kashyap, Y. & Sawhney, K. J. S. Speckle-based portable device for in-situ metrology of x-ray mirrors at Diamond Light Source. *Proc. SPIE* vol. 10385 (2017).

33. Zdora, M. C. State of the Art of X-ray Speckle-Based Phase-Contrast and Dark-Field Imaging. *J. Imaging* **4**, 60 (2018).

34. Berujon, S. *et al.* X-ray optics and beam characterization using random modulation. *arXiv.org* (2019).

35. Wang, H., Kashyap, Y. & Sawhney, K. From synchrotron radiation to lab source: Advanced speckle-based X-ray imaging using abrasive paper. *Sci. Rep.* **6**, 1–9 (2016).

36. Wang, H., Moriconi, S. & Sawhney, K. Nano-precision metrology of X-ray mirrors

with laser speckle angular measurement. *Light Sci. Appl.* **10**, 195 (2021).

37. Mimura, H. *et al.* Relative angle determinable stitching interferometry for hard x-ray reflective optics. *Rev. Sci. Instrum.* **76**, (2005).

38. Yumoto, H. *et al.* Stitching-angle measurable microscopic-interferometer: Surface-figure metrology tool for hard X-ray nanofocusing mirrors with large curvature. *Nucl. Instruments Methods Phys. Res. Sect. A Accel. Spectrometers, Detect. Assoc. Equip.* **616**, 203–206 (2010).

39. Idir, M., Kaznatcheev, K., Dovillaire, G., Legrand, J. & Rungsawang, R. A 2D high accuracy slope measuring system based on a Stitching Shack Hartmann Optical Head. *Opt. Express* **22**, 2770 (2014).

40. Huang, L., Xue, J., Gao, B. & Idir, M. One-dimensional angular-measurement-based stitching interferometry. *Opt. Express* **26**, 9882 (2018).

41. Assoufid, L. *et al.* Development of a high-performance gantry system for a new generation of optical slope measuring profilers. *Nucl. Instruments Methods Phys. Res. Sect. A Accel. Spectrometers, Detect. Assoc. Equip.* **710**, 31–36 (2013).

42. von Bieren, K. aspherical optical surfaces Pencil beam interferometer for aspherical optical surfaces. *Laser Diagnostics* **0343**, 101–108 (1982).

43. Irick, S. C. Determining surface profile from sequential interference patterns from a long tracer profiler. *Rev. Sci. Instrum.* **63**, 1432–1435 (1992).

44. von Bieren, K. Interferometry of wave fronts reflected off conical surfaces. *Appl. Opt.* **22**, 2109 (1983).

45. Takacs, P. Z., Qian, S. & Colbert, J. Design Of A Long Trace Surface Profiler. *Metrol. Fig. Finish* **0749**, 59 (1987).

46. Qian, S. & Takacs, P. Nano-Accuracy Surface Figure Metrology of Precision Optics. in *Modern Metrology Concerns* (ed. Cocco, D. L.) (InTech, 2012).

47. Siewert, F., Noll, T., Schlegel, T., Zeschke, T. & Lammert, H. The Nanometer Optical Component Measuring Machine: A new Sub-nm Topography Measuring Device for X-ray Optics at BESSY. *AIP Conf. Proc.* **705**, 847–850 (2004).

48. Alcock, S. G. *et al.* The Diamond-NOM: A non-contact profiler capable of

characterizing optical figure error with sub-nanometre repeatability. *Nucl. Instruments Methods Phys. Res. Sect. A Accel. Spectrometers, Detect. Assoc. Equip.* **616**, 224–228 (2010).

49. Nistea, I.-T., Alcock, S. G., Bazan da Silva, M. & Sawhney, K. J. S. The Optical Metrology Laboratory at Diamond: pushing the limits of nano-metrology. **1110906**, 5 (2019).

50. MÖLLER-WEDEL OPTICAL GmbH. Electronic Autocollimators of ELCOMAT & ELCOMAT direct Product Lines. https://www.haag-streit.com/moeller-wedel-optical/products/electronic-autocollimators.

51. Nistea, I. *et al.* Diamond-VeNOM: a high-speed slope profiler for characterizing x-ray mirrors. *Proc. SPIE* vol. 12695 (2023).

52. Yashchuk, V. V. *et al.* Sub-microradian surface slope metrology with the ALS Developmental Long Trace Profiler. *Nucl. Instruments Methods Phys. Res. Sect. A Accel. Spectrometers, Detect. Assoc. Equip.* **616**, 212–223 (2010).

53. Qian, S., Geckeler, R. D., Just, A., Idir, M. & Wu, X. Approaching sub-50 nanoradian measurements by reducing the saw-tooth deviation of the autocollimator in the Nano-Optic-Measuring Machine. *Nucl. Instruments Methods Phys. Res. Sect. A Accel. Spectrometers, Detect. Assoc. Equip.* **785**, 206–212 (2015).

54. Thetford, A. *Optical shop testing*. *Optics & Laser Technology* vol. 11 (1979).

55. Guenther, B. D. & Steel, D. G. Encyclopedia of modern optics. in *Encyclopedia of Modern Optics* 351–356 (2005).

56. Huang, L. *et al.* Stitching interferometry for synchrotron mirror metrology at National Synchrotron Light Source II (NSLS-II). *Opt. Lasers Eng.* **124**, (2020).

57. Bruker Nano, I. ContourGT-X User Manual. (2012).

58. EPICS - Experimental Physics and Industrial Control System. https://epics-controls.org.

59. Rommeveaux, A. *et al.* Second metrology round-robin of APS, ESRF and SPring-8 laboratories of elliptical and spherical hard-x-ray mirrors. *Proc. SPIE* (2007).

60. Sutter, J. P., Amboage, M., Hayama, S. & Daz-Moreno, S. Geometrical and wave-optical effects on the performance of a bent-crystal dispersive X-ray spectrometer. *Nucl. Instruments Methods Phys. Res. Sect. A Accel. Spectrometers, Detect. Assoc. Equip.* **621**, 627–636 (2010).

61. Malitson, I. H. Interspecimen Comparison of the Refractive Index of Fused Silica. *J. Opt. Soc. Am.* **55**, 1205–1209 (1965).

62. Pan, B., Qian, K., Xie, H. & Asundi, A. Two-dimensional digital image correlation for in-plane displacement and strain measurement: A review. *Meas. Sci. Technol.* **20**, (2009).

63. Leonardis, A. *et al.* Computer Vision – ECCV 2006 SURF: Speeded Up Robust Features. *Comput. Vis. – ECCV 2006* **3951**, 404-417–417 (2006).

64. Bay, H., Ess, A., Tuytelaars, T. & Van Gool, L. Speeded-Up Robust Features (SURF). *Comput. Vis. Image Underst.* **110**, 346–359 (2008).

65. Fienup, J. R. Reconstruction of an object from the modulus of its Fourier transform. *Opt. Lett.* **3**, 27 (1978).

66. Fienup, J. R. Phase retrieval algorithms: a comparison. *Appl. Opt.* **21**, 2758 (1982).

67. Guizar-Sicairos, M., Thurman, S. T. & Fienup, J. R. Efficient subpixel image registration algorithms. *Opt. Lett.* **33**, 156 (2008).

68. Fisher, G. H. & Welsch, B. T. FLCT: A Fast, Efficient Method for Performing Local Correlation Tracking. *arXiv.org* 1–9 (2007).

69. Bharati, S., Khan, T.Z., Podder, P., Hung, N. Q. A Comparative Analysis of Image Denoising Problem: Noise Models, Denoising Filters and Applications. in *Cognitive Internet of Medical Things for Smart Healthcare. Studies in Systems, Decision and Control* vol. 311 (Springer, 2021).

70. Shapiro, L. G. . G. C. S. *Computer Vision*. (Prentice-Hall, 2001).

71. Takacs, P. Z. Standardization of methods for extracting statistics from surface profile measurements. *Instrumentation, Metrol. Stand. Nanomanufacturing, Opt. Semicond. VIII* **9173**, 917309 (2014).

72. Harvey, J. E. Modeling the Image Quality of Enhanced Reflectance X-Ray

Multilayers as a Surface Power Spectral Density Filter Function. *Appl. Opt.* **34**, 3715–3726 (1995).

73. Nyquist, H. Certain Topics in Telegraph Transmission Theory. *Trans. Am. Inst. Electr. Eng.* **47**, 617–644 (1928).

74. Blackman, R. B. & Tukey, J. W. The Measurement of Power Spectra from the Point of View of Communications Engineering — Part I. *Bell Syst. Tech. J.* **37**, 485–569 (1958).

75. Alcock, S. G., Ludbrook, G. D., Owen, T. & Dockree, R. Using the power spectral density method to characterise the surface topography of optical surfaces. *Adv. Metrol. X-Ray EUV Opt. III* **7801**, 780108 (2010).

76. Alcock, S. G. *et al.* A novel instrument for generating angular increments of 1 nanoradian. *Rev. Sci. Instrum.* **86**, 125108–125108 (2015).

77. Laundy, D. *et al.* Development of a multi-lane X-ray mirror providing variable beam sizes. *Rev. Sci. Instrum.* **87**, 1–6 (2016).

78. Hand, M. *et al.* Ion beam figuring and optical metrology system for synchrotron x-ray mirrors. *Proc. SPIE* vol. 11109 (2019).

79. Alcock, Simon; Yacoot,Andrew; Ince,Rabia; Patel, H. Generating and measuring pico-radian angles. *Metrologia* **59**, 1–15 (2022).

7. Appendix A: Comparison of the Data Acquisition and Storage Methods

Table 45: Comparison of the SAM data acquisition and storage methods

Experiment Number	Description	Method
1	Saved images	Single images acquired and saved on SSD and after performed Cross-correlation and data analysis
2	Saved average of 3 images	Multiple images acquired, loaded in the RAM of PC and average of each pixel intensity matrix saved as .tiff image and stored on SSD and after performed DIC and data analysis
3	Saved average of 6 images	
4	Performed cross- correlation on live images and then saved single images	Used INCC value of 3 and after performed Cross-correlation and data analysis
5	Cross-corr. on image saved single images	Used INCC value of 5 on Exp.4. First Images saved and after performed DIC and data analysis
6	Cross-correlation on live images and then saved average of 3 images	Multiple images acquired, loaded in the RAM of PC and average of each pixel intensity matrix, performed DIC, saved results in .csv file and saved as .tiff images on SSD.
7	Cross-correlation on live images and then saved average of 6 images	
8	Cross-correlation on live images and then NOT saved single images	Multiple images acquired, loaded in the RAM of PC and average of each pixel intensity matrix, performed DIC, saved results in .csv file on SSD.

RESULTS								
	EXP.1	**EXP.2**	**EXP.3**	**EXP.4**	**EXP.5**	**EXP.6**	**EXP.7**	**EXP.8**
Number of images	500							
Scan Time taken	35 mins	49 mis	63 mins	40 mins	/	60 mins	87 min	40 mins
ROI size [px]	1000*1000 (y*x) [2600:3600,1100:2100]							
INCC iteration	5	5	5	3	5	3	3	5
Mean y [px]	-0.00132	0.00187	0.00148	2.23E-4	8.26E-4	-7.83E-4	-2.30E-4	-1.62E-4
Mean x [px]	-6.30E-4	2.19E-4	2.38E-4	-6.23E-4	0.00207	-3.19E-4	-9.39E-4	-0.00123

RMS y [px]	**0.05037**	0.0633	0.07715	0.05685	0.05489	0.07136	0.09106	0.05172
RMS x [px]	**0.02626**	0.0328	0.03771	0.03015	0.03985	0.03571	0.04136	0.02968
ROI size [px]	1500*1500 (y*x) [850:2350,2350:3850]							
Mean y [px]	-0.00132	0.00163	0.00122					
Mean x (px)	-7.13E-4	-1.89E-4	-2.63E-4					
SD y (px)	0.0519	0.06495	0.07879					
SD x (px)	0.0253	0.03147	0.03579					
RMS y (px)	**0.05187**	0.0649	0.07872					
RMS x (px)	**0.02531**	0.03144	0.03575					
ROI size [px]	2000*2000 (y*x) [600:2600,2100:4100]							
MEAN y (px)	-0.00108	0.00131	9.48E-4					
MEAN x (px)	-2.36E-4	-1.59E-4	-4.68E-5					
SD y (px)	0.05081	0.06294	0.07639					
SD x (px)	0.02472	0.03083	0.03499					
RMS y (px)	**0.05077**	0.06289	0.07632					
RMS x (px)	**0.02469**	0.0308	0.03496					
Edge x/y [px]	50/50							
SIGMA	10							

8. Appendix B: Model of the Cylindrical Surface Profile

8.1. Slope

The slope is calculated as derivative of figure profile:

$$\frac{\partial}{\partial x}\left(\tau * \sqrt{RoC^2 - \left(x - x_{offset}\right)^2} + z_{offset}\right)$$

Differentiate the sum term by term and factor out constants:

$$= \frac{\partial}{\partial x}\left(z_{offset}\right) + \tau * \left(\frac{\partial}{\partial x}\left(\sqrt{RoC^2 - \left(x - x_{offset}\right)^2}\right)\right)$$

The derivative of z_{offset} is zero:

$$= \tau * \left(\frac{\partial}{\partial x}\left(\sqrt{RoC^2 - \left(x - x_{offset}\right)^2}\right)\right) + 0$$

Now simplifying the above expression using the chain rule:

$$= \frac{\partial}{\partial x}\left(\sqrt{RoC^2 - \left(x - x_{offset}\right)^2}\right) = \frac{\partial\sqrt{u}}{\partial u} * \frac{\partial u}{\partial x}$$

where $u = RoC^2 - \left(x - x_{offset}\right)^2$ and $\frac{\partial}{\partial u}\left(\sqrt{u}\right) = \frac{1}{2*\sqrt{u}}$:

$$= \tau * \left(\frac{\frac{\partial}{\partial x}\left(RoC^2 - \left(x - x_{offset}\right)^2\right)}{2 * \sqrt{RoC^2 - \left(x - x_{offset}\right)^2}}\right)$$

Differentiate the sum term by term and factor out constants:

$$= \left(\frac{\partial}{\partial x}(RoC^2) - \frac{\partial}{\partial x}\left(\left(x - x_{offset}\right)^2\right)\right) * \frac{\tau}{2\sqrt{RoC^2 - (x - x_{offset})^2}}$$

The derivative of r^2 is zero:

$$= \frac{\tau * \left(-\left(\frac{\partial}{\partial x}\left((x - x_{offset})^2\right)\right) + 0\right)}{2\sqrt{RoC^2 - (x - x_{offset})^2}}$$

Using the chain rule:

$$= \frac{\partial}{\partial x}\left(\left(x - x_{offset}\right)^2\right) = \frac{\partial u^2}{\partial u}\frac{\partial u}{\partial x}$$

Where $u = x - x_{offset}$ and $\frac{\partial}{\partial u}(u^2) = 2u$:

$$= -\frac{\tau}{2\sqrt{RoC^2 - \left(x - x_{offset}\right)^2}} * \left(2(x - x_{offset})\left(\frac{\partial}{\partial x}(x - x_{offset})\right)\right)$$

Simplify the expression:

$$= -\frac{\tau * (x - x_{offset})\left(\frac{\partial}{\partial x}(x - x_{offset})\right)}{\sqrt{RoC^2 - (x - x_{offset})^2}}$$

Differentiate the sum term by term:

$$= -\frac{\tau * \left(x - x_{offset}\right)}{\sqrt{RoC^2 - \left(x - x_{offset}\right)^2}} * \left(\frac{\partial}{\partial x}\left(-x_{offset}\right) + \frac{\partial}{\partial x}(x)\right)$$

The derivative of $-x_{offset}$ is 0:

$$= -\frac{\tau * \left(x - x_{offset}\right)}{\sqrt{RoC^2 - \left(x - x_{offset}\right)^2}} * \left(\frac{\partial}{\partial x}(x) + 0\right)$$

Now simplify the above expression:

The derivative of x is 1:

$$= -\left(\tau * \frac{\left(x - x_{offset}\right)}{\sqrt{RoC^2 - \left(x_{offset} - x\right)^2}} * 1\right)$$

$$Figure\ slope\ [rad] = -\left(\tau * \frac{\left(x - x_{offset}\right)}{\sqrt{RoC^2 - \left(x_{offset} - x\right)^2}}\right)$$

8.2. Inverse of Local Radius of Curvature

Possible derivation from slope mathematical model:

$$\frac{\partial}{\partial x}\left(-\tau * \frac{(x - x_{offset})}{\sqrt{RoC^2 - (x_{offset} - x)^2}}\right)$$

Factor out constants:

$$= -\tau * \left(\frac{\partial}{\partial x}\left(\frac{x - x_{offset}}{\sqrt{RoC^2 - (x - x_{offset})^2}}\right)\right)$$

Use the product rule $\frac{\partial}{\partial x}(uv) = v\frac{\partial u}{\partial x} + u\frac{\partial v}{\partial x}$, where $u = x - x_{offset}$ and $v = \frac{1}{\sqrt{RoC^2 - (x - x_{offset})^2}}$:

$$= -\tau * \left(\frac{\frac{\partial}{\partial x}(x - x_{offset})}{\sqrt{RoC^2 - (x - x_{offset})^2}} + (x - x_{offset}) * \left(\frac{\partial}{\partial x}\left(\left(RoC^2 - (x - x_{offset})^2\right)^{-1/2}\right)\right)\right)$$

Differentiate the sum term by term:

$$= -\tau * \left((x - x_{offset}) * \left(\frac{\partial}{\partial x}\left(\left(RoC^2 - (x - x_{offset})^2\right)^{-1/2}\right)\right) + \left(\frac{\partial}{\partial x}(-x_{offset}) + \frac{\partial}{\partial x}(x)\right) * \frac{1}{\sqrt{RoC^2 - (x - x_{offset})^2}}\right)$$

The derivative of $-x_{offset}$ is zero:

$$= -\tau * \left(\left(x - x_{offset}\right) * \left(\frac{\partial}{\partial x} \left(\left(RoC^2 - (x - x_{offset})^2\right)^{-1/2} \right) \right) + \frac{\frac{\partial}{\partial x}(x) + 0}{\sqrt{RoC^2 - (x - x_{offset})^2}} \right)$$

Simplify the expression:

$$= -\tau * \left(\frac{\frac{\partial}{\partial x}(x)}{\sqrt{RoC^2 - (x - x_{offset})^2}} + \left(x - x_{offset}\right) * \left(\frac{\partial}{\partial x} \left(\left(RoC^2 - (x - x_{offset})^2\right)^{-1/2} \right) \right) \right)$$

The derivative of x is 1:

$$= -\tau * \left(\left(x - x_{offset}\right) * \left(\frac{\partial}{\partial x} \left(\frac{1}{\sqrt{RoC^2 - \left(x - x_{offset}\right)^2}} \right) \right) + 1 * \frac{1}{\sqrt{RoC^2 - (x - x_{offset})^2}} \right)$$

Using the chain rule, $\frac{\partial}{\partial x}\left(\frac{1}{\sqrt{RoC^2 - \left(x - x_{offset}\right)^2}}\right) = \frac{\partial}{\partial u}\frac{1}{\sqrt{u}}\frac{\partial u}{\partial x}$ where $u = RoC^2 - \left(x - x_{offset}\right)^2$ and $\frac{\partial}{\partial u}\left(\frac{1}{\sqrt{u}}\right) = -\frac{1}{2u^{3/2}}$:

$$= -\tau * \left(\frac{1}{\sqrt{RoC^2 - (x - x_{offset})^2}} + \left(x - x_{offset}\right) * \left(-\frac{\frac{\partial}{\partial x}\left(RoC^2 - (x - x_{offset})^2\right)}{2 * \left(RoC^2 - (x - x_{offset})^2\right)^{3/2}} \right) \right)$$

Differentiate the sum term by term and factor out constants:

$$= -\tau\left(\frac{1}{\sqrt{RoC^2-\left(x-x_{offset}\right)^2}}\right.$$
$$\left.-\left(\frac{\partial}{\partial x}(RoC^2)-\frac{\partial}{\partial x}\left(\left(x-x_{offset}\right)^2\right)\right)\frac{x-x_{offset}}{2*\left(RoC^2-\left(x-x_{offset}\right)^2\right)^{3/2}}\right)$$

The derivative of RoC^2 is zero:

$$= -\tau*\left(\frac{1}{\sqrt{RoC^2-(x-x_{offset})^2}}-\frac{\left(x-x_{offset}\right)*\left(-\left(\frac{\partial}{\partial x}\left((x-x_{offset})^2\right)\right)+0\right)}{2*\left(RoC^2-(x-x_{offset})^2\right)^{3/2}}\right)$$

Simplify the expression:

$$= -\tau*\left(\frac{1}{\sqrt{RoC^2-(x-x_{offset})^2}}+\frac{\left(x-x_{offset}\right)*\left(\frac{\partial}{\partial x}\left((x-x_{offset})^2\right)\right)}{2*\left(RoC^2-(x-x_{offset})^2\right)^{3/2}}\right)$$

Using the chain rule, $\frac{\partial}{\partial x}\left(\left(x-x_{offset}\right)^2\right)=\frac{\partial u^2}{\partial u}\frac{\partial u}{\partial x}$, where $u=x-h$ and $\frac{\partial}{\partial u}(u^2)=2u$:

$$= -\tau*\left(\frac{1}{\sqrt{RoC^2-(x-x_{offset})^2}}+\left(2*\left(x-x_{offset}\right)\left(\frac{\partial}{\partial x}\left(x-x_{offset}\right)\right)\right)\right.$$
$$\left.*\frac{x-x_{offset}}{2*\left(RoC^2-(x-x_{offset})^2\right)^{3/2}}\right)$$

Simplify the expression:

$$= -\tau*\left(\frac{1}{\sqrt{RoC^2-(x-x_{offset})^2}}+\frac{\left(x-x_{offset}\right)^2*\left(\frac{\partial}{\partial x}\left(x-x_{offset}\right)\right)}{\left(RoC^2-(x-x_{offset})^2\right)^{3/2}}\right)$$

Differentiate the sum term by term:

$$= -\tau * \left(\frac{1}{\sqrt{RoC^2 - \left(x - x_{offset}\right)^2}} + \left(\frac{\partial}{\partial x}\left(-x_{offset}\right) + \frac{\partial}{\partial x}(x) \right) * \frac{(-h+x)^2}{\left(RoC^2 - (x - x_{offset})^2\right)^{3/2}} \right)$$

The derivative of $-x_{offset}$ is zero:

$$= -\tau * \left(\frac{1}{\sqrt{RoC^2 - (x - x_{offset})^2}} + \frac{(x - x_{offset})^2 * \left(\frac{\partial}{\partial x}(x) + 0\right)}{\left(RoC^2 - (x - x_{offset})^2\right)^{3/2}} \right)$$

Simplify the expression:

$$= -\tau * \left(\frac{1}{\sqrt{RoC^2 - (x - x_{offset})^2}} + \frac{(x - x_{offset})^2 * \left(\frac{\partial}{\partial x}(x)\right)}{\left(RoC^2 - (x - x_{offset})^2\right)^{3/2}} \right)$$

The derivative of x is 1:

$$= -\tau * \left(\frac{1}{\sqrt{RoC^2 - \left(x - x_{offset}\right)^2}} + 1 * \frac{(x - x_{offset})^2}{\left(RoC^2 - (x - x_{offset})^2\right)^{3/2}} \right)$$

Simplify the expression:

$$Figure\ Inv.LRC = -\tau * \frac{RoC^2}{\left(-{x_{offset}}^2 + RoC^2 + 2 * x_{offset} * x - x^2\right)^{3/2}}$$

9. Appendix C: Results of the Slope Simulation using NANGO

Table 46: SAM Mode 1-2 accuracy. NOM slope amplified by 50 times

Mode	DIC Edge x [px]	DIC Edge y [px]	ROI [y*x]	DIC ROI [y*x] diff. [%]	N. of scans	ASF [urad/px]	Slope [µrad/mm]	Diff. [%]
Profile simulated: NOM slope error multiplied 50 times [µrad] **Method of comparison:** Comparing slope of linear regression of NOM and SAM slope error (µrad/mm)							Slope=-0.725 SD=0.00449	0
2	300	50	1400*1400	0	2	2.3578	Slope= -0.73037 SD=0.00445	+0.74
1	300	50	1400*1400	0	2	2.3578	Slope=- 0.73122 SD=0.00447	+0.85
2	300	50	2592*1944	+253.19	2	2.3578	Slope=- 0.73219 SD=0.00446	+0.99
1	300	50	2592*1944	+253.19	2	2.3578	Slope=- 0.73304 SD=0.00448	+1.10
2	10	5	2592*1944	+378.29	2	2.3578	Slope=- 0.73105 SD=0.00447	+0.83
Average displacement (mode 2) DIC [px]					0.077372661			
Total range (mode 1) DIC [px]					From -24.58425032 to 26.68327124			

Table 47: SAM Mode 1-2 accuracy. NOM slope amplified by 10 times

Mode	DIC Edge x [px]	DIC Edge y [px]	ROI [y*x]	DIC ROI [y*x] diff. [%]	N. of scans	ASF [urad/px]	Slope [µrad/mm]	Diff. [%]
Profile simulated: NOM slope error multiplied 10 times [µrad] **Method of comparison:** Comparing slope of linear regression of NOM and SAM slope error (µrad/mm)							Slope=-0.145 SD=8.98272E-4	0
2	300	50	1400*1400	0%	2	2.3578	Slope=- 0.14704 SD=2.7437E-18	+1.4
1	300	50	1400*1400	0%	2	2.3578	Slope=- 0.14504 SD=8.9698E-4	+0.03
2	10	5	1400*1400	+84.44	2	2.3578	Slope=- 0.14372 SD=8.947E-4	-0.89
1	10	5	1400*1400	+84.44	2	2.3578	Slope=- 0.14505 SD=8.9698E-4	+0.03
2	10	5	2592*1944	+378.29	2	2.3578	Slope=- 0.14562 SD=8.98115E-4	+0.42
1	10	5	2592*1944	+378.29	2	2.3359	Slope= -0.14412 SD=8.9911E-4	-0.6
1	10	5	2592*1944	+378.29	2	2.3578	Slope= -0.14609 SD=9.03299E-4	+0.75
Average displacement (mode 2) DIC [px]					0.014746474			
Total range (mode 1) DIC [px]					From -5.130382723 to 5.289280191			

Table 48: Mode 1-2 accuracy. NOM slope amplified by 5, used average of 2 scans

Mode	DIC Edge x [px]	DIC Edge y [px]	ROI [y*x]	DIC ROI [y*x] diff. [%]	N. of scans	ASF [urad/px]	Slope [µrad/mm]	Diff. [%]
Profile simulated: NOM slope error multiplied 5 times [µrad] **Method of comparison:** Comparing slope of linear regression of NOM and SAM slope error (µrad/mm)							Slope=-0.0725 SD=8.98272E-4	0
2	300	50	1400*1400	0	2	2.3578	Slope=- 0.07772 SD=4.55149E-4	+7.2
1	300	50	1400*1400	0	2	2.3578	Slope=- 0.07723 SD=4.54189E-4	+6.5
2	10	5	1400*1400	+84.44	2	2.3578	Slope=- 0.07945 SD=4.53613E-4	+9.5
1	10	5	1400*1400	+84.44	2	2.3578	Slope=- 0.07726 SD=4.52127E-4	+6.5
2	10	5	2592*1944	+378.29	2	2.3578	Slope=- 0.07629 SD=4.49471E-4	+5.22
1	10	5	2592*1944	+378.29	2	2.3578	Slope= -0.07658 SD=4.48566E-4	+5.6
Average displacement (mode 2) DIC [px]					0.008045646			
Total range (mode 1) DIC [px]					From -2.648281702 to 2.748094398			

Table 49: Mode 1-2 accuracy. NOM slope amplified by 5, used average of 6 scans

Mode	DIC Edge x [px]	DIC Edge y [px]	ROI [y*x]	DIC ROI [y*x] diff. [%]	N. of scans	ASF [urad/px]	Slope [µrad/mm]	Diff. [%]
Profile simulated: NOM slope error multiplied 5 times [µrad] **Method of comparison:** Comparing slope of linear regression of NOM and SAM slope error (µrad/mm)							Slope=-0.0725 SD=8.98272E-4	0
2	300	50	1400*1400	0	6	2.3578	Slope= -0.0762 SD=4.53106E-4	+5.1
1	300	50	1400*1400	0	6	2.3578	Slope= -0.07586 SD=4.52042E-4	+4.63
2	10	5	1400*1400	+84.44	6	2.3578	Slope= -0.07782 SD=4.52884E-4	+7.33
1	10	5	1400*1400	+84.44	6	2.3578	Slope= -0.07566 SD=4.51349E-4	+4.35
2	10	5	2592*1944	+378.29	6	2.3578	Slope= -0.07533 SD=E-4.5233E-4	+3.9
1	10	5	2592*1944	+378.29	6	2.3578	Slope= -0.07558 SD=4.51486E-4	+4.24